FLUORESCENT NANOPARTICLES

A PROBE TO STUDY THE MOLECULAR TRAFFICKING OF SOMATOSTATIN

By

Varun Kumaraswamy Annayya Chetty Sreenivasan

A THESIS SUBMITTED TO MACQUARIE UNIVERSITY
FOR THE DEGREE OF
DOCTOR OF PHILOSOPHY
DEPARTMENT OF PHYSICS AND ASTRONOMY
OCTOBER 2012

MACQUARIE
UNIVERSITY
FACULTY OF SCIENCE

Except where acknowledged in the customary manner, the material presented in this thesis is, to the best of my knowledge, original and has not been submitted in whole or part for a degree in any university.

Several parts of this thesis materialized as a result of collaborative efforts with my supervisors and other research institutions. Their contributions are recognised and have been duly acknowledged at the respective sections.

Varun Kumaraswamy Annayya Chetty Sreenivasan

Dedicated to my parents...

Acknowledgements

My special thanks to dad, Sreenivasan K A and mom, Vanaja R S, who supported me on the pursuit of a doctoral degree, and enduring three-and-a-half years of loneliness. Thanks to my brother, Harinarayan Sreenivasan, who has always stood by my decision on undertaking post-graduate training and academia.

I express my gratitude towards my supervisor, Andrei Zvyagin, without whom this project and thesis would not have happened. His motivation and optimistic views on every aspect of this project has always been a key player. Thank you very much for maintaining a very friendly relationship, and providing scientific, as well as moral support.

I appreciate the brainstorming meetings and emails with Ann Goodchild, my associate supervisor, that materialized as turning points in the course of this thesis. I appreciate her continued support.

My unofficial co-supervisor, Mark Connor, provided some of the key ideas and suggested awesome experiments that were crucial for the success of this thesis. I appreciate his welcoming attitude and encouragement. Thanks to his "rocking lab fleet" (Marina Santiago, Alisa Knapman, Marika Heblinski, Rozhin Ashgari, Philip Bennallack, William Redmond, Michelle Haddrill, Dharmica Mistry and Jordyn Stuart), who made the lab an unforgettable place.

Many thanks to Sergey Deyev. My first first-authored paper would not have happened without his input. Untimely meetings with him and brainstorming has increased my knowledge in biochemistry considerably. I will remember his mantra: "Hope for

the best, and prepare for the worst" and "Never use more than half of what you have (precious protein solutions)"! Thanks to his lab members for sharing the chimeric proteins.

Timothy Kelf, my friend and lab post-doc, has been invaluable in the early years of my Ph.D, and helped me at my sour/bitter research pit stops. Thanks for being one of the unfortunates to read several early drafts of this thesis.

Thanks to Eun Ju Kim for showing me the ropes for the biological aspects of the project. I enjoyed her company.

I express my appreciation to Jinjun Sun, a post-doc in my early PhD life. I still remember our endless days of work in the lab at APAF.

Thanks to the APAF and Pia Jenson for mass-spectroscopic analysis of proteins.

Thanks to Macquarie University for providing me with research scholarship (iMQRES) and research funding (MQ PGRF, FoS PGRF).

I express appreciation towards the colleagues and friends in the Department of Physics and Astronomy, in particular Jipeng Lin.

Thanks to the staff at Macquarie University (Carol McNaught, Regina Dunford, Susan Law, Laura Yang, Lisa Chanell, Christine Hale and Tamara Leo) for managing a smooth work environment and support.

I am lucky to have Jana Say and Andrew Edmonds, as friends. While Jana is fun to be with, Andy is a geek, with a lot to learn from. Thanks guys.

Finally, a billion thanks to David Inglis. He has occupied a special place in my life – as a dearest friend, a knowledgeable colleague, a master chef, a bike-fixer, a surf-coach, a family guy and in fact, a role model. He and his family (Lisa, Saiph and Rigel) made my stay in Australia remarkable and memorable.

List of Publications

Peer Reviewed Publications

1. **Varun K. A. Sreenivasan**, Eun J. Kim, Ann K. Goodchild, Mark Connor and Andrei V. Zyvagin, "Targeting somatostatin receptors using *in situ*-bioconjugated luminescent nanoparticles", *Nanomedicine, available online*, 2012

2. Mushtaq A. Sobhan, **Varun K. A. Sreenivasan**, Michael J. Withford and Ewa M. Goldys, "Non-specific internalization of laser ablated pure gold nanoparticles in pancreatic tumour cell", *Colloid Surf. B-Biointerfaces*, Vol. 92, pp. 190, 2012

3. Ekaterina A. Ivukina, **Varun K. A. Sreenivasan**, Oleg A. Stremovskiy, Boris V. Veryugin, Sergey V. Lukash, Andrei V. Zvyagin, Sergey M. Deyev, and R. V. Petrov, "Fluorescent nanodiamond bioconjugates on the base of barnase:barstar module", *Dokl. Biochem. Biophys.*, Vol. 440, pp. 231, 2011

4. **Varun K. A. Sreenivasan**, Oleg A. Stremovskiy, Timothy A. Kelf, Marika Heblinski, Ann K. Goodchild, Mark Connor, Sergey M. Deyev and Andrei V. Zvyagin, "Pharmacological characterization of a recombinant, fluorescent somatostatin receptor agonist", *Bioconjugate Chem.*, Vol. 22, pp. 1768, 2011

5. **Varun K. A. Sreenivasan**, Ekaterina A. Ivukina, Wei Deng, Timothy A. Kelf, Tatyana A. Zdobnova, Sergey V. Lukash, Boris V. Veryugin, Oleg A. Stremovskiy, Andrei V. Zvyagin and Sergey M. Deyev, "Barstar:barnase – a versatile platform for colloidal diamond bioconjugation", *J. Mater. Chem.*, Vol. 21, pp. 65-68, 2011

6. T A Kelf, **V K A Sreenivasan**, J Sun, E J Kim, E M Goldys and A V Zvyagin, "Non-specific cellular uptake of surface-functionalized quantum dots", *Nanotechnology*, Vol. 21, Article # 285105, 2010

Conference Presentations and Posters

1. **Varun K. A. Sreenivasan**, Ekaterina A. Ivukina, Timothy A. Kelf, Oleg A. Stremovskiy, Ann K. Goodchild, Mark Connor, Sergey M. Deyev and Andrei V. Zvyagin, "Interfacing nanodiamonds for single molecular optical-biomedical imaging", *IQEC/CLEO Pacific Rim*, 2011

2. **Varun K. A. Sreenivasan**, Ekaterina A. Ivukina, Timothy A. Kelf, Oleg A. Stremovskiy, Ann K. Goodchild, Mark Connor, Sergey M. Deyev and Andrei V. Zvyagin, "Functionalizing luminescent nano-diamonds with proteins for targeted tumor delivery", *Gordon Research Conference on Cancer Nanotechnology*, 2011

3. **Varun K. A. Sreenivasan**, Ekaterina A. Ivukina, Wei Deng, Timothy A. Kelf, Eun J. Kim, Marika Heblinski, Ann K. Goodchild, Mark Connor, Sergey M. Deyev and Andrei V. Zvyagin, "Dressing-up nanoparticles for biomedical applications", *KOALA*, 2010

4. **Varun K. A. Sreenivasan**, Eun J. Kim, Timothy A. Kelf, Vikram J. Tallapragada, Ewa M. Goldys, Ann K. Goodchild and Andrei V. Zyvagin, "Biologically active peptide facilitates quantum-dot cellular uptake", *International Conference on Nanoscience and Nanotechnology (ICONN)*, 2010

5. **Varun K. A. Sreenivasan**, Jinjun Sun, Eun J. Kim, Timothy A. Kelf, Vikram J. Tallapragada, David W. Inglis, Krystyna D. Tomsia, Ewa M. Goldys, Ann K. Goodchild and Andrei V. Zyvagin, "An investigation into the non-specific binding of commercially available quantum dots", *Light In Life Science (LILS)*, 2009

Abstract

Somatostatin is a biological molecule that serves important physiological functions in a human body, including the regulation of blood pressure and growth. These functions are furnished by a set of complex interactions between somatostatin and other participating biomolecules. The main goal of this Ph.D. project was to develop tools based on fluorescent nanoparticles that can report on these interactions at a molecular scale. Fluorescent nanoparticles offer the advantages of protein-comparable size, high detection sensitivity, biocompatibility, and physical, chemical and photophysical stabilities, in comparison with many conventional molecular probes.

Three key milestones of this project included: (i) Elucidating and harnessing the interactions of nanoparticles with biological molecules and cells. In particular, two types of nanoparticle-cell interactions were investigated: non-specific interactions, characterized by poorly controllable parameters, such as nanoparticle size, charge and surface chemical groups; and specific interactions, characterized by a precise communication protocol of a particular cell type with a nanoparticle surface, grafted with a specific ligand. As a result of these investigations, the non-specific interaction channel was inhibited, whereas the somatostatin-specific interaction channel was activated. (ii) Development of a universal biofunctionalization methodology to assemble robust, versatile nanoparticular and biomolecular modules. Specifically, an affinity molecular pair based biofunctionalization platform was developed, which allowed a 'pot-mix' procedure to attach biomolecules onto nanoparticle surfaces. (iii) Design, synthesis and demonstration of a biologically active nanoparticle-somatostatin complex. This included two

stages: characterization of the receptor-binding activity of somatostatin ligands loaded with a fluorescent tag, such as a red fluorescent protein; and introduction and testing of a two-stage nanoparticle biofunctionalization and receptor-mediated internalization procedure, which allowed to circumvent the loss of the somatostatin-nanoparticle biological activity. Identification and rectification of the loss of biological activity has been one of the core accomplishments. Such an assembly has been demonstrated to be suitable for observing the somatostatin-cell interactions.

A comprehensive, multi-stage program for tagging fluorescent nanoparticles to a targeting biomolecule has been incepted and carried out to a successful completion. The prospects of deploying fluorescent nanoparticle labeling technology is far-reaching, ranging from *in vivo* investigations of neuronal machinery to tumor diagnosis and treatment. This work is believed to provide a tangible contribution to nanotechnology and life sciences.

Contents

1

General Introduction and Outline

Precise and harmonious molecular interactions nurture life by supporting a great variety of physiological functions. Understanding life can be summarized in two simple questions – '*why* and *how* these molecules interact?' and '*what* the outcomes of these interactions are?'. While '*why*' may be philosophically addressed (and will be ignored), answering the questions '*how*' and '*what*' scientifically is non-trivial due to the complexity, and time- and length-scales of these interactions. Most of the scientific and technological efforts have been focussed on accessing these time- and length-scales. Advances in the areas of molecular detection and isolation, ultrafast devices and microscopy has enabled us progress in our pursuit towards this goal.

More recently, efforts to meet the challenges of small-length scales has led to the emergence of the field of nanotechnology. At the current state, nanotechnology refers to the control and manipulation of structures at the nanometer scale, where *unusual*

material properties may be witnessed[199]. The significance of nanotechnology extends to a number of arenas, including basic and applied research, industry and healthcare. Nanotechnology, as a discipline, emerged in the late 1990s, arguably incepted by the dinner lecture "There is a lot of room at the bottom", delivered by Richard Feynman on the 29th of December, 1959[129].

A particular class of nanotechnological material – nanoparticles – have enabled rapid progress towards better understanding and control of the biomolecular interactions, because of the following key properties. Firstly, in virtue of the conspicuousness of nanoparticles, biomolecules of interest can be specifically tagged and tracked for long periods of time. This is possible by attaching the molecule or its complementary terminal to nanoparticles, in order to render the biomolecule visible. Secondly, certain nanoparticles change their measurable properties (for example, color) when a molecular binding event occurs, therefore suitable for sensing application. Thirdly, the use of nanoparticles allows realization of novel biomolecular separation methods, such as protein purification. Finally, nanoparticles can be used as a vehicle, for genetic or drug cargo delivery to specific locations in cells or tissues, suitable for both diagnostic and therapeutic applications.

The first property of nanoparticles is of particular interest to this PhD project, whereby a complete multistage program of fluorescent nanotechnology application to tag and investigate molecular pathways will be demonstrated. Somatostatin (SST) is chosen as the targeting molecule. Since 1980s, SST has been known to participate in crucial functions of the body, including the control of blood pressure, breathing, metabolism, memory, growth etc. However, many questions pertaining to such SST-mediated regulation processes still remain unanswered. Fluorescent nanoparticles represent as promising molecular probes to provide an insight into these processes. The goal of this project was the development and demonstration of a nanoparticle-based tool for the visualization of the molecular dynamics of somatostatin in cells, and its potential use for tumor diagnosis. Stages during the development of the nanoparticle-somatostatin probe are documented progressively in this work.

1.1 Thesis Outline

This thesis contains 7 chapters, including two introductory, an experimental methods and four results chapters.

- Introductory chapters

  - Chapters 2 and 3 cover basic physical and biological concepts and brief literature reviews pertinent to this thesis, respectively.

- Experimental methodology

  - Chapter 4 documents the details of common experimental procedures used throughout the PhD project.

- Experimental results and discussions.

  - Chapter 5, named 'Talking to the cells', documents the development, characterization and application of a novel, genetically engineered, fluorescent somatostatin molecule. This chapter also introduces techniques with which the somatostatin-cell interactions were characterized and controlled.

  - In Chapter 6, the characterization of several commercially available fluorescent semiconductor nanoparticle samples is addressed, aiming at selection of the optimal nanoparticle probes for somatostatin imaging. The selection criteria included minimal fluorescence background due to non-specific, uncontrollable internalization of nanoparticles. The parameters that influence non-specific attachment and uptake of nanoparticles in cells, including temperature, were investigated and analyzed to determine the optimal nanoparticle probe for several experimental demonstrations described in this work.

  - In Chapter 7, the development of a versatile platform for attachment of biomolecules to nanoparticle surface is described. Fluorescent nanodiamonds were used as the model nanoparticles. The developed strategy was confirmed to be easy, versatile and robust at the same time.

– In Chapter 8, the details of the molecular imaging of somatostatin using fluorescent nanoparticles is described. All the previously developed techniques coalesce, resulting in a specific and sensitive fluorescent somatostatin probe.

- Appendices

  – Appendices A, B and C contain programs (graphical user interfaces) written in MATLAB for automated cell counting and analyzing large data sets.

  – Appendix D contains the copy of two biosafety approvals that were obtained to carry out cell-based experiments reported in this thesis.

2

Fluorescence – Basics, Imaging and Nanoparticles

Fluorescence, fluorescence microscopy and nanoparticles form the corner stones of this thesis. Introduction of important and relevant terminologies related to fluorescence, followed by brief discussions on the conventional fluorescence methods, and their shortcomings, in the context of optical microscopy, are addressed in the first part of this chapter. These discussions usher the necessity of novel fluorescent materials, where nanoparticles play the key role, in virtue of a blend of their physiochemical and photo physical properties. The origin of the nanoparticle fluorescence, and a brief outlook of the main approaches of fluorescent nanoparticle-assisted optical imaging are addressed in the second half of the chapter.

Contents

2.1 The Phenomenon of Fluorescence

Fluorescence is the emission of light by a substance that has absorbed electromagnetic radiation, usually at a different spectral band. The shift in spectral band of the light emitted by fluorescence, when compared to the absorbed light (also termed 'excitation light'), allows their decoupling by employing spectral filtration techniques, enabling suppression of the excitation light. The mode of acquisition of the fluorescent light can be tailored in such a way that the information regarding the location, distribution and functional state of an ensemble of fluorescence emitters can be probed; leading to advanced imaging, sensing and manipulation of the fluorescent material. Fluorescence as a probing tool is currently used in a range of areas including astronomy, geology, meteorology, biophysics, biochemistry and medicine. This section focusses on the origin and main properties of fluorescence, starting with a brief historical note. Further information on these topics is readily available in various text books[19,143].

Historical evidences suggest that fluorescence was first observed as a phenomenon of blue glow from the chemical matlaline[260] present in wood, by a Spanish physician and botanist, Nicholas Monardes in 1565. More descriptive studies of the fluorescence appeared only in the 19th century, when Herschel[107] observed the ultraviolet (UV) region of the sunlight induced a diffuse blue glow of quinine solution. More investigative experiments on this glow by Stokes[245], in 1852, led to the discovery of the "Stokes shift", which will be discussed below. At present, fluorescence is well addressed experimentally, wide spread in investigative and practical procedures, and a theoretical framework on its origin is reasonably established.

Fluorescence of materials is typically a result of its constituent molecules' fluorescent responses, and it takes place in three consecutive steps (see Figure 2.1) – (1) absorption and conversion of excitation light energy to electronic and vibrational energy of the fluorescent molecule, (2) probable loss of the vibrational energy to environment and (3) conversion of the resultant electronic energy, back into light. These steps can be understood using Jablonski energy level diagram, as shown in Figure 2.1 and explained below.
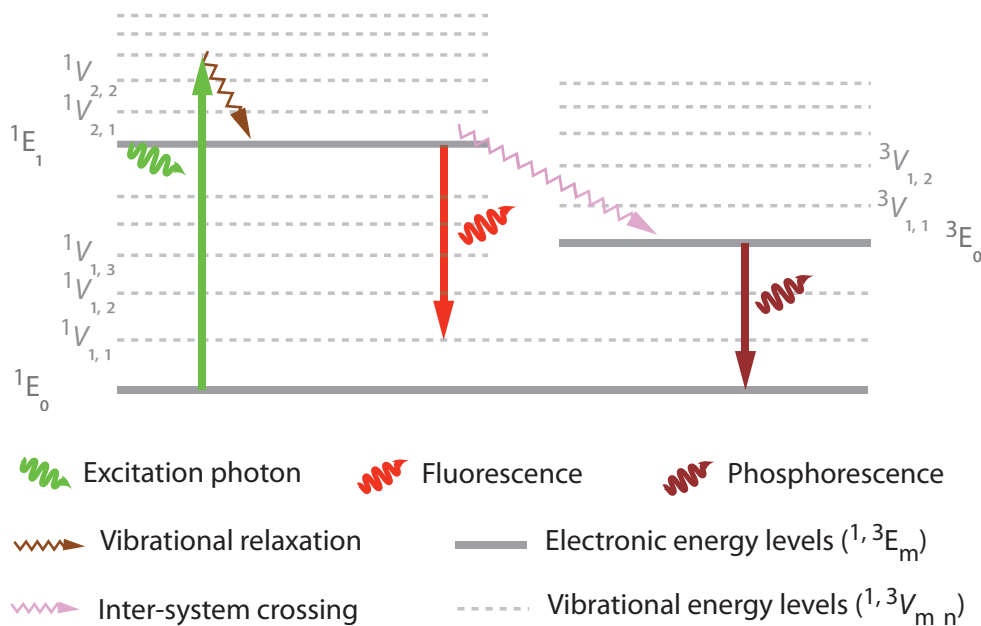
Figure 2.1: A Jablonski energy diagram depicting possible transitions that occur after absorption of light. Upward arrow denote molecular excitation, whereas downward arrows show relaxations. V and E denote vibrational and electronic energy levels, respectively. Subscripts denote the order of the energy level, and $V_{m,n}$ are the vibrational energy levels within the $E_m{}^{th}$ electronic energy level. Superscripts of E and V correspond to the degeneracy of the levels – ^{1} is singlet and ^{3} is triplet.

A Jablonski diagram is a schematic representation of energy levels that a molecule can occupy, as a function of a characteristic of the levels, called degeneracy[143]. Degeneracy refers to the number of ways in which the total spin of unpaired electrons can orient with respect to its orbital angular momentum, as allowed by quantum mechanics[19]. Degeneracy of energy levels influence the transitions by which a molecule can accept or emit electromagnetic energy, as will be discussed. Total energy of a molecule is a sum of its rotational (not shown), vibrational and electronic energies. The Born-Oppenheimer approximation suggests that a molecule can occupy different vibrational states at each electronic state, as shown in Figure 2.1. At room temperature, a molecule usually occupies the lowest electronic energy level (ground state). By absorbing a photon in the electromagnetic spectral region, the molecule can transit to a higher electronic level (excited state), shown by the green arrow, upwards in

Figure 2.1. These transitions are usually accompanied by promotions to higher vibrational states[†]. Such an excited molecule undergoes quick vibrational relaxation to the lowest vibrational level (that is, $^1E_1$), by non-radiatively dissipating its energy to the environment. It is the radiative relaxation from $^1E_1$ to the ground state ($^1E_0$) or, more often, to one of its higher vibrational states – $^1V_{1,1}$, $^1V_{1,2}$, $^1V_{1,3}$, ... that gives rise to fluorescence (see Figure 2.1, red downward arrow). The loss of the excitation energy by two vibrational relaxations in one round-trip accounts for Stokes shift, where the energy of the emitted photon is lower than that of the absorbed photon. For example, a UV photon absorbed by quinine is down-converted in energy to an emitted photon in the visible spectral range, e. g., a blue photon, causing the blue glow observed by Stokes[245] and Herschel[107].

Another process closely related to fluorescence is called phosphorescence. This occurs in molecules, which return back to the ground state via an alternative process of the inter-system crossing. Inter-system crossing occurs when a molecule transits from a particular degeneracy state to another. In Figure 2.1, the energy levels on the left are of degeneracy = 1 (singlet states), while those on the right are of degeneracy = 3 (triplet states), and the inter-system crossing is shown by a pink, ragged arrow. A molecule undergoing inter-system crossing is usually referred to be 'trapped', as a radiative relaxation from the triplet state ($^3E_0$) back to the ground singlet state ($^1E_0$) is inefficient. It takes much longer time (usually ranges from milliseconds to minutes, as compared to a few nanoseconds in the case of direct transitions) for the molecule to return back to the ground state, and the associated emission is called phosphorescence. Phosphorescence is the reason some materials glow in the dark after exposure to bright light. Phosphorescence was first observed by a French physicist Edmond Becquerel, even before Stokes observed fluorescence[260]. Fluorescence and phosphorescence are grouped into a broader class of photoluminescence. Hereafter, we will focus on the phenomenon of fluorescence.

[†]This is a manifestation of the Frank-Condon principle[19]

2.1.1   Fluorescence - Properties and Measurements Methods

Main fluorescence properties and measurement methods are discussed in this section. Many of these methods were instrumental in the course of this project.

2.1.1.1   Fluorescence Spectra

The configuration of large number of vibrational and electronic energy levels of a molecule, as shown in Figure 2.1, and differences in efficiencies of radiative relaxations between them give rise to an energy- (or wavelength-) dependent fluorescence emission intensity, usually measured as fluorescence emission spectra. A representative emission spectra of a well known fluorescent species (a fluorophore), anthracene, obtained under excitation at two different wavelengths, 340 nm and 357 nm, are shown in Figure 2.2. Three peaks in the emission spectra correspond to radiative relaxations of the molecule from the excited state to three vibrational levels at the ground electronic state. Note that the profile of the fluorescence emission spectra is independent of the excitation wavelength, although variation in intensity can be observed. This is due to the wavelength-dependent absorption of the excitation light, which can, in turn, be represented as a fluorescence excitation spectra [see Figure 2.2]. Three peaks in the fluorescence excitation spectra correspond to the excitations from the ground state to three vibrational states in the excited electronic level. The fluorescence emission and excitation spectra are generally acquired using a fluorescence spectrometer or a fluorimeter, which is detailed in Section 4.1.2.

2.1.1.2   Quantum Efficiency and Quantum Yield

After a molecule transits to the excited state by absorbing light, the probability of undergoing radiative relaxation versus vibrational relaxation determines the fluorescence efficiency. The fluorescence efficiency, otherwise known as quantum efficiency of fluorescence (η), is a ratio of the number of photons emitted to the number of molecules in the excited state[167]. Quantum yield (QY) is another closely related parameter, defined as the ratio of number of photons emitted to the number of photons absorbed, and
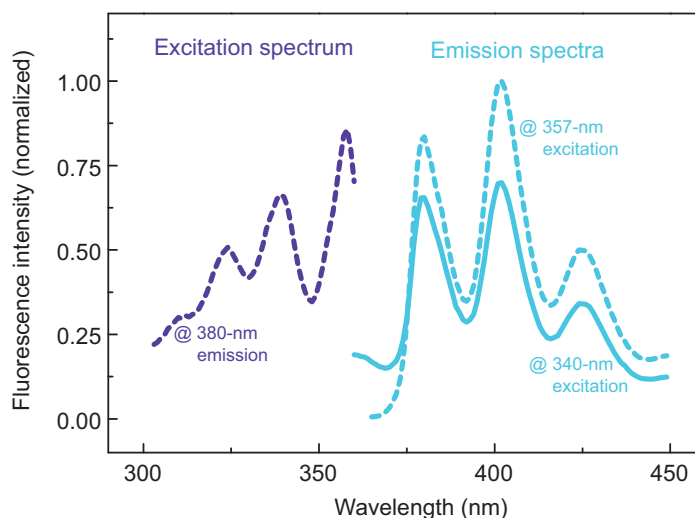
Figure 2.2: Fluorescence emission and excitation spectra of anthracene. Two emission spectra were acquired at excitation wavelengths of 340 nm (solid cyan line) and 357 nm (dashed cyan line). An excitation spectrum was acquired with emission wavelength fixed at 380 nm (dashed purple line).

should not be confused with the quantum efficiency. These and other terminologies associated with fluorescence are systematically presented by Melhuish[167], in an article published by the International Union of Pure and Applied Chemistry (IUPAC).

2.1.1.3   Fluorescence Lifetime

Fluorescence lifetime (τ) is defined as the time required for the fluorescence intensity to decay from an initial value (measured at t = 0) to e^{-1} of that value[167]. Considering a fluorophore with two energy levels, it is the average time a molecule spends in the excited state before relaxing to the ground state. In case of organic fluorophores, τ ranges from 1 ns to 10 ns, and is determined by the rates of both radiative and non-radiative relaxations from the fluorophores' excited state[143]. Fluorescence lifetimes are usually measured by phase fluorimetry or flash fluorimetry[191]. In the phase fluorimetery method, τ is determined by measuring the shift in phase of the emitted light following excitation by an intensity-modulated light[223]. In the flash fluorimetery method, short pulses of light are used for the excitation, followed by recording the fluorescence decay signal. The fluorescence lifetime(s) is determined by single- (or multi-) exponential

fitting.

2.1.2   Applications of Fluorescence

A record of applications of fluorescence and phosphorescence commenced within decades after its discovery. Becquerel proposed coating the inner surface of electric discharge tubes to convert the generated UV light to visible, which is still widespread in modern fluorescent lighting. Another early application of fluorescence was reported in 1887, in hydrogeology, where the path of the Danube river was traced by pouring and tracking ten liters of concentrated disodium salt of fluorescein (uranin)[260]. A great number of applications of fluorescence has since been developed such as, genetic forensics[238], pollution detection[121], healthcare[25,148,195], molecular sensing[8], macromolecular sequencing[243], histology[41], cellular and molecular biology[149,240] etc. Fluorescence imaging and microscopy represents an important application scope that is relevant to this thesis.

2.2   Fluorescence Microscopy

Traditionally, microscopy is considered as an optical magnification technique to overcome the limits of native ocular resolution, in order to visualize minute spatial details. The use of magnifying tools have been dated back to the Assyrians of 600 B. C., based on the archeological remains of crude lenses. However, documented accounts on microscopes are only available since the 16th-17th century, by Galileo Galilei, Robert Hooke and Antoni van Leeuwenhoek[208,261]. Since then, development of microscopy proceeded at a high rate. At present, microscopy usually refers to the the technology of magnification, in combination with one or the other modes of contrast enhancement to separate regions under investigation (the signal) from the rest (background)[152]. The modes of contrast mostly rely on specific properties of the sample (intrinsic or extrinsic) including spatial variations of transparency, fluorescence, birefringence, scattering, refractive index, thickness, fluorescence lifetime and nonlinear optical properties[231].

Fluorescence microscopy relies on the contrast provided by fluorescent molecules in a sample, whose main property is the emission of fluorescence light, after absorbing

appropriate excitation light of a narrow spectral band. The Stokes shifted fluorescence emission allows an almost complete isolation of the fluorescent signal from the excitation light and ambient background by using wavelength-selective filtering and detection optics. A conventional fluorescence microscope can allow visualization of single fluorescent molecules separated by several hundred nanometers, as determined by the Rayleigh criterion[33]. The resolution and background suppression can be further improved by employing: confocal fluorescence microscopy[240], time gated fluorescence microscopy[230], multi-photon fluorescence microscopy[62], up conversion microscopy[51], and their combinations. A cutting-edge advancement in fluorescence microscopy, namely, the STochastic Optical Reconstruction Microscopy (STORM) offers very high resolutions ≈ 50 nm even in 3D specimens[264].

Fluorescent molecules that provide contrast for microscopic visualization, also known as fluorophores, can be classified into intrinsic or extrinsic (or endogenous or exogenous), depending on their natural or introduced fluorescence properties. The naturally occurring fluorescent molecules including tryptophan, nicotinamide adenine dinucleotide (NADH), ADH, chlorophyll etc. are examples of intrinsic fluorophores[143]. At the same time, technological advances in biochemistry and molecular labeling has enabled the attachment of extrinsic fluorescence molecules (or, simply, fluorescent probes) to specific molecules of interest in a biological specimen. For example, Figure 2.3 shows the image of a cluster of three rat pancreatic cells, whose nuclei and cell membranes were labeled using two fluorescent probes, Hoechst 33342, and fluorescent nanoparticles, respectively. Hoechst 33342 is a well known fluorescent probe that binds specifically to certain grooves in a DNA strand to render them visible[242], while treatment of cells with nanoparticles under certain conditions is known to enable membrane labeling[132].

The library of fluorescent probes currently available for labeling is vast and ever growing[10] (e. g., *Handbook of fluorescent probes and research products*[102]). In general, these probes comprise of two components a fluorophore and a targeting, or sensing group[10,128]. This concept is illustrated in Figure 2.4. The targeting group allows the fluorophore to be tagged to a specific site of the specimen; this strategy will be utilized throughout this thesis (for example, an antibody bound to a dye). In some cases

Figure 2.3: Image of a cluster of three pancreatic tumor cells co-labeled with Hoechst 33342 and fluorescent nanoparticles to visualize nuclei and membranes, respectively. The image was acquired using fluorescence confocal microscopy. Scale bar 10 μm.

targeting groups are replaced with sensing groups, which report on the event of substrate binding as a change in fluorescence. For example, Calcium Green-1, shown in Figure 2.4, contains a chelator as the sensing group, which binds to free Ca^{2+} in a solution. The fluorescence spectra before and after Ca^{2+} binding are different, enabling measurement of the ion-concentration from the resultant spectral shift. Fura-2AM[94] is another example of a Ca^{2+}-sensitive fluorescent probe that is used in Chapter 5. Until late 1990s, most probes contained organic compounds as its fluorophore moiety. Some of these included: fluorescein isothiocyanate, 4',6-diamidino-2-phenylindol (DAPI), propidium iodide[43], anthracene[61], rhodamine[98] etc. However, organic fluorophores have several shortcomings.

2.2.0.1   Typical Shortcomings of Organic Fluorophores

1. They have broad emission spectra, which poses limitations on the number of probes that can be used simultaneously. Therefore, they have a limited scope for multicolor imaging (also known as spectral multiplexing), where more than three types of molecules are to be co-labeled in a sample[185]. Figure 2.5 shows the emission spectra of series of alexa-fluors and their spectral overlap[185], which clearly demonstrates the limitation imposed by their fluorescence spectral width on multiplexing.
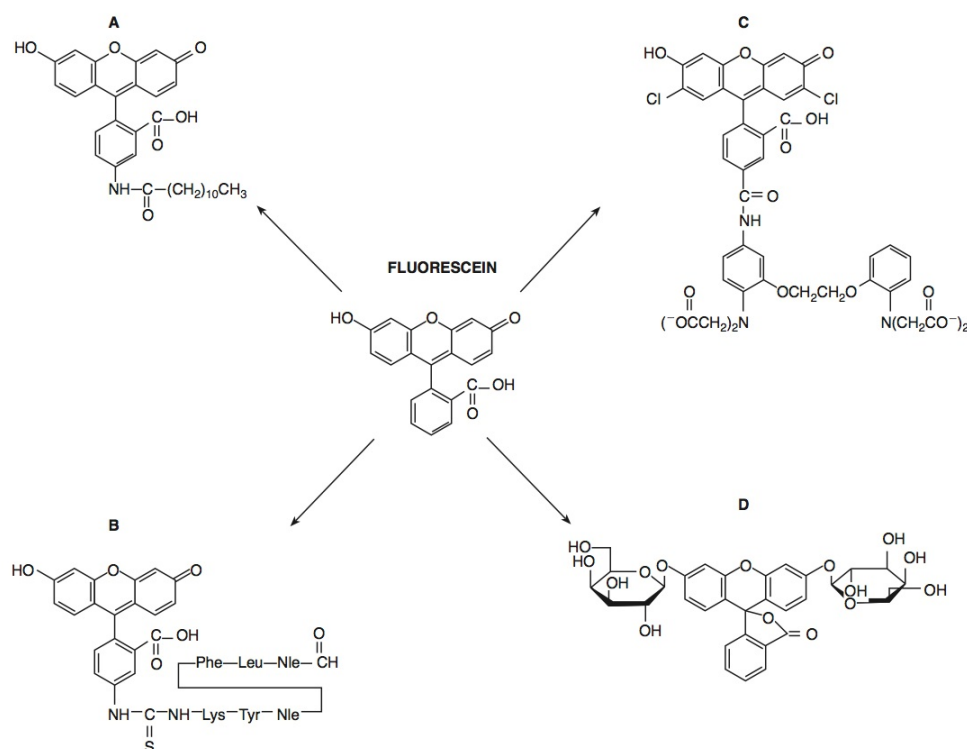
Figure 2.4: Fluorescent probes containing fluorescein as the fluorophore. They are named after the targeting molecule attached to fluorescein: (A) 5-Dodecanoylaminofluorescein, a liphophilic probe allowing membrane labeling; (B) fluorescein coupled to a hexapeptide formyl-Nle-Leu-Phe-Nle-Tyr-Lys, a fluorescent probe to label the chemotactic peptide receptor of neutrophils; (C) Calcium Green-1 consisting of dichlorofluorescein coupled to the Ca^{2+}-chelator, BAPTA; (D) fluorescein di-β-D-galactopyranoside, a fluorogenic substrate for β-galactosidase. Reproduced from the paper by Johnson[128] with copyright clearance.

2. The fluorescence from organic fluorophores tends to decay upon prolonged exposure to the excitation light – a phenomenon called photobleaching. This precludes their use in time-lapse fluorescent imaging, especially in real-time with small ensembles of fluorophores[91,168]. A plot and corresponding images that show rapid photobleaching of a green fluorescent protein sample upon exposure to 514-nm laser are presented in Figure 2.6.

3. The emission and excitation spectra (intensity and wavelength) of organic fluorophores are often susceptible to environmental changes, such as pH[176], osmolarity (see Figure 2.7) and attachment of targeting moieties[185].

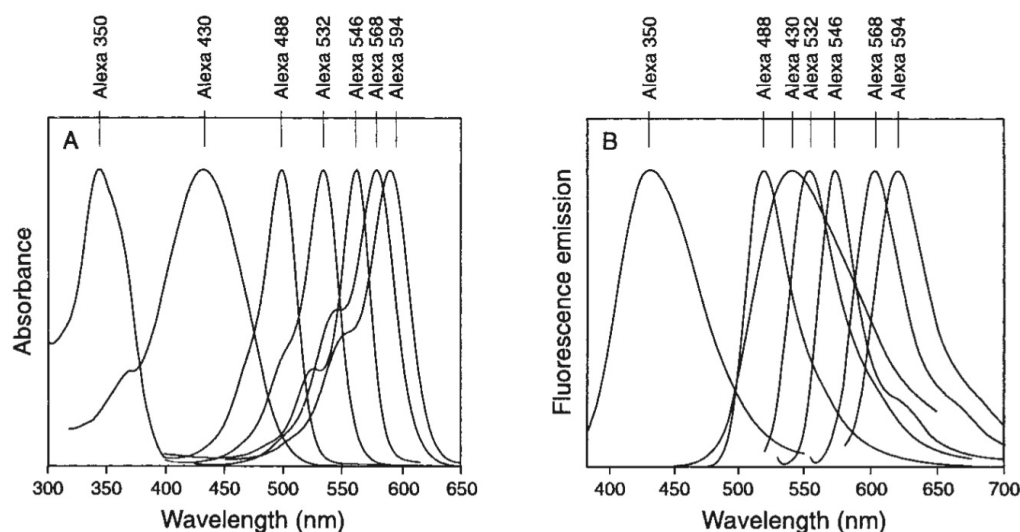4. Many of the commonly used organic fluorophores, even those approved for clinical

Figure 2.5: Normalized fluorescence excitation (A) and emission (B) spectra of a range of alexa fluorophores. Reproduced from the paper by Panchuk-Voloshina et al.[185] with copyright clearance.
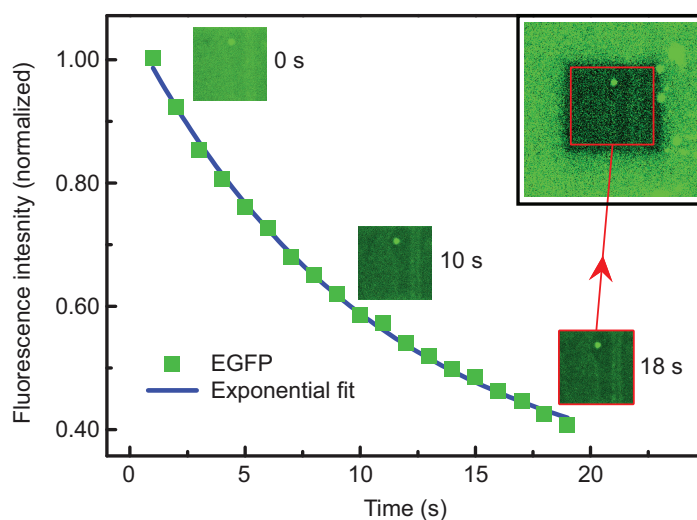

Figure 2.6: Photobleaching of enhanced green fluorescent protein (EGFP) deposited on a glass slide. Green data points are the mean (normalized) pixel values of the images acquired using a fluorescence confocal microscope, at time lapse periods, with the laser excitation at a wavelength of 488 nm. Blue line is an exponential fit. Sample images at three time-points (0 s, 10 s and 18 s) are presented as snippets adjacent to their respective data points. Inset shows a zoomed out picture obtained after 18 s, which clearly demonstrates the photobleached area. Red box is 18 μm $\times$ 18 μm.
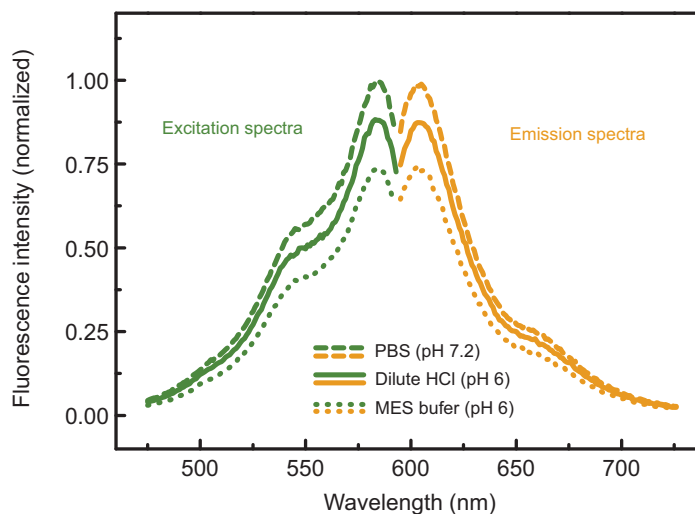
Figure 2.7: Variation in the fluorescence intensity of a monomeric red fluorescent protein (mRFP)-containing fluorescent probe, SST-mRFP (see Chapter 5 for details), at different pH and osmolarity conditions. MES is 2-(N-morpholino)ethanesulfonic acid; PBS is phosphate buffered saline.

use, are toxic[10].

5. Fluorescence quantum yields of organic molecules are low, usually below 50%. The quantum yield of infrared dyes are much lower, despite being very desirable for deep tissue observations, because of their fluorescence emission falling in the so-called "biological tissue transparency window" – the spectral region between 670 - 900 nm, characterized by minimal optical extinction.

The above mentioned drawbacks of organic fluorophores stipulate a need for robust and efficient alternatives that have narrow fluorescence emission spectra, low toxicity, and allow easy labeling to a targeting/sensing moiety. The development of nanotechnology in late 20th century resulted in a range of nanoparticles that were capable of satisfying most of these criteria. It is worth mentioning that in some cases, the drawbacks of the organic fluorophores noted above can be exploited for some specific applications. For example, fluorescence recovery after photobleaching (FRAP) relies on the photobleaching of fluorophores in a small microscopic region, which recovers over time by diffusion of unbleached fluorophores from the surrounding media. The

time scale of recovery provides valuable information on the diffusion coefficient of the fluorophore, and therefore, the size of the molecule or viscosity of the medium.

2.3   Nanoparticles for Fluorescence Microscopy

Materials that were not immediately attractive as fluorophores exhibited new, valuable properties at the nanometer scale. Indeed, when particle dimensions approach the length scales of electronic wave functions, the optical properties deviate (significantly) from those of bulk material. Nanoparticles can ameliorate the shortcomings of organic fluorophores, provided they have the following properties:

1. *Chemical and fluorescence stability*: Biological applications require that extrinsic fluorophores are stable and inert under various chemical and biochemical environments.

2. *High contrast*: Increased contrast enables visualization of molecular probes with high sensitivity. In fluorescence microscopy, this can be achieved by using fluorophores with high fluorescence efficiency, large or negative stokes shift, large fluorescence lifetime etc.

3. *Biocompatibility*: A nanoparticle that allows easy attachment of targeting or sensing molecules is desirable.

4. *Controllable size*: Optimal size of nanoparticle required for labeling application is still debated. It typically ranges from 5 nm to 100 nm.

5. *Non-toxicity*: It is essential that extrinsic fluorophores introduced into a biological system are inert and non-toxic.

6. *Other modes of contrast*: It is often desired that a sample labeled by a fluorescent probe is observable by alternative means, such as electron microscopy, which can provide resolution at the nanometer level.

At present, the library of nanoparticles that fulfill most of these criteria is quite large, and include semiconductor nanoparticles (quantum dots)[11,110], fluorophore impregnated matrices (especially silica or latex)[282], color center-containing nanocrystals (fluorescent nanodiamonds), up conversion nanophosphors[103] and other core-shell particles (metal-core with fluorescent shell). Each of these are unique in terms of their size, fluorescence quantum efficiency, fluorescence spectral response, surface chemistry etc. Discussions on the origin of their fluorescence, other characteristics, and applications will be limited to two of these particles – quantum dots and fluorescent nanodiamonds.

2.4 Quantum Dots (QDs)

QDs are nanometer-sized semiconductor crystals that generally contain several thousand atoms[210]. They display outstanding optical properties, including high absorption cross-section and fluorescence quantum yield. These exceptional properties arise from their unique quantum structure, as discussed below.

2.4.1 QD Quantum Structure

In a bulk semiconductor, electronic energy levels are grouped into valence and conduction bands, separated by an energy gap, as presented in Figure 2.8 along with their corresponding energy level densities (or the density of states[†])[16,135]. At room temperature, most of the electrons occupy the valence band, but gets transferred to the conduction band by absorbing energy greater than that of the energy gap. This leads to generation of a positively charged 'hole' in the valence band. When an excited electron and a hole are in the vicinity, they may experience Coloumb attraction and form an exciton pair[210]. The wave function of an exciton pair normally extends over distances that correspond to multiple lattice spacings. In CdSe crystals, this distance is ≈ 5 nm[210]. If the size of the semiconductor material approaches this dimension, the density of states will undergo modifications leading to the unique optical properties of

---

[†]Density of states is defined as the number of accessible levels located per interval of energy, and is usually presented as a function of the energy.
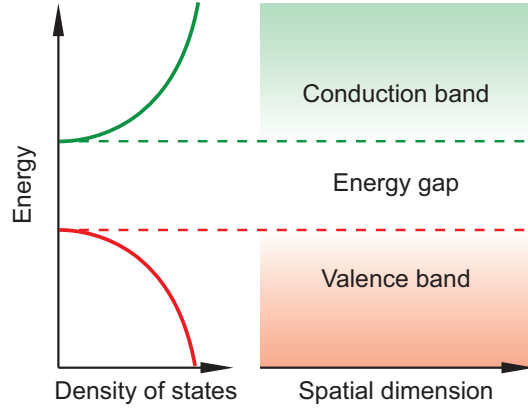
Figure 2.8: Left panel shows the density of states in a bulk semiconductor, resulting in the formation of the conduction and valence bands. The gap between the bands, where the density is zero, is called an energy band gap.

the QD.

Upon etching a bulk semiconductor to make a sheet, several nanometers in thickness, the excitons experience one-dimensional confinement[233]. This structure is referred to as a "quantum well", where the density of states in the two bands cease to be a continuum and takes the form of a sum series of Heaviside step function[†], as shown in Figure 2.9. Etching the semiconductor again in a perpendicular direction would confine the excitons in two-dimensions – a structure referred to as a "quantum wire". In this case the density of states can be expressed as a sum series of Heaviside functions with quadratic divisors, as plotted in Figure 2.9. When the excitons are confined in all three dimensions the system is referred to as a "quantum dot". Here, the energy level structure is treated in the framework of quantum mechanics using a model of "particle in a box", where the density of states is non-zero only at the quantized energy levels expressed in Equation 2.1 (see Figure 2.9).

$$E_{n_x,n_y,n_z} = \frac{\hbar^2 \pi^2}{2m_e} \times \left[\left(\frac{n_x^2}{L_x^2} \right) + \left(\frac{n_y^2}{L_y^2} \right) + \left(\frac{n_z^2}{L_z^2} \right) \right] \tag{2.1}$$

where, E is the energy of the state (n_x, n_y, n_z); m_e is the mass of an electron, and L is the length along the x, y or z axes. A similar equation can be also written for the

---

[†]Heaviside step function, $\mathcal{H}(x)$, is a discontinuous function, whose value is zero for x < 0 and unity for x > 0
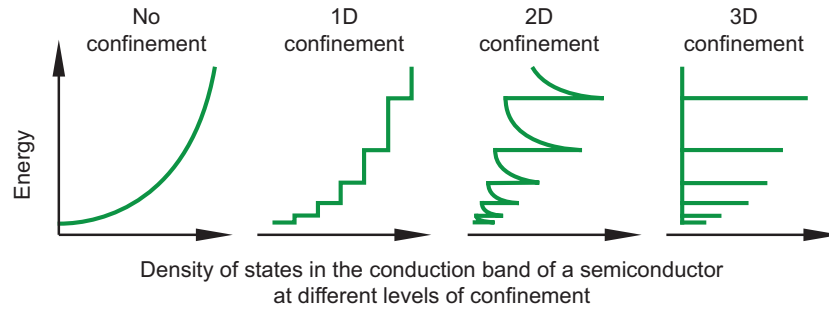
Figure 2.9: The density of states is dependent on the spatial confinement of an exciton. Increasing degrees of confinement causes density of states to depart from a continuous function towards discrete energy levels[233].

energy levels in the valence band.

One of the important consequences of Equation 2.1 is the dependence of the energy levels on the dimension (L_x, L_y, L_z). Upon reducing the size of a QD, the energy levels become more separated, which alters its optical properties (see Section 2.4.2).

2.4.1.1   Direct and Indirect Band Gap Semiconductors

Sometimes, the energy levels of a semiconductor are presented in the theoretical $\boldsymbol{k}$[†]-space or momentum $(\boldsymbol{p} = \hbar\boldsymbol{k})$ space, in order to classify them based on their optical properties. In a plot of the energy vs. $|\boldsymbol{k}|$, the extrema of the conduction and valence bands of silicon and germanium appear horizontally misaligned, as shown in Figure 2.10(a). Such semiconductors are classified as indirect band gap semiconductors[135]. This, essentially, implies that the momenta of the electrons and holes are unequal. In semiconductors such as gallium arsenide or cadmium selenide (CdSe), the extrema of the two bands are aligned [see Figure 2.10(b)], and are classified as direct band gap semiconductors[135]. Most of the III-V or II-VI semiconductors[‡] are characterized as direct band gap semiconductors. The implications of this classification are experienced in their optical properties and is discussed in the following sections.

[†]Bold font is used to denote a vector

[‡]III-V and II-VI semiconductors are formed by mixing elements from the respective groups of the periodic table, at a particular ratio
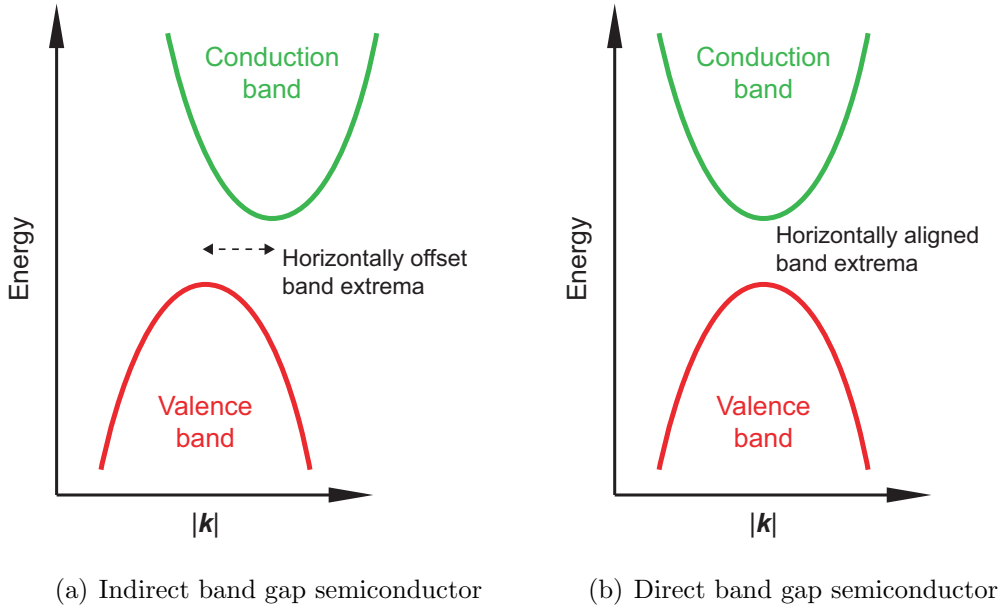
(a) Indirect band gap semiconductor   (b) Direct band gap semiconductor

Figure 2.10: Schematic diagram of the energy bands in (a) indirect and (b) direct band gap semiconductors, in the $\boldsymbol{k}$-space.

2.4.2   Absorption and Fluorescence in QDs

The absorption spectra of a CdSe-based QD are shown in Figure 2.11. The spectral position critically depends on the QD size, because of the size-dependent energy levels according to Equation 2.1. As the QD size is reduced, the energy gap increases, causing a shift in the spectrum to the higher energy (blue shift). QD spectra features a local maxima at the longer wavelength, which represents the exciton absorption band, as it corresponds to the energy required for the generation of an exciton pair. Absorption at the shorter wavelengths is explained by transitions to the higher energy levels in the conduction band. Despite the quantized energy levels in a QD, the spectral features are broad mainly because of the two factors: firstly, the energy levels of QD particles in an ensemble can vary significantly, due to the size distribution[210]; and secondly, because of spectral diffusion, i. e., random dynamic shift in the position of, the otherwise, sharp spectral lines. Spectral diffusion occurs because of the Stark effect caused by dynamic trapping of charges or due to spin fluctuations[217].

The energy absorbed by a QD to form an exciton pair is re-emitted by a radiative pathway or dissipated by non-radiative relaxations. The radiative relaxation can be
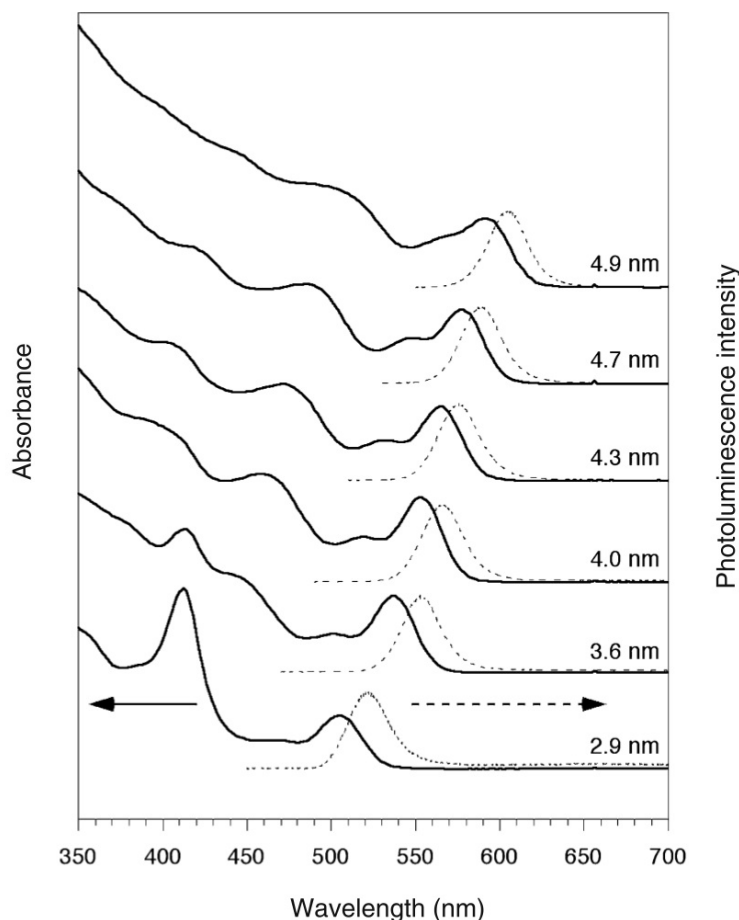
Figure 2.11: Absorption (solid) and fluorescence (dotted) spectra (normalized) of CdSe QDs of difference sizes (2.9 nm to 4.9 nm). Spectra vertically shifted for clarity. Reproduced from the book by Rogach[210].

fluorescence or phosphorescence, depending on whether the transition is spin-allowed or forbidden, respectively, as was discussed in Section 2.1. The fluorescence spectra of CdSe QDs of a range of sizes are shown in Figure 2.11 (dashed line)[210]. It can be seen that the fluorescence spectral peaks are shifted from the exciton absorption band, towards the longer wavelength. This Stokes shift arises from the degeneracy of the exciton energy levels, as reported by experiments and modeled theoretically[72,180] (shown in Figure 2.12 for a CdSe QD). The absorption is most efficient to the second and third degenerate levels in the excited state, from where the excitons relax non-radiatively to the first degenerate level. This relaxation usually occurs via energy transfer into the crystal lattice as vibrations – also referred to as phonons. The system
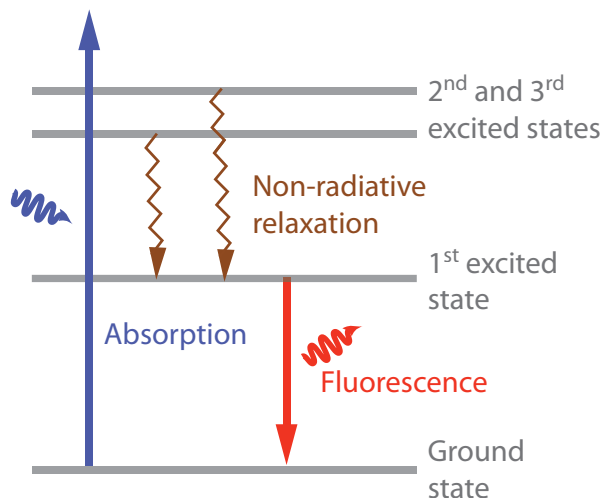
Figure 2.12: Schematic representation of degenerate exciton energy states of CdSe QDs involved in the absorption and emission processes. Adapted from the book by Rogach[210].

returns to the ground state via the radiative relaxation (giving rise to fluorescence). The efficiency of the radiative relaxation is dependent on whether the semiconductor band gap is direct or indirect. Radiative relaxations in the indirect band gap semiconductors are not favored because photons can only be emitted with the assistance of phonons, in order to conserve the energy and momentum in the conduction and valence bands (see Figure 2.10). As the momenta of the electrons and holes overlap in direct band gap semiconductors, a photon with zero momentum can satisfy the energy conservation criteria. This is one of the reasons why most QDs are composed of III-V or II-VI semiconductors with a direct band gap, as opposed to group IV semiconductors, Si or Ge, which have indirect band gaps.

QD fluorescence spectra are usually sharp (20 nm to 40 nm wide), and is mostly limited by the size distribution and spectral diffusion[59], as for the absorption peaks, discussed before. The sharp and size-dependent fluorescence emission spectra enable using QDs of varying sizes to label multiple targets in a sample for spectrally multiplexed imaging with little cross-talk. (see Section 2.2.0.1).

2.4.3 Quantum Dot Synthesis and Considerations

One of the first demonstrations of synthesizing monodisperse CdX (X = Sulfur, Selenium or Tellurium) QDs was reported by Murray et al.[175], in 1993. They used a high temperature procedure, where a super-saturated solution containing Cd- and X-ions underwent rapid nucleations followed by controlled growth, forming uniformly sized QDs. Currently, this is one of the most widely used methods of synthesizing colloidal QDs suitable for biolabeling applications[70,80,110,115,189]. Micelle assisted synthesis[275], and γ-irradiation and microwave-based procedures[68] are also used. Most QDs are composed of direct band gap CdSe, with well understood energy level structure and established synthesis techniques[276].

The quantum yield of QDs reported by Murray et al.[175] was low ($\approx 10\%$ with respect to rhodamine) due to the distorted energy levels at the surface, caused by dangling surface bonds, stoichiometric variations and surface tension[110]. These localized surface energy levels act as electron-traps, preventing exciton formation and recombination, yielding significantly longer fluorescence lifetimes and higher rates of non-radiative relaxation. Most of the recent QDs feature a core/shell geometry that passivates the core surface by reducing the density of surface states, resulting in improvements of the quantum yield ($> 50\%$) and lowering of the lifetime[59,110,192] [see Figure 2.13]. While CdSe serve as the core, the shell is made from semiconductors with a larger band gap (for example, ZnS or CdS; see Figure 2.14), and a matching lattice structure. Further modifications of these core/shell QDs are necessary for their use in biological applications because of their hydrophobic surface and instability in polar solvents[59,110].

2.4.4 Biocompatible QDs

Biological applications of QDs demand stability in aqueous solvents. This can be achieved by attachment of polar groups to the surface of the core/shell QDs, and was first demonstrated by Chan and Nie[48] and Bruchez et al.[39], in 1998. Chan and Nie[48] functionalized CdSe/ZnS QDs with carboxylic acid, using a stabilizing mercapto
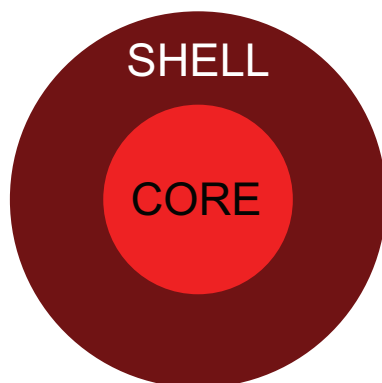
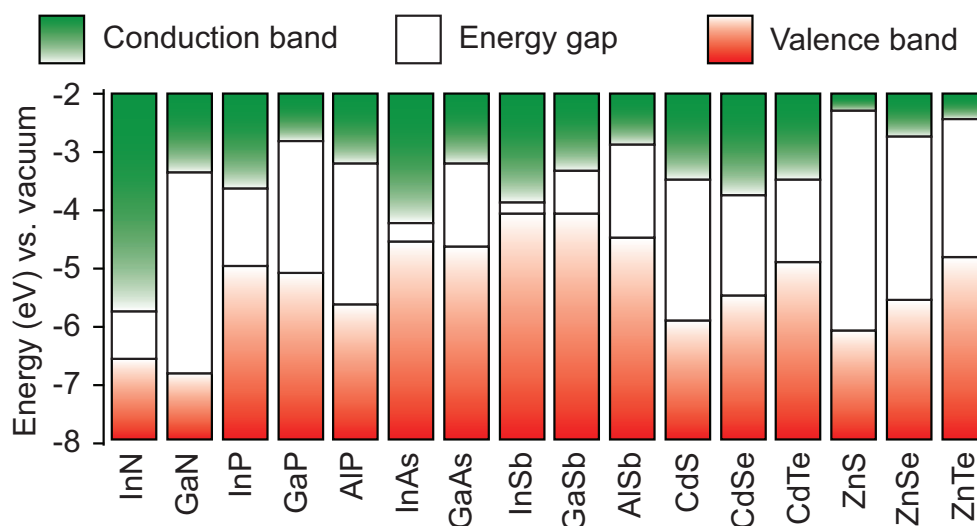Figure 2.13: Schematic digram of a QD featuring a core/shell geometry.

Figure 2.14: Electronic energy levels of selected III-V and II-VI semiconductors. Reproduced from the book by Rogach[210].

acetic acid on the QD surface, via affinity interactions between the -SH (mercapto or sulfhydryl group) and zinc (Zn) atom. The exposed carboxylic acid groups served as anchor points to proteins, such as, antibodies and transferrin[229]. Bruchez et al.[39] relied on capping the ZnS shell using a silica based polymer terminated with carboxyl groups for attachment of proteins. Many other methods of rendering QDs water soluble and biocompatible have been reported[68,80,166,168,189,196]. Currently, the technology of QD synthesis is mature, and biocompatible QDs are widely commercially available, with a large choice of surface chemical groups for attachment of targeting or sensing moieties. Some of these methods will be discussed in further contextual detail in Chapter 8.

2.4.5 Drawbacks of QDs

Despite the exceptionally high fluorescence efficiency, small size, commercial availability and size-tunable fluorescence wavelengths of QDs, their applications in biology and medicine present several challenges, with fluorescence intermittency[180] and toxicity[73] being the most important. Fluorescence intermittency (or blinking) of QDs is a well-known phenomenon[180], and is regarded detrimental for real-time tracking of QD-tagged biomolecules for molecular trafficking studies[55]. Despite the progress towards QD blinking suppression[113], this remains a problem although some studies made use of blinking to tell apart individual QDs from their aggregates in cellular environment[58].

Biological toxicity of QDs originate from the dissolution of heavy metals (Cd) used in their core[63]. Several methods to overcome toxicity have been put forward, including using a stable shell, non-toxic core etc[162,200]. It has been reported that the QD internalization by cells solely accounted for cytotoxicity, therefore toxicity can be diminished by preventing their cellular uptake using an uptake-inhibiting polymer coating[73]. Despite these efforts, cytotoxicity of QDs is still a hotly debated issue. Taken together, these drawbacks call for other biocompatible, photophysically and chemically robust nanoparticles for scientific research, as well as related clinical applications.

2.5 Fluorescent Nanodiamonds

2.5.1 General Introduction

Nanodiamonds are nanocrystals (1 nm < diameter < 100 nm) of diamond – a an allotrope[†] of carbon, where the atoms are held together by covalent bonds, formed by sharing electrons in SP^3 hybridized orbitals with four similar neighboring atoms. This gives rise to a tetrahedrally symmetric crystal structure, as artistically depicted in Figure 2.15(a). It can be interpreted as two inter-penetrating face centered cubic lattices, diagonally shifted from each other by a distance of $\sqrt{3}\frac{a}{2}$, where a is the dimension of the cube, whose value is 3.57 Å for diamond. Nanodiamonds are expected to inherit

---

[†]Allotropes are the different physical forms in which a material can exist. For example, graphite and diamond are both allotropes of carbon.

(a) A perfect diamond lattice

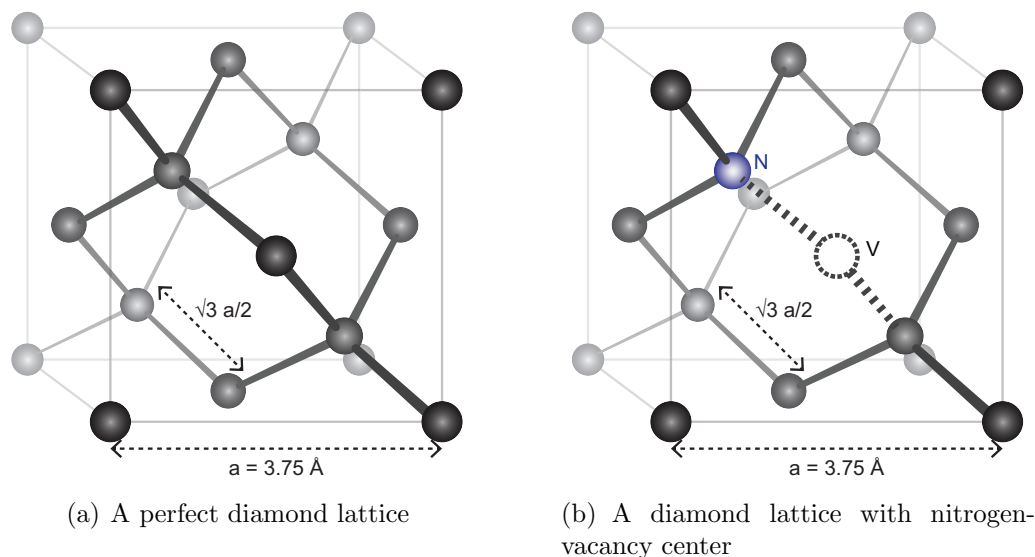(b) A diamond lattice with nitrogen-vacancy center

Figure 2.15: Artistic representations of a (a) perfect and (b) nitrogen-vacancy center-containing diamond lattice. Each carbon atom (black/gray sphere) is linked to four neighboring ones, via covalent bonds (rods). Nitrogen atom (N) is shown as blue sphere, whereas a vacancy (V) is shown as a dotted circle. Bonds are shown only to the atoms within a cube and the opacity is reduced for far away atoms, to aid visualization. Dotted bonds show the original structure in a lattice with defect to aid visualization.

the inertness of the diamond host core, and their (cyto)toxicity has been demonstrated to be low.

Nanodiamonds can be rendered fluorescent by implantation of *point defects* or *color centers* in the host diamond crystal. In general, defects occur when the atomic arrangement is distorted, and point defects are characterized by localization to one or two atoms, without a long range order. Point defects are classified into three basic types: a vacancy, substitution or an interstitial inclusion[135]. They may also occur in combinations. In a diamond lattice, the substitutional or interstitial defects are limited to small atoms, including hydrogen, nitrogen and silicon[269]. Sometimes, the substitutional defects are also combined with a vacancy defect. For example, a nitrogen-vacancy (N-V) center represents a substitutional nitrogen atom next to a vacancy, as portrayed in Figure 2.15(b). N-V centers have been investigated quite extensively in both bulk and nano-sized diamond crystals, due to their unique optical properties, which will be discussed below.

2.5.2   The Nitrogen-Vacancy (N-V) Center

Historically, diamonds were classified into several types, including Ia, Ib, IIa and IIb (and other subclasses), based on their optical properties. The optical properties have been identified as due to different impurities[236]. For example, Ib diamonds contain significant concentrations of nitrogen impurity, mostly as substitutional defects. On the other hand type Ia diamonds contain nitrogen in aggregates[170]. N-V center is one of the most commonly investigated point defects in type Ib diamonds[236]. N-V centers are rarely found in untreated diamonds, despite the nitrogen abundance. They are formed by irradiation of type Ib diamonds with high-energy electrons or light ions, followed by annealing at temperatures above 800 ^{o}C[161,170]. While irradiation creates a vacancy and a substitutional carbon defect, annealing allows thermal diffusion of the vacancy, which settles in the neighborhood of a substitutional nitrogen. Under low irradiation conditions, only a portion of the substitutional nitrogen defects are converted to N-V centers, allowing the remaining nitrogens to donate electrons, to create negatively charged, N-V$^-$ centers[170]. At high irradiation doses, as all the substitutional nitrogens are converted to N-V centers, they remain neutrally charged (i. e., N-V^0). Fluorescence nanodiamonds used in this project predominantly contained N-V$^-$ centers, referred to as N-V.

Until recently, the optical properties of N-V centers and the associated energy levels and transitions, were investigated on bulk diamonds[92,97,127], which are also applicable to N-V centers in nanodiamonds, except for very small particles (sized < 10 nm), where the centers are nanometer-proximal to the surface[34]. A simplified Jablonski diagram of the N-V$^-$ center is shown in Figure 2.16, where the electronic transitions that give rise to absorption and fluorescence are shown by upward and downward arrows, respectively[66,211]. Absorption of photons with energy = 1.945 eV (or wavelength, λ = 637 nm) causes transition from the ground state, $^3A_2$, to the excited triplet state, ^3E, while the absorption of the higher energy photons takes them to one of the higher vibrational states in ^3E. The wavelength dependence of these transitions is shown, as an absorption spectrum, in Figure 2.17. The sharp peak in the spectrum, at 637 nm (638 nm in Figure), is called a zero-phonon line, which corresponds to a transition that
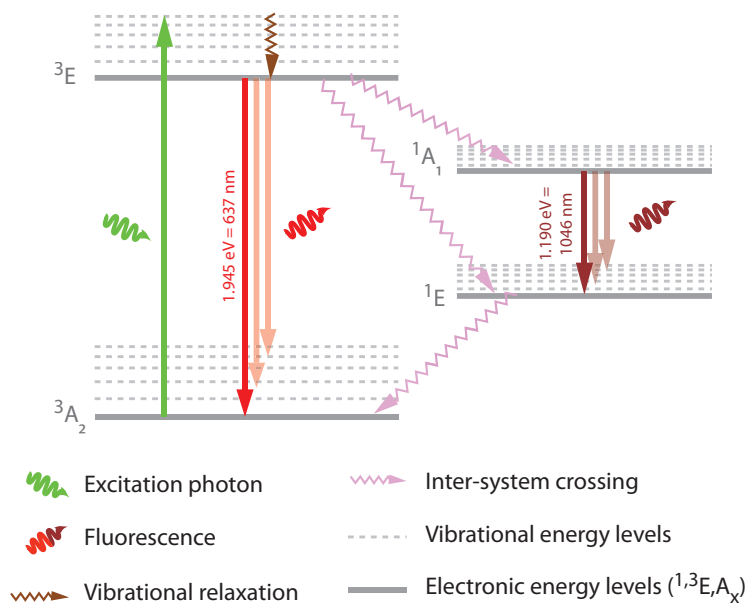
Figure 2.16: A Jablonski diagram showing the energy levels of an N-V$^-$ center in a diamond crystal. Zero phonon fluorescence lines are shown in bright red and brown arrows, whereas relaxations to the higher vibrational states are shown by translucent arrows. Energy level nomenclatures (E and A) are derived from molecular orbital symmetries and group theory. The superscripts (^{1} and ^{3}) denote whether the energy levels are singlet or triplet, respectively. See Section 2.1 for details. Energy levels not shown to scale. Splitting of the triplet states are not shown for simplicity. Adapted from the study by Doherty et al. [66].

does not involve phonons. "Blue-shifted" broad peaks correspond to the transitions to the higher vibrational states. Subsequently, the system reaches ^{3}E via vibrational relaxation (also called phonon-assisted relaxation).

An N-V center in the ^{3}E state can return to the ground state via two paths. The first path is via direct radiative relaxation from ^{3}E to ^{3}A$_2$, or to one of its vibrational states, giving rise to intense fluorescence at a wavelength of 637 nm (the zero-phonon line) or longer (phonon assisted). These transitions are shown as red arrows in Figure 2.16. The wavelength dependence of the emission is shown as a fluorescence emission spectrum in Figure 2.18(a). Similar to the absorption spectrum, the fluorescence spectrum also consists of a sharp peak at 637 nm that corresponds to the zero-phonon line. Relaxations to one of the vibrational states give rise to the, broad, phonon assisted band, to the right of the zero phonon line. In the second relaxation path, an N-V center undergoes rapid intersystem crossing from ^{3}E to ^{1}A$_1$[†66,211], followed by relaxation to the lower

---

[†]Intersystem crossing is favored only under certain spin-allowed situations

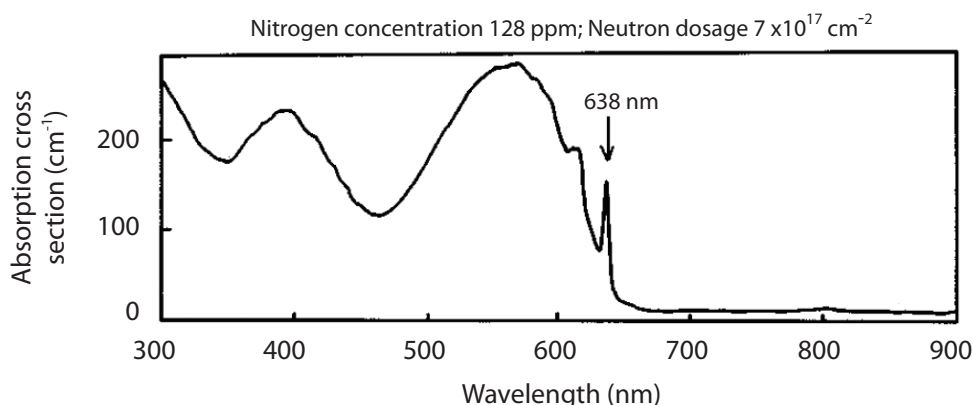Nitrogen concentration 128 ppm; Neutron dosage 7 x10^{17} cm^{-2}

Figure 2.17: Optical absorption spectrum of a type Ib bulk diamond (nitrogen concentration = 128 ppm or 2.25×10^{19} cm^{-3}) irradiated with neutrons (7×10^{17} cm^{-2}) and annealed at 900 °C, acquired at 80 K. The lowest energy (or highest wavelength) peak is at 638 nm, corresponding to the zero phonon line. A 1-nm shift (from the widely accepted 637-nm zero phonon line) is likely due to an error in the spectral calibration. Reprinted figure with permission from Mita[170]. Copyright (1996) by the American Physical Society.

singlet state, ^{1}E, via radiative (see Figure 2.16) or non-radiative processes (not shown in Figure). The radiative relaxation has been shown to give rise to infrared fluorescence at $\lambda = 1046$ nm[211]. However, this fluorescence is weak, due to the competition with the non-radiative processes, and is ignored. The N-V center makes a transition to the ground state, ^{3}A$_2$, via intersystem crossing. Taken together, these processes complete a cycle of the excitation light absorption and fluorescence light emission.

2.5.3 Characteristics and Applications of Fluorescent Nanodiamonds

The N-V center emission properties hold in nanodiamonds. As an example, Figure 2.18(b) shows the fluorescence emission spectrum from an aqueous colloid of N-V center containing fluorescent nanodiamonds. This closely resembles the spectra of that in the bulk, except for a small peak at 575 nm, which originates from the neutral (N-V^0) center, formed due to the excess electron irradiation. Hereafter, the abbreviation ND and FND will be used to denote pristine and N-V center-containing (fluorescent) nanodiamonds, respectively. The N-V center fluorescence of FND is highly efficient ($\eta \approx 80\%$[284]) and extremely photostable[277].
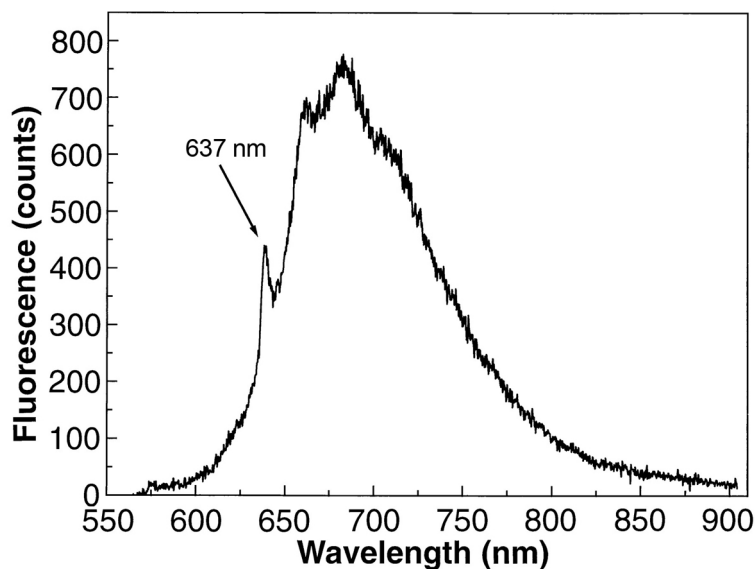
(a) Fluorescence emission spectrum of an N-V center in 100-μm thick type Ib diamond crystal, under 514-nm laser excitation. From Gruber et al.[92]. Reprinted with permission from AAAS.
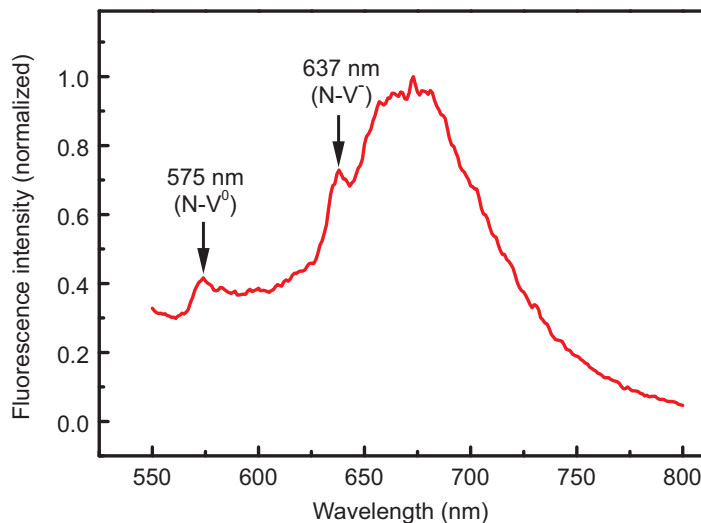
(b) Fluorescence emission spectrum of colloidal solution of N-V center-containing 140-nm fluorescent nanodiamond particles, under 532 nm laser excitation.

Figure 2.18: Fluorescence emission spectrum of the N-V center in (a) bulk diamond and (b) nanodiamond crystal matrix. 575-nm and 637-nm peaks correspond to the zero-phonon lines originating from N-V centers at the charge-states of N-V^0 and N-V$^-$, respectively.

In 2005, Yu et al.[277] proposed the use of FNDs as molecular probes for biological imaging, in light of these unprecedented photo-physical properties, in addition to their excellent biocompatibility and robustness[226]. They demonstrated fluorescence confocal imaging of FNDs in human kidney cells, and also showed that FNDs were non-cytotoxic. In the following years, numerous papers on the use of FNDs for biolabeling have been reported[77,172,177,221,239]. Recently, the main research focus towards using FND for bio-labeling application has been on establishing methods for attachment of targeting or sensing groups on the FND surfaces, termed biofunctionalization, which represents and important focus of this thesis. Detailed discussions on biofunctionalization of FNDs are presented in Chapter 7.

FNDs also form a strong base for quantum computing and communication[27], nanometer scale magnetometry[17], electric field sensing etc[66]. These applications are dependent on the spin-orbital interactions in an N-V center, that give rise to preferential transitions between the degenerate states[100], which also depend on external magnetic (Zeeman effect)[178] and electric fields (Stark effect)[251]. This field dependence can also be used to probe the orientation of nanodiamond particles for detecting rotational dynamics of biomolecules, as demonstrated by McGuinness et al.[165]. Detailed discussions of these mechanisms fall beyond the scope of this chapter. A recent, comprehensive review on the FND applications, by Aharonovich et al.[6], is a recommended source of information.

2.6 Summary and Goal

Fluorescent probes allow visualization of biomolecules with a high-sensitivity and resolution. Conventionally, the fluorophore part of these probes consisted of organic compounds, which presented several shortcomings, including photobleaching, toxicity and critical dependence of fluorescence on the environmental conditions. Fluorescent nanoparticles, including quantum dots and fluorescent nanodiamonds offer solutions to these shortcomings. Quantum dots are semiconductor nanoparticles, whose fluorescence originates from the quantum confinement effects. Their advantages include high

quantum efficiency, wavelength tunability and commercial availability. Fluorescence in nanodiamonds originate from nitrogen-vacancy color centers in the diamond crystal host. Besides the color center-derived fluorescence, which offers advantages of high quantum efficiency and immunity to environmental conditions, its diamond composition makes them biocompatible and non-toxic. Apart from the exceptional fluorescence properties of these nanoparticles, their large surface-to-volume ratio can also serve as a vehicle for the transport and delivery of cargo, including genetic material and drug.

The goal of this thesis is the development of a fluorescent nanoparticle-based probe to enable visualization of biomolecules, with an important example being somatostatin. Discussion of somatostatin, it properties and biological functions, will be provided in the next chapter.

3

Related Biological Aspects

This introductory chapter encompasses the basics of biological processes, main concepts and terminologies relevant to this thesis. The chapter begins with brief, educational descriptions of cells and cellular mechanisms[9,253], which narrows down to more specialized description of somatostatin before long. Biological and biomedical relevance of somatostatin associated cellular processes are reviewed based on the seminal and contemporary contributions.

Contents

3.1   The Cell

All living systems are made of cells – the smallest living unit of life[9]. Figure 3.1 portrays the basic structure of a eukaryotic cell and its appearance under an optical microscope. Essentially, the cell is a membrane-bound compartment with an aqueous interior that hosts a large variety of molecules, the key ones[†] being DNA, proteins and phospholipids. DNA is a chain formed by the four nucleotides – adenine (A), cytosine (C), guanine (G) and thymine (T) – interconnected by phosphodiester bonds. Normally, DNA is located within the nucleus of a cell. Segments of DNA, called genes, carry information to encode proteins, which are chains of amino acids linked by amide bonds. The names and chemical structures of the 20 canonical amino acids presently known are shown in Table 3.1. The sequence of nucleotides in a gene determines the sequence of amino acids in the protein that it encodes. Proteins serve several functions, including structure (e. g., actin forms a cytoskeleton)[224], catalyzing reactions (e. g., phosphodiesterases break DNA)[9], transporting molecules (haemoglobin carries oxygen)[253] and mediating intra/inter-cellular communication (insulin regulates glucose metabolism)[52]. Phospholipids assemble to create a double layered membrane – the cell membrane – that separates the cellular interior (intracellular) from its surrounding (extracellular). Cell membranes provide means for controlled communication between a cell and its environment, by the process of cell signaling.


[†]While there are several other molecules that are also necessary for the proper functioning of a cell, the choice of these three has been made with the contents of this thesis in mind
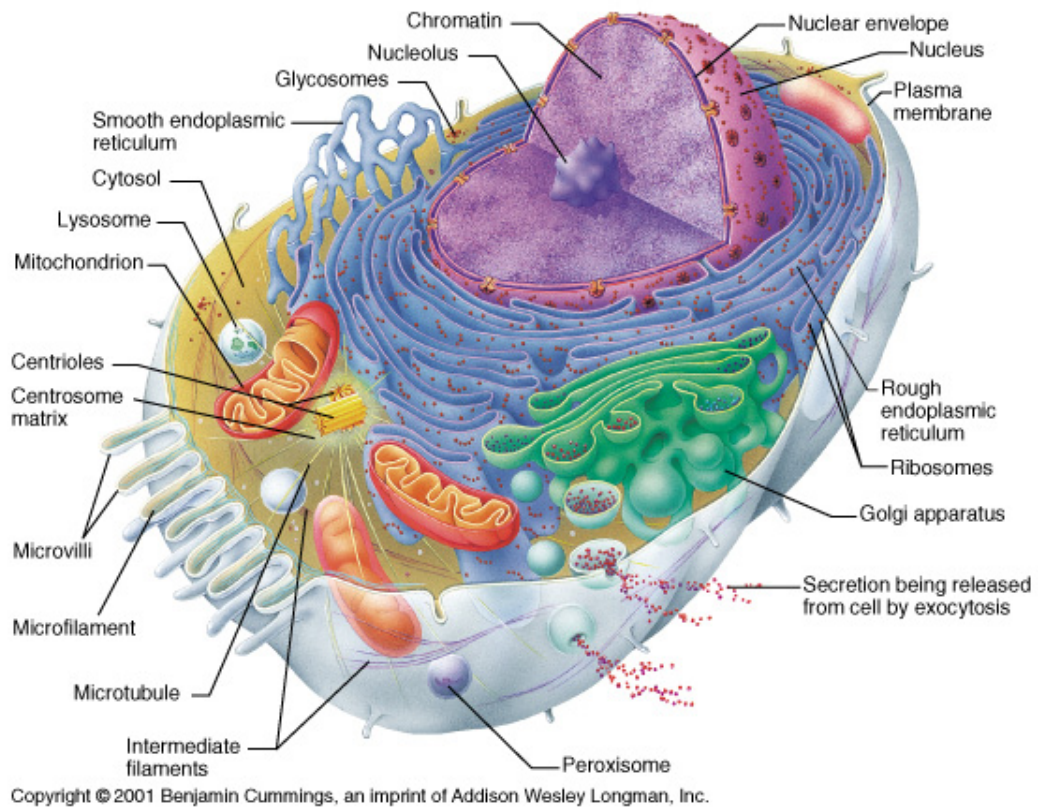
(a) Artistic representation of a generic eukaryotic cell, identifying the organelles. Reproduced from a website[2] with permission under the terms of Creative Commons license (http://creativecommons.org/licenses/by-sa/3.0/).
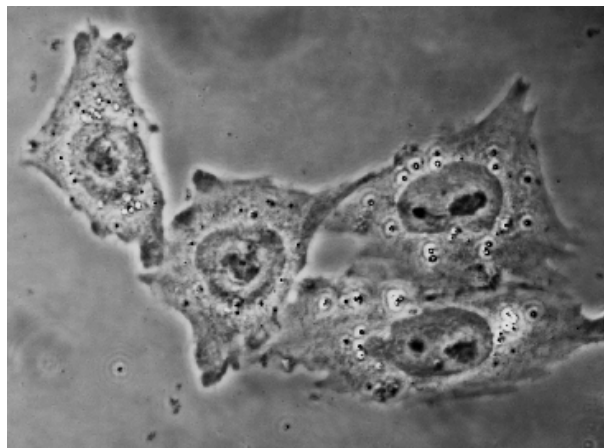

(b) Optical micrograph of a cluster of four chinese hamster ovary cells. The image is 110-μm wide.

Figure 3.1: Cell

Table 3.1: Amino acids, with corresponding three- and one-alphabetic representations, chemical formulae and structures. H atoms are not shown. The CO_2-CH-NH_2 group on the left hand side is common among all the amino acids. Structures drawn using the software Accelrys Draw 4.0 (academic license).
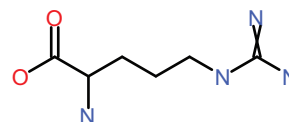
Alanine
Ala, A
$C_3H_7N_1O_2$
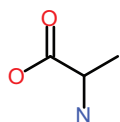
Arginine
Arg, R
$C_6H_{14}N_4O_2$
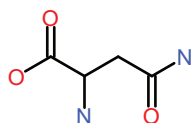
Asparagine
Asn, N
$C_4H_8N_2O_3$

Aspartic acid
Asp, D
$C_4H_7N_1O_4$
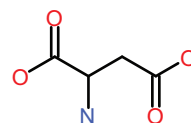
Cysteine
Cys, C
$C_3H_7N_1O_2S_1$
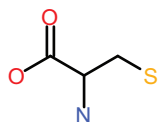
Glutamic acid
Glu, E
$C_5H_9N_1O_4$
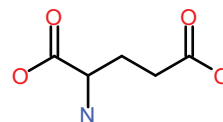
Glutamine
Gln, Q
$C_5H_{10}N_2O_3$
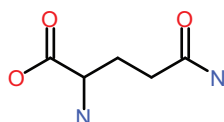
Glycine
Gly, G
$C_2H_5N_1O_2$
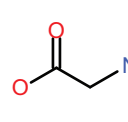
Histidine
His, H
$C_6H_9N_3O_2$
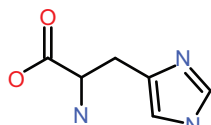
Isoleucine
Ile, I
$C_6H_{13}N_1O_2$
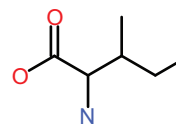
Leucine
Leu, L
$C_6H_{13}N_1O_2$
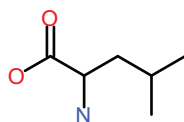
Lysine
Lys, K
$C_6H_{14}N_2O_2$
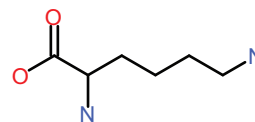
Methionine
Met, M
$C_5H_{11}N_1O_2S_1$
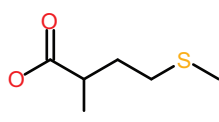
Phenylalanine
Phe, F
$C_9H_{11}N_1O_2$
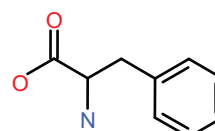
Proline
Pro, P
$C_5H_9N_1O_2$
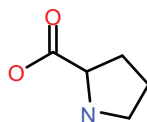
Serine
Ser, S
$C_3H_7N_1O_3$
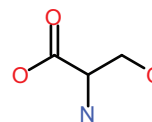
Threonine
Thr, T
$C_4H_9N_1O_3$
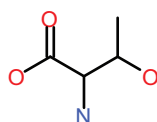
Tryptophan
Trp, W
$C_{11}H_{12}N_2O_2$
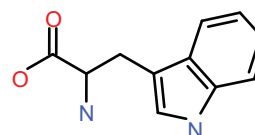
Tyrosine
Tyr, Y
$C_9H_{11}N_1O_3$
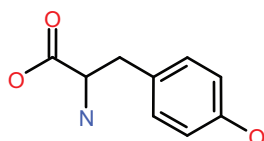
Valine
Val, V
$C_5H_{11}N_1O_2$
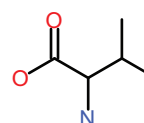
3.2 Cell Signaling

In a multicellular organism, cells coordinate their actions by communicating with each other and continuously adjusting their machinery, in order to bring each cell into a concerted synchronous action, subordinated by the organism as a whole. This type of coordination is achieved by means of secreting and recognizing signaling molecules, which includes amino acids, peptides[†], nucleotides, steroids, fatty acid derivatives and dissolved gases such as nitric oxide and carbon monoxide[9]. Signaling molecules (or ligands[‡]) secreted by one cell are recognized by their corresponding receptors located on or inside another cell. Small hydrophobic ligands, including steroids and vitamin D, can penetrate the cell membrane, and are able to bind to intracellular receptors to directly influence gene transcription[§]. On the other hand, hydrophilic signaling molecules, which include most peptides, proteins and amino acids, bind to transmembrane receptors[¶].

Transmembrane receptors are of three kinds: (1) ion-channel linked receptors, (2) enzyme linked receptors and (3) G-protein coupled receptors (GPCRs)[9]. Ion-channel linked receptors respond to ligand binding by opening or closing transmembrane channels through which ions move in and out of the cell. Enzyme linked receptors have their ligand-binding domain on the external cell-surface and an enzymatic domain in the interior. Ligand-binding causes change in enzymatic activity. GPCRs act indirectly by regulating its effectors or secondary messengers, ultimately changing gene transcription. GPCRs are more relevant to this thesis and will be discussed in a little more detail.

[†]A peptide is a chain of < 50 amino acids, in contrast to larger proteins.

[‡]Ligands are molecules that bind to a target protein.

[§]Transcription is the process of conversion of information from DNA to RNA – an intermediate step in the synthesis of the corresponding protein.

[¶]Transmembrane receptors are large proteins that span across the cell membrane, and have intracellular and extracellular domains.

3.2.1 GPCRs

GPCRs are the largest family of transmembrane receptors. More than 850 genes encode GPCRs that recognize a wide variety of ligands, including adrenalin, somatostatin, enkephalins and glucagon and the receptors that mediate perception of vision, olfaction and taste[106,216,274]. All the GPCRs share a basic structure with seven transmembrane alpha helices[†], shown in Figure 3.2[79]. These receptors couple to a family of guanidine nucleotide-binding proteins (or G-proteins) in order to transduce the signal of the ligand-binding. The G-proteins are heterotrimeric, made of the subunits G_α, G_β and G_γ. The functioning of G-proteins is schematized in Figure 3.3. After the activation of GPCRs by their respective ligands, the G-protein subunits dissociate to activate secondary messengers, which changes downstream signaling proteins and ultimately results in modulation of gene transcription. Several subtypes of G_α, G_β and G_γ exist, and each of them potentially couple to a different secondary messenger system. The identity of G_α is used to define a whole G-protein trimeric complex, because the same $G_{\beta,\gamma}$-subunits can associate with different G_α-subtypes[106]. A rigorous discussion on the G-protein subunits, secondary messenger systems and how it ultimately effects gene transcription is out of the scope of this thesis, and is available in a large number of reviews[82,106,163,169,216]. The rest of the thesis is focussed on one type of GPCR – the somatostatin receptor.

3.3 Somatostatin - A Peptidic Signaling Molecule

Somatostatin represents a collection of two peptidic signaling molecules. The smaller one was first isolated from the hypothalamus of a sheep, by Brazeau et al.[35] in 1973, attempting to identify a mysterious biochemical that inhibited the release of the pituitary gland-derived growth hormone, somatotropin. The isolated peptide extract was named somatotropin release inhibiting factor or SRIF, currently known as somatostatin-14 (SST-14), based on the number of amino acids. The authors also identified the amino

---

[†]Alpha helix is a common secondary structure of a protein where every amino acid residue is connected to its 4th neighbor on the either sides of the sequence via hydrogen bond, forming a spiral structure.
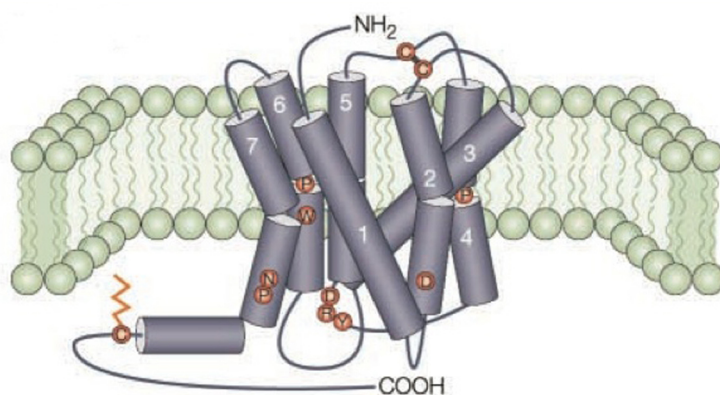
Figure 3.2: Schematic of a generic G-protein coupled receptor. The seven cylindrical structures represent the transmembrane alpha helices. Reprinted by permission from Macmillan Publishers Ltd: Nature Reviews Drug Discovery[79], copyright (2002).
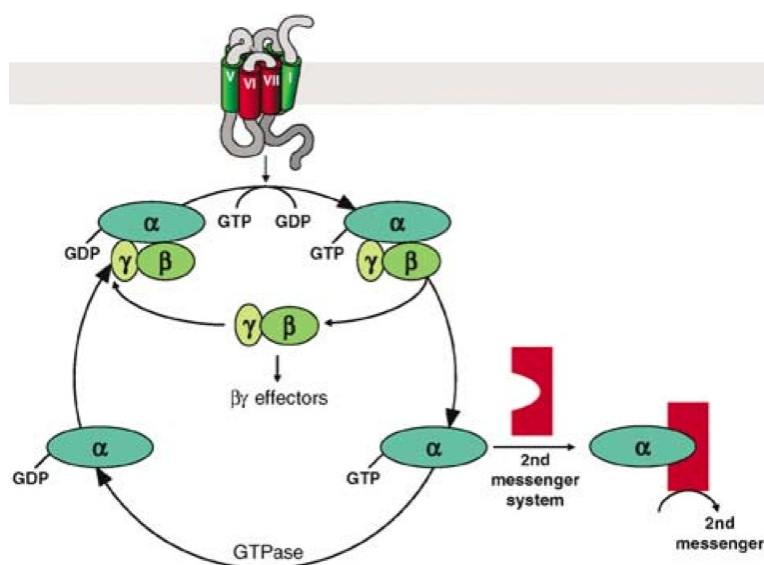
Figure 3.3: The working cycle of a G-protein. Ligand binding to the GPCR causes replacement of GDP to GTP. The GTP-bound G_α and the dissociated $G_{\beta,\gamma}$ activate their respective secondary messenger systems (or effectors). Hydrolysis of GTP by the enzymatic action of G_α serves as a time-regulator and reverts back to the GDP-bound state. Abbreviations: GDP (guanidine diphosphate), GTP (guanidine triphosphate), GTPase (enzymatic domain of the G_α that converts GTP to GDP). Reproduced from Milligan and Kostenis[169] with copyright clearance under Creative Commons license.

acid sequence and basic structure of the SST-14, shown in Figure 3.4. Pradayrol et al.[198] in 1980 identified the larger variant based on its immunoreactivity similar to that of SST-14, but with a different chromatographic behavior. It was found to be an N-terminally extended form of SST-14 and was called somatostatin-28 (SST-28).

Initially, the SST-28 was considered to be a precursor in the cellular synthesis of SST-14, but the study by Montminy et al.[173] revealed that both SST-14 and SST-28 were biologically significant, and were derived from the same precursor protein preprosomatostatin. In this era, both SST-14 and SST-28 were extensively investigated and their major function was identified as the regulation of the release of secondary hormones[26,46,184,187,272], which will be discussed shortly. Among these functions, SST-14 predominantly regulates the activity in pancreas, stomach and neural tissues, and is virtually the only form found in retina and certain neurons[187]. In brain, the less abundant SST-28 only accounts for 20 - 30% of the total activity[187]. Therefore, we will mostly limit our discussions to the functions and applications of SST-14 and use its shorter notation, SST, throughout this thesis.

Apart from the two natural somatostatin analogs, several other synthetic mimics of somatostatin have been reported, in both peptidic and non-peptidic forms[57,74]. All the peptidic forms, including the most popular, 8 amino acid-long octreotide, contain the pharmacore of SST: the -PWKT- sequence – the part of the molecule that contributes most to its biological activity[22]. Smaller peptidic-analogs of somatostatin that contain only 6 amino acids have also been reported[265,266]. However, the pharmacores used in these small analogues are slightly modified with the tryptophan residue in its D-isomeric configuration, in order to improve their stability and functional potency[12,99,266] (see Figure 3.5). Even the non-peptidic forms, such as the L-779,976, include some of the pharmacore structures, and were designed based on computational modeling and experimental iterations[212].
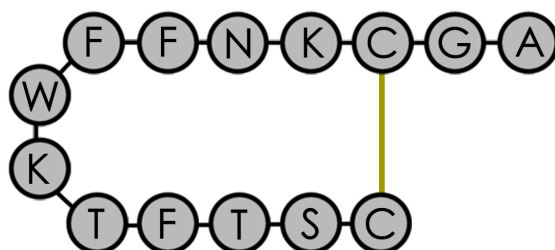
Figure 3.4: Schematic of a somatostatin-14 (SST) molecule, presented as a chain of amino acids in the single letter code. Alanine residue is at the N-terminal. The yellow line represents a naturally existing disulfide bond between the two cysteine residues.

Figure 3.5: A list of popular peptidic analogs of Somatostatin. SST-28, SST-14 and cortistatin (CST) are the only naturally expressed forms. Cortistatin (CST) is natural peptide closely related to SST[156]. Reprinted by permission from Macmillan Publishers Ltd: Frontiers in Neuroendocrinology[187], copyright (1999).
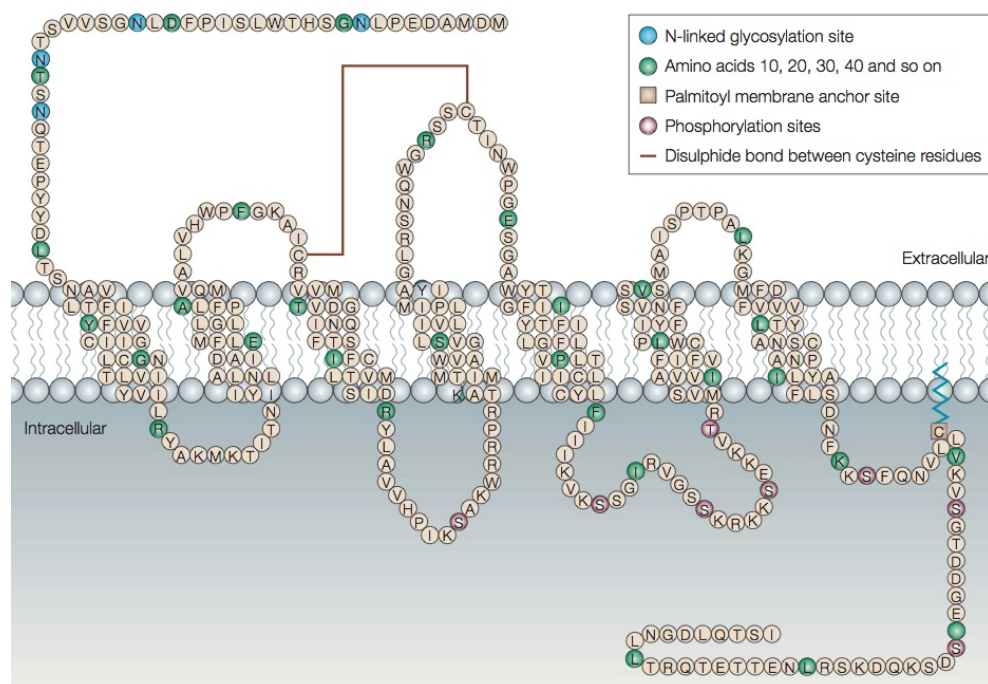
Figure 3.6: Structure of the transmembrane somatostatin receptors (sst) exemplified by that of the subtype, sst_{2A}. Reprinted by permission from Macmillan Publishers Ltd: Nature Reviews Drug Discovery[272], copyright (2003).

3.3.1 Somatostatin Receptors and its Subtypes

In the years after the discovery of SST, its functions were rigorously researched. However, until late 1980s, the cellular mechanisms by which SST-sensing and signal transduction occurred remained unknown. Several functional observations suggested the existence of GPCRs of SST[104,193,267]. In the early 1990s, Yamada et al.[274], Vanetti et al.[263] and others identified the genes and cloned the six receptor subtypes that SST binds and activates. These receptor subtypes were named sst_1, sst_{2A}, sst_{2B}, sst_3, sst_4 and sst_5, and will collectively be referred as sst. *Note that capital 'SST' and small 'sst' represent the ligand and receptor, respectively throughout this thesis.* The 6 subtypes are encoded by 5 different genes, which allows differential expression levels in tissues[36,187]. The sst_{2A} and sst_{2B} were found to be encoded by the same gene SSTR2[†], but spliced at different lengths at the C-terminal. The amino acid sequence and basic structure of sst, exemplified by the sst_{2A}, is presented in Figure 3.6[272].

[†]SSTRX is the gene that encodes the receptor subtype sst_X

Unlike the native SST, most synthetic analogs are sst-subtype specific[47,57,184]. In mid - late 1980s, prior to the identification of the five distinct subtypes, the somatostatin receptors were subgrouped under SRIF1 or SRIF2, based on the affinity and biological activity of the octreotide[22,266]. Later, it was discovered that the octreotide had high affinity towards the subtypes sst_{2A}, sst_{2B}, sst_3 and sst_5, earlier classified under the subgroup SRIF1[116]. Octreotide was unable to activate the subtypes sst_1 and sst_4, classified under the subgroup SRIF2. All the subtypes within a subgroup demonstrate high genetic similarity, which may explain their similar octreotide activity. In the recent years, the subtype-based classification is used more prominently[184]. In addition to the receptor agonists such as SST, octreotide and lanreotide, that bind and activate ssts, there are molecules classified as antagonists that bind, but do not activate sst(s)[47]. The antagonists merely occupy the binding site on the sst molecule, preventing further agonist binding. They are also highly receptor subtype specific, and are commonly used for verification of agonist specificities[47].

3.4   Biological and Biomedical Relevance of SST

The SST and its analogues activate the sst(s) in unique ways, and modulate the function of a cell. Before the intricacies in these mechanisms are unfolded, it is considered appropriate to understand why such an expedition is of interest. The following subsections will describe the relevance of SST in the human body and its function and how this significance is currently exploited in the healthcare system.

3.4.1   Tissue Distribution of Somatostatin

Enormous amount of research on SST and sst has been motivated by their abundance and significance in human tissues. Soon after the isolation of SST from hypothalamus, where it regulates the growth hormone release, SST or sst were found in several other locations including the central nervous system, pancreas, gut, kidney, lymphatic tissues, thyroid, pituitary, adrenal glands etc.[40,187]. In brain, SST contributes towards
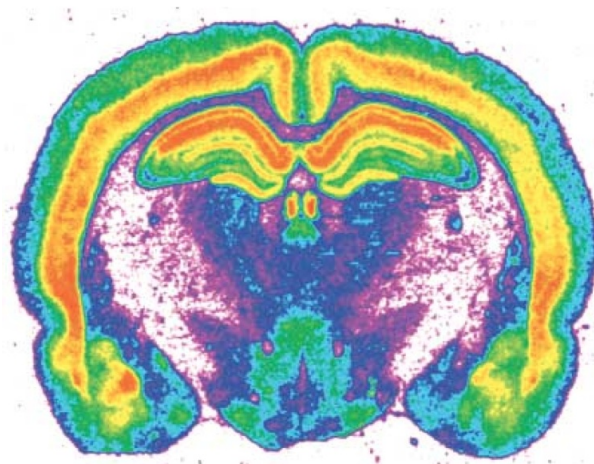
Figure 3.7: Autoradiographic distribution of the binding sites of radioactive somatostatin analog in a coronal section of an adult rat brain. False color image, where red and white represent maximum and minimum binding, respectively. The brain section portrayed corresponds to plate 34 of the 4th Edition of the book – The Rat Brain in Stereotaxic Coordinates, by Paxinos and Watson[190]. Reprinted by permission from Macmillan Publishers Ltd: Nature Reviews Drug Discovery[272], copyright (2003).

neurotransmission, neuronal plasticity and memory, pain-sensation, hormonal secretion, other autonomous functions, such as breathing and blood pressure, etc.[30,36,41]. A map of a section of the brain, color-coded according to the density of sst is presented in Figure 3.7[272]. In pancreas, SST regulates the levels of both glucagon and insulin, thus playing an important role in the regulation of glucose[45,247,248]. SST regulates the secretion of digestive juices in the gastric lining and absorption of nutrients from the intestine[139]. sst(s) have also been observed to be over-expressed in cancerous cells, especially in the neuroendocrine tumors[207], with expression density varying between individuals[206]. In most tissues, sst_2 is the predominant subtype – possibly a biased interpretation because many of these observations were made by using the octreotide-binding assays[207].

3.4.2 Biomedical Relevance of Somatostatin

The abundance of SST and sst in human tissues has been acknowledged by their diagnostic and therapeutic applications, especially in the areas pertaining to two medical conditions: acromegaly and tumors[222,244].

Acromegaly is a rare, chronic and disabling disease that arises due to over-production of the growth hormone and insulin-like growth factor-1, because of improper functioning of the pituitary gland[112]. Symptoms vary between patients, complicating initial diagnosis. Figure 3.8 summarizes most of them[159]. The primary goals of therapy are (1) removal of symptoms including reduction of growth, (2) prevention of re-growth and (3) improvement of the long term outcome[244]. Reduction in the blood level of the growth hormone to < 2.5 μg.L^{-1} has been documented to reduce the extra growth and mortality rate[244]. Injection of blood-stabilized analogs of SST reduces the release of the growth hormone[184] and inhibit cell proliferation[171]. However, ≈ 3 injections per day was required to maintain the growth hormone at the normal level. Development of slow-releasing Sandostatin® LAR® has resulted in a dramatic decrease in the number of injections required to one per four weeks, significantly improving ease of the therapy[86].

Even before all the sst(s) were identified and cloned, increased SST binding to tumorous tissues and cells, both *in vivo*[75,222] and *in vitro*[104], was observed. Thereafter, SST and its radiolabeled analogs were proposed for tumor-related clinical applications, including diagnosis by scintigraphy[31,262], prognosis, radiotherapy[37,234] and therapy based on its anti-proliferative effects[206,234]. The latter strategy was, however, argued upon, because the activity of SST was tissue dependent, likely to be due to differential expression of sst-subtypes among tissues. Consolidated data on the the expression levels of the different sst-subtypes in various kinds of tumor, based on the quantity of mRNA, as determined using reverse transcription polymerase chain reaction (RT-PCR), northern blotting and *in situ* hybridization methods, is readily available in the paper by Hofland and Lamberts[112]. Currently, sst-based cancer imaging is an established clinical method.

Another clinical application of SST analogs is the treatment of acute pancreatitis[118,257], however, controversies still exist on its efficacy[18]. Several secondary applications based on this method, including the indirect verification of therapeutic gene delivery systems, have been proposed[283]. Improvement of somatostatin-based diagnosis and therapy of patients with acromegaly, neuroendocrine tumors or other conditions
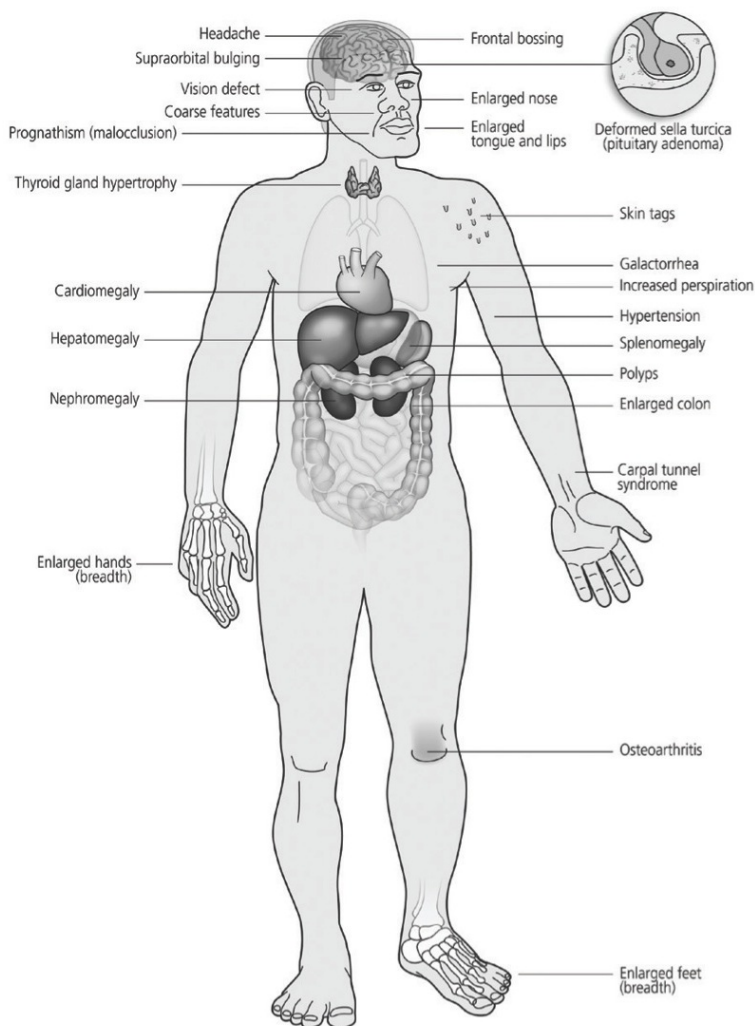
Figure 3.8: Signs and symptoms of acromegaly. Reproduced with permission from Ludlam and Anthony [159]

demand comprehensive understanding of the functioning of the sst(s) and its downstream signaling mechanisms. The following sections are devoted to discussions of these mechanisms.

3.5   SST Signaling Pathways

sst(s) belong to the family of GPCRs, introduced earlier [7,193,203]. They couple to one or more of the G-proteins subtypes – $G_{i/o}$, G_s, G_q, G_{12}, G_{14} or G_{16} – to transduce the sst:SST binding event into intracellular signals via secondary messengers [154].

These messengers include the adenylyl cyclase[126,203], phospholipase A_2[145], phospholipase C[7,254], calcium ions[182,252], guanylyl cyclase[46], nitric oxide[46], ion (e. g., potassium) channels[193] and several others. Reviews on how the transduction occurs and their consequences are available in the literature[37,46,184,187], and will not be discussed in any detail, except for the two more relevant downstream mechanisms – opening of the K^+-channels and calcium mobilization. The mechanism of K^+-channel opening in cells offers a signal transduction mechanism in which the primary effect is the efflux (or influx) of K^+ ions, resulting in a negative increase (or decrease) of the cellular membrane potential (see Section 5.6.1 for detailed discussion). This, in turn, causes activation of a variety of membrane potential-dependent cellular mechanisms, including modulation of membrane associated hormones and ion-channels (e. g., Ca^{2+}-channels). The types of K^+-channels that may be activated or inactivated after sst-activation are numerous, including inwardly rectifying K^+-channels, non-inactivating voltage-sensitive K^+-channels, transient outward K^+-channels, Ca^{2+}-activated K^+-channels and ATP-sensitive K^+-channels. While some are activated directly by the G-protein subunits, the others are activated by secondary effectors (for example, Ca^+ or ATP). These variations are highly dependent on the cell and sst subtype under consideration. SST-based sst-activation can also result in decrease or increase of cytoplasmic Ca^{2+} concentration. Once again, the type of modulation is determined by the cell type and sst subtype. More information on these processes is available in Sections 5.6.1 and 5.6.2. Another aspect of the intracellular signaling pathway, which, in a way, forms the soul of this thesis is discussed in the following section.

3.6 sst-Mediated Internalization

Soon after ligands bind to their respective receptors on the cell-surface, which is the first step in the cell signaling mechanism, the process of the receptor-mediated internalization may be initiated. As a result, a receptor-bound ligand enters the cell via pits on the membrane that eventually bud off to form intracellular vesicles[83], as shown in Figure 3.9. Several years before the identification of sst(s), Draznin et al.[69] observed
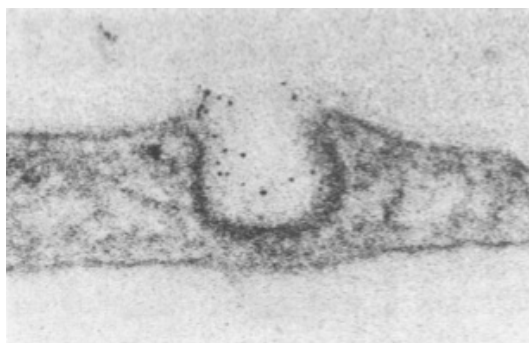
Figure 3.9: Electron micrograph showing the internalization of Low density lipoprotein (LDL)-ferritin (black dots) in a coated-pit on the cell-surface of the normal human fibroblast. Several minutes later, such pits detached from the surface to form vesicles within which LDL-ferritin were taken into the cell. Ferritin is a protein that stores and releases iron in a controlled fashion. Reproduced with permission from Brown and Goldstein[38].

that the rat anterior pituitary cells internalized SST molecules bound to gold nanoparticles. This process is referred to as the sst-mediated internalization or sst-mediated endocytosis.

In general, the internalized receptors and ligands are transported via a series of intracellular organelles, including (1) endocytotic vesicles, (2) early endosomes, (3) late endosomes and (4) lysosomes, where they are degraded, except if they are recycled back to the surface[124,140], as portrayed in Figure 3.10. In 1987, Viguerie et al.[267] investigated time scales associated with the dynamics of the receptor binding, internalization and degradation of SST in pancreatic acini[†], using its radioactive iodine-bound analog ^{125}I-[Tyr$_{11}$] SST. They reported that a maximum internalization of $\approx 10\%$ of the membrane-bound radioligand reached within several minutes of SST addition. The radioligand was also degraded and expelled to the extracellular space as smaller fragments, which stabilized after ≈ 1 hr. They demonstrated separable dynamics of sst:^{125}I-[Tyr$_{11}$] SST binding and internalization, by the modulation of temperature. Addition of ^{125}I-[Tyr$_{11}$] SST to the cells at 5 ^{o}C resulted in the receptor binding, but internalization began only after elevating temperature to 37 ^{o}C, showing that the sst-mediated internalization is an active process that occurs only at physiological temperatures.

Contradictorily, Presky and Schonbrunn[201] reported that SST was unable to evoke

---

[†]Pancreatic acini is the exocrine region of the pancreas, and is responsible for the production of digestive enzymes.
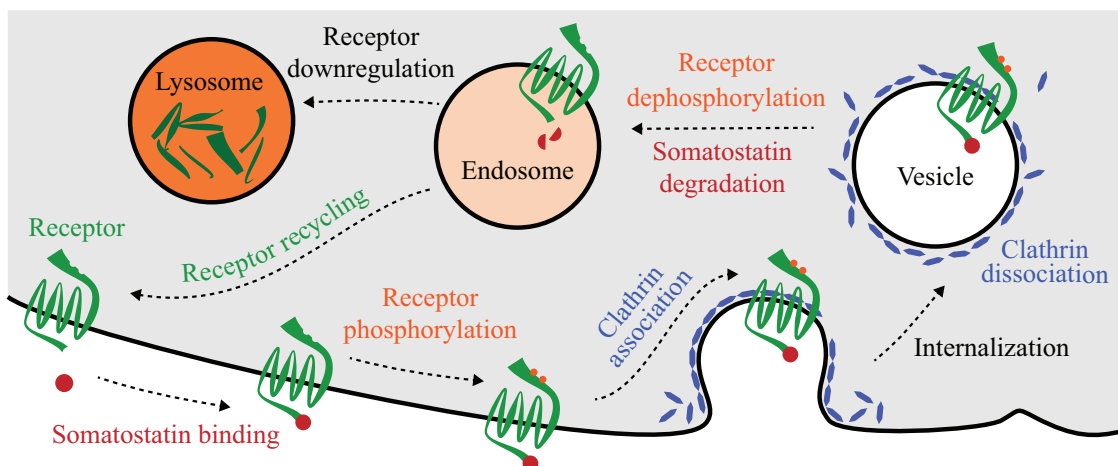
Figure 3.10: A schematic representation of receptor-mediated internalization of bound ligands. The internalized receptor:ligand complexes are directed to endosomes and eventually sequestered into lysosomes for degradation or recycled to the cell surface. Phosphorylation is a process where phosphate groups are added to the Ser or Thr residues in the receptor to alter its ligand-binding affinity. De-phosphorylation usually occurs in the endosomes. Adapted from Hofland and Lamberts[112].

the sst-mediated internalization in the GH4C1 pituitary cell line. Instead, it resulted in an increase of sst density on the cell surface. This was, in turn, in contradiction with the report by Heisler and Srikant[104], who observed a decrease in the response upon pretreatment of SST in mouse anterior pituitary tumor (AtT-20) cells. The plausible reason for these contradictions might be the differential expression of the sst-subtypes across various cell types[151], and their distinct downstream signaling mechanisms[124]. To avoid contradictions arising due to the subtype dependency, more recent experiments have been carried out on cells that expressed only one receptor subtype or used subtype-specific SST-analogs.

Hipkin et al.[111], used a clone of the pituitary tumor cells (GH-R2) modified to over-express sst_{2A}. In order to reduce the activation of any endogenously expressed subtypes, they used the selective agonist – octreotide. They concluded that post-sst:SST binding events, including (a) receptor-phosphorylation[†], (b) receptor-desensitization[‡] and (c)

[†]Phosphorylation the process where the state of a protein is modified by the addition of phosphate groups to certain residues, by protein kinases.

[‡]Desensitization is a phenomena where pretreatment of cells with agonists causes reduction in cellular response to further agonist addition. Desensitization is a major concept in pharmaceutical

receptor:ligand-internalization were closely related, and occurred within a few minutes of the octreotide addition. Later, Beaumont et al.[24] suggested the sst-internalization to be a major contributor towards the desensitization or receptor down-regulation in the neuroblastoma × glioma hybrid cell line – NG108-15. In other words, the internalization resulted in a reduction of the receptor density on the cell-surface. Reassuringly, an increased desensitization was also observed in the cells treated with monensin – an inhibitor of the receptor recycling. It appeared as if the cells modulated the level of desensitization by controlling the rate of the receptor recycling.

In 1997, Koenig et al.[136] carried out an extensive investigation on parameters that influenced the sst-mediated internalization using a sst_2-specific agonist, ^{125}I-BIM-23027, in the Neuro2A neuroblastoma cell line. They studied several characteristics of the internalization, including the time scale, extracellular pH, temperature, specificity, ATP dependence, mechanism of vesicle formation, recycling and intracellular/extracellular degradation. Internalization, which saturated in $\approx$ 20 min after the radioligand addition, did not vary significantly between pH 5 and 7.4. However, it was very much dependent on the temperature and other external agents that either depleted ATP, prevented normal functioning of G-proteins or precluded the clathrin pit formation (see Section 6.3.2 for more details on clathrin pits). While the stable hexapeptide, ^{125}I-BIM-23027, underwent non-destructive recycling after internalization, the ^{125}I-SST suffered degradation by both extracellular and intracellular agents. However, they were able to moderate the extracellular degradation using a specific protease inhibitor – bacitracin (see Figure 3.11).

Again, in 1998, Koenig et al.[137] reported on similar experiments, using chinese hamster ovary (CHO) cells that heterologously expressed sst_2 receptor subtype. A significantly reduced rate of ^{125}I-SST-degradation was observed in both extracellular media and intracellular extracts. They observed significant recycling of both ^{125}I-SST and ^{125}I-BIM-23027, contradictory to their previous observations in 1997. The different cell types used for these investigations might be the reason for this discrepancy. Roosterman et al.[214] determined the cause of degradation to be endopeptidases (such as

---

research, where the drug potency may decrease as a result of long-term usage[112].
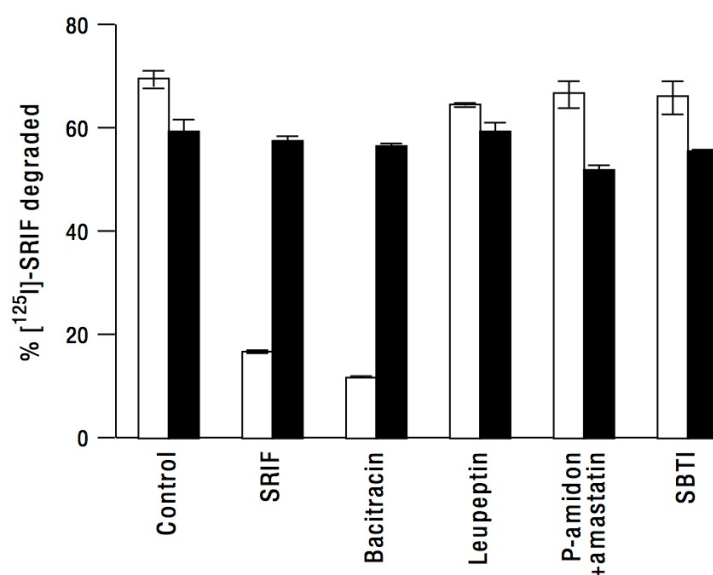
Figure 3.11: Degradation of extracellular (open bars) and intracellular (solid bars) ^{125}I-SST after 10-min incubation with the Neuro2A cells, represented as a percentage of bound radioligand. Addition of native SST (denoted as SRIF) or protease inhibitors – bacitracin, leupeptin, phosphoramidon + amastatin or soybean trypsin inhibitor – were expected to counter the degradation. SST and bacitracin only reduced the extracellular degradation. Reproduced with permission from Koenig et al.[136]

the endothelin-converting enzyme-1) after the internalized ligands reached endosomes in the HEK-293 cells.

So far, these reports indicate that the sst:SST binding and the resultant cellular responses are complex, and are highly dependent on the ligand type, receptor subtypes and cell types. More conclusive observations require determination of intracellular localization of the receptor:ligand complex. However, radiolabeling techniques cannot provide such resolution. The use of microscopic visualization techniques, similar to the one reported by Draznin et al.[69], in 1985, was able to overcome this shortcoming. Most of the microscopic observations were made by using sst-labeling, rather than SST[41,47,85,149,156,209,256], as will be apparent from the following paragraphs.

One of the first reports on optical visualization of the internalization, by Nouel et al.[181], described the use of a fluorescently labeled SST-analog. The authors were able to visually demonstrate the differences in spatial distribution of fluorescent SST

internalized by the transfected COS-7 cells expressing sst_1 or sst_2, and their respective temperature dependencies. They found that the fluorescence from SST bound to sst_1 remained localized very close to the cell membrane, possibly in non-internalized caveolaes (see Section 6.3.2 for a description of caveolae). On the other hand, in agreement with most of the previous reports, the fluorescent SST was efficiently internalized, via sst_{2A} within several minutes. In another study by the same group[219] sst-immunolabeling techniques were employed on the AtT-20 cells that endogenously expressed four receptor subtypes – sst_1, sst_2, sst_4, and sst_5. They also determined that the sst-mediated internalization was a necessary step for the regulation of the growth hormone expression.

Krisch et al.[140] reported on nanogold based labeling to locate sst_2 or SST in glioma cells, by using electron microscopy. Due to technical reasons, they were unable to stain both, the ligand and the receptor, at the same time, which would have been a direct demonstration of sst-mediated internalization of SST. Stroh et al.[246] showed that only sst_2 and sst_5 activation caused the internalization in hippocampal neurons. The internalization was also stopped by phenylarsine oxide – a known inhibitor of the internalization.

Over the last decade, finer details of internalization, for example oligomerization of the receptors and association with additional molecules before internalization has been unfolded. High levels of the sst(s) expression has been shown to cause receptor dimerization[209] in the CHO-K1 cells. Even in the cells that expressed sst(s) at a lower density, where they existed as monomers in the basal state, the SST-induced activation caused dimerization, as shown in Figure 3.12(a). The dimerization was also sub-type specific – sst_5 only formed dimers with itself or heterodimers with sst_1, but not with sst_4. Also, interestingly, formation of dimers with sst_5 was essential for the sst_1-mediated internalization. In contradiction to these observations, Grant et al.[85] demonstrated that sst_2, heterologously expressed in CHO-K1 and human embryonic kidney (HEK-293) cells, existed as oligomers in their basal state. They dissociated to form monomers upon SST-addition, in a dose-dependent manner [see Figure 3.12(b)]. Very recently, in 2010, Grant and Kumar[84] determined that $G_{i/o}$-proteins are responsible for the
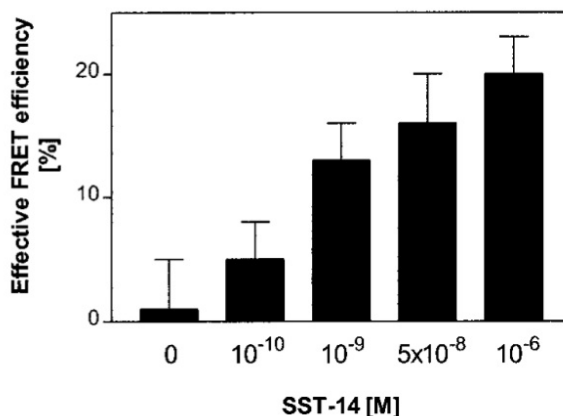
(a) CHO-K1 cells expressing relatively low density $(B_{max} = 160 \pm 30$ fmol.mg$^{-1})$ of sst$_5$.
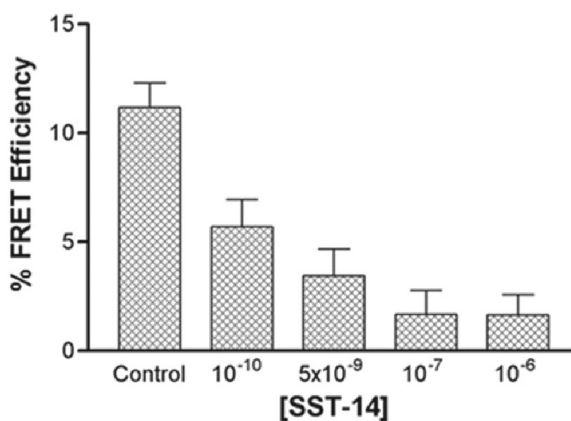
(b) CHO-K1 cells expressing relatively higher density $(B_{max} = 435 \pm 33$ fmol.mg$^{-1})$ of sst$_2$.

Figure 3.12: Change in the efficiency of fluorescence resonant energy transfer (FRET) in accordance with SST-dose in CHO-K1 cells transfected with fluorescent versions of either of the two sst-subtypes. FRET efficiency reported on the extent of sst-dimerization. Figures reproduced with permissions from (a) Rocheville et al.[209] and (b) Grant et al.[85].

maintenance and regulation of sst$_2$ homodimers and sst$_2$/sst$_5$ heterodimers. These observations again indicate how the consequences of the sst:SST binding depend on the cell type and the receptor subtype.

Tulipano et al.[256] studied the participation of molecules such as β-arrestin in the downstream mechanisms that occur after the SST-induced sst activation. β-arrestin functions as a docking protein that link the receptors to the components of cellular machinery essential for internalization. They found that the subtypes sst$_{2A}$, sst$_3$ and sst$_5$ quickly (< 1 min) associated with β-arrestin, shown in Figure 3.13. However,
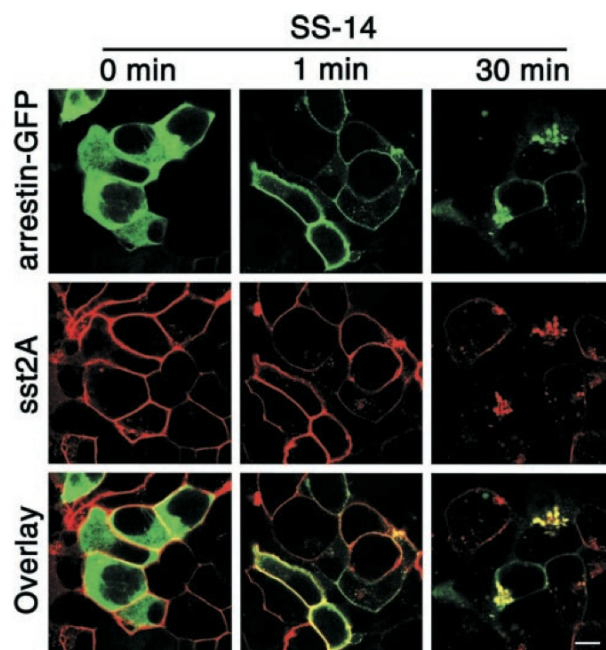
Figure 3.13: Co-trafficking of β-arrestin and sst_{2A} into early endosomes in the HEK-293 cells exposed to SST (SS-14) for 0 min, 1 min or 30 min. Scalebar 10 μm. Figure reproduced with permission from Tulipano et al.[256]

this was not observed after activation of sst_1 or sst_4. They also found that sst_{2A} underwent rapid recycling, whereas sst_3 was routed for lysosomal degradation, despite the similar β-arrestin association pattern. Later, a study on the sst_3-expressing rat insulinoma cells, by Roosterman et al.[213], revealed that sst_3 degradation only occurred under chronic stimulation with SST, whereas they were efficiently recycled under mild conditions. In either case, the internalized SST was routed to lysosomes for degradation.

Similar to the observations previously made using radiolabeling techniques, Liu et al.[156] found that cell signaling and internalization not only depended on the receptor subtype, but also on the SST-analog. Internalization rates of different permutations of the agonists and receptor subtypes was evaluated by Cescato et al.[47], to compile a dataset relevant to pre-clinical ligands-screening for tumor targeting. As an example, dependence of the sst_3-mediated internalization on the agonist type is shown in Figure 3.14.

A very detailed study on the dynamics of sst_{2A}-mediated internalization in live
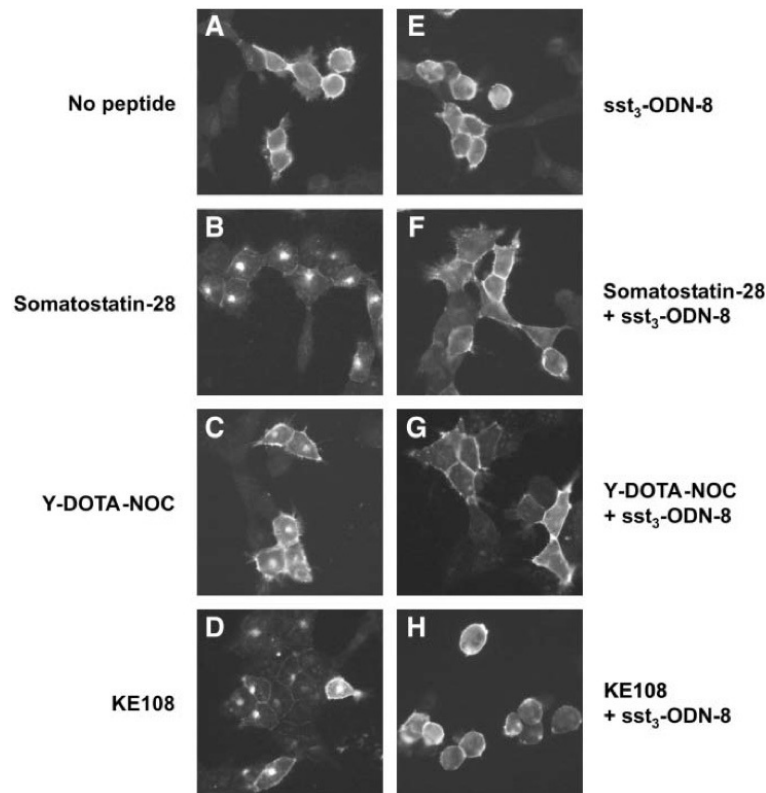
Figure 3.14: Difference in the level of sst$_3$-mediated internalization induced by various agonists in HEK cells (left). The agonists are unable to induce internalization in the presence of the sst$_3$-specific antagonist sst3-ODN-8 (right). The antagonist by itself does not activate internalization. Reprinted by permission of the Society of Nuclear Medicine from: Cescato R, Schulz S, Waser B, et al. Internalization of sst2, sst3, and sst5 Receptors: Effects of Somatostatin Agonists and Antagonists. J Nucl Med. 2006; 47(3): 502-511[47], Figure 3.

hippocampal neurons was presented by Lelouvier et al.[149]. They found that the sst$_{2A}$-mediated internalization of octreotide started with the association of β-arrestin, followed by the formation of receptor clusters, which soon accumulated within pre-formed clathrin-coated pits, and eventually got internalized. The whole process took only < 10 min. Most studies on sst$_1$ did not report on internalization after agonist activation, except for a few, including the paper by Roosterman et al.[215]. From the existing body of evidence, Jacobs and Schulz[124] created an sst-specific internalization diagram, shown in Figure 3.15, a version of Figure 3.10. Later, it was found that the receptor desensitization process, β-arrestin binding and internalization are controlled by phosphorylation of different amino acid residues of the sst$_{2A}$ in transfected CHO-K1 cells[225].
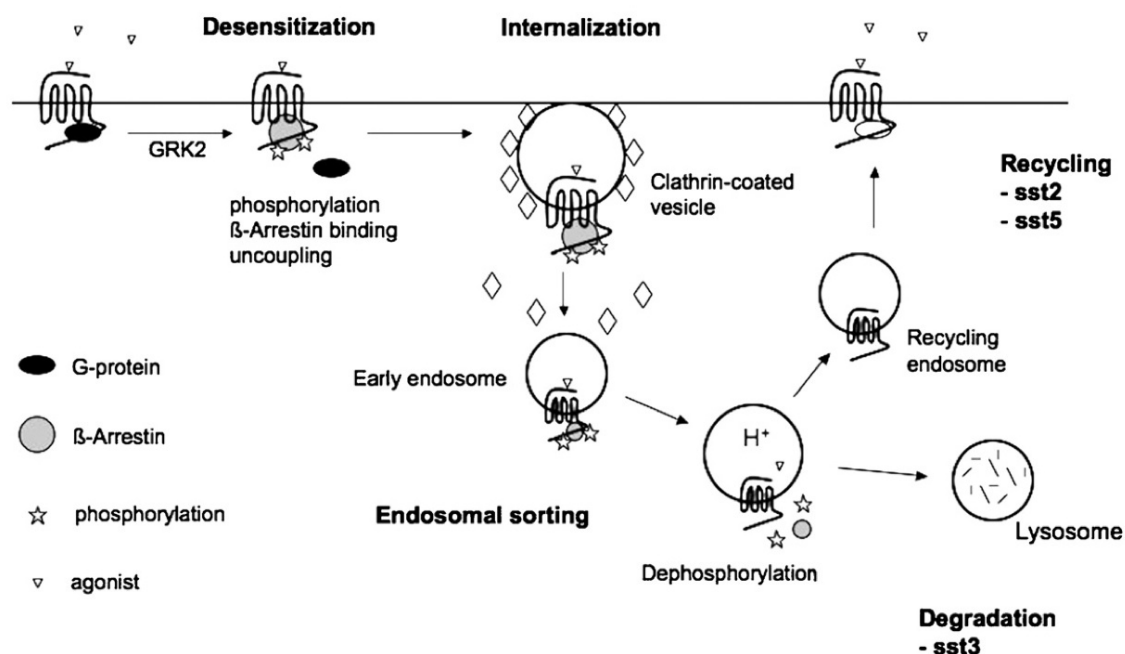
Figure 3.15: Agonist addition causes activation, phosphorylation and desensitization of receptors, followed by recruitment of β-arrestin. The process of receptor oligomerization or de-oligomerization is not shown. The activated agonist:receptor:arrestin complexes are internalized and trafficked via various intracellular compartments. The receptors may either be recycled or sent to the lysosomes for degradation. Nearly the entire pool of internalized sst_2 and sst_5 is recycled, whereas the sst_3 are routed to lysosomes and sustains a down-regulation. GRK2 is a kinase which phosphorylates sst(s). Reprinted from Publication Molecular and Cellular Endocrinology, 286(1-2), Jacobs and Schulz, Intracellular trafficking of somatostatin receptors, 58-62, Copyright (2008), with permission from Elsevier[124].

Such deep understanding on the functioning of the sst-expressing cells upon SST-binding and activation has tremendously fostered the SST-based diagnostic and therapeutic tools[31,37,46,112,159,206,234,247,262,272]. One of the breakthroughs in optical tumor targeting was reported by Becker et al.[25] and Licha et al.[150] in 2001. They developed a near-infrared fluorescent dye to label octreotide molecules, in order to target subcutaneous tumor xenografts in mice, as shown in Figure 3.16. Two similar instances of sst-based fluorescent tumor targeting have since been reported[5,138]. It should be noted that a significant amount of labeled SST (or analog) also accumulated in other non-targeted tissues including liver, kidney and pancreas, in these studies. Re-uptake of the SST analogues by the proximal tubular cells (PTCs) in kidney by the sst-mediated
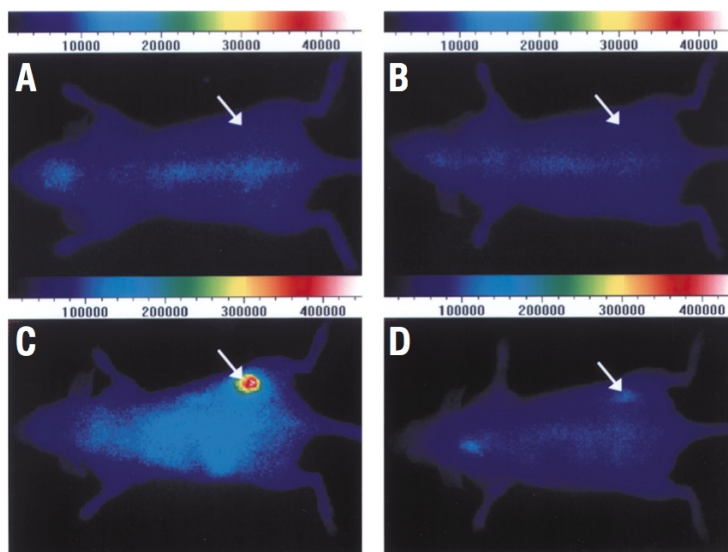
Figure 3.16: Specific and long-lasting in vivo targeting of tumors. Top and bottom images show RIN38/sst$_2$ tumor-bearing nude mice before and 6 hr after intravenous injection of active (A, C) or inactive (B, D) fluorescent-octreotide, respectively. Reprinted by permission from Macmillan Publishers Ltd: Nature Biotechnology[25], copyright (2001).

internalization has even been speculated to be the cause of nephrotoxicity during radiolabeled octreotide-based cancer therapy[21]. Therefore, further improvement in our understanding of the events accompanying the sst:SST binding is believed to contribute towards betterment of tools used in clinical practices.

3.7 Conclusion and Goal

Somatostatin is an abundant peptide that serves a variety of significant functions across the human body, including regulation of blood pressure, respiration, metabolism etc. These functions can be harnessed for improvement of healthcare, which, in turn, demands better understanding of the underlying mechanisms. The primary goal of this thesis was the development of a tool to facilitate this understanding. A nanoparticle attached to a somatostatin molecule was believed to serve as a fluorescent beacon furnishing this goal, by providing the ability to monitor its localization within a cell or a tissue. One of the other areas that benefits from such a tool is tumor targeting, based on the over-expression of somatostatin receptors in tumors.

Next chapter addresses the experimental aspects of the development, characterization and optimization of novel nanoparticle-somatostatin complex.

4

Experimental Methodology

The protocols of experiments that were frequently performed in the project are described in this chapter. Wherever required, a brief explanation of the basic principle is also provided. Protocols that were only used in specialized situations are not included in this chapter.

Contents

4.1   Characterization of Fluorescent Labels

A diverse collection of labels were used in this project for highlighting biomolecules, which included organic fluorophores and fluorescent nanoparticles. These contrast agents were characterized in terms of their photo physical, physical and physiochemical properties. The experiments carried out for these characterizations are detailed in this section.

4.1.1   Absorption Spectrum

The absorption coefficient of a molecule/nanoparticle quantifies the efficiency with which it absorbs light energy. The absorption coefficient is related to the transparency of the material by Equation 4.1[78].

$$\frac{I_t(\lambda)}{I_o(\lambda)} = e^{\alpha(\lambda)CL} \qquad \qquad The\ Beer - Lambert's\ law \qquad \qquad (4.1)$$

where, $I_t(\lambda)$ and $I_o(\lambda)$ are the transmitted and incident light intensities at the wavelength λ, $\alpha(\lambda)$ is the absorption coefficient–an intrinsic property of the sample– at the wavelength λ, C is the concentration of molecule/nanoparticle and L is the path-length of interaction between the sample and the light.

In the areas of chemistry, biochemistry and biophysics, absorption-related measurements are used for quantitating the concentration of molecules with known values of absorption cross section. An absorption spectrometer typically consists of a broad-band light source, a monochromator, sample chamber and a set of detectors for measuring the intensity of light before and after passing through the sample. The light from the broad-band source is wavelength-filtered by the monochromator, passed through the sample chamber and collected by the detector. A plot of the dependence of percentage-absorption (or percentage transmission) on the wavelength of light is referred to as the absorption spectrum of the sample.

A Cary 5000 UV-Vis-NIR Spectrometer (Varian Inc.) represented as an absorption spectrometer for this thesis. Sample in the solution format was loaded in a quartz

cuvette (NSG Precision Cells; path length = 4 mm) and placed in the sample chamber. The spectrometer was programmed to acquire the % transmission values across the desired wavelength region, typically from 200 nm to 800 nm. Wherever required, a control spectrum was obtained using a reference sample. The data was exported in ASCII format and analyzed. The unknown parameter of the sample (either the absorption coefficient or the concentration) was calculated using Equation 4.1.

4.1.2   Fluorescence Spectrum

The efficiency with which a fluorescent label can convert its electronic energy at the excited state to emit light is known as its fluorescence quantum efficiency. The wavelength-dependency of the quantum efficiency gives rise to a fluorescence emission spectrum, which is unique for each label. A similar wavelength dependence is also observed during excitation, known as the excitation spectrum, and is closely related to the absorption spectrum. These spectra are useful for quantitation of very low (sub nano molar) concentrations. In this project, a Fluorolog Tau3 system (JY Horiba; Figure 4.1) represented as a fluorescence spectrometer, with which fluorescence excitation and emission spectra were measured.

A typical fluorescence spectrometer consists of a broad band light source, excitation monochromator, sample holder, collection lens, emission monochromator and a set of detectors for measuring intensities of the incident and emitted light. The emission detector is usually placed at a right angle with respect to the incident light path, in order to eliminate direct light. At dilute concentrations, the fluorescence intensity is linearly dependent on the concentration. However, generally, the fluorescence values are often arbitrary, because it is dependent on various parameters such as, the sample holder geometry and light beam shape.

For fluorescence measurements, samples were prepared in a solution form, transferred into a quartz cuvette and placed in the sample chamber. The Fluorolog was programmed to acquire excitation/emission spectra within a particular wavelength range. In order to obtain reproducible spectra, the emission and excitation spectra
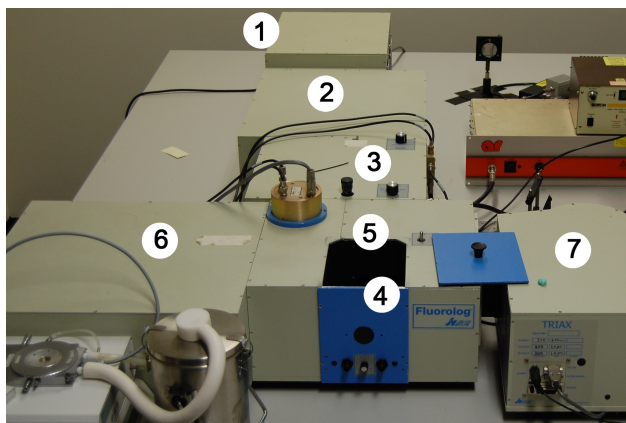
Figure 4.1: Fluorolog Tau3 system, identifying components
1 - Broadband light source
2 - Excitation monochromator
3 - External light source switcher
4 - Sample chamber
5, 6 & 7 - Detection optics

were obtained at peak excitation and emission wavelengths, respectively, using a two-step iteration process (see Section 5.5.2.1). The data was exported and the reference baseline was subtracted.

4.1.3 Size

Size measurements described in this thesis were usually performed using the technique of dynamic light scattering (DLS). DLS enabled the prediction of the distribution of hydrodynamic diameters of an ensemble of nanoparticles suspended in a colloid, based on the fluctuations in the intensity of the scattered light.

A typical DLS instrument consists of a laser source, a sample chamber and a very fast detector (sub millisecond detection times), mounted at a specific angle from the incident laser beam path. The light from the laser source is scattered by the particles in the sample, and is collected by the detector. However, the scattered intensity is dynamic, because the particles in the solution undergo diffusion. The rate of this random fluctuation is dependent on the diffusion coefficient, which is inversely proportional to the hydrodynamic radius of the particle, given by Equation 4.2. Analysis on the temporal fluctuations in the scattered intensity is used to calculate the hydrodynamic diameter (or radius) of the particle. The method used to extract temporal information from the scattered light is known as autocorrelation. A discussion on autocorrelation is beyond the scope of this thesis.

Figure 4.2: Zetasizer Nano-ZS; identifying components
1 - Location of the nbuilt 633 nm laser source
2 - Sample chamber, with temperature control
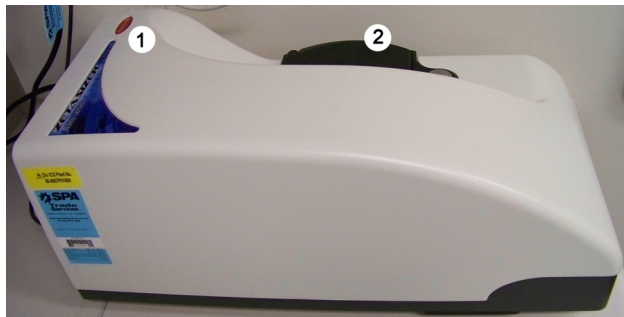
$$D = \frac{\kappa T}{6\pi\eta R} \qquad Stoke - Einstein\ Equation \qquad (4.2)$$

where, D is the diffusion coefficient of the particle, κ is the Boltzman's constant, T is the temperature, η is the viscosity of the solvent and R is the radius of the particle.

Zetasizer Nano-ZS (Malvern; shown in figure 4.2) was used as the DLS-based instrument for measuring the size distribution of nanoparticle in a colloid. The nanoparticles (quantum dots or nanodiamonds) were dispersed in an aqueous solvent at an appropriate concentration, generally determined by trial and error. The solution was transferred into a clear-zeta-cell (Malvern), without bubble formation, as per the instruction manual. Physical properties of the solvent and the solute, for example refractive index and viscosity, were fed into the computer and the Zetasizer was programmed to perform the following tasks:

1. Equilibrate the sample temperature to 25 ^{o}C for 10 min. This ensured that there were no convection currents inside the solution chamber, which might influence the thermodynamic diffusion by introducing drift. This step was found to be critical during winter, because of the higher temperature difference between the sample and the sample-chamber.

2. Automatically identify the number of averages to be performed, depending on sample quality.

3. Perform a multi-modal curve fit to the autocorrelation data and calculate a size-distribution.

The softwares' inbuilt quality control algorithm performed tests on data from each sample and reported whether the measurement was reliable. If not, the reasons and troubleshooting suggestions were provided. Some of the common reasons for unreliable data were too low or high particle concentration and particle aggregation. It was observed that a sample concentrations, which yielded scattering count-rates of ≈ 300 kcps (with an attenuator setting of 6 units) yielded most reliable data. In cases where aggregation was observed, the sample was sonicated prior to measurement. The output files were analyzed to measure the peak(s) of the size distributions.

4.1.4   Zeta-potential

Zeta-potential is a physical property that is related to the electrostatic charge associated with a solid/liquid interface. It is a useful parameter for the quantitation of the surface charge of nanoparticles, whose absolute value is often difficult to measure. Zeta-potential is defined as the electrostatic potential originated from the surface charge, measured at the fluid slippage plane. Slippage plane is a virtual boundary that separates the fluid, which moves along with the nanoparticle, from the fluid, which stays with the stationary bulk solvent. The concept of zeta-potential arises from the mathematical expression of a directly measurable physical parameter - the electrophoretic mobility (μ_e). They are related to each other by Equation 4.3.

$$\mu_e = \frac{2\epsilon\zeta f(ka)}{3\eta} \tag{4.3}$$

where, ϵ is the dielctric constant, ζ is the zeta-potential, $f(ka)$ is the Henry's function (whose value is 1.5 under certain conditions that satisfy the Smoluchowski approximation), η is the viscosity and μ_e is the electrophoretic mobility, which can be expressed as:

$$\mu_e = \frac{v}{E} \tag{4.4}$$

where, v is the velocity of the particle, under an applied electric field, E.

Zeta-potentials of nanoparticles used in this project were measured using a Zeta-sizer, shown in Figure 4.2. The nanoparticle colloid was prepared in an aqueous solvent and transferred into a clear zeta cell. The cuvette was placed into the Zetasizer sample chamber and material parameters were entered into the Zetasizer software and was programmed to perform the following steps:

1. Equilibrate the sample temperature to 25 ^oC for 10 min.

2. Automatically determine the number of averages to be performed, depending on quality of the measurement data.

After performing automatic analysis on the acquired data, Zetasizer outputs a histogram of zeta-potentials of particles in an aqueous colloid. However, it fails to provide a histogram if the sample conductivity exceeds 5 msiemens.cm^{-1}, in which case only an average zeta-potential value is computed. Inappropriate colloidal concentration, aggregation or non-equilibrial temperature often resulted in poor data quality, as was notified by the software. Altering the concentration or brief sonication usually improved the data quality and reliability.

4.2   Cell Culture

Immortalized tumor cells were used in the thesis to perform *in vitro* experiments in order to characterize the biological activity of proteins, nanoparticles and nanoparticle-protein complexes. Four different types of cells were used, and they all expressed somatostatin-receptors (either endogenous or transfected). They were the AR42J, GH4C1, AtT-20 and CHO-K1 (gene modified) cells. This section details each of these cell-lines, including the protocols for their regular maintenance, storage and restoration.

4.2.1 AR42J Cells

The AR42J cells were obtained from the biological resource center, ATCC (American Type culture collection) (ATCC No. CRL-1492$^{\text{TM}}$). These are adherent (that can be grown on a bottom surface of a vessel) epithelial cells, and originally obtained from a tumorous pancreatic tissue of a brown rat (*Rattus norvegicus*, strain: Wistar). The AR42J cells endogenously express somatostatin receptors.

4.2.1.1 Growth Condition

Generally, cell cultures are maintained in a liquid complete growth medium, which contains a base media, supplemented with animal-derived serum and auxiliary antibiotics to prevent contamination. F-12K was used as the base media to culture the AR42J cells and was supplemented with 20 %fetal bovine serum (FBS). After preparation, the complete growth media was filtered through a 0.22 μm filter, for sterilization and stored at 4 ^{o}C.

Normally, the cells were grown in tissue culture flasks with complete growth media, inside an incubator (Thermo Scientific) maintained at 37 °C and 5% CO_2 under a humid environment. 5% CO_2 was used to maintain the physiological pH of the culture media, which contained carbonates as buffering agents. The humidity minimized evaporation of the media, which would otherwise alter the osmolarity, resulting in cell death. All the cell culture related procedures and experiments were carried out inside a laminar flow hood, and it was a general practice to wipe the bench and objects with 70% ethanol solution for sterilization. All fluid transfers were carried out using disposable serological pipettes, attached to a motorized pipette-man (BD Falcon). Liquid waste were collected and treated with bleach solution before disposal into a sink. Solid wastes were autoclaved and disposed appropriately.

4.2.1.2 Thawing

Cells were procured in frozen condition (in dry ice). To initiate their growth, the frozen cell suspension was thawed and re-suspended into 10-mL of pre-warmed (to

37 ºC) complete growth media. The 10-mL cell suspension was centrifuged (@ 100 × g for 5 min) and resuspended in fresh, pre-warmed complete growth media, in order to remove cryo-protectants [usually dimethyl sulfoxide (DMSO)]. The suspension was transferred to a culture flask (Blue vented-cap, tissue culture treated) (BD Falcon, Australia) at a final density of approximately 11,000 - 15,000 cells.cm^{-2} and placed in an incubator. The cells were grown overnight and the culture media was renewed on the next day to remove traces of cryo-protectants. Later on the normal propagation protocol was followed.

4.2.1.3   Propagation

The AR42J cells grew in clusters attached to the floor of the culture flask. Under normal conditions the complete growth media was renewed every 2-3 days. In one week, the cells formed large clusters, at which point they were seeded into a new culture flask after 1:3 to 1:5 dilution, a procedure referred to as 'passaging'. For passaging, the cells were first washed with PBS (phosphate buffered saline) devoid of $CaCl_2$ and $MgCl_2$. The washing procedure rendered the cells less adherent, as $CaCl_2$ and $MgCl_2$ facilitate adhesion. The cells were treated with a solution containing 0.25% (w.v^{-1}) trypsin and 0.53-mM ethylenediaminetetraacetic acid (EDTA) in PBS for $\approx$ 2 min at 37 ºC or until the cells appeared spherical under a transmission, phase-contrast microscope. The enzyme, trypsin, promoted cell detachment as it cleaved the adhesive proteins on the cell surface. EDTA promoted the process by scavenging Ca^{2+} and Mg^{2+}-ions by chelation. This procedure was carefully carried out, because of risk of over-exposure to trypsin causing cell-death.

In order to break cell clusters, fresh, pre-warmed complete growth media was added and the solution was triturated several times using a serological pipette. A portion of this solution was added to a new culture flask containing appropriate quantity of pre-warmed complete growth media. The complete passaging procedure was carried out, approximately, once a week to sustain the AR42J cell culture. A maximum of 50 passages were carried out, after which a fresh culture was started.

4.2.1.4 Storage

Generally, cells are kept frozen for three reasons: (1) long term storage (2) transportation and (3) for maintaining batches with low passage cycles. Several cell freezing protocols exist, and most of them use one way or the other to minimize crystal formation during the freezing procedure. Crystal formation can rupture the cell membrane, rendering the cells non-viable. 10% DMSO was added to the complete growth media to prepare freezing medium.

The cells were grown normally until they reached confluence. At this point, they were detached from the culture flask using Trypsin, as described above. The trypsinized cell-suspension were re-suspended in pre-warmed complete growth media and centrifuged (@ 100 ×g for 5 min) and resuspended in half of the freezing media maintained at room temperature. The second half of the freezing media that was maintained at 4 °C was added drop-wise, allowing a gradual reduction of temperature. This cell-suspension was transferred into 2 mL cryo-vials and placed inside a Mr. Frosty[†] and transferred into a -80 °C freezer. The next day, the cryo-vials were transferred from Mr. Frosty to a -137 °C freezer or a liquid nitrogen dewar.

4.2.2 GH4C1 Cells

The GH4C1 cells were obtained from ATCC (ATCC No. CCL-82.2[TM]). They are loosely adherent epithelial cells, and originally obtained from tumorous pituitary tissue of a brown rat (*Rattus norvegicus*, strain: Wistar-Furth). The GH4C1 cells endogenously express somatostatin receptors[201].

4.2.2.1 Growth, Thaw, Propagation and Storage

The complete growth medium to culture GH4C1 cells contained Ham's F10 medium as the based medium, to which 2.5% FBS and 15% horse serum (HS) were added. Except the different growth medium, the procedures used to thaw, passage and store the cell were similar to that used for culturing the AR42J cells.

[†]Mr. Frosty is a trademarked product, designed to regulate the rate of temperature drop to 1 °C.min⁻¹, when placed inside a -80 °C freezer

4.2.3   AtT-20 Cells

The AtT-20 cells are of adherent type, and originally obtained from tumorous pituitary tissue of a mouse (*Mus musculus*, strain: LAF1). These cells were obtained from collaborator Prof. Mark Connor. They endogenously express four of the five known somatostatin receptor subtypes including the sst_1, sst_2, sst_4 and sst_5 [188].

4.2.3.1   Growth, Thaw, Propagation and Storage

The complete growth medium to grow the AtT-20 cells contained Dulbecco's Modified Eagle Medium (DMEM), to which 10% FBS and 50/5-μg penicillin/streptomycin were added. Cells were thawed and grown using procedures similar to that described above.

4.2.4   CHO-K1 Cells

The genetically modified chinese hamster ovary (CHO-K1) cells were obtained from PerkinElmer, Australia (Catalogue No. ES-521-C). They expressed human somatostatin 2A receptor (sst_{2A}), up to a density of 10 pmol.mg^{-1} of membrane proteins.

4.2.4.1   Growth, Thaw, Propagation and Storage

The complete growth media for the CHO-K1 cells composed of Hams's F12 (the base media), 10% FBS and 400-μg.mL^{-1} geneticin (G418, Invitrogen). Geneticin was used to select the cells that expressed sst_{2A}. Similar to the AtT-20 cells, these cells also grew in monolayers. The cell density was measured in terms of the number of cells per square centimeter, using a home-made Matlab based program, detailed in Appendix A. Under normal growth conditions, passages were done every second day. The procedures used for thawing, passaging and freezing were similar to the other cell lines described earlier.
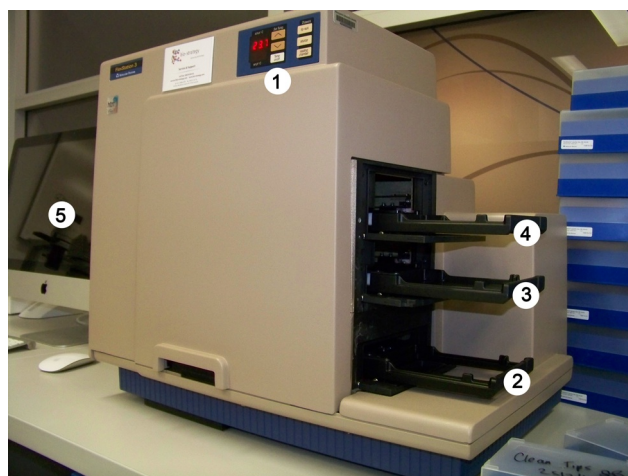
Figure 4.3: FlexStation 3, identifying components
1 - Control panel
2 - Cell culture plate tray
3 - Compound plate tray
4 - Pipette tip box tray
5 - Computer for control

4.3 Cell Signaling Experiments

The biological activity of the somatostatin, nanoparticle, or somatostatin-nanoparticle complexes were investigated using three types of cellular responses. These included changes in membrane potential, changes in cytoplasmic concentration of Ca^{2+} and receptor-mediated endocytosis.

4.3.1 Membrane Potential Assay

The membrane potential of cells were monitored quantitatively using a membrane potential-sensitive fluorescent dye. The assay was carried out using The FlexStation 3 (Molecular devices, see Figure 4.3) - a micro plate reader, with robotic fluid-transfer capabilities. The procedures used for cell preparation and carrying out the assay are detailed below.

4.3.1.1 Cell Cultivation

The AtT-20 cells were cultivated in a black-wall, flat, clear-bottom, 96-well plate (Costar) until reaching confluency. On the evening before the day of the assay, the complete growth media in the wells was replaced with 100-μL.well^{-1} Lebovitz L-15 medium, supplemented with 1% FBS and placed inside a 37 ^{o}C incubator. Lebovitz L-15 media was used for the assay because its pH is independent of CO_2, and the FlexStation 3 was not connected to a CO_2 regulator.

4.3.1.2 Experimental Procedure

A membrane potential sensitive fluorescent dye was purchased from Molecular Devices (Blue dye, Cat# R8034), as a part of a FLIPR membrane potential assay kit. The blue-colored dye, supplied in a powder format was dissolved in 100 mL of low-potassium version of the recommended buffer, containing 143.7-mM NaCl, 18.35-mM HEPES, 0.34-mM Na_2HPO_4, 4.17-mM $NaHCO_3$, 0.44-mM KH_2PO_4, 0.83-mM $MgSO_4$, 1.05-mM $MgCl_2$, 1.26-mM $CaCl_2$ and 5.5-mM D-Glucose. The prepared dye solution was stored in a -80 ^{o}C freezer for later use.

In preparation for the assay, 100-μL pre-warmed dye-solution was added to each well in the cell culture plate. The cell culture plate was placed inside the incubator for 30 min. Meanwhile, drugs solutions (for example, somatostatin) of 5$\times$ or 10$\times$ final concentrations were prepared in the low potassium modified buffer and distributed in a clear-wall, v-bottom, 96-well compound plate. Normally, each column in the compound plate was dedicated for a particular drug, with each row containing incrementally increasing (logarithmic scale) drug concentrations. This facilitated the data analysis to obtain a drug concentration-response curve. The cell culture plate, the source plate and a box containing specialized black-pipette tips were loaded into the FlexStation, to perform the assay. The dark pipette tips ensured minimal backscattering and pipette-derived fluorescence. The FlexStation greatly reduced the complexity of the assay, because all the fluid transfers and fluorescence read-outs were automated after the plates were loaded. It also allowed monitoring the fluorescence changes (therefore the cell-membrane potential) in real-time.

The FlexStation was programmed to perform the following tasks, using the software Softmax Pro:

1. Acquire the fluorescence intensity with excitation and emission wavelengths fixed at 530 nm and 565 nm, respectively, with emission cut-off filter at 550 nm (with auto-mode enabled) once every few seconds for several minutes.

2. At a particular time point, add 50 μL of the 5$\times$ (or 22 μL of the 10$\times$) concentrated drug solution from a specific column in source plate to that in the cell culture

plate, which already contained 200 μL of solution.

3. Immediately after the addition, triturate the solution in the culture plate, in order to reach a uniform drug concentration throughout each well.

4. After the fluorescence reading, export the data as a time sequence for each well.

All the assays were repeated at least three times independently, each in triplicates or quadruplicates.

The fluorescence readings were calibrated using blank and negative controls. Blank controls were obtained from a column of wells, which were devoid of cells, but was otherwise treated similarly. The negative controls were obtained from wells in which the added compound solutions were devoid of drugs. All the assays were repeated at least three times independently, each in triplicates or quadruplicates.

4.3.1.3 Data Analysis

The time course of fluorescence fluctuations was exported from the Softmax Pro as a time series in ASCII format. All the data analyses were performed using a self-built Matlab based graphical user interface (GUI), detailed in Appendix B. Firstly, a mean blank control time series was obtained by averaging all the blank control data, which was subtracted from all the time series data. Next, the percentage drop in fluorescence from each well after drug addition was obtained and offset using that from the negative controls. The corrected percentage change in fluorescence was proportional to the change in cellular membrane potentials.

Where appropriate, a concentration dose-response curve was generated from the normalized and averaged data corresponding to each drug. For an example, see Figure 5.9. The potency of the drug was calculated in terms of pEC_{50} values, calculated by performing a sigmoidal fit to the dose-response curves, using Equations 4.5 and 4.6. Origin academic version 8.1 was used to perform plotting and curve-fitting.

$$R = \frac{R_{min} - R_{max}}{1 + ([D]/EC_{50})^k} + R_{max} \qquad \text{Logistic equation} \qquad (4.5)$$

$$pEC_{50} = -\log EC_{50} \tag{4.6}$$

where, R = Response (or the percentage change in fluorescence); the subscripts max and min represent saturation and minimum responses, respectively

[D] = Concentration of the drug

EC_{50} = Concentration of drug resulting in 50% saturation response

k = Fitting parameter, which determined the steepness of the curve

4.3.2 Ca^{2+} Mobilization Assay

Activation of somatostatin receptors in certain cells triggers the release (or intake) of Ca^{2+} into the cytoplasm. This response was used to evaluate the biological activity of biomolecules, nanoparticle and nanoparticle-biomolecule complexes in this thesis. Intracellular concentration of calcium ($[Ca^{2+}]$) was measured using a fluorescent, indicator-dye (Fura-2AM, Invitrogen), whose fluorescence excitation spectrum was dependent on the concentration (see Figure 5.10). Typically, such indicators consist of a Ca^{2+}-chelator group (like EGTA or BAPTA) and a stilbene-like fluorophore[94]. The chelators bind to free Ca^{2+}-ions, thereby influencing the spectra of the fluorophore. The Ca^{2+} mobilization assay was carried out using a FlexStation.

4.3.2.1   Experimental Procedure

The assay was performed in HEPES Buffered Saline (HBS), containing 140-mM NaCl, 2-mM KCl, 2.5-mM $CaCl_2$, 1-mM $MgCl_2$, 20-mM HEPES, 10-mM D-Glucose, 2.5-mM Probenecid and 0.05% BSA (Bovine Serum Albumin), which was adjusted to pH 7.4±0.1 and an osmolality of 330±40 mosmol.kg^{-1}, unless otherwise specified. Probenecid was used to enhance the entry of Fura-2AM into the cells. HBS+Ca was the same as HBS except that it contained 20-mM $CaCl_2$. In HBS-Ca buffer, $CaCl_2$ was replaced with 10-mM ethylene glycol-bis[b-aminoethylether]-N,N,N',N'-tetraacetic acid (EGTA), which selectively chelates free Ca^{2+}-ions.

The CHO-K1 cells were cultivated in a black walled, flat-clear-bottom, 96-well plate

until reaching confluence. The cells were washed once with HBS to remove esterases[†] in the cell growth media that can affect the cell-permeability of Fura-2AM. 200 μL of 2-μM Fura-2AM solution, prepared in HBS, was added to the wells in the culture plate and incubated for 1 hr at 37 ^{o}C. This process allowed the weakly membrane permeant Fura-2AM to enter the cell. One column of cells in the plate was not loaded with Fura-2AM, instead 200 μL of HBS was added, which served as the blank control to obtain the level of the background fluorescence.

The cells were washed 4$\times$ with HBS to remove extracellular Fura-2AM and placed inside the incubator for another 30 min. This allowed the esterases in the cell to remove hydrophobic groups in the Fura-2AM molecule (which provides membrane permeability) restoring its sensitivity to Ca^{2+}-ions. The cells were washed with HBS once again and placed inside the FlexStation to carry out the assay. One column of wells were dedicated for obtaining maximum and minimum control data. 200 μL of HBS+Ca and HBS-Ca were added to four wells each.

The drugs to be analyzed were prepared in HBS at 5$\times$ or 10$\times$ the final concentration and distributed in a compound plate. For maximum and minimum controls solutions digitonin (a detergent that permeates cell membranes leading to equilibration of extracellular and intracellular solutions) was used instead of drugs. The culture plate, compound plate and a pipette tip box were loaded into the FlexStation, and programmed to perform the following procedure:

1. Acquire the intensity of fluorescence emission at 510 nm under two alternating excitation wavelengths of 340 nm and 380 nm, every few seconds over a period of several minutes.

2. Add 50 μL of the 5$\times$ concentrated drug or 22-μL digitonin solution from a specific column in the source plate to that in the cell culture plate, at a particular time point.

3. Triturate the solution three times after adding drug/digitonin.

[†]Esterases are enzymes that cleave ester bonds

4. After completion, export the data as a time sequence for each well.

All the assays were repeated at least three times independently, each in triplicates or quadruplicates.

4.3.2.2 Data Analysis

The time course of fluorescence fluctuations was exported from the Softmax Pro as a time series in ASCII format. All the data analyses were performed using a self-built Matlab based graphical user interface (GUI), detailed in Appendix C. Firstly, the average background signal was calculated using the data obtained from the blank control well, which was subtracted from all the time series data. The time-series of fluorescence intensities at the two excitation wavelengths were converted to a time dependent intracellular $[Ca^{2+}]$ using Equation 4.7[94].

$$[Ca^{2+}] = K_d \times \frac{R - (S_{f340}/S_{f380})}{(S_{b340}/S_{b380}) - R} \times \frac{S_{f380}}{S_{b380}} \tag{4.7}$$

where, K_d = Effective dissociation constant of chelation of Ca^{2+}-ions by Fura-2AM. The value of K_d used was 224 nM as determined by Grynkiewicz et al.[94]

R = Ratio of background subtracted fluorescence intensities at 340 nm and 380 nm excitations, respectively

S_{f340} = Background subtracted fluorescence at 340-nm excitation after digitonin addition to the cells in HBS-Ca buffer

S_{f380} = Background subtracted fluorescence at 380-nm excitation after digitonin addition to the cells in HBS-Ca buffer

S_{b340} = Background subtracted fluorescence at 340-nm excitation after digitonin addition to the cells in HBS+Ca buffer

S_{b380} = Background subtracted fluorescence at 380-nm excitation after digitonin addition to the cells in HBS+Ca buffer

From the obtained $[Ca^{2+}]$ time series, the increase in intracellular $[Ca^{2+}]$ upon

Table 4.1: Calibration of the cell culture microscope, equipped with a CCD camera

Objective	4×	10×	20×	40×
Image size	680 px	172 px	340 px	672 px
Actual size	1 mm	100 μm	100 μm	100 μm

addition of drugs was measured for each well. Where appropriate, a normalized concentration-response curve was plotted. For example, see Figure 5.12. The pEC$_{50}$ values of drugs were calculated using Equations 4.5 and 4.6.

4.4 Microscopy

Microscopy was one of the important elements in this thesis. Several microscopes, equipped with unique contrast mechanisms were used, and will be discussed in the following Subsections.

4.4.1 Cell Culture Microscope

A Zeiss inverted microscope equipped with bright field, transmission and phase contrast optics was used to determine the cell growth rate and passaging conditions. A CCD-camera attached to the microscope allowed recording images and videos of cells. It was also used for counting cell density, using a home-build Matlab-based program (see Appendix A for details). The scale of the images obtained using this camera/microscope set up is presented in Table 4.1.

4.4.2 Leica TCS SP Confocal Microscope

All the fluorescence images presented in this thesis were acquired using one of the three fluorescence confocal microscopes (Leica TCS SP, SP2 and SP5), of which one is shown in Figure 4.4. All three microscopes were equipped with a variety of lasers for confocal imaging, mercury/neon lamps for full field fluorescence imaging and halogen lamps

for transmission bright-field imaging. The detection optics included photomultiplier tubes and CCD cameras for confocal and full field modes, respectively. In the confocal mode, an acousto-optic beam splitter (AOBS) provided versatile choice of selecting the wavelength bands for detection. However, in the full-field mode, the fluorescence excitation and emission wavelength bands were controlled using filter-dichroic cubes. In the confocal mode, these microscopes allowed multidimensional data acquisition, including fluorescence spectra corresponding to each pixel in the images, 3-D stacks and temp-course imaging. The choice of the microscope was primarily determined by the features and availability. For example, while the Leica TCS SP system offered the phase contrast imaging capability in transillumination mode, the TCS SP2 system was equipped with 405 nm laser allowing imaging of blue emitting dyes, such as Hoechst. Further details on the specific capabilities of SP and SP2 systems are available in the website: http://physics.mq.edu.au/~goldys/MicroscopeBooking/index.php. The SP5 system located within the Australian School of Advanced Medicine was equipped with a super-continuum laser and allowed visualization dyes (e. g., red fluorescent proteins in Section 5.7.1) that were inefficiently excited with the other microscopes.

Most often, the images were acquired in a 512 px × 512 px format, and exported as a TIFF file. These images were processed and analyzed using the free software Image J or Matlab (university license).

4.5   Summary

In summary, this chapter describes the general instrumentation and methodologies that were used for this thesis. More specific information on the settings and procedures used for particular experiments are described as required.
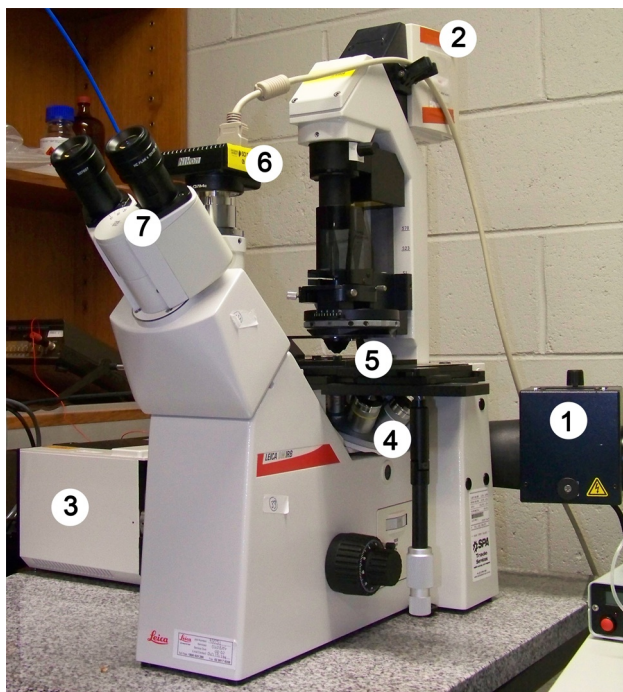
Figure 4.4: Leica TCS SP confocal fluorescence microscope, identifying components
1 - Mercury lamp
2 - Halogen lamp
3 - Confocal scanning head, AOBS & detectors
4 - Objective turret
5 - Sample stage
6 - Full field imaging camera
7 - Binoculars

<div align="right">

5

</div>

Talking to the Cells

This chapter is based on the journal publication:

Varun K. A. Sreenivasan, Oleg A. Stremovskiy, Timothy A. Kelf, Marika Heblinski, Ann K. Goodchild, Mark Connor, Sergey M. Deyev and Andrei V. Zvyagin, "Pharmacological Characterization of a Recombinant, Fluorescent Somatostatin Receptor Agonist", *Bioconjugate Chem.*, 2011[240]

The chapter begins with a summarized version of Chapter 3, focussing on the cellular events related to somatostatin. The existing literature ushers towards the development of a fluorescently labeled somatostatin probe, which was able to communicate specifically with cells. Response of the cells were used to characterize the newly developed fluorescent somatostatin probe.

Contents

5.1   Recap and Introduction

A cell is a complex system, where a multitude of biomolecules conspire in a concerted effort to activate specific intracellular events. Due to the highly intertwined biomolecular interactions, information regarding the contribution of one type of biomolecule towards a particular event can rarely be identified by experiments performed in isolation. However, it is possible to highlight or single-out a particular type of molecule under investigation, in order to characterize its role. This can be realized by using a molecular probe or label that can be visualized, while not affecting the rest of the 'molecular soup' – a process termed specific labeling.

Somatostatin receptors (ssts, introduced in Chapter 3) are set of biomolecules, whose activation initiates a chain of intracellular events. It includes the six subtypes, sst_1, sst_{2A}, sst_{2B}, sst_3, sst_4 or sst_5. All these subtypes belong to class of proteins called the G-protein coupled receptors. They are all cell membrane-associated proteins, whose 3-D structure spans across the bilipid layer. This allows the receptors' extracellular domain to sense extracellular signals and transduce them into the intracellular space - the beginning of a complex chain of intracellular signaling events[106]. In regards to sst, the extracellular signal constitutes binding of a ligand, somatostatin-14 (SST). The intracellular signaling events that occur after the sst:SST[†] binding include changes in cellular membrane potential, concentration of ions[7,182,193] and even long-term changes, such as gene expression[219]. Often, these events are also accompanied by intake of the bound sst:SST complex into the cell – a process called internalization (or endocytosis).

[†]':'symbol denotes a non-covalent binding between the SST and sst
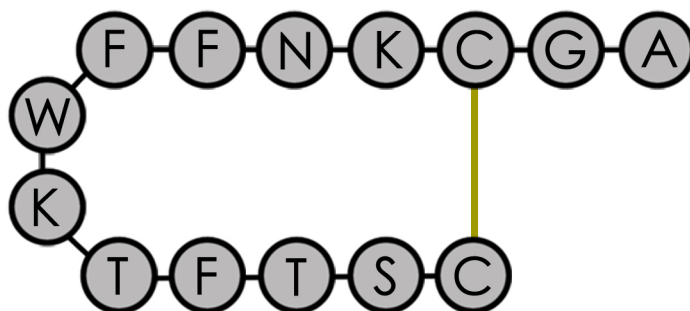
Figure 5.1: Schematic of a somatostatin-14 (SST) molecule, presented as a chain of amino acids in single letter code. The yellow line represents the naturally existing disulfide bond between the two cysteine residues. Reproduced from Figure 3.4

SST is a peptide (a small protein, presented as an amino acid chain in Figure 5.1), which takes part in a variety of significant processes in the body by activating sst[40]. In neurons located at specific regions in the brain, SST functions as a neurotransmitter and modifies central control of blood pressure[41] and respiration[42]. In the pituitary gland and pancreas, SST is a hormone that controls the release of secondary hormones which in turn inhibit growth[205] and affect glucose metabolism[247], respectively. Apart from behaving differently in different organs, the intracellular effects upon SST-binding can also vary between cell types. One of the reasons for the cell type-dependence is that sst can take form of any of its six subtypes, which are expressed differentially in cell types. An example of the differential behavior is the absence of SST-internalization after the activation of the receptor subtypes – sst_1 or sst_4, in comparison with the efficient internalization by sst_{2A}[47].

A large portion of the current understanding about the intracellular events that occur after SST:sst binding, including the activation and internalization, have been elucidated by the following methods: (a) immunocytochemical labeling of sst[47,84†], (b) probing other molecules involved in the intracellular signaling chain[225] or (c) a combination of these methods[95,256]. However, none of these methods allows one to answer

---

†It is important to note the immunocytochemical labeling only reveals the spatial localization of the receptor (sst) and not of the ligand (SST)

some of the significant questions pertaining to the fate of SST molecule, such as: (1) what is the cellular/sub-cellular localization of SST molecule after being internalized?, (2) how long does the SST molecule remain bound to the sst? etc[69]. These details would be invaluable in devising a tool for sst-targeted drug delivery, conceivable for applications such as diagnosis and therapeutics of neuroendocrine tumors[37]. Addressing these questions require SST-molecules that can be visualized, which can be realized by means of specific molecular labeling. Additionally, development of conspicuous SST-molecules will also enable localization of somatostatin receptors in biological tissues, particularly useful for diagnosis of neuroendocrine tumors, where the somatostatin receptors are over-expressed.

5.2 Labeled Somatostatin Molecules

Majority of studies that probe the molecular pathways of SST were carried out using radioactively (mostly iodine-125) labeled ligands[95,137,205,219], except for a handful that will be discussed shortly. Radioligands (i. e., radiolabeled SSTs) allow ensemble-based and statistically accurate characterization of the interactions (such as the binding affinity) of SST with the receptors and consequential intracellular events (such as internalization). However, a limitation of this approach is its inherently poor spatial resolution, which precludes any level of detail on the intracellular localization of SST. Radiolabeling methods also introduce workplace hazards, which demand cumbersome experimental procedures and radiation-safety approvals. In addition, the short half-life of certain radioactive isotopes causes decrease in sensitivity over time – dictating shorter shelf-lives. In comparison, optical labeling of SST would enable safe, easy, robust and, most importantly, detailed visualization of SST-related intracellular events.

The development and application of a few optically labeled SST analogs have been reported in the literature, all based on organic fluorophores. The first fluorescently labeled SST-analogs were reported by Nouel et al.[181], Sarret et al.[219] and Stroh et al.[246] during the years 1997 to 2000. They had developed a Bodipy-conjugated [D-Trp8] SST-analog to investigate the sst-mediated internalization in COS 7 cells, AtT-20 cells and

neurons, respectively. Later, in 2001, Licha et al.[150] and Becker et al.[25] developed a new, cyanine dye-conjugated SST-analog for *in vivo* tumor targeting. Kostenich et al.[138] also reported on labeling tumors using several types of fluorescent analogs of the SST pharmacore. Despite these advances, tagging of SST molecules with fluorescent dyes using chemical conjugation methods suffer from inherent disadvantages, for example, poorly reproducible reactions yielding uncontrolled molecular labeling ratio, ultimately leading to loss of potency[138]. To overcome problems with the chemical reactions, a genetic engineering approach was considered more appropriate to label SST molecules with fluorescent probes, and is addressed in this chapter.

SST was genetically fused with a monomeric red fluorescent protein (mRFP), yielding a chimeric protein, SST-mRFP. Its biochemical, optical and pharmacological properties were characterized and compared with the native components. Apart from the development of a novel fluorescent version of somatostatin, another motive of the work presented in this chapter was to explicitly address the ill effects of attaching other external moieties to SST. This understanding was considered critical for the development of a nanoparticle based fluorescent probe for SST, which would enable *in vivo* applications like tumor targeting and drug delivery. We found that SST-mRFP held much promise as a molecule for the investigation of the biomolecular events that occur after sst:SST binding.

5.3   Production of Recombinant, SST-mRFP

A recombinant, fluorescent analog of SST was designed and constructed by Prof. Sergey M. Deyev and co-workers at the Institute of Bioorganic Chemistry, Russian Academy of Sciences, Moscow, Russia. Its construction relied on the fusion of the N-terminal of SST and the C-terminal of mRFP, with a flexible intermediate linker (-Gly Gly Gly Gly-, in three letter amino acid code), forming the chimeric protein complex SST-mRFP. An additional Histidine tag in the complex facilitated the extraction and purification process. *Escherichia coli* (BL21 strain) transfected with the in-house engineered plasmid expressed the SST-mRFP protein complex. The amino acid sequence of this engineered

complex is presented in Table 5.1.

Table 5.1: Amino acid sequence of the SST-mRFP complex, represented in the three letter code. The horizontal line represents a disulphide bond between the two cysteine residues.

Met	Arg	Gly	Ser	His 5	His	His	His	His	His 10	Gly	Ser	Gly	Ser	Met 15
Asp	Pro	Met	Ala	Ser 20	Ser	Glu	Asp	Val	Ile 25	Lys	Glu	Phe	Met	Arg 30
Phe	Lys	Val	Arg	Met 35	Glu	Gly	Ser	Val	Asn 40	Gly	His	Glu	Phe	Glu 45
Ile	Glu	Gly	Glu	Gly 50	Glu	Gly	Arg	Pro	Tyr 55	Glu	Gly	Thr	Gln	Thr 60
Ala	Lys	Lue	Lys	Val 65	Thr	Lys	Gly	Gly	Pro 70	Lue	Pro	Phe	Ala	Trp 75
Asp	Ile	Lue	Ser	Pro 80	Gln	Phe	Gln	Tyr	Gly 85	Ser	Lys	Ala	Tyr	Val 90
Lys	His	Pro	Ala	Asp 95	Ile	Pro	Asp	Tyr	Lue 100	Lys	Lue	Ser	Phe	Pro 105
Glu	Gly	Phe	Lys	Trp 110	Glu	Arg	Val	Met	Asn 115	Phe	Glu	Asp	Gly	Gly 120
Val	Val	Thr	Val	Thr 125	Gln	Asp	Ser	Ser	Lue 130	Gln	Asp	Gly	Glu	Phe 135
Ile	Tyr	Lys	Val	Lys 140	Lue	Arg	Gly	Thr	Asn 145	Phe	Pro	Ser	Asp	Gly 150
Pro	Val	Met	Gln	Lys 155	Lys	Thr	Met	Gly	Trp 160	Glu	Ala	Ser	Thr	Glu 165
Arg	Met	Tyr	Pro	Glu 170	Asp	Gly	Ala	Lue	Lys 175	Gly	Glu	Ile	Lys	Met 180
Arg	Lue	Lys	Lue	Lys 185	Asp	Gly	Gly	His	Tyr 190	Asp	Ala	Glu	Val	Lys 195
Thr	Thr	Tyr	Met	Ala 200	Lys	Lys	Pro	Val	Gln 205	Lue	Pro	Gly	Ala	Tyr 210
Lys	Thr	Asp	Ile	Lys 215	Lue	Asp	Ile	Thr	Ser 220	His	Asn	Glu	Asp	Tyr 225
Thr	Ile	Val	Glu	Gln 230	Tyr	Glu	Arg	Ala	Glu 235	Gly	Arg	His	Ser	Thr 240
Gly	Ala	Pro	Ser	Thr 245	Pro	Pro	Gly	Gly	Gly 250	Gly	Ser	Ala	Gly	Cys 255
Lys	Asn	Phe	Phe	Trp 260	Lys	Thr	Phe	Thr	Ser 265	Cys				

The protein was extracted by cell lysis and purified using SDS-PAGE electrophoresis. The concentration of the purified protein solution was estimated by optical absorption measurements at a wavelength of 280 nm and was stored at 4 ^{o}C.

The molecular mass of SST-mRFP was determined from the amino acid sequence

to be 29.73 kDa. This recombinant protein was subject to extensive characterization to evaluate its biochemical, optical and pharmacological properties, as detailed in Sections 5.4, 5.5 and 5.6 respectively, followed by specific biomolecular event-labeling applications.

5.4 Biochemical Characterization of SST-mRFP

Protein modifications, including the fusion of SST with mRFP reported here, demand extensive follow-up biochemical characterizations. These include the verification of the amino acid sequence and structural integrity. In the case of SST-mRFP, the recombinant technology used for production ensured correct amino acid sequence, and was therefore not fully verified. However, two characteristics that required further biochemical confirmation were:

1. Existence of the disulfide bond in the SST moiety of the recombinant SST-mRFP complex.

2. The stability of SST-mRFP complex in a solution. For example, the existence of oligomers in a solution.

These two biochemical properties were characterized using mass spectroscopy and gel filtration based analyses, respectively.

5.4.1 Disulfide Bond Characterization

Native SST molecule contains a disulfide bond between the two cysteine residues (C_3 and C_{14}) (see Figure 5.1). Disulfide bonds (-S-S-) are formed by the oxidization of two -SH (also referred to as sulfhydryl or mercapto) groups that belong to neighboring cysteine residues. The disulfide bond in an SST molecule is critical for maintaining the 'hairpin bend' in its structure, which is necessary for its receptor binding/activation. Its absence has been reported to hamper biological activity[150].

In short peptides, the existence of a disulphide bond can be verified by mass measurements, which would detect the mass contributed by the 2 H atoms. However, in

large proteins like SST-mRFP (MW 29.73 kDa), such a verification is difficult, because the contribution of the 2 H atoms towards the total mass is infinitesimal. It is possible to overcome this difficulty by cleaving SST-mRFP to obtain smaller sub-sequences. One of these sub-sequences that contained the disulfide bond was analyzed by mass spectroscopy. This analysis was performed by the Australian Protein Analysis Facility (APAF), Macquarie University. The details and key ideas behind this analysis are discussed below.

Trypsin is a digestive enzyme that cleaves proteins. The cleavage, however, occurs only at specific locations in a protein's amino acid chain, specifically, C-terminal sides of the amino acids Lysine and Arginine, except if the ensuing residue is a Proline. Therefore, sub-sequences that would be produced by the trypsin-based cleavage of a protein can be determined *a priori*. The trypsin-cleavage locations in an SST-mRFP molecule, significant for our disulfide bond analysis, were determined to be (demarcated by |) ... Glu$_{235}$ Gly Arg | His Ser Thr$_{240}$ Gly Ala Pro Ser Thr$_{245}$ Pro Pro Gly Gly Gly$_{250}$ Gly Ser Ala Gly Cys$_{255}$ Lys |Asn Phe Phe Trp$_{260}$ Lys | Thr Phe Thr Ser$_{265}$ Cys. As the disulfide bond under investigation was between the underlined cysteine residues in 2nd and 4th sub-sequences, the mass spectroscopy analysis of the disulfide bond became relatively straightforward. A single mass peak at 2180.95 Da (corresponding to the peptide fragment His Ser The Gly Ala Pro Ser Thr Pro Pro Gly Gly Gly Gly Ser Ala Gly Thr Phe Thr Ser Cys=Cys Lys[†]) would report on the presence of this disulfide bond, whereas two mass peaks at 1625.73 Da and 558.22 Da (corresponding to the sub-sequences His Ser Thr Gly Ala Pro Ser The Pro Pro Gly Gly Gly Gly Ser Ala Gly Cys Lys and Thr Phe Thr Ser Cys, respectively) would report otherwise. Figure 5.2 shows the mass spectrum of trypsin-digested SST-mRFP indicating the presence of a disulfide bond, manifested as a mass-peak at 2180.93 Da.

In order to confirm the identity of the peak at 2180.93 Da the disulfide bond was cleaved, which yielded mass peaks corresponding to the two smaller sub-sequences His Ser Thr Gly Ala Pro Ser The Pro Pro Gly Gly Gly Gly Ser Ala Gly Cys Lys and Thr Phe Thr Ser Cys. This

---

[†]The representation Bbb...Bbb Bbb Xxx ...Xxx Xxx Cys=Cys Zzz Zzz...Zzz denotes the two sub-sequences Xxx...Xxx Xxx Cys and Bbb...Bbb Bbb Cys Zzz Zzz...Zzz linked by a disulfide between the two underlined Cysteine residues

Figure 5.2: Mass spectrum of trypsin-digested SST-mRFP. The peak at 2180.93 Da confirmed the correct disulfide bond in SST-mRFP.
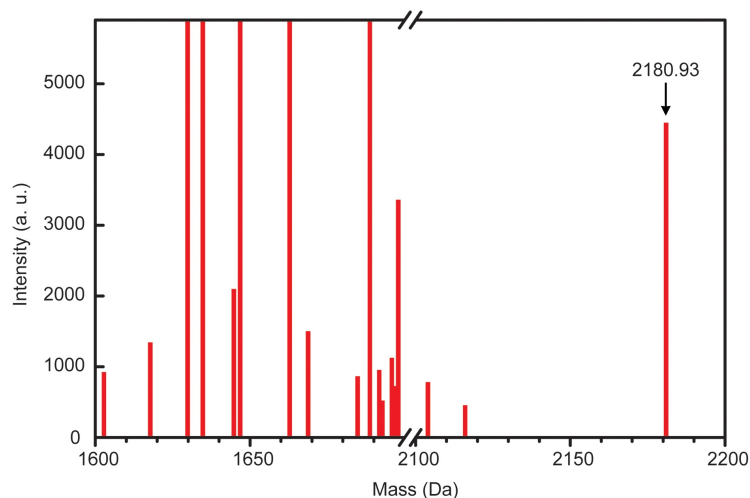
Figure 5.3: Mass spectrum of trypsin-digested, DTT-reduced and IAA-alkylated SST-mRFP. The peak at 1682.73 confirmed the identity of the subsequence observed in Figure 5.2.
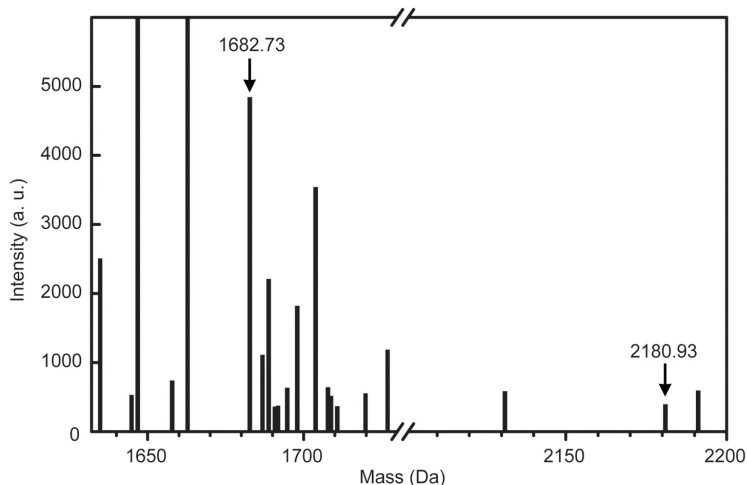
procedure was carried out by the treatment of trypsinated SST-mRFP with dithiothreitol (DTT) and Iodoacetamide (IAA). DTT is a reducing agent that breaks disulfide bonds (-S-S-) to form two separate -SH groups. Subsequent alkylation using IAA permanently modified the separated -SH groups, forming -SH-CH_2-CO-NH_2, thus preventing spontaneous re-formation of the disulfide bond. It is important to note that IAA-based modification of the -SH groups also increased the molecular mass of newly formed sub-sequences by 57 Da each. Thus, if the 2180.93-Da peak observed in Figure 5.2 actually represented the sub-sequence His Ser Thr Gly Ala Pro Ser The Pro Pro Gly Gly Gly Gly Ser Ala Gly Thr Phe Thr Ser Cys=Cys Lys, then, subsequent DTT and IAA treatments would generate two new peaks at 1682.75 Da and 615.24 Da, corresponding to the alkylated sub-sequences His Ser Thr Gly Ala Pro Ser The Pro Pro Gly Gly Gly Gly Ser Ala Gly Cys Lys and Thr Phe Thr

Ser Cys, respectively. A peak was detected at 1682.73 Da, as shown in Figure 5.3, however, the peak at 615.24 Da was undetected, most likely due to the lower sensitivity of the instrument for short peptides. A diminished peak at 2180.93 Da was also observed (see Figure 5.3), corresponding to the unreacted, original sub-sequence. Therefore, the SST-moiety in the SST-mRFP complex did contain the disulfide bond that stabilizes the hairpin bend in the molecule, which dictates biological activity.

### 5.4.2   Characterization of Oligomerization

Red fluorescent proteins (RFP) have tendency for oligomerization[44]. Several mutated forms of RFP have been developed, whose resistance to oligomerization has been progressively improving. One notable form is the monomeric-red fluorescent protein (mRFP)[44], which showed exceptional monomeric stability. Therefore, this became our choice of fluorophore for SST-labeling. Despite the recent advances, it was important to assess the aggregation propensity of the newly developed chimeric protein, SST-mRFP. Aggregation of SST-mRFP was undesirable as this could result in a loss of biological activity of the SST-moiety. Therefore, a size-based separation procedure was carried out to report on the oligomerization state of SST-mRFP in a buffer solution[†].

Superdex 200 10/300 GL Column (GE Healthcare) is a size-based protein separation device. It can be used to separate proteins based on the size-dependent mobility of molecules through a gel-column. As an increase in the degree of oligomerization (dimer, trimer, tetramer, etc.) would result in incremental size changes, this approach was considered appropriate for the identification of SST-mRFP oligomers. Figure 5.4(a) shows the protein content versus eluted fractions obtained by passing SST-mRFP solution through the size separation gel. Two peaks, labeled SST-mRFP (monomeric) and SST-mRFP (dimeric), were identified using molecular mass benchmarks acquired using the Tricorn Superdex 200 protein standards. It is noteworthy that higher degrees of oligomerization were not observed. Characterization of another batch of SST-mRFP is shown in Figure 5.4(b), in which the dimer:monomer ratio was greater than that of

---

[†]This size-based characterization of oligomerization was carried out by the team lead by Prof. Sergey M. Deyev

batch # 1. This difference in extent of oligomerization may be due to the differences in the buffers used during the protein extraction from *E. coli*, its purification and storage. Therefore, a straight forward improvement of the monomeric stability of SST-mRFP was presumed possible by optimizing the storage conditions.
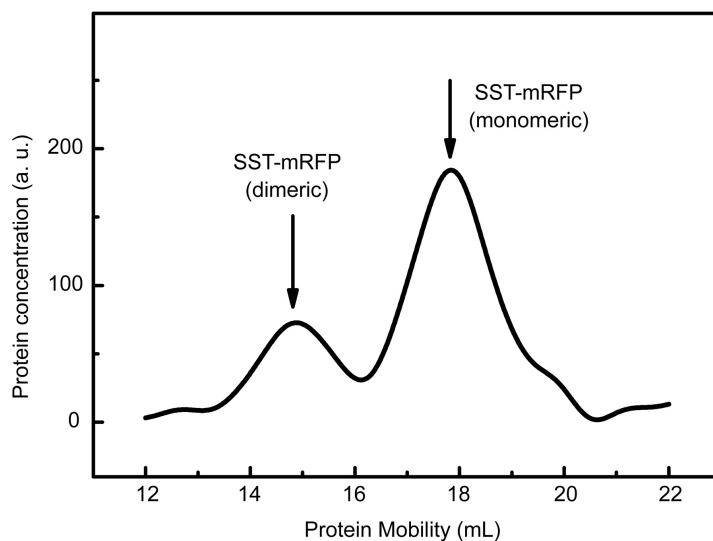
(a) SST-mRFP batch#1. Number of repeats = 1.
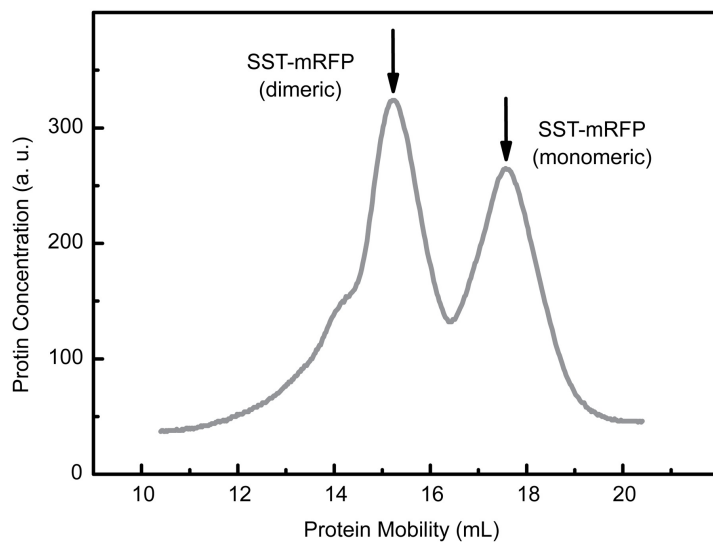
(b) SST-mRFP batch#2. Number of repeats = 1.

Figure 5.4: The protein concentration as a function of the eluted volume, obtained from the size-exclusion chromatography of two batches of SST-mRFP. The peaks were identified to be monomeric and dimeric SST-mRFP molecules, using size calibration standards. The proportions of monomeric and dimeric forms comprising the SST-mRFP solutions varied from batch to batch.
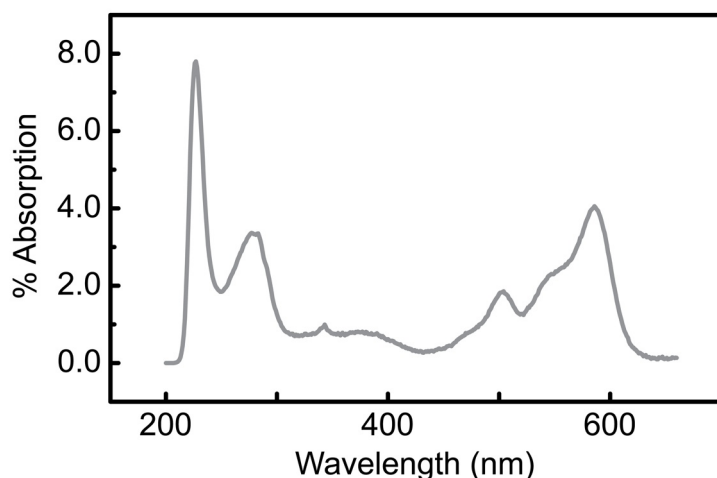
Figure 5.5: Optical absorption spectrum of SST-mRFP solution, prepared in PBS (pH 7.2). Baseline correction was performed. Number of repeats = 1.

5.5 Optical Characterization of SST-mRFP

This section addresses the effect of modification on optical properties of mRFP. Optical properties of a fluorophore, specifically, fluorescence spectra are highly dependent on its environment and 3-D molecular structure[4]. Therefore, the SST-mRFP complex was optically characterized.

5.5.1 Absorption Spectral Characterization

Absorption spectrum of 1-μM SST-mRFP solution, prepared in PBS (phosphate buffered saline, pH 7.2), was acquired using Cary UV-Vis spectrometer (see Section 4.1.1 for details). A baseline-corrected spectrum is presented in Figure 5.5, which resembled that of the mRFP reported by Campbell et al.[44]. Using the Beer-Lambert's law (Equation 4.1), the molar absorption coefficient (equivalent to the molar extinction coefficient in case of negligible scattering) was calculated to be 92,000 $M^{-1}cm^{-1}$.

5.5.2 Fluorescence Spectral Characterization

Fluorescence spectra of SST-mRFP and mRFP are presented in Figure 5.6. Both the excitation and emission spectra of SST-mRFP were identical to that of mRFP. This, in conjunction with the absorption spectral measurements, indicated that the structure of the mRFP moiety in the SST-mRFP recombinant complex was unperturbed.

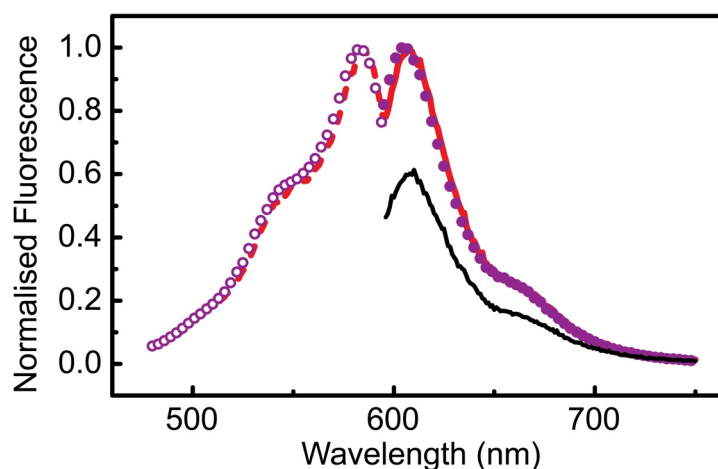Figure 5.6: Fluorescence spectra of mRFP and SST-mRFP. Excitation spectra of mRFP (open circles) and SST-mRFP (dashed line). Emission spectra of mRFP (closed circles), SST-mRFP (thick solid line) and SST-mRFP treated with paraformaldehyde for 20 min (thin solid line). The presented spectra of untreated mRFP and SST-mRFP is a representative of at least three repeats. The paraformaldehyde treatment was carried out once.

Biological application of SST-mRFP as an optical probe demanded photostability in diverse chemical/biochemical environments i. e., the fluorescence yield for a given excitation light intensity should be invariant. One important example of environmental variations is the addition of paraformaldehyde, a biochemical reagent used for long-term storage of a biological specimen. It cross-links proteins and introduces stability to the morphological structure of biological specimen. The cross linking process was predicted to be detrimental to the fluorescence of SST-mRFP, which appealed for further characterization of its stability. SST-mRFP was treated with 3.7 % paraformaldehyde and a time lapse series of fluorescence spectra were acquired, and the peak intensity values are plotted in Figure 5.7. It was observed that after an initial drop of $\approx 40\%$, the fluorescence intensity reached a stable value. As cross-linking takes several hours to days[134], this drop is likely to be due to other effects including formation of polar bonds, and was considered beyond the scope of this investigation. The fluorescence emission spectra at the final time-point (20 min) is shown in Figure 5.6. Despite the drop in intensity, the measured spectral profile was identical to that of the untreated sample.
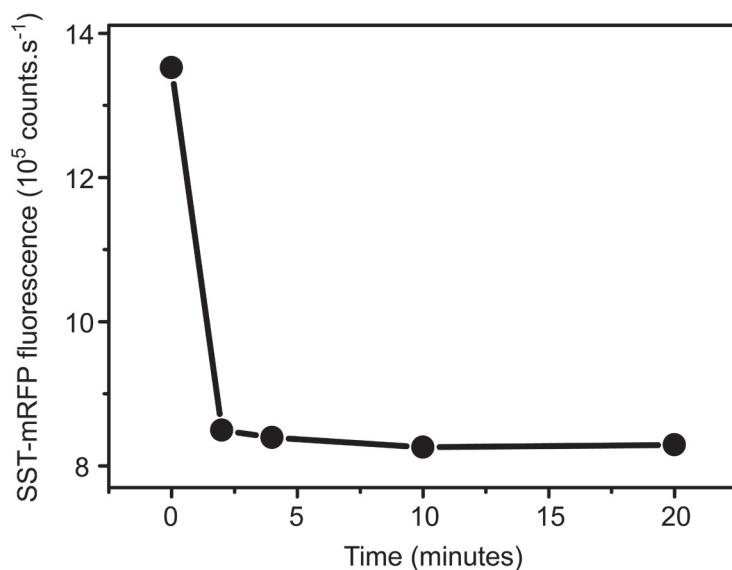
Figure 5.7: Time course of change in SST-mRFP fluorescence after the addition of 3.7% paraformaldehyde. Number of repeats = 1.

5.5.2.1 Method

The spectral measurements were carried out using a fluorimeter, as described in Section 4.1.2. Briefly, mRFP or SST-mRFP solutions were prepared in PBS and loaded into a quartz cuvette (NSG Precision Cells, Inc., USA). The cuvette was placed inside the fluorimeter and the excitation and emission spectra were acquired. As emission and excitation spectra of fluorescent molecules in general are dependent on the wavelengths of excitation and emission, respectively, the procedure described below was used to obtain the peak intensity spectra.

1. A fluorescence emission spectrum was obtained with the excitation wavelength fixed at 580 nm, chosen based on the spectral details of mRFP available in literature[44]. The obtained spectrum revealed a peak emission-wavelength at 605 nm.

2. With the emission wavelength fixed at 605 nm, a fluorescence excitation spectrum was acquired. The peak excitation-wavelength was identified to be 584 nm. Note, this is different from the excitation wavelength initially used.

3. A final emission spectrum was acquired under excitation at a wavelength of 584 nm.

4. Baseline fluorescence excitation (with emission fixed at 605 nm) and emission

(excitation fixed at 584 nm) spectra were obtained from PBS or water.

For the paraformaldehyde treatment, 100 mL of 37% paraformaldehyde was added to 900-mL SST-mRFP solution, prepared in PBS. Fluorescence emission spectrum was measured every few seconds after the addition under 584-nm optical excitation. To obtain the fluorescence intensity at the 0 s time point, 100-mL water was used instead of paraformaldehyde, in order to correct for the dilution.

The observations from the optical characterizations confirmed that the mRFP moiety in the SST-mRFP complex was structurally and functionally identical to a pristine mRFP molecule.

5.6 Biological Characterization of SST-mRFP

The biological function of SST-mRFP, in terms of its potency to bind and activate the receptors (sst), was compared to that of SST, based on two measurable processes that constituted the intracellular signaling chain. Immediately following the sst-activation, some cell-types exhibited changes in membrane potential[193], whereas others responded by a transient increase in the level of Ca^{2+} in the cytoplasm[182,254]. These will be discussed in the following subsections. A summary of all the biological characterization and imaging experiments is compiled in Table 5.2.

5.6.1 Membrane Potential

5.6.1.1 Cell Signaling

Mammalian cells actively maintain unequal concentrations of charged-ions on either sides of the cell membrane (i. e. the intracellular and extracellular ion-concentrations). This is achieved as a result of the balance between the ion-gradient and resultant potential difference across the cell membrane - the so-called electrochemical equilibrium. In a multi-ion system, the potential difference, called the membrane potential, is related

Table 5.2: Number of cell-based experiments carried out using SST and SST-mRFP

Experiment type	Section	Ligand	Cell Type (Transfected)	Independent repeats	Replicates
Membrane potential assay	5.6.1	SST	AtT-20 (WT)	4	3
		SST-mRFP	AtT-20 (WT)	4	3
Ca^{2+} mobilization assay	5.6.2	SST	CHO-K1 (sst$_{2A}$)	4	3
		SST-mRFP	CHO-K1 (sst$_{2A}$)	4	3
		SST-mRFP + PTX	CHO-K1 (sst$_{2A}$)	1	1
SST-mRFP-assisted imaging	5.7.1	SST-mRFP/mRFP	AtT-20 (WT)	1	–
		SST-mRFP/mRFP	CHO-K1 (sst$_{2A}$)	> 5	–
Immunocytochemistry	5.7.2	–	CHO-K1 (sst$_{2A}$)	> 5	–
		SST	CHO-K1 (sst$_{2A}$)	> 5	–
		SST-mRFP	CHO-K1 (sst$_{2A}$)	> 3	–
		SST-mRFP + BIM 23627	CHO-K1 (sst$_{2A}$)	2	–

to the intracellular and extracellular ion-concentrations according to the Goldman-Hodgkin-Katz Equation[109], given below.

$$E_m = \frac{RT}{F} \ln \frac{\sum_i^N P_{M_i^+}[M_i^+]_{out} + \sum_j^M P_{A_j^-}[A_j^-]_{in}}{\sum_i^N P_{M_i^+}[M_i^+]_{in} + \sum_j^M P_{A_j^-}[A_j^-]_{out}} \tag{5.1}$$

where, E_m is membrane potential at the electrochemical equilibrium

R is the ideal gas constant

T is the temperature in kelvins

F is the Faraday's constant, in coulombs per mole

$P_{M_i^+}$ is the membrane permeability of the ith cation

$P_{A_j^-}$ is the membrane permeability of the jth anion

$[M_i^+]$ is the concentration of the ith cation and

$[A_j^-]$ is the concentration of the jth anion

suffixes 'in' and 'out' represent the parameter inside and outside of the cell respectively.

It is important to note that the membrane potential not only depends on concentration differences, but also on the transmembrane permeabilities of each type of ion. As K^+, Na^+ and Cl^- dominate the ion-system in most eukaryotic cells, the above Equation can be simplified as:

$$E_{K,Na,Cl} = \frac{RT}{F} \ln \frac{P_{Na^+}[Na^+]_{out} + P_{K^+}[K^+]_{out} + P_{Cl^-}[Cl^-]_{in}}{P_{Na^+}[Na^+]_{in} + P_{K^+}[K^+]_{in} + P_{Cl^-}[Cl^-]_{out}} \tag{5.2}$$

When cells are in the basal state, the concentration of Cl^- and Na^+ are higher outside than the inside of the cell, whereas K^+ are concentrated in the interior. This is maintained by a class of transmembrane proteins called ion pumps, which transport ions across the cell membrane via an ATP-driven, energy-dependent process[9]. Also, since the transmembrane permeability of K^+ is greater than that of Na^+, the membrane potential of a cell in the basal state varies between -20 mV and -200 mV, depending on cell type (the potential of the interior of the cell with respect to the extracellular medium)[9]. However, after stimulation (e. g. binding and activation of sst by SST), a

transient increase in the permeability of a particular type of the ion-channel may occur (some times also referred to as the opening of channels). This causes a flow of ions, resulting in a change in the membrane potential.

Activation of sst causes opening of certain types of K^+ channels[193]. The increase of the net transmembrane permeability of K^+ causes an efflux of these positive ions, driven by the concentration gradient, resulting in a negative-increase (for example, from -40 mV to -70 mV) of the membrane potential - a process referred to as 'hyperpolarization'. After this transient hyperpolarization, the cell gradually returns back to the resting state, with the help of ATP-driven ion pumps. Thus, one can effectively measure the 'biological activity' of SST (or SST-mRFP) by measuring the level of hyperpolarization.

5.6.1.2   Monitoring the Membrane Potential

A conventional method of measuring changes in the membrane potential (in fact, the consequential trans-membrane ion current), upon stimulation by SST is by using a technique called cell-electrophysiology, also known as patch-clamping. In this technique, ion currents generated upon the receptor stimulation are measured in individual cells by means of micro-electrodes clamped onto the cell membrane, with respect to a reference electrode in the fluid surrounding the cell[193]. However, this is a complex method. Membrane potential-sensitive dyes represent one of the recent developments in this field, allowing an advantageous automated cell population assay, as opposed to a single cell analysis. These electrically charged dyes, such as the negatively charged R8034 (bulk FLIPR membrane potential assay kit, Molecular Devices), enter or leave the cell depending on the membrane potential[3]. Outside the cell, the fluorescence of the dye is inhibited by a membrane-impermeable quencher molecule. Therefore, a drop in fluorescence corresponds to efflux of the dye due to cellular hyperpolarization, whereas a rise indicates depolarization.

The biological function of our recombinant protein, SST-mRFP, was characterized and compared to that of SST by using a fluorescence-based assay of the membrane

potential of sst-expressing cells, using a FlexStation (FlexStation 3, Molecular Devices; see Section 4.3.1 for details). SST and SST-mRFP solutions were added to the cells, while the membrane potential responses were recorded as changes in the level of fluorescence.

5.6.1.3   Membrane Potential Assay Results

The wild type AtT-20 cells that expressed sst-receptors (subtypes sst_1, sst_2, sst_4, and sst_5)[188] were used for this assay. Representative time courses of the membrane potential-dependent fluorescence, before, during and after the addition of SST at three (100 pM, 3 nM and 100 nM) concentrations to the AtT-20 cells, are presented in Figure 5.8. The fluorescence intensity was found to be stable in the cells in the basal state. Addition of SST at concentrations greater than >100 pM (at a time = 100 s, demarcated by arrow) resulted in hyperpolarization of the cells that manifested as a sharp decrease in the fluorescence intensity. The drop in the fluorescence intensity (i. e., the degree of hyperpolarization) was dependent on the concentration of the SST added.

The temporal evolution of fluorescence following the addition of various concentrations of SST and SST-mRFP, ranging from 0.1 nM to 1 μM, were recorded. Hyperpolarization response corresponding to each addition was calculated by measuring the maximum drop in fluorescence (demarcated by the dashed '{' in Figure 5.8). A graph of hyperpolarization response versus agonist concentration (also known as a dose-response curve) is presented in Figure 5.9. The potencies of SST and SST-mRFP were calculated in terms of the concentration that was required to stimulate a half maximal hyperpolarization, the value known as EC_{50}. Another quantity, which can be used to represent potency, is the pEC_{50} value, defined as a negative $\log_{10}$ of EC_{50}. These values were obtained by fitting the dose-response curves to a logistic Equation (Equation 4.5). The pEC_{50} values of SST and SST-mRFP were found to be 8.4 ± 0.3 and 6.1 ± 0.2, respectively.
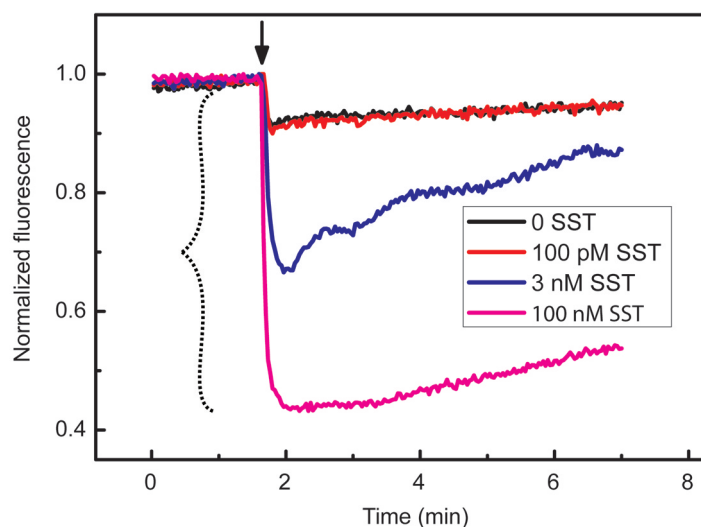
Figure 5.8: Time course of fluorescence intensity in membrane potential assay performed on the AtT-20 cells. Black arrow at 100 s marks the time point of somatostatin (SST) addition. The drop in fluorescence indicated hyperpolarization of the cell membrane, and was dependent on the SST concentration. The dashed '{' is the maximum drop in fluorescence upon stimulation by 100-nM SST. The step-drop in fluorescence upon addition of 0 SST was because of dilution of the dye. The data presented is a representative of at least five independent experiments, each performed in triplicate.
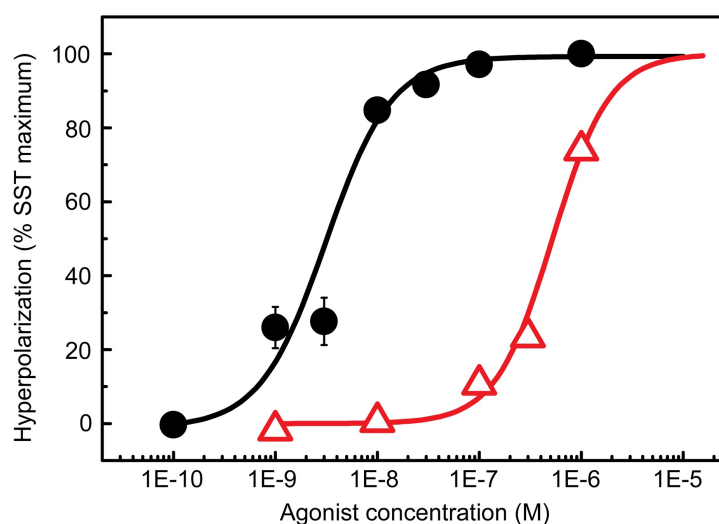

Figure 5.9: Agonist concentration dependent membrane hyperpolarization in AtT-20 cells. The cells were treated with a range of concentrations of SST (black circles) or SST-mRFP (red, open triangles). The data presented is a representative of at least four independent experiments, each performed in triplicate. The error bars are standard error of mean from the triplicates.

Figure 5.10: Fluorescence excitation spectra for 1 μM Fura-2 at 20 ^{o}C in buffers with free Ca^{2+} values ranging from <1 nM to >10 μM. Reproduced with permission from Grynkiewicz et al.[94].
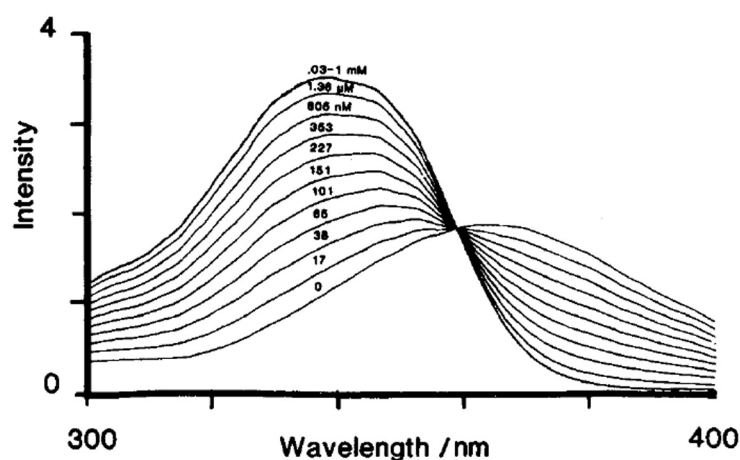
5.6.2 Calcium Mobilization

5.6.2.1 Cell Signaling

Cytoplasm normally contains very low concentration of Ca^{2+}, maintained by ion pumps, which actively sequesters them inside the organelles including the endoplasmic reticulum and mitochondria[9]. However, in the event of a Ca^{2+} dependent signaling pathway, a transient increase in the cytoplasmic concentration occurs[7,252]. This increase may also trigger several downstream signaling proteins[9], which will not be discussed here. Ca^{2+} dependent signaling pathway is engaged upon the stimulation of sst_{2A}-expressing CHO-K1 (chinese hamster ovarian) cells by SST[182]. Thus, the potency of SST-mRFP, to activate heterologously expressed sst_{2A} in CHO-K1 cells, was again evaluated.

5.6.2.2 Monitoring Calcium Concentration

One method to probe the intracellular/cytoplasmic $[Ca^{2+}]$ (the concentration of Ca^{2+}) is by using calcium-sensitive dyes. Fura-2AM is an organic dye whose fluorescence excitation spectrum depends on whether it is bound to a Ca^{2+}. The dependence of its fluorescence under varying $[Ca^{2+}]$, measured by Grynkiewicz et al.[94], is shown in Figure 5.10. Rather than a change in intensity, Fura-2AM exhibits a shift in the peak excitation wavelength from 380 nm to 340 nm as the $[Ca^{2+}]$ is increased from 0 to 0.03 mM or greater, respectively. Thus, the ratio of the fluorescence intensities at 340 nm and

380 nm excitations reports on the absolute $[Ca^{2+}]$. The ratiometric methodology also ensures that the concentration calculations are independent of parameters such as the concentration of the Fura-2AM, absolute intensity of the excitation source and number of cells in the culture. This technique also allows non-destructive determination of $[Ca^{2+}]$ in the cytoplasm of a live cell.

A Fura-2AM based $[Ca^{2+}]$ assay was used to measure the potency of SST-mRFP to activate heterologously expressed sst_{2A} in CHO-K1 cells. The experimental details and the method of analysis were described in Section 4.3.2. In short, SST and SST-mRFP solutions were added to the cells pre-treated with Fura-2AM, while the fluorescence emission at 510 nm was being recorded, under temporally interleaved excitation wavelengths of 340 nm and 380 nm. The time course data were processed and analyzed using the Equation 4.7 in order to obtain absolute values of intracellular $[Ca^{2+}]$.

5.6.2.3   Calcium Assay Results

Figures 5.11(a) and 5.11(b) are time courses of Fura-2AM-fluorescence emissions, detected at a wavelength of 510 nm under optical excitation at wavelengths 340 nm and 380 nm, respectively. Upon the addition of SST, a transient increase of fluorescence under 340 nm excitation, accompanied by a decrease in the fluorescence under 380 nm excitation, was observed. According to Figure 5.10, this observation suggested an increase in the cytoplasmic $[Ca^{2+}]$ upon SST-addition.

The time courses of $[Ca^{2+}]$, calculated using the method described in Section 4.3.2, are presented in Figure 5.11(c). Upon SST treatment, the cytoplasmic $[Ca^{2+}]$ in CHO-K1 cells increased for a short period of time (< 1 min). The increase of $[Ca^{2+}]$ was most likely due to its release from the intracellular repositories[182] or an influx from the extracellular medium via the activated Ca^{2+} channels[252]. After a few minutes, the cells returned to their basal state, by restoring the $[Ca^{2+}]$, presumably by active Ca^{2+} pumps.

The maximum increase in the $[Ca^{2+}]$ was observed to be dependent on the concentration of the SST (see Figure 5.11(c)). Similar experiments were performed with the recombinant analog, SST-mRFP. Plots of the maximum increase in the cytoplasmic
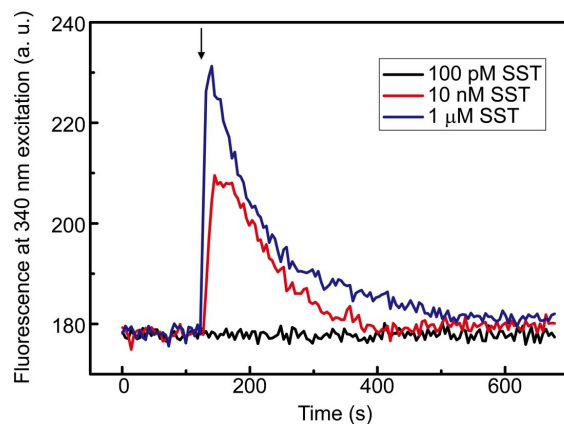
(a) Detected at a wavelength of 510 nm under excitation at 340 nm
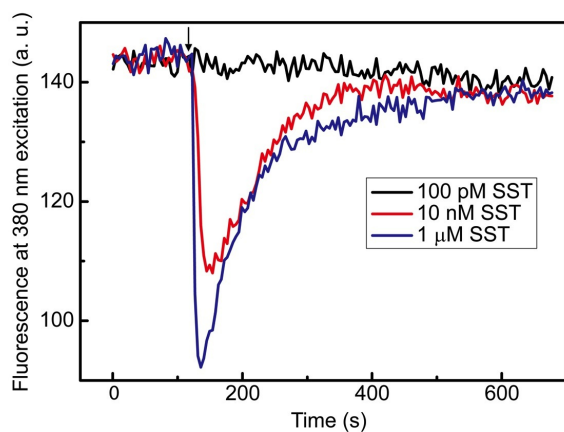
(b) Detected at a wavelength of 510 nm under excitation at 380 nm
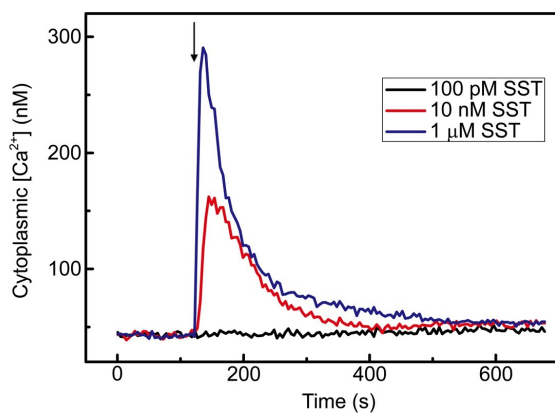
(c) $[Ca^{2+}]$ calculated using the Equation 4.7, using data from Figures (a) and (b)

Figure 5.11: (a, b) Time courses of fluorescence from Fura-2AM, in heterologously sst-expressing CHO-K1 cells. (c) The course of cytoplasmic Ca^{2+} concentration was calculated from the plots (a) and (b), and it transiently increased in response to SST addition (at 120 s, demarcated by an arrow). The data presented here is a representative of at least three independent experiments, each performed in triplicate.

Figure 5.12: Increase in intracellular $[Ca^{2+}]$ vs. concentration of SST (black circles) or SST-mRFP (open, red triangles) added to sst_{2A} expressing CHO-K1 cells. Addition of SST-mRFP to cells pre-treated with pertu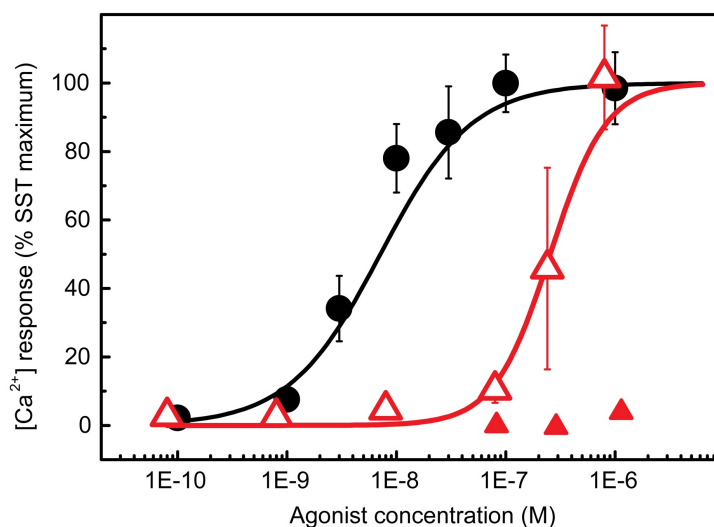ssis toxin shows little increase in $[Ca^{2+}]$ (closed, red triangles). Data presented is a representative of three independent experiments, each performed in triplicate, except in the case of pertussis toxin treated cells, which was carried out once. The error bars are standard error of mean from the triplicates.

$[Ca^{2+}]$ versus the concentration of SST or SST-mRFP are presented in Figure 5.12. The potency of SST and SST-mRFP, calculated in terms of pEC_{50} values, were 7.8 ± 0.5 and 6.3 ± 0.3, respectively. These values were obtained by fitting the dose-response data to a logistic equation (Equation 4.5).

G-proteins (specifically, the sub-units $G_{\alpha\ i/o}$) are vital contributors to the intracellular signaling chain that is initialized by the activation of sst upon agonist binding[95]. Pertussis toxin (PTX) is a chemical released by the bacterium *Bordetella pertussis*, which alters the function of $G_{\alpha\ i/o}$-subunits resulting in the blockage of signaling chain[9,203]. In order to confirm that the observed increase in $[Ca^{2+}]$ upon SST-mRFP addition was mediated through $G_{\alpha\ i/o}$-proteins, the sst_{2A}-expressing CHO-K1 cells were pretreated overnight with 200-ng.mL^{-1} PTX. In these PTX-treated cells, SST-mRFP addition caused little change in $[Ca^{2+}]$, thus confirming the participation of $G_{\alpha\ i/o}$ in the signaling chain (see Figure 5.12).

Both membrane potential and calcium assays yielded lower pEC$_{50}$-values of SST-mRFP in comparison with that of SST (p-values of 0.00004 and 0.004, respectively, determined using a two sample t-test). This is likely due to the following reasons:

1. The dimerization of SST-mRFP, as discussed in Section 5.4.2, reduced the number of monomeric SST-mRFP molecules, resulting in the reduction of the effective agonist concentration. However, this argument assumes that the dimeric SST-mRFP is impotent.

2. mRFP molecule, which is relatively large, caused hindrance to the sst:SST-mRFP binding process.

5.7   Applications of SST-mRFP

In most sst-expressing cells the agonist (SST or analogs) causes activation and internalization of receptors, along with the agonist – one of the concluding events in the complex intracellular signaling cascade. The chimeric protein, SST-mRFP, which we designed and characterized, was used to image this process. In Sections 5.4 to 5.6, SST-mRFP was shown to be a stable and relatively potent analog of SST that exhibited a high optical contrast, thus serving as a fluorophore to probe the sst:SST binding and associated events. As a next step, to image the scenery in which the SST binds to sst, we used immunocytochemical labeling of sst(s). Together, the two high-contrast fluorescent labels reported on the intracellular fate of the internalized sst:SST complexes - a detail that no other approach could deliver.

5.7.1   SST-mRFP-assisted imaging

The mRFP-fluorescence was used to determine the intracellular localization of internalized SST-mRFP in the wild type AtT-20 cells (that endogenously expressed sst) and CHO-K1 cells (that heterologously expressed sst$_{2A}$). Images of these cells, treated with 1 μM or 100 nM SST-mRFP for 20 min, obtained by using a fluorescence confocal microscope, are shown in Figures 5.13 and 5.14. The SST-mRFP molecules were

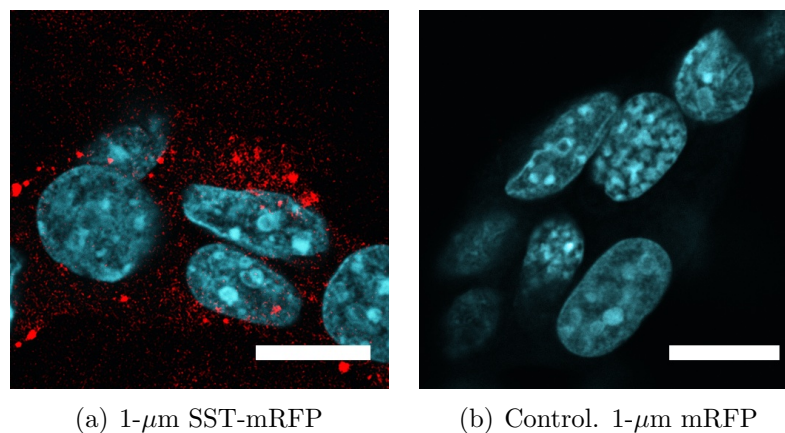(a) 1-μm SST-mRFP (b) Control. 1-μm mRFP

Figure 5.13: Fluorescence confocal images of the wild type AtT-20 cells that endogenously expressed sst, incubated with SST-mRFP or mRFP for 20 min. The cells were co-labeled with Hoechst 33342, fluorescent nuclear stain. mRFP- and Hoechst-fluorescence are color-coded in red and blue, respectively. Images presented are a representative of three independent experiments. Scale-bar 15 μm.

found to be translocated to perinuclear regions of the cells and observable as bright spots. Generally, the internalized ligands are transported via a series of intracellular organelles, including (1) endocytotic vesicles, (2) early endosomes, (3) late endosomes and (4) lysosomes, where they are degraded[124,140]. The time taken for the internalized molecules to reach each of these organelles is highly dependent on the physiochemical conditions exterior to the cell and receptor- and cell-types. In light of the existing literature[69,181,279] and the 20-min time duration, the internalized SST-mRFP molecules were likely to be sequestered in early endosomes. Longer incubation time (30 min) caused reduction in the SST-mRFP-fluorescence (data not shown), and was therefore not repeated.

The specificity of SST-mRFP towards sst was confirmed by the negligible internalization of the mRFP by the cells. The higher uptake of SST-mRFP by the CHO-K1 cells in comparison with that by the AtT-20 cells was likely due to the higher sst-expression density. The receptor densities in these cells were *a priori* known to be 10 pmol.mg^{-1}[†] and 1.2 pmol.mg^{-1} [104], respectively. The ability to probe the internalization of SST-mRFP in the wild type cells, that express sst endogenously demonstrated the value of the newly developed chimeric fluorescent probe.

[†]The sst$_{2A}$ expression density in CHO-K1 cells was determined by the supplier

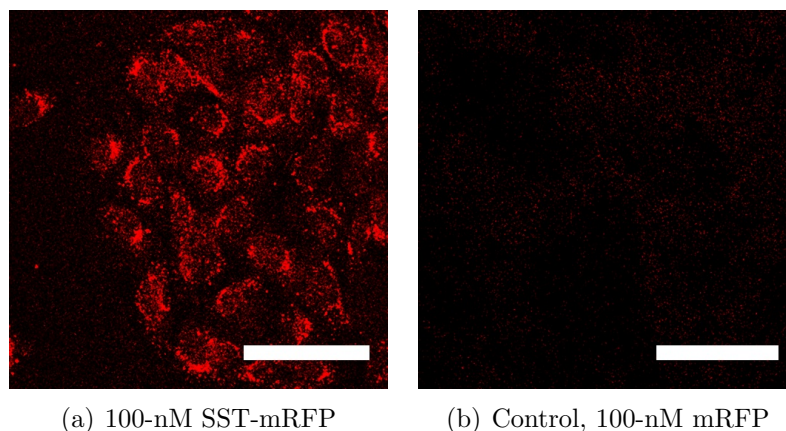(a) 100-nM SST-mRFP   (b) Control, 100-nM mRFP

Figure 5.14: Fluorescence confocal images of heterologously sst$_{2A}$-expressing CHO-K1 cells, incubated with (a) SST-mRFP or (b) mRFP for 20 min. mRFP-derived fluorescence is coded in red. Images presented are a representative of at least three independent experiments. Scale-bar 50 μm.

5.7.2   Immunocytochemical Labeling of sst$_{2A}$

The SST-mRFP-fluorescence localized inside the cell and the negative control experiments with mRFP alone demonstrated the specificity of sst:SST binding. However, it did not provide an absolute confirmation on the internalization pathway - whether or not it was sst-mediated? Answering this question demanded an immunocytochemical labeling (explained shortly) procedure to highlight the sst. A spatial overlap of fluorescence from the immunocytochemically labeled sst and the optically active SST-mRFP would be a strong evidence for sst-mediated internalization. Such double-labeling would also provide information on how long the receptor:ligand (sst:SST-mRFP) complex remains intact after internalization.

Immunocytochemistry (or immunocytochemical labeling, used interchangeably) is an indirect labeling technique that is deployed in situations, where a direct labeling of a biomolecule is not possible, for example, labeling of the sst$_{2A}$ expressed by cells[†]. Immunocytochemical labeling relies on a class of proteins called antibodies that attain

---

[†]More arduous methods of direct labeling proteins expressed by cells include gene modification, resulting in the expression of fluorescently labeled protein analogs

affinity towards a predetermined antigen[†] during their production. Antibodies that are pre-labeled with a fluorophore, target and bind to the antigen. This process renders the antigen visible under a fluorescence microscope. It is also note-worthy that immunocytochemistry is seldom performed on living cells/tissues for reasons to be clarified in the following sections. An antibody directed against the sst_{2A}, expressed by CHO-K1 cells, was used for the immunocytochemical labeling. The wild type AtT-20 cells expressed several sst-subtypes at low densities, which demanded distinct receptor-targeting antibodies of high sensitivities. Therefore, immunocytochemical labeling of AtT-20 cells was not performed.

In addition to being a tool to confirm the sst-mediated internalization of SST-mRFP, the immunocytochemical labeling also provided a means to probe the receptors alone, especially when non-fluorescent SST-analogs were used. Figure 5.15 illustrated this capability, where the intracellular localization of sst_{2A} was imaged before and after activating CHO-K1 cells with a native (non-fluorescent) ligand, SST. In a basal state, the fluorescence from the immunocytochemically labeled sst_{2A} appeared to outline the cell membranes [see Figure 5.15(a)]. This finding was in good agreement with previous reports that the sst_{2A} are normally expressed on the cell membranes[156]. However, shortly (20 min) after activating the cells using 100-nM SST, the sst_{2A} were predominantly found to be internalized and localized mainly inside the cells. They appeared as bright spots in the perinuclear regions [see Figure 5.15(b)], in excellent agreement with previous reports[156]. The time scale of the SST-stimulated receptor internalization observed here was similar to the internalization of the SST-mRFP seen earlier[137], providing further evidence of the sst-mediated internalization of SST-mRFP. The details of the immunocytochemistry procedure for the CHO-K1 cells is discussed in Section 5.7.3.1.

Confirmation on the sst_{2A}-mediated internalization of ligands could only be made by double labeling - i. e., using a fluorescent ligand, SST-mRFP, and immunocytochemical labeling of the receptor, sst_{2A}. To this aim, immunocytochemistry was performed

---

[†]'Antigen', a term used in conjunction with 'antibody', is a concept in immunocytochemical labeling techniques. Antigen refers to a biomolecule or a part of that biomolecule, to which a given antibody has affinity
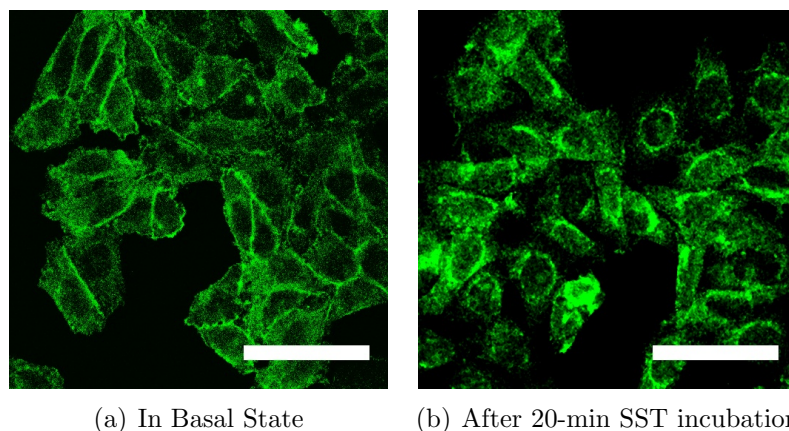
(a) In Basal State   (b) After 20-min SST incubation

Figure 5.15: Immunocytochemically labeled sst_{2A} in serum starved CHO-K1 cells before and after SST-treatment. 1° and 2° dilution factors were 1:125 and 1:500, respectively. Images are a representative of at least three independent experiments. Scale-bar 50 μm.

on the SST-mRFP (100 nM) treated, sst_{2A}-expressing, CHO-K1 cells, and the fluorescence confocal microscopy images are presented in Figure 5.16. An overlay of images corresponding to the mRFP-derived fluorescence of the ligand [Figure 5.16(a)] and immunocytochemical fluorescence of the receptor [Figure 5.16(b)] revealed a high degree of spatial overlap, depicted by the co-localized occurrence of red and green spots, mixing to form yellow [see Figure 5.16(c)]. These observations strongly suggested that (i) the SST-mRFP internalization observed previously was indeed sst-mediated and (ii) post internalization, the sst:SST-mRFP complex remained intact at least during the investigated time-scales.

Further evidence regarding the sst:SST-mRFP binding specificity and sst_{2A}-mediated internalization was obtained using antagonist competition experiment. Antagonists are receptor-binding ligands that, unlike agonists, do not activate the receptors or cause internalization[149]. Antagonists occupy the binding domains of receptors and prevent further agonist binding and activation[47]. For the somatostatin receptor, sst_{2A}, SST and SST-mRFP are agonists and BIM 23627 is an antagonist[255]. Incubation of the CHO-K1 cells with a mixture of 100-nM SST-mRFP and 10-μM BIM 23627 resulted in a competition for the sst-binding - therefore the name, *antagonist competition*. Consequently, the fraction of sst that was occupied and activated by SST-mRFP was determined by the relative concentrations and binding affinities of SST-mRFP and BIM 23627. Due
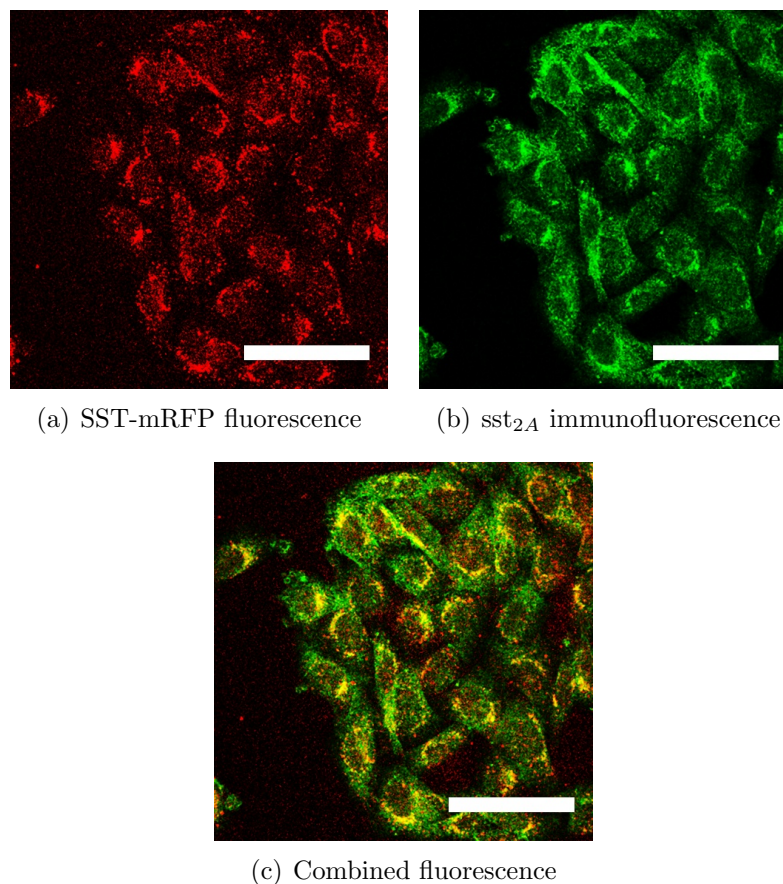
(a) SST-mRFP fluorescence

(b) sst_{2A} immunofluorescence

(c) Combined fluorescence

Figure 5.16: Fluorescence confocal images of sst_{2A}-expressing CHO-K1 cells, treated with 100-nM SST-mRFP and later immunocytochemically labeled to visualize sst_{2A}, under different wavelengths. Images are a representative of at least three independent experiments. Scale-bar 50 μm.

to the 100-fold higher concentration of the antagonist, only a negligible fraction of sst_{2A} was activated, thus resulting in little internalization of SST-mRFP [see Figure 5.17(a)]. Immunocytochemical labeling also revealed unactivated and membrane bound sst_{2A}, similar to what was observed in basal conditions [compare Figures 5.15(a) and 5.17(b)].

These experiments provide confirmations on the agonist activity of SST-moiety of the SST-mRFP fusion protein and at the same time demonstrates its prospects for basic research in elucidating SST-dependent activation of sst(s).
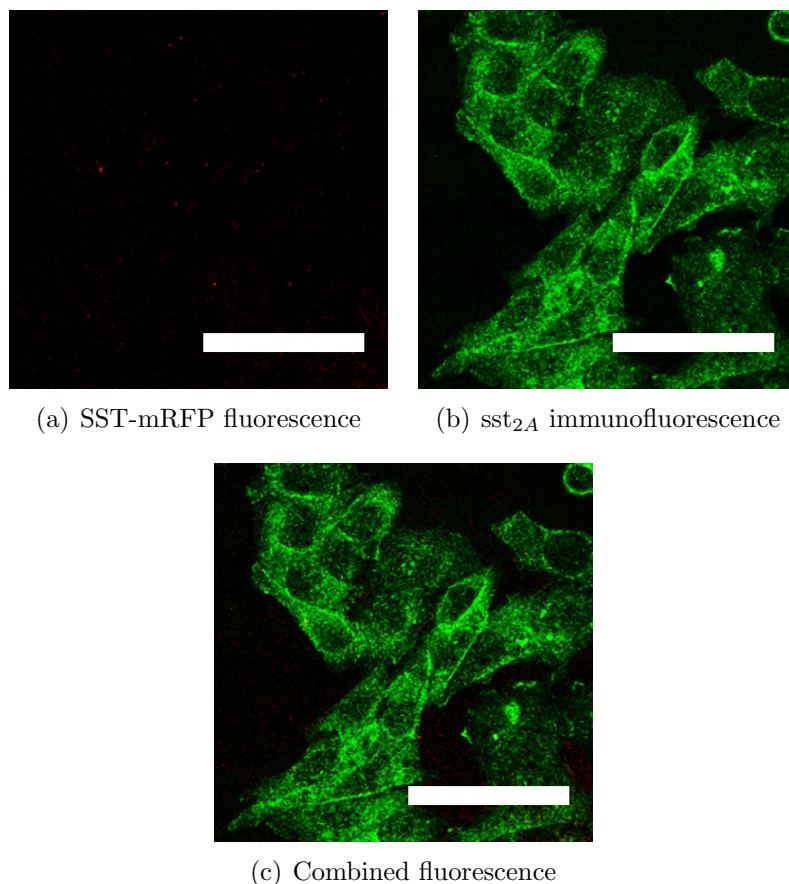
(a) SST-mRFP fluorescence

(b) sst$_{2A}$ immunofluorescence

(c) Combined fluorescence

Figure 5.17: Fluorescence confocal images of sst$_{2A}$-expressing CHO-K1 cells, treated with 100-nM SST-mRFP, in the presence of **10-μm BIM 23627 (antagonist)**, and later immunocytochemically labeled to visualize sst$_{2A}$, under different wavelengths. Images presented are a representative of two independent experiments. Scale-bar 50 μm.

5.7.3   Detailed Cell Imaging Methodology

Endogenously sst-expressing AtT-20 cells and heterologously sst$_{2A}$-expressing CHO-K1 cells (see Section 4.2 for details on normal cell culture procedure) were seeded on culture slides (BD Falcon, Australia). They were incubated with 100 nM - 1 μM of SST, SST-mRFP or mRFP, prepared in PBS+CM (PBS with additional 0.1% BSA, 20-mM D-Glucose, 0.9-mM CaCl$_2$ and 0.5-mM MgCl$_2$), for time periods ranging from 10 - 30 min at 37 ^{o}C. Note that if buffers devoid of CaCl$_2$ and MgCl$_2$ were used, cells were found to detach from the glass substrate. The substrate-bound cells were washed with PBSCM (PBS with additional 0.9 mM CaCl$_2$ and 0.5 mM MgCl$_2$) and fixed† with 3.7%

---

†Fixation is a procedure that permanently arrests all biological processes, while preserving the morphology

paraformaldehyde (Sigma Aldrich, Australia) solution. For immunocytochemical labeling of sst_{2A}, expressed in CHO-K1 cells, additional steps were carried out (detailed in the following Section 5.7.3.1). The slides were sealed with coverslips and imaged using the Leica TCS SP5 fluorescence confocal microscope (see Section 4.4) to localize SST-mRFP, using the mRFP-originated fluorescence, or sst_{2A}, using immunocytochemical fluorescence. A super-continuum laser, filtered to a laser excitation band centered at 584 nm, was used to excite the mRFP, an Argon laser emission at 488 nm was used to excite the antibody-conjugated fluorescein isothiocyanate (FITC), and the emission from a 405 nm laser diode was used to image the nuclear stain – hoechst.

5.7.3.1   Immunocytochemical Labeling of sst_{2A}-Expressing CHO-K1 cells

An immunocytochemical procedure to label sst_{2A} is schematically presented in Figure 5.18. This procedure relies on a class of proteins, called antibodies, that are pre-programmed to target their antigens. In general, antigens are organic molecules that includes short peptides and large proteins. In a large protein, however, the region of where antibody binding occurs is called a *binding epitope* or, simply, an *epitope*.

Conventionally, in immunocytochemistry, the antigen containing sample is incubated with a primary antibody, followed by a secondary antibody. The primary antibody targets and binds to the antigen, whereas the fluorescently-tagged secondary antibody binds to the *a priory* known epitope on the primary antibody. A primary antibody targeting an intracellular epitope (Glu_{355} Thr Gln Arg Thr Leu_{360} Leu Asn Gly Asp Leu_{365} Gln Thr Ser Ile) of the trans-membrane receptor, sst_{2A}, was purchased from Biotrend Chemikalien, Germany. This primary antibody also hosted a 'donkey epitope', by virtue of the fact that this antibody was extracted from donkey's serum. Therefore, a secondary antibody tagged with FITC and targeted against donkey epitopes was used for the final labeling step. Although the key components in immunocytochemistry are the primary and secondary antibodies, it required additional preparative cell-treatments to address the two points noted below:

1. Antibodies require entry into the cell to bind to the intracellular epitopes. But, these large proteins ($\approx$ 150 kDa) are unable to diffuse across the cell membrane.
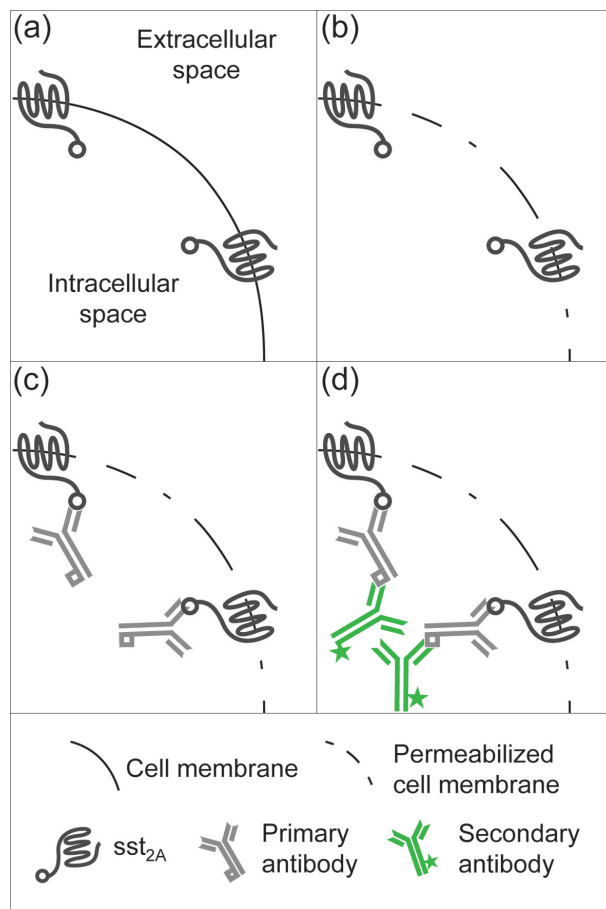
Figure 5.18: A schematic of the immunocytochemical labeling procedure to label sst_{2A}. (a) Cell with intact cell membrane; (b) permeabilized cell membrane with perforations that facilitates antibody entry, (c) binding of primary antibody to the intracellular epitope on the sst_{2A} and (d) binding of a dye-conjugated secondary antibody to an epitope on the primary antibody, in turn rendering fluorescent contrast to sst_{2A}

This demanded a procedure called 'permeabilization', where a detergent can be used to perforate the cell-membrane, creating microscopic gateways for the antibody.

2. Antibodies being large proteins are notoriously efficient in non-specific binding, which would result in poor labeling contrast. To ensure that the primary and secondary antibodies did not bind non-specifically to cells, a procedure called 'blocking' was necessary.

Several optimization experiments were necessary to obtain acceptable immunocyto-chemical labeling contrast, because it was critically dependent on the type and concentration of several biochemical components listed above. The following procedure was determined to most suitable and was strictly followed to obtain the images described in Section 5.7.2.

1. Cell preparation: The sst_{2A}-expressing CHO-K1 cells were serum starved overnight with 1% FBS in the culture media.

2. Biological experiment: The cells were treated with SST, SST-mRFP or mRFP solutions prepared in PBS+CM. For antagonist competition experiments BIM 23627 was added to these solutions. This was followed by two wash steps using PBSCM.

3. Fixation: The cells were treated with 3.7 % paraformaldehyde solution prepared in PBSCM for 20 min at room temperature. Fixation was followed by two wash steps using PBSCM.

4. Permeabilization: The cells were treated with 0.2 % triton X-100 (Sigma Aldrich, Australia) solution prepared in PBS for 15 min at room temperature. Permeabilization was followed by two wash steps using PBS.

5. Blocking procedure: Blocking buffer constituted a solution of 1 % bovine serum albumin (BSA) prepared in PBS. The cells were treated with the blocking buffer for 1 hr at room temperature.

6. Primary antibody: Working solution of sst_{2A}-antibody was prepared by diluting the purchased stock-solution by a factor of 1:125[†] into the blocking buffer. This working solution was prepared 2 hr prior to the 1-hr long cell incubation. Subsequently, the cells were washed four times using the blocking buffer to remove unbound primary antibody molecules.

[†]In general, antibodies are sold commercially in the form of concentrated solutions of unknown molar concentration. However, a range of empirically-determined dilution factors is usually recommended by the vendor in order to obtain highest antibody labeling

7. Secondary antibody: FITC-conjugated anti-donkey antibody was prepared by 1:500 dilution into the blocking buffer. The cells were treated for 1 hr at room temperature.

8. The cells were washed twice with PBS and prepared for imaging, as previously noted.

5.7.3.2   Immunocytochemical Optimization

The immunocytochemical labeling protocol listed above was finalized after a series of experiments, wherein the following parameters were optimized. Some of these parameters required iterative optimizations as they were mutually dependent.

1. Fixation and permeabilization condition

2. Primary and secondary antibody concentration

3. Cell condition

4. Antibody preparation and blocking buffer

5. Confirmation of antibody specificity

Firstly, the influence of the fixation and permeabilization conditions on the immunocytochemical labeling contrast was evaluated, and is illustrated in Figure 5.19. Here, the sst_{2A}-expressing CHO-K1 cells were fixed and permeabilized in different ways prior to the antibody incubations (primary and secondary antibody dilutions factors were 1:250 and 1:250, respectively). Immunocytochemistry using an un-permeabilized batch of cells resulted in a complete lack of labeling [see Figure 5.19(a)]. This observation conformed with our knowledge that (i) the binding epitope of the primary antibody on the sst_{2A} was intracellular and (ii) unperforated cell membranes were impermeable
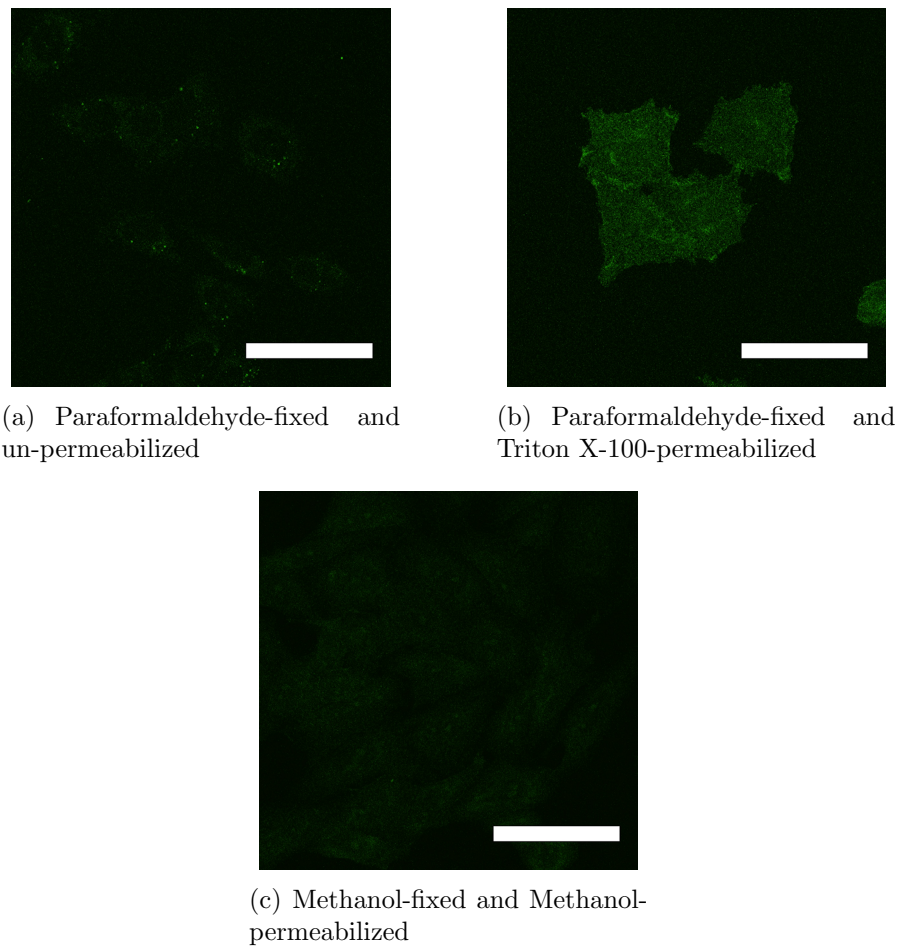
(a) Paraformaldehyde-fixed and un-permeabilized

(b) Paraformaldehyde-fixed and Triton X-100-permeabilized

(c) Methanol-fixed and Methanol-permeabilized

Figure 5.19: Effect of fixation and permeabilization on the immunocytochemical labeling of sst_{2A} in CHO-K1 cells. Scale-bar 50 μm.

to the antibodies. Permeabilization of the paraformaldehyde-fixed CHO-K1 cells using Triton X-100 solution yielded the higher contrast than that using methanol-fixation & -permeabilization. Therefore, 3.7% paraformaldehyde solution and 0.2% Triton X-100 represented the fixation and permeabilization agents of choice for all the subsequent experiments.

Next, the dilution factors of sst_{2A}-targeting primary and FITC-conjugated secondary antibodies were optimized (see Figure 5.20). 1:62 - 1:125 and 1:500 dilutions of primary and secondary antibodies, respectively, provided the highest contrast (1% BSA in PBS was used as the blocking buffer to prepare these solutions). These two parameters were again optimized in the next step.
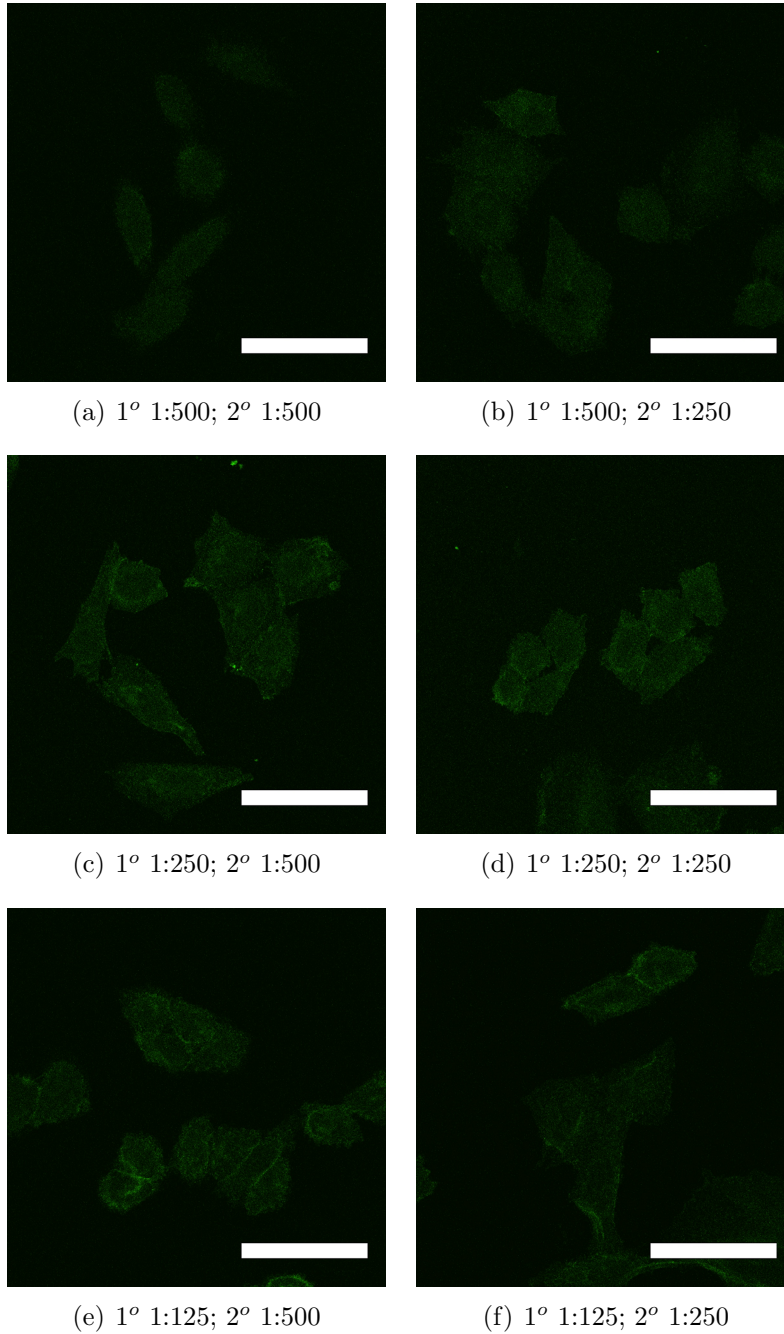
(a) 1° 1:500; 2° 1:500

(b) 1° 1:500; 2° 1:250

(c) 1° 1:250; 2° 1:500

(d) 1° 1:250; 2° 1:250

(e) 1° 1:125; 2° 1:500

(f) 1° 1:125; 2° 1:250

Figure 5.20: continued...

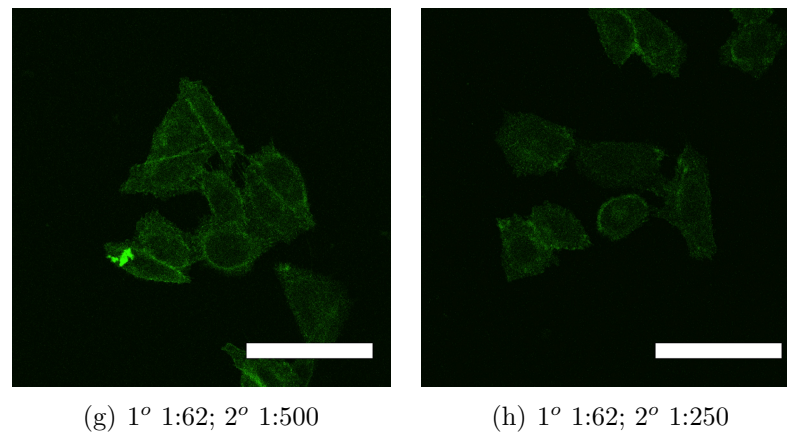(g) 1° 1:62; 2° 1:500   (h) 1° 1:62; 2° 1:250

Figure 5.20: Optimization of primary (1°) and secondary (2°) antibody concentrations to immunocytochemically label sst_{2A} in CHO-K1 cells. Fixed, permeabilized cells were treated with varying dilutions of 1° and 2° antibodies. Scale-bar 50 μm.

In addition to the type and concentration of biochemicals used, condition of the cells used also influenced the labeling contrast. As mentioned in Section 4.2, the cells were normally grown in a culture media that contained 10% animal-serum. The biochemical composition of serum is generally undetermined and can result in unfavorable experimental conditions. Moreover serum may also contain traces of somatostatin (or analogs), which can undesirably activate the cells. In order to better control the experimental conditions, a procedure called *serum starvation* was carried out. To serum starve, the cells were grown in a culture media that contained reduced concentrations of serum (1%) overnight before the experiment. As serum starvation was expected to alter the labeling conditions, the primary and secondary antibodies dilution factors were again optimized under these conditions. The fluorescence confocal images obtained from this set of experiments are presented in Figure 5.21. Serum starvation resulted in higher labeling contrast in general, and was found to be optimal at primary and secondary antibody dilutions of 1:125 and 1:500, respectively. These parameters were used for the subsequent experiments.

Further optimization was carried using antibody solutions prepared by two methods that differed in the time point of addition of the blocking agent, BSA. To treat the first batch of cells, 1% BSA was added to the primary antibody solution prepared at 1:125 dilution in PBS, 2 hrs prior to cell incubation. For the second batch, 1% BSA was
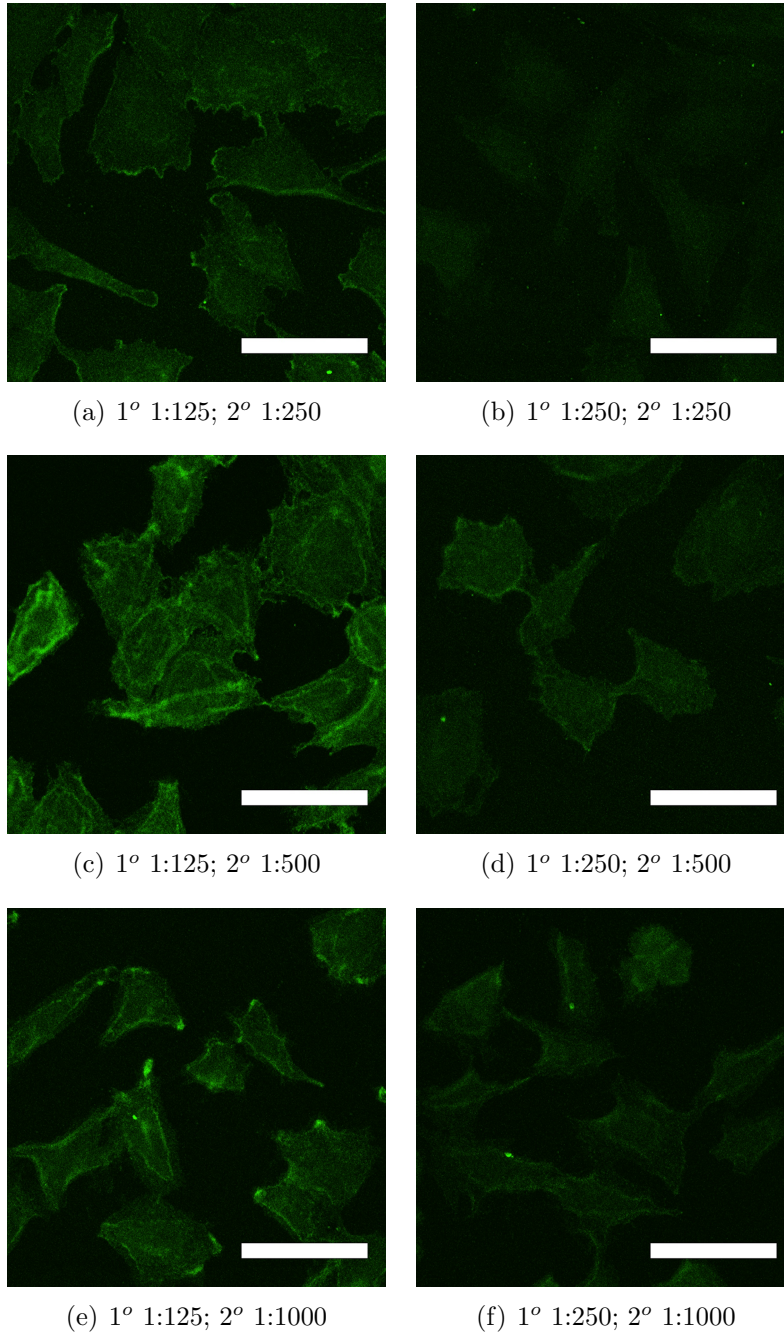
(a) 1º 1:125; 2º 1:250

(b) 1º 1:250; 2º 1:250

(c) 1º 1:125; 2º 1:500

(d) 1º 1:250; 2º 1:500

(e) 1º 1:125; 2º 1:1000

(f) 1º 1:250; 2º 1:1000

Figure 5.21: continued...

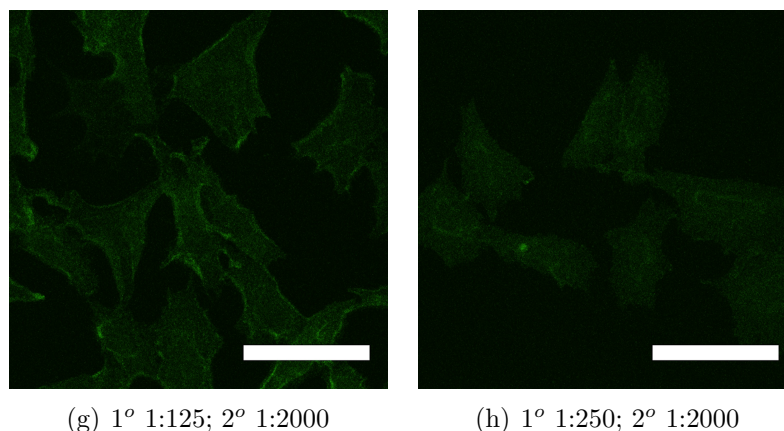(g) 1° 1:125; 2° 1:2000   (h) 1° 1:250; 2° 1:2000

Figure 5.21: Optimization of primary (1°) and secondary (2°) antibody concentrations to immunocytochemically label sst_{2A} in serum starved CHO-K1 cells. Fixed, permeabilized cells were treated with varying dilutions of 1° and 2° antibodies. Scale-bar 50 μm.

added into the primary antibody solution (1:125 in PBS) immediately before the cell incubation. The labeling contrast was found to be higher in the first batch of cells (see Figure 5.22). A similar experiment was carried out using 5% HS (horse serum) instead of 1% BSA as the blocking agent. A comparison of Figure 5.23 with Figure 5.22, revealed the superiority of BSA. These conditions were finalized for all the subsequent immunocytochemical labeling performed on the CHO-K1 cells.

It was also necessary to confirm the specificity of the antibody binding. The specificity of the secondary antibody was confirmed by carrying out negative control experiments without using primary antibodies. No labeling was present (data not shown).

To determine the level of non-specific binding of primary antibody, the method of antigen pre-binding was used. The principle behind this was that primary antibodies that are pre-bound to its antigen, i. e., sst_{2A}, would be unable to bind to sst_{2A} expressed in the cell. Antigens are normally purchased from the same vendor as antibodies. In our case, instead of the whole sst_{2A} protein, a short peptide sequence that resembled the antibody-binding epitope of the sst_{2A} was purchased from Biotrend Chemikalien, Germany. The primary antibody solution was mixed with 10-μg.mL^{-1} of the antigen, 2 hrs before the cell incubation. The images presented in Figure 5.24 reported the specificity of the primary antibody, where antigen pre-binding resulted in a complete loss of immunocytochemical labeling.
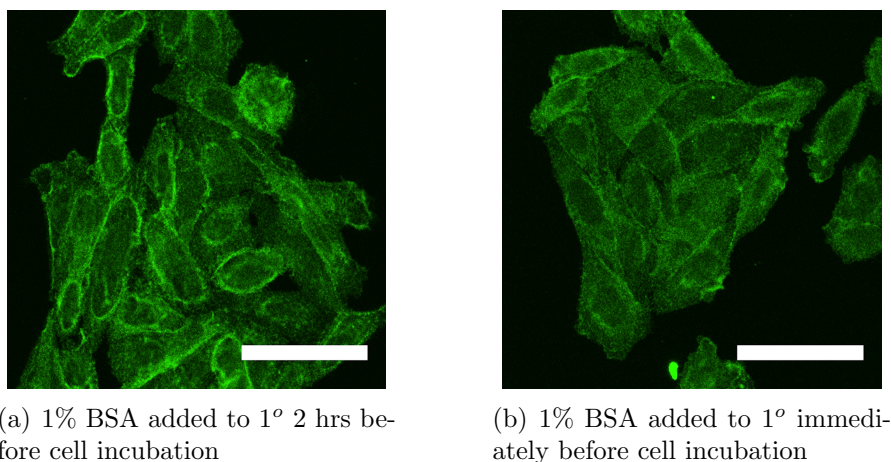
(a) 1% BSA added to 1° 2 hrs before cell incubation

(b) 1% BSA added to 1° immediately before cell incubation

Figure 5.22: Effect of method of preparation of primary antibody (1°) on the immunocytochemical labeling of sst$_{2A}$ in serum starved CHO-K1 cells. The blocking agent, 1% BSA, was added to the primary antibody solution (a) 2 hrs or (b) immediately before cell-incubation. 1° and 2° dilution factors were 1:125 and 1:500, respectively. Scale-bar 50 μm.

(a) 5% HS added to 1° 2 hrs before cell incubation
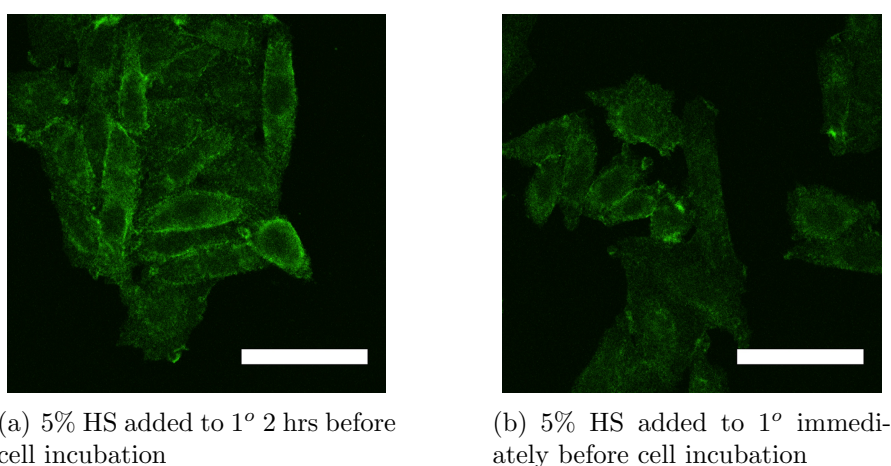

(b) 5% HS added to 1° immediately before cell incubation

Figure 5.23: Effect of method of preparation of primary antibody (1°) on the immunocytochemical labeling of sst$_{2A}$ in serum starved CHO-K1 cells. The blocking agent, 5% HS, was added to the primary antibody solution (a) 2 hrs or (b) immediately before cell-incubation. 1° and 2° dilution factors were 1:125 and 1:500, respectively. Scale-bar 50 μm.

5.8   Summary and Discussions

Somatostatin (SST) is a ubiquitous and physiologically significant peptide hormone and neurotransmitter[40,187]. Its biological functions have been investigated for several decades using labeled analogs, including some that used fluorescent labels[25,181]. These fluorescent analogs were prepared based on chemical reactions to link SST with a fluorophore. We report, for the first time, on the development of a novel, genetically
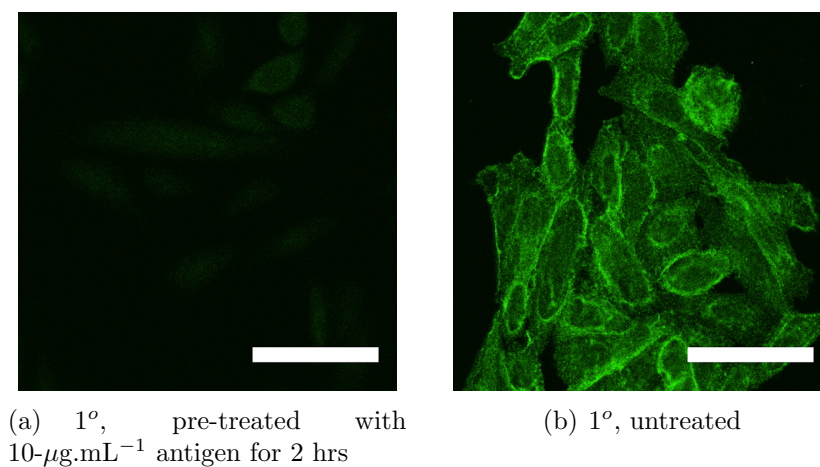
(a) 1°, pre-treated with 10-μg.mL^{-1} antigen for 2 hrs

(b) 1°, untreated

Figure 5.24: Evaluation of specificity of the immunocytochemical labeling of sst$_{2A}$ in serum starved CHO-K1 cells, using the method of antigen-prebinding. Cells were incubated with primary antibody (1°) solutions (a) with or (b) without excess antigen. 1° and 2° dilution factors were 1:125 and 1:500, respectively. Scale-bar 50 μm.

engineered fluorescent analog of SST – aimed to eliminate the inherent variability associated with chemical reactions and to yield a reproducible and easy to synthesize analog[138]. Monomeric red fluorescent protein (mRFP) represented as the fluorophore in the genetically engineered complex SST-mRFP, in virtue of its superior biochemical and optical properties[44]. The produced SST-mRFP protein complex was characterized extensively in terms of its biochemical, optical and biological properties and functionality. This recombinant protein was used to investigate ligand-activated receptor (sst) internalization in two sst-expressing cell types.

Biochemical properties: The correct primary molecular structure, i. e., the amino acid sequence of the complex was ensured by the recombinant nature of SST-mRFP production. Other biochemical characteristics, however, were verified using specialized analytical techniques. Firstly, the disulfide bond bridge between the two Cys (3, 14) residues in a native SST molecule has been shown to be important for its biological activity[150]. Therefore, the presence of the correct disulfide bond in the SST-mRFP complex was verified by carrying out a specialized mass spectroscopy based analysis. At the same time, it is interesting to note that Harris[99] reported that the linear, reduced form of SST was as active as the native one. Secondly, oligomerization – which has been reported to be one of the inherent properties of red fluorescent proteins, despite

the efforts to create more stable variants like, mRFP[44] – was potentially detrimental to the biological activity of the SST-moiety of the complex. Using a size-exclusion chromatography based method, SST-mRFP was found to have a mild propensity for dimerization. However, the observed dimerization was found to be dependent on the purification and storage buffer conditions. Thus, it is envisaged that the sample mass-fraction separation will yield monomeric proteins, suitable for applications.

Optical properties: Modification of an mRFP molecule, by fusing an SST moiety, was suspected to affect its optical characteristics. Therefore, the absorption and fluorescence spectral features of SST-mRFP were characterized and compared to that of the unmodified mRFP. The absorption spectra of SST-mRFP (Figure 5.5) matched to a large extent with that of mRFP[44], with a molar absorption coefficient of $\approx$ 92,000 $M^{-1}.cm^{-1}$. The fluorescent excitation and emission spectra of SST and SST-mRFP were found to be identical (Figure 5.6), with the peak wavelength values coinciding at 584 nm and 605 nm, respectively. The SST-mRFP was also found to be resistant to the harsh biochemical cross-linker – paraformaldehyde (see Figures 5.6 and 5.7). A 40% decrease in the fluorescence intensity was observed upon the addition of paraformaldehyde, however the emission spectral shape remained unaffected.

Biological properties: SST-mRFP was characterized in terms of its potency to activate the intracellular signaling chain, and was benchmarked with that of SST. The cell membrane hyperpolarization[193] and transient increase in cytoplasmic in Ca^{2+} concentration[7] were selected as measurable events in the intracellular signaling chain. Therefore, assays of the membrane potential and Ca^{2+} mobilization were carried out. The dose-response curves of membrane potential in wild type AtT-20 cells, shown in Figure 5.9, suggested that the potency of SST-mRFP was about 100-fold lower than that of SST (pEC_{50} values of 6.1 ± 0.2 and 8.43 ± 0.3, respectively). The lower potency was also observed in the Ca^{2+} mobilization assay (refer to Figure 5.12; pEC_{50} values of 6.3 ± 0.3 and 7.8 ± 0.5, respectively). The reduced potency of SST-mRFP was either due to the dimerization of SST-mRFP or due to the stearic effects contributed by the bulky mRFP molecule. The SST-mRFP was found to act via a pertussis toxin-dependent pathway, similar to that of SST[203].

Applications: Activation of ssts by SST has been shown to result in rapid internalization of ssts, using immunocytochemistry[136]. Internalization of the ligand, SST, along with receptor has also been observed using its labeled analogs[69,214]. Our study also conformed with these reports, where the endogenously sst-expressing AtT-20 and heterologously sst_{2A}-expressing CHO-K1 cells, efficiently and specifically internalized SST-mRFP molecules within the investigated time period of 20 min (see Figures 5.13 and 5.14). Several more investigations on the finer details of the sst-mediated SST internalization have been reported. For example, in the RIN38 cells that heterologously expressed sst_2, the sst_2:SST complex has been observed to stay intact after internalization for as long as 1 hr[25]. On the other hand, in HEK cells that expressed sst_{2A}, the internalized SST was degraded by enzymes in early endosomes and the remains were recycled to the cellular exterior[214]. The fate of the SST was not only dependent on the type of the cell, but also on the sst-subtype. For example, in heterologously sst_3-expressing RIN cells, degradation of the internalized SST occurred even before reaching the endosomes, in endocytotic vesicles[213]. On the other hand, in RIN cells that heterologously expressed sst_1, SST bypassed the degradative processes and was recycled back to the extracellular space[215]. Such finer details on the ligand internalization was unavailable in the case of CHO-K1 cells. Our observations using the SST-mRFP in conjunction with the immunocytochemical labeling of the sst_{2A}, showed that the receptor:ligand complex remained intact during the investigated time scale of 20 min (see Figure 5.16). They were found to be localized in the perinuclear regions. Longer incubation time (30 min) resulted in decrease in SST-mRFP fluorescence intensity – likely to be indicative of intracellular degradation. The sst-mediation in the internalization of SST-mRFP was confirmed using an antagonist competition experiment, where no internalization was observed (see Figure 5.17).

5.9 Conclusion and Perspective

A potent fluorescent analog of somatostatin – SST-mRFP – was designed, synthesized, characterized and applied for *in vitro* imaging of sst-mediated internalization. The

specificity and the brightness of SST-mRFP was valuable in providing insight to the finer details of internalization. SST-mRFP holds promise for *in vivo* applications, for example, to determine the fate of the ligand after it undergoes sst-mediated internalization in the group of neurons that regulate blood pressure and respiration. Results from the characterization assays suggested that the attachment of external moieties to SST may cause reduction of its potency.

Besides the development of a fluorescent probe, the experiments reported here also formed a biological basis required for the development of a nanoparticle-based fluorescent somatostatin probe, described in Chapter 8. Next two chapters are aimed at understanding how pristine nanoparticles interact with cells, and how they can be interfaced with biomolecules.

6

Non-specific Nanoparticle Internalization

This chapter is based on the journal publication:

Timothy A. Kelf, **Varun K. A. Sreenivasan**, Jinjun Sun, Eun J Kim, Ewa M Goldys and Andrei V. Zvyagin*, "Non-specific cellular uptake of surface-functionalized quantum dots", *Nanotechnology*, 2010[132]

This chapter describes investigations on non-specific internalization of commercially available quantum dots by cells and the factors influencing them. The chapter starts with a contextual definition of non-specific internalization, followed by a brief description of the types of quantum dots and cells used in this study. The level of non-specific internalization was evaluated by using fluorescence confocal microscopy, with an attempt to identify the reasons for differences in its variation, including the properties of the quantum dots itself and other experimental conditions.

Contents

6.1   Introduction

A cell interacts with its surroundings, via its membrane, and uptake material from the extracellular medium in order to sustain its lifecycle. The mechanism of this uptake is known as endocytosis or internalization, which can be broadly classified as specific or non-specific. The specific internalization is more-or-less well understood and usually occurs as a response to cellular activation by specific molecules. The receptor-mediated

endocytosis is one of the best examples of specific internalization, and is observed in most cell-types. This process is regulated by receptors, located on the cells, that are only activated by receptor-specific ligands. The mechanisms of specific internalization is routinely investigated in fundamental research to better understand cell-signaling. These investigations rely on the use of probes or labels, which highlight the molecules that take part in the internalization process. A fluorescent label based study on the internalization of somatostatin receptors, which occurs soon after the activation by somatostatin, was discussed in the previous chapter.

Non-specific internalization, on the other hand, is by-far less understood and is classified as an extraneous cellular-process. Although the stimulus that is required to trigger a non-specific internalization is not fully understood, it is thought to be initiated by physiochemical interactions between molecules/particles in the medium with the cell membrane. The amount of non-specific internalization that occurs is assumed to be determined by the cell-type, type of the molecule/particle, experimental conditions etc. Because of this, molecules or particles that are originally destined to undergo specific internalization might be taken up by cells via the non-specific pathway. In label-based investigations of the specific internalization, the non-specifically internalized labels manifest as background signal. Therefore, it is critical to understand the non-specific interactions of nanoparticles with the cells under consideration, for more controlled somatostatin labeling reported in the later chapters of this thesis. This chapter discusses on the non-specific internalization of a type of fluorescent probe - the quantum dot (QD), which was discussed in Chapter 2.

Briefly, QD represents a nanometer-sized core made of a crystalline semiconductor, whose photo-excitation is governed by the quantum confinement effect[11], resulting in fluorescence. This effect manifests as the nanocrystal core size-dependent wavelength of fluorescence-emission, which facilitates spectrally multiplexed labeling strategies[49]. The QD nano crystals are surface passivated with a semiconductor shell, in order to improve the fluorescence and to protect the core from the environmental damage and fluorescence quenching. In commercially available QDs, the resultant core/shell structure is capped with an auxiliary polymer layer to avoid potential cytotoxicity and

improve photostability. The auxiliary polymer layer also enhances the hydrophilicity, making the QDs suitable as fluorescent contrast agents for specific biolabeling. Improvements on the core-synthesis and polymer coating techniques in the recent years has resulted in its performance surpassing that of the conventional fluorescent probes. Conventional probes are organic dye molecules and are vulnerable to chemical attack and long exposure to bright light[277]. QDs on the other hand are resistant to these environmental conditions and are suitable for most specific biolabeling applications.

During the specific labeling procedure, some of the QDs will also undergo non-specific internalization. This gives rise to a non-zero background in the signal acquisition procedure, for example, imaging. Characterization of non-specific internalization can aid better design of QD-based probes for specific labeling with reduced background. Several independent reports suggested that the non-specific uptake of nanoparticles (NPs), such as QDs, were dependent on various parameters, including its concentration, size[53,204], surface chemistry (charge and hydrophobicity)[117], cell-type[279] and other experimental conditions, for example, temperature. The objective of this part of the Ph.D. project was to perform a series of experiments to evaluate the effects of some of these parameters in governing the rate of non-specific internalization of commercially available QDs. The results of these experiments became invaluable for the design of a QD-based specific fluorescent probe, which will be discussed in Chapter 8.

6.2   Systems Under Investigation

6.2.1   Commercial Quantum Dots

Commercially available QDs are being used in many labeling applications[48,77,114] and were considered an ideal replacement for the red fluorescent protein, which was used to label somatostatin in the previous chapter. This motivated us to investigate the non-specific internalization rates of a range of different commercially available QDs, in an expectation to arrive at a few QD-types that show the lowest rate of non-specific internalization.

QDs were distributed mainly by two companies: Invitrogen and eBiosciences, under the names of Qdot® and eFluor®, respectively. They will be represented as QD_i and QD_e, respectively throughout this chapter. These QDs are usually encapsulated with a layer of proprietary polymers, which render them stable in aqueous solutions and also expose either of the two chemical functional groups: Carboxyl or Amine. Some of these QDs may also contain an additional layer of macromolecules including Streptavidin[†] (Sav)- and poly-ethylene glycol (PEG)-coating. Such chemical functional groups and macromolecules causes modification of charge or hydrophobicity of the pristine QD, thereby altering the rate of non-specific internalization.

The seven types of QDs that were used in this study are listed in Figure 6.1. All these QDs had a narrow emission peak at 605 nm. Three of them were purchased from Invitrogen, which contained either carboxyl-groups, amine-terminated PEGs or streptavidin on the surface, represented by $C\text{-}QD_i$, $N\text{-}pQD_i$ and $Sav\text{-}QD_i$, respectively. A fourth type was synthesized from $C\text{-}QD_i$ by carrying out a chemical reaction with ethylene diamine ($NH2\text{-}CH_2\text{-}CH_2\text{-}NH_2$), which resulted in the conversion of surface carboxyl groups to amino groups, thus forming $N\text{-}CC\text{-}QD_i$. Two other types of QDs were purchased from eBiosciences. These contained a layer of PEG, which was terminated either by carboxyl or by amine groups, and represented by $C\text{-}pQD_e$ and $N\text{-}pQD_e$, respectively. The $C\text{-}pQD_e$ was also modified with ethylene diamine, in order to investigate on the effect of charge on QD-uptake, to produce $N\text{-}CC\text{-}pQD_e$.

6.2.1.1 Quantum Dot Characterization

The size and surface charge of the purchased (and modified) QDs were measured using a Zetasizer (see Sections 4.1.3 and 4.1.4 for details) and presented in Table 6.1. The size of the purchased QDs, represented by their hydrodynamic diameters[‡], were measured to be ≈ 20 nm. The zeta-potential, which is a measure of the surface charge, was

---

[†]Streptavidin is a commonly used protein for interfacing applications because of its highly affine binding to Biotin

[‡]hydrodynamic diameter is the diameter of an effective spherical particle, which experiences same diffusion. It is often an overestimate the geometric average diameter by roughly 10%
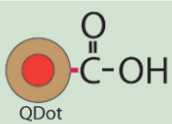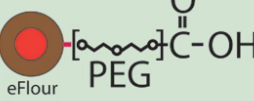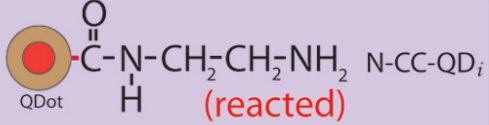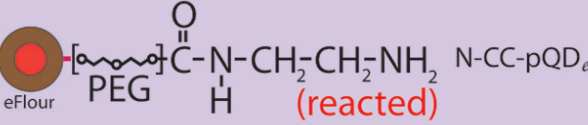
Figure 6.1: The schematics and names of the QDs used in this chapter. Except the last two QD-types, all the others were commercially available.

observed to be negative, irrespective of the type of the surface group (carboxyl, amino or streptavidin). However, the zeta-potential was found to be dependent on the presence of surface PEG- or Sav-coating.

The optical properties of the QDs were characterized in terms of their absorption and fluorescence spectra, in order to calculate their quantum efficiencies. As purchased, the quantum efficiency of C-QD$_i$ was found to be 2.5 times greater than that of C-QD$_e$. The bright orange color of the C-QD$_i$ and C-pQD$_e$ solutions faded to pale brown during the modification reaction to synthesize N-CC-QD$_i$ and N-CC-pQD$_e$, respectively. This was particularly apparent in the reaction of C-QD$_e$ to produce N-CC-QD$_e$. A comparison of the quantum efficiencies[†], before and after reactions, revealed that the C-QD$_i$ and C-pQD$_e$ suffered a 2.5- and 10-fold drop in their quantum efficiencies during the reaction, respectively. The drop in their quantum efficiency was the reason for the discoloration. The different fluorescence stabilities of these QDs is an indication of the variation in the chemical stability of the surface-polymer coating. Disintegration of the polymer coating, which provided colloidal stability to the QDs, also resulted in formation of aggregates of $\approx$ 100 nm soon after the reaction (see

---

[†]Quantum efficiency is a parameter which is used to represent fluorescence efficiency. It is the ratio of the number of emitted to the absorbed photons. It is normally represented as a percentage

Table 6.1: Characteristics and internalization rates of seven QD-types, arranged in the decreasing order of internalization by the AtT-20 cells. The diameter and zeta-potentials of the QDs were measured in PBS.

QD-type	Diameter (nm)	Zeta-potential (mV)	Normalized internalization		
			AR42J	GH4C1	AtT-20
N-CC-QD$_i$	100	-32	0.225	0.419	1.000
C-QD$_i$	28	-31	0.120	-	0.082
N-pQD$_e$	23	-2	0.030	0.027	0.078
N-CC-pQD$_e$	24	-12	0.024	0.035	0.078
C-pQD$_e$	22	-12	0.029	0.002	0.018
SA-QD$_i$	20	-15	0.039	0.043	0.012
N-pQD$_i$	21	-2	0.005	0.008	0.002

Table 6.1).

6.2.1.2   Method of Chemical Modification

For converting the carboxyl groups on the surface of C-QD$_i$ and C-pQD$_e$ into amine groups, 400 fmole (1 molar equivalent) of these QDs were diluted in 400-μL MES[†] buffer containing 2-mM EDTA[‡] (pH = 6). Freshly prepared and room temperature equilibrated aqueous solutions containing 10-mg.mL^{-1} 1-ethyl-3-(3-dimethylaminopropyl) carbodiimide (EDC) and 20-mg.mL^{-1} sulfo-N-hydroxysuccinimide (sulfo-NHS) was added to each of the QD solutions to activate the surface carboxyl groups. The reaction solution was incubated at room temperature with gentle shaking for 15 min. Subsequently, an excess of ethylene diamine was added along with 50 μL of 5$\times$ sodium borate buffer (pH = 8.4). After 1 hr of room temperature incubation with gentle shaking, free EDC, sulfo-NHS and ethylene-diamine were removed by using a desalting column (Prepacked Sephadex G-25 medium column, GE Healthcare), equilibrated with phosphate buffer saline (PBS; pH = 7.2). The eluted solution contained the modified quantum dots N-CC-QD$_i$ and N-CC-pQD$_e$, respectively.

[†]MES is 2-(N-morpholino)ethanesulfonic acid

[‡]EDTA is ethylenediamine tetra acetic acid

6.2.2   Cell Types

In consideration of the future goal of using QD-based probes for imaging the specific internalization of somatostatin molecules, three cell-types that expressed somatostatin receptors were chosen for this study. These were the AR42J (rat pancreatic tumor-derived), GH4C1 (rat pituitary tumor-derived) and the AtT-20 (mouse pituitary tumor-derived) cell lines. Details of the cell lines including the growth conditions are described in Chapter 4. The cells were incubated with the seven QD-types to evaluate the rate of non-specific internalization.

6.2.2.1   Method

On the day before experiments, cells were transferred into eight chambered culture slides (BD Falcon) and incubated overnight in their respective culture media. The cells were incubated with a QD solution of required concentration, prepared in 300-μL PBS with additional $CaCl_2$ (0.9 mM), $MgCl_2$ (0.5 mM), bovine serum albumin (BSA; 0.1%) and D-glucose (20 mM) at 37 ^{o}C and 5% CO_2 for the required time period. In some cases, the cells were treated with 0.5-M sucrose solution before the QD-incubation. After the QD-incubation, cells were washed twice with PBS and fixed using 3.7% (w.v^{-1}) paraformaldehyde solution for 20 min followed by a PBS wash. In some cases, cell nuclei were stained using 10-μM Hoechst 33342 solution, prepared in PBS, for 10 min at room temperature, followed by two wash steps with PBS. The slides were sealed and imaged with a fluorescence confocal microscope.

6.3   Characteristics of Internalization

Prior to a detailed investigation on the variations in internalization-rates of the different QD-types in the three cell-lines, some of its basic properties, including the effects of temperature and time duration, were characterized. These experiments were performed on the AR42J cells and C-QD$_i$ particles, which were chosen as the preliminary models based on our previous observations on their efficient internalization.

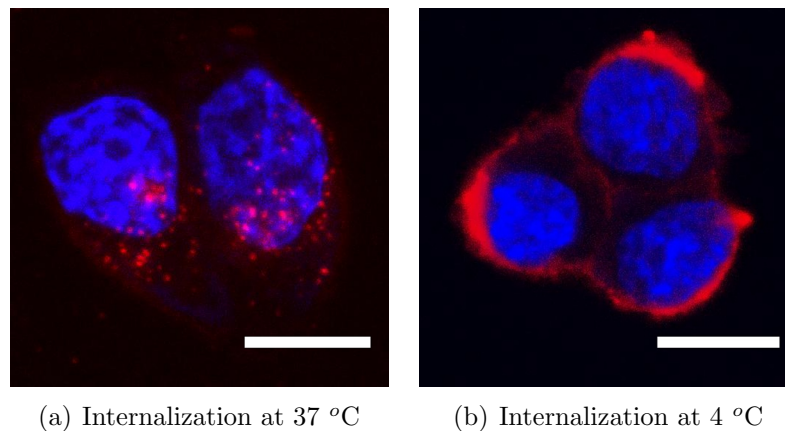(a) Internalization at 37 ^{o}C (b) Internalization at 4 ^{o}C

Figure 6.2: The difference in the rate of internalization of 20-nM C-QD$_i$ by the AR42J cells, maintained at different temperatures. Red and blue represents the fluorescence signal from the QD and stained nuclei, respectively. Scalebar 10 μm.

6.3.1 Effect of Temperature

Most cellular processes are suspended upon reduction of temperature. This is because the cells require energy to perform these active processes, for which they depend on molecules of adenosine triphosphate (ATP)[9]. Under cold conditions, the generation and distribution of ATP molecules becomes greatly reduced and causes cessation of the active cellular processes. Passive processes on the other hand do not rely on ATP, and can continue even under such conditions. Therefore, by measuring the effect of temperature, it was possible to determine whether the QD-internalization was active or passive. Figure 6.2 represents the difference in internalization of AR42J incubated with C-QD$_i$ at 37 ^{o}C or 4 ^{o}C. At 4 ^{o}C, the QDs did not enter the cells, instead were membrane-bound. This suggested that the internalization of C-QD$_i$ was an active process, which occur only at physiological temperatures. This also inferred that prior to the internalization, the C-QD$_i$ particles attach themselves onto the cell-membrane, although the forces that enable this attachment is yet to be identified.

6.3.2   Mechanisms of Internalization

The process of internalization is initiated by the formation of inward invaginations in the cell membrane. The extracellular particles or molecules to be internalized are captured in such invaginations, which subsequently gets encapsulated as they form cytoplasmic vesicles. Various mechanisms of internalizations exists, and are distinguished based on the molecules that support the formation and closure of the invaginations. Two main mechanisms that are engaged to uptake nanometer-size particles occur via caveolae[14] and clathrin-coated invaginations[108] and will be discussed later in this chapter. The micrographs of clathrin-coated invaginations are presented in Figure 6.3.

The type of internalization by which the $C\text{-}QD_i$ uptake occurred was identified by using a specialized blocker that inhibited one of these mechanisms. The study by Heuser and Anderson[108] reported that pre-treatment of cells with high concentrations of sucrose resulted in inability of cells to initiate clathrin-mediated internalization. This happened because sucrose prevented the formation of the large cage-like supramolecular structure of clathrin. Figure 6.4 presents fluorescence confocal images of the AR42J cells incubated with 20-nM $C\text{-}QD_i$, with or without sucrose (0.5 M) pre-treatment. The sucrose pre-treated cells failed to internalize the QDs and indicated that the internalization observed in the untreated cell occurred via clathrin-coated pits.

6.3.3   Time-scale of Internalization

The model AR42J cells were treated with 2-nM $C\text{-}QD_i$ for a range of time periods. Figure 6.5 presents the fluorescence intensity of the internalized $C\text{-}QD_i$[†], as a function of incubation-time. The rapid increase of intracellular QD signal in the 5 to 10 min period followed by saturation suggested that the $C\text{-}QD_i$ internalization occurred via a specific mechanism, likely after receptor activation; as internalization via non-specific mechanisms do not saturate. The time taken for the initialization of internalization

---

[†]The internalization was quantified by means of the fluorescence from the QDs associated with the cells, excluding the membrane bound signal
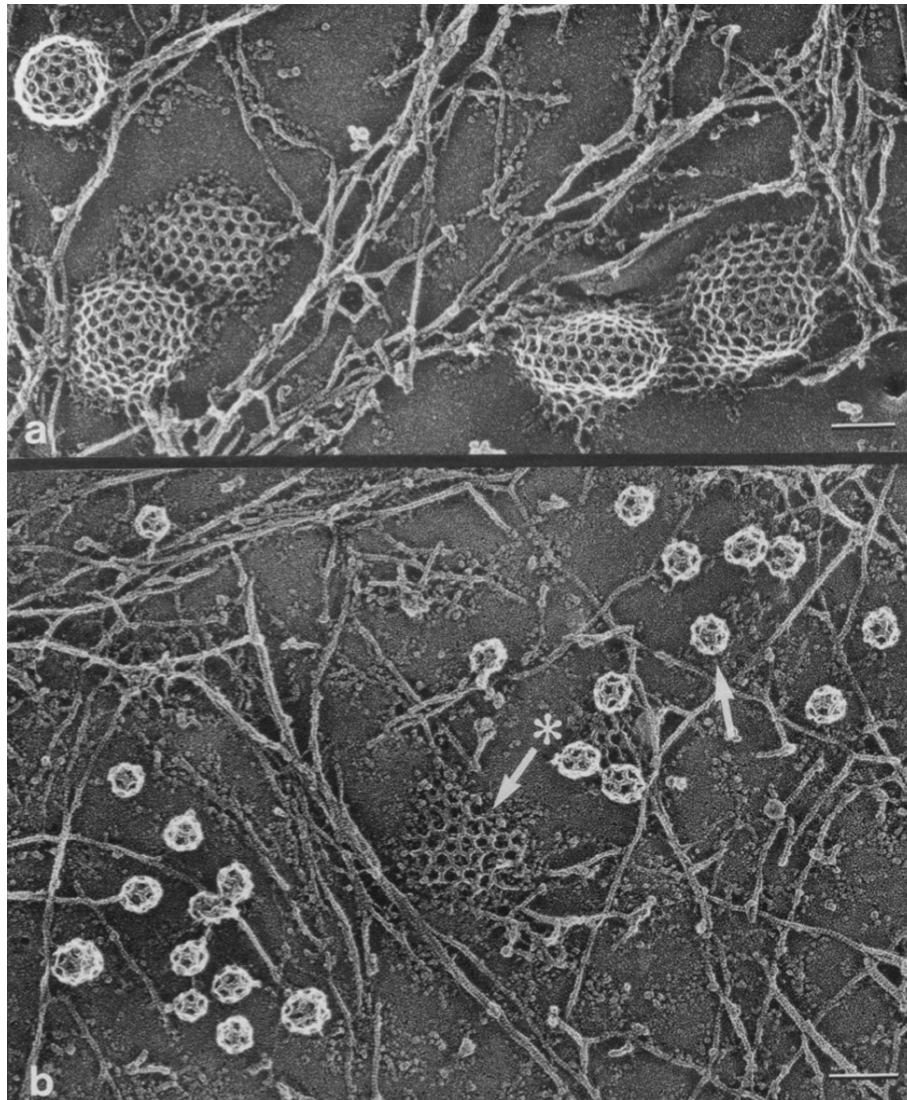
Figure 6.3: Survey views of clathrin lattices on the inner surface of a normal chick fibroblast (a), compared with lattices on a fibroblast pre-treated with 0.45-M sucrose for 30 min at 37 ^{o}C (b). In normal cells, various stages of clathrin lattice assembly and curvature were seen. In hypertonic cells, membrane-attached lattices were reduced to flat remnants (such as the one at the *) and were replaced by numerous clathrin microcages (one of which is indicated by the arrow). Scalebar 0.1 μm. Reproduced with permission from Heuser and Anderson[108]

and the amount of maximum internalization were dictated by the temporal activity and the abundance of the receptors, respectively.

These results suggested that the C-QD$_i$ (carboxylated quantum dots) undergo efficient internalization by the AR42J cells via a specific, probably, receptor-mediated,
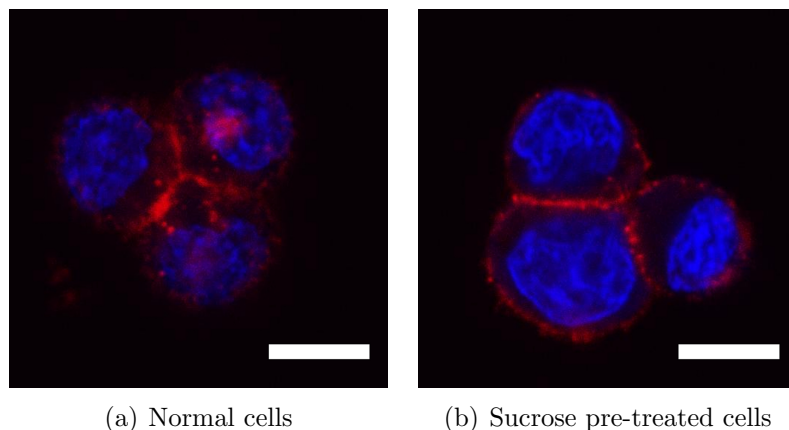
(a) Normal cells   (b) Sucrose pre-treated cells

Figure 6.4: The cessation of internalization of the C-QD$_i$ by pre-treating the AR42J cells with hypertonic (0.5-mM) sucrose solution. Red and blue represents the fluorescence signal from the QD and hoechst-stained nuclei, respectively. 488-nm argon laser and 405-nm diode laser emissions were used to excite the QD and hoechst, respectively. The fluorescence emission from the QD was collected between 585 nm and 605 nm. Scalebar 10 μm.
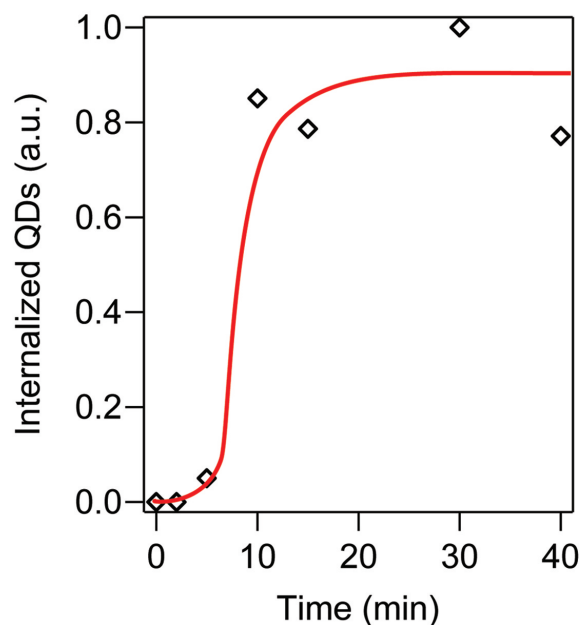

Figure 6.5: The increase in the number of C-QD$_i$ internalized by the AR42J cells on increasing incubation time.

process. A similar conclusion was also reached in the study by Zhang and Monteiro-Riviere[279] who observed that two types of carboxyl-functionalized QDs with different fluorescence wavelengths mutually inhibited each others internalization, probably because they both required the same set of receptors. Despite the observed specificity, in this thesis we will classify the QD-internalization as a non-specific process, because the receptor-types that are required to initiate the internalization could be numerous and remain unidentified.

6.4   Internalization of Quantum Dots by Cell-types

All the seven QD-types were incubated with the three cell types at identical conditions, to compare the rate of internalization between the 21 possible combinations. A QD incubation time of 60 min was chosen based on the data presented in Figure 6.5, where the internalization saturated within $\approx$ 10 min of incubation. Figure 6.6 shows some of the images of these cells treated with the QDs. From the raw images, the net internalization was quantitated in terms of the intensity of QD-derived fluorescence. This was obtained by integrating the value of pixels enclosed by the cell membrane, while carefully excluding the pixels corresponding to the membrane-bound QDs. The calculated intensity values were scaled using the relative quantum yields of each of the QD-type, in order to obtain a number based quantitation. The scaled intensities were normalized to obtain the values tabulated in Table 6.1 and graphically presented in Figure 6.7.

The overall trend in the internalization between different QD-types was roughly similar across all the three cell-lines. This suggested that it was the QD surface properties that mostly determined the rate of internalization. The dependence of internalization on the macromolecular moieties and chemical functional groups are individually addressed in the following subsections.
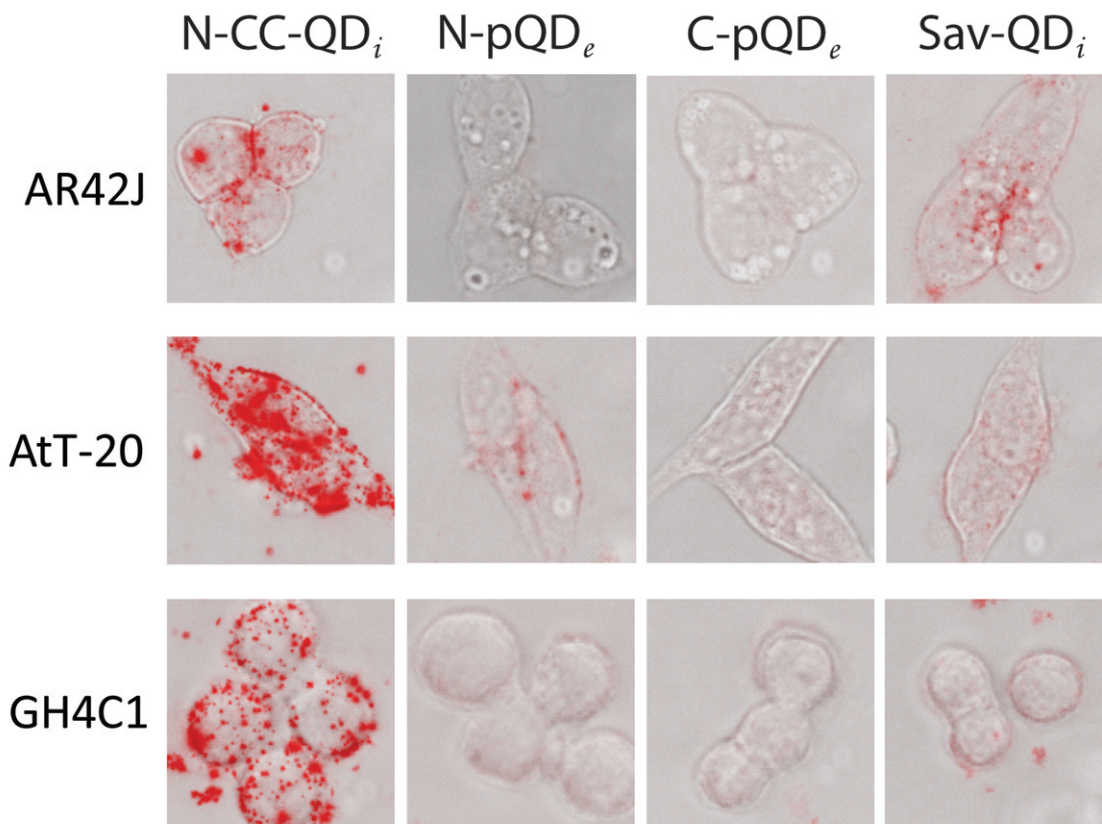
Figure 6.6: Representative images of the three types of cells incubated with some of the QD-types. Red, which represents the QD-derived fluorescence, is overlaid with the bright field transmission image. Each image panel size is 37.5 μm $\times$ 37.5 μm.

6.4.1 The Effect of PEG Coating

It is apparent from the data that the presence of macromolecules, like PEG, on the QD surface results in a steep reduction of internalization, for example, from 0.225 to 0.005 by the AR42J cells for the N-CC-QD$_i$ and N-pQD$_i$, respectively. While precise reasons behind the significantly reduced internalization of PEG-derivatized NPs are still debated, a number of consistent observations have been presented in the literature[64,117,268,279]. From Figure 6.8, which attempts to correlate the internalization rates and zeta-potentials of the different QD-types, these PEG- derivatized QDs were also observed to have zeta-potentials closer to zero than their pristine counterparts. This is because, the PEG molecules neutralizes the charge associated with the surface of pristine QDs.

The charge neutralization occurs, because the PEG molecules impose restrictions on
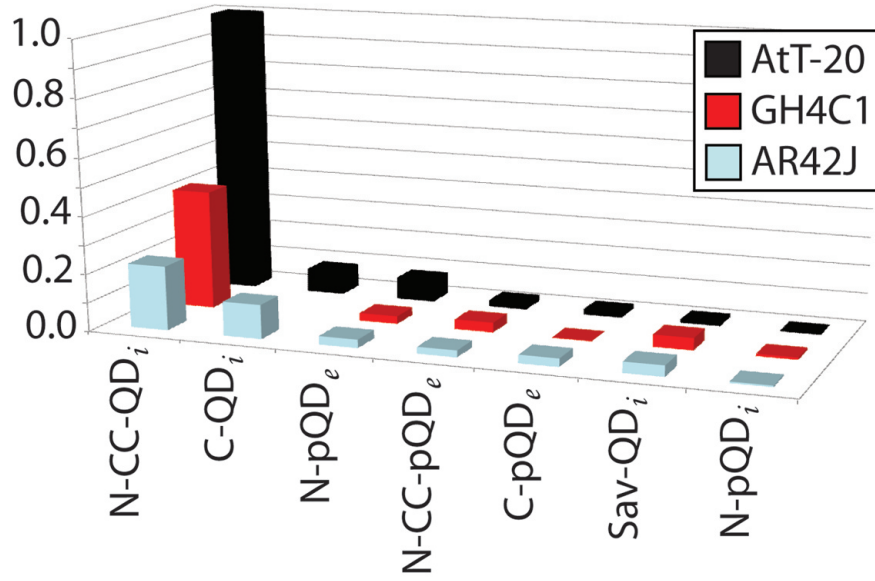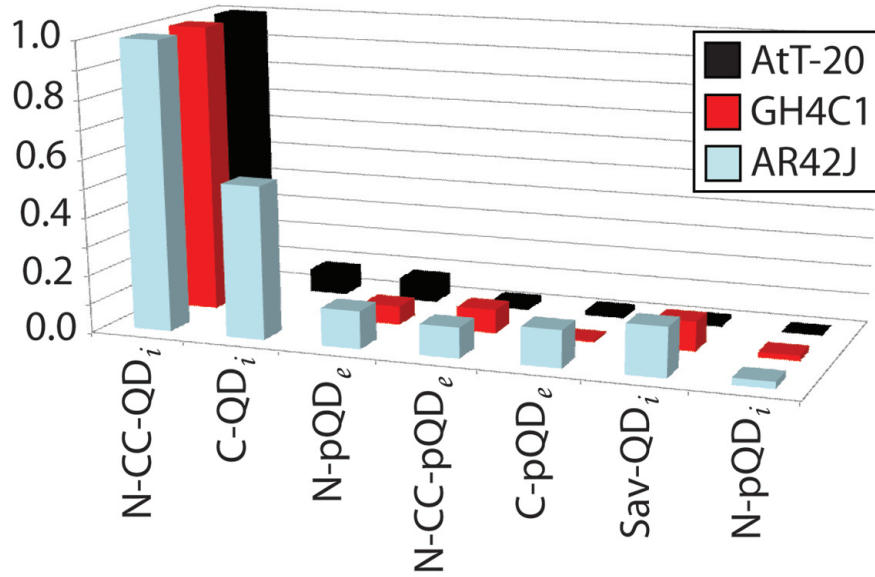
(a) Normalized to that of N-CC-QD$_i$ quantum dots in AtT-20 cells

(b) Normalized across each cell type data to that of N-CC-QD$_i$

Figure 6.7: Variations in the rate of internalization among the different QD and cell types. The raw data was corrected for the QD-quantum efficiencies and normalized by two methods, presented in (a) and (b).

the liquid flow near the QD and shifts the fluid slippage plane farther from the particle surface. This shift manifests as a reduction in the magnitude of the zeta-potential, which is defined as the surface charge-generated electrostatic potential at the fluid
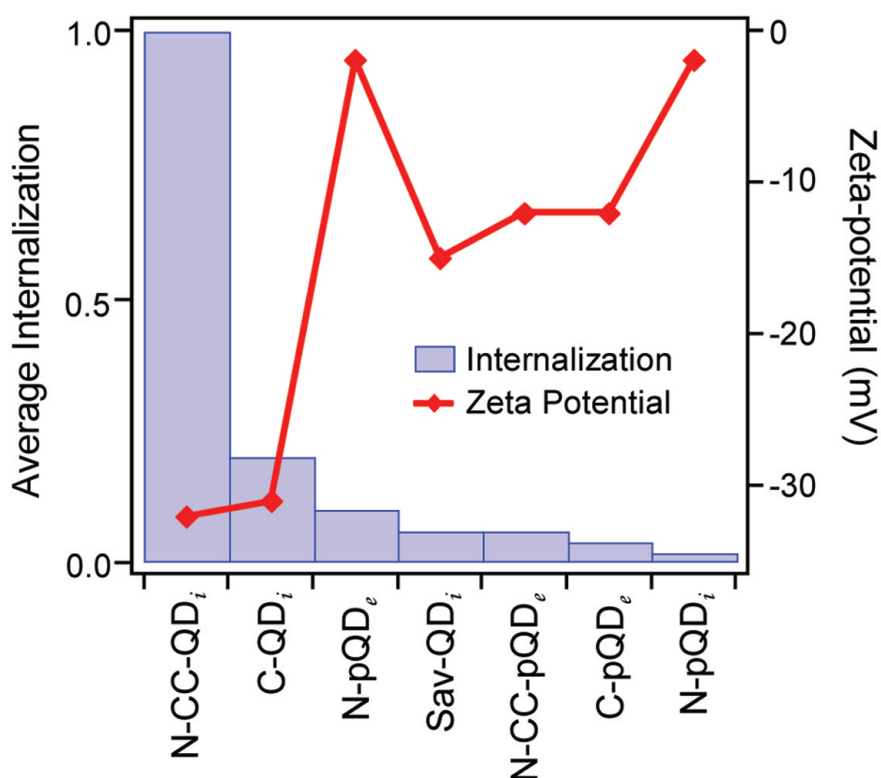
Figure 6.8: A plot that reveals the dependency of internalization on the zeta-potentials of the different QD-types.

slippage plane[158,174]. Besides shifting the slippage plane, the PEG layer also contributes towards charge screening. As per previous reports, the extent of neutralization by both these phenomena was determined by the length of the PEG and the density of its coating on the NP-surface. To verify this effect, PEG molecules of different lengths (measured in terms of their molecular weights of 3400 Da and 5000 Da) were conjugated to $C\text{-}QD_i$ at different surface densities using a reaction similar to that described in Section 6.2.1.2.

Our theoretical calculations based on geometric packing (ratio of surface are of QDs to the size of PEG molecules) suggested that a QD-particle can accommodate up to 400 molecules of PEG. For the experiments, the number of PEG molecules conjugated on a QD was empirically controlled by adjusting the amount of PEG added during the reaction. At the maximum PEG surface density the measured zeta potential was close to zero, showing an almost complete screening of the QD surface charge (see
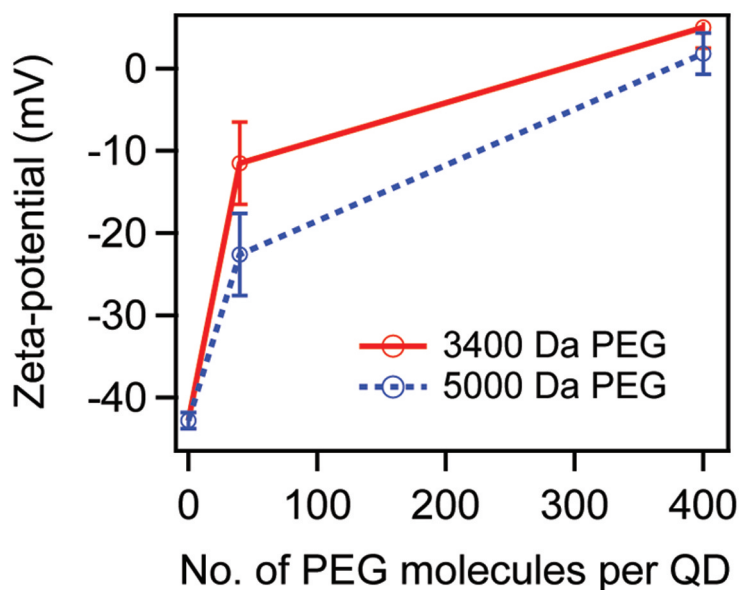
Figure 6.9: QD-surface charge neutralization upon PEG coating. As the number of PEG molecules attached to the QD-surface is increased, the charge on the native QD-surface is screened, resulting in a reduction of the zeta-potential.

Figure 6.9). Under this condition, the Zetasizer-based size measurements indicated that the PEG layer was 2-nm thick. As the surface density was reduced, the absolute value of the surface charge increased, approaching that of the uncoated C-QD$_i$. The change in zeta-potentials that was observed after the conjugation of both PEG types were identical.

Previous literature suggested that a balance between the PEG length and surface density was important for optimal design of the surface of an NP[174]. When densely packed, PEG covers the majority of QD-surface, and these long molecules align perpendicular to the surface, giving rise to a 'brush-like' architecture. At a lower density the flexible PEG-chains are bent and conforms to a mushroom type state, giving rise to a different set of surface properties. The small, but noticeable differences in internalization between the different types of PEG-coated QDs used here is probably due to the differences in the coating density and the length of PEGs used by the two manufacturers.

6.4.2 The Effect of Streptavidin Coating

The Sav-coated QD (Sav-QD_i) showed a reduced zeta-potential and non-zero internalization (see Table 6.1). According to previous literature, Sav-coated NPs underwent increased non-specific internalization, which was expected because of their biologically active nature. Sav is a protein, which has a high binding affinity to biotin, also known as Vitamin H. Since biotin is present in the culture medium and can be adsorbed onto the cell membrane, it can act as an anchor for the initial binding of Sav-QD_i, thereby promoting internalization[114]. According to another report, the internalization of Sav-QD_i can be facilitated by the amino acid sequence -RYD- in a Sav molecule, whose structure sufficiently resembles that of the sequence, -RGD-, recognized by many cell adhesion-related molecules[13]. Thirdly, there can be non-specific internalization through pinocytosis, which is a common pathway for internalization of a broad class of extraneous materials, including QDs. We tested the first pathway by pre-binding biotin to the streptavidin-coated QDs, and found no discernible change in the level of internalization. This ruled out the possibility of internalization via the biotin-mediated pathway. The second pathway was more difficult to test, however the total observed internalization levels of the streptavidin-coated QDs were broadly comparable to the lowest levels of internalization of the other (PEG-containing) QDs, that were limited to the pinocytosis pathway. This suggested that pinocytosis was the dominant mechanism that contributed towards the internalization of Sav-QD_i.

6.4.3 Other Effects Reported in the Literature

Out of the large number of NP-related parameters that can influence the rate of non-specific internalization, our hands-on investigations were limited to a few that were described earlier, because we used commercially available QDs. Some of the parameters unaccessible due to this reason included the QD-shape, QD-size and other potentially significant macromolecular surface functional groups, which can alter physiochemical properties. All the QDs used for this investigation had an ellipsoidal geometry, as can
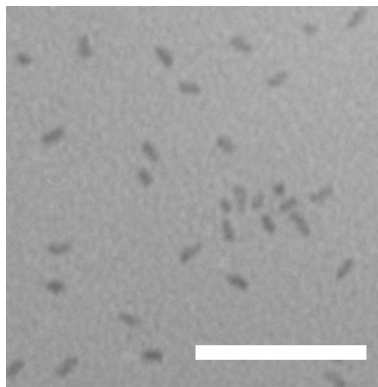
Figure 6.10: A transmission electron micrograph of C-QD$_i$. Scalebar 50 nm.
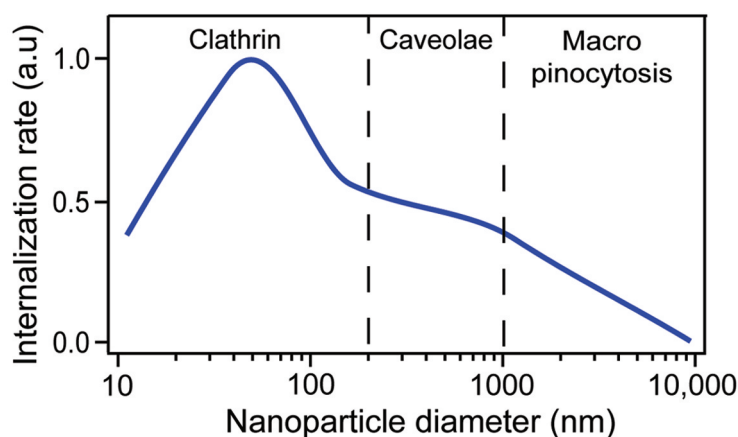

Figure 6.11: The size of the NPs determined the rate of non-specific internalization. This plot was obtained by combining a large amount of data scattered across the literature.

be observed in the micrograph presented in Figure 6.10, obtained by using a transmission electron microscope. It can also be seen from Table 6.1 that the hydrodynamic size of all the procured QDs were $\approx$ 20 nm[†]. In order to acknowledge the size-dependency of the rate of non-specific NP-internalization, we consolidated the information scattered among several reports[53,54,87,204,280] to generate a plot which showed this dependency, and is presented in Figure 6.11. A brief outlook on the cellular mechanisms that assist internalization of particles belonging to different size ranges was considered necessary to appreciate this data, and is therefore discussed in the following paragraphs.

Three classes of internalization mechanism span the broad particle size, ranging

---

[†]This value is different from that measured using the electron microscope, because these QDs contained a polymer layer that did not provide electron-contrast

from a few nanometers to micrometers, and they occur via clathrin-mediated vesicles, caveolae or macro-pinocytosis. Clathrin-mediated pathways are predominant for internalization of NPs smaller than 200 nm. The non-specific internalization of NPs in this size range is hypothesized to be initiated by adsorption of random proteins from the culture medium onto the particles surface, followed by their internalization via receptor-mediated pathways. Therefore, the rate of internalization is dependent on the available receptors on the cell surface and the number of receptors that a single NP is able to trigger when it adheres to the membrane. 50-nm sized particles have been shown to be most efficiently internalized by this mechanism, both experimentally[53] and theoretically[280]. For NPs <50 nm, several closely spaced particles are required to trigger the formation of a clathrin-coated vesicle[204]. As a result, the rate of internalization per particle is reduced, which is manifested as the descending slope at sizes below 50 nm in Figure 6.11. A theoretical model based on the balance between free energy required to drive NPs into the cell and diffusion kinetics of the recruitment of receptors to the binding site also arrived at similar conclusions[280]. Particle sizes larger than 50 nm engage many more receptors than the threshold required to initialize internalization, soon leaving the cell membrane deprived of receptors. Further internalization occurs only after the receptors are recycled back to the cell membrane, which takes time and lowers the rate of uptake.

The clathrin-mediated internalization mechanism cannot transport NPs larger than ≈ 200 nm, because of the fixed size of their spherical crystalline structure (see Figure 6.3). Cells recruit alternative internalization pathways for these particles. Particles falling in the size range of 200 nm to 1 μm are mostly transported in caveolaes. They are lipid-rich structures, which form Ω-shaped pits in the cell membrane (see Figure **??**), within which these particles are enclosed and endocytosed. This process is less efficient than that of the clathrin-mediated internalization. For particles larger than a micron (up to 5 μm in diameter), the effect of macro- pinocytosis becomes important. This requires ruffling of the cell membrane to form large troughs, which can subsequently bud in the form of large vesicles into the cell. This is a genuinely non-specific process,

and highly dependent on the cell type and experimental conditions. The internalization rate drops dramatically above around 1 μm due to the difficulty in forming these large vesicles.

Particle shape has also been shown to play a role in the internalization[87], which furthers the complexity. The shapes are important because they also govern the area by which the cell perceives their presence. In some way, the arguments made above are also applicable here.

Another parameter which was attempted to be elucidated was the NP surface charge. QDs with negatively (-COOH) and positively (-NH$_2$) charged functional groups were procured, and expected to have negative and positive zeta-potentials, respectively. However, we observed that their zeta-potentials were always negative and the values presented in Table 6.1 suggested that the zeta-potential is primarily determined by the surface charge of the pristine QDs, rather than the functional groups. This prevented us from arriving at accurate conclusions, but previous reports[174,183,268] suggested that both positively and negatively charged molecules can be efficiently internalized into cell, by utilizing interactions with various charged proteins located on the cell membrane[76,164,228]. Near neutral QDs with hydroxyl (OH) surface functionalization, exhibited greatly reduced non-specific internalization[130], in contrast with the carboxyl or amino functional groups. These arguments indicated that charge is an important parameter to understand non-specific internalization characteristics. For all the QDs used in this thesis, the charge-, size- and shape-dependencies of internalization can be overlooked, because these parameters were found to be consistent among all of the commercial QDs that we tested.

6.5 Summary

NPs are popular as probes for biolabeling. But, their non-specific internalization manifest as noise during the biolabeling procedure. Several types of QDs, which served as our model NPs, and cells were screened and compared for the rate of non-specific internalization. The parameters that govern the non-specific internalization process

were also identified.

Preliminary characterization of non-specific internalization: Initial experiments with the quantum dots that contained carboxyl functional groups suggested that these particles were internalized by the AR42J cells by a rather specific process. Three observations supported this conclusion: (i) The QD internalization was ceased by maintaining the cells at a low temperature (see Figure 6.2). Low temperatures are known to reduce the rate of energy production, which is required for most specific internalization processes. (ii) The cells pre-treated with hypertonic solutions of sucrose were unable to internalize the QDs (see Figure 6.4). High concentrations of sucrose reportedly prevented formation of the clathrin-coated pits, which take part in many receptor-mediated internalization processes[108]. (iii) The observed QD-internalization saturated over time (see Figure 6.5). The saturation indicated that the internalization required activation of a set of receptors, which were saturated by adding the QDs. Despite the specificity, internalization of the commercially available QDs were classified under non-specific processes, because the receptors that initiate the internalization remain undetermined and may vary between cell-types, experimental conditions etc.

Characterization of the QD-types: Five types of QDs were purchased from two major vendors. Two of them were further modified chemically in order to understand the effect of surface charge on the rate of non-specific internalization. Figure 6.1 tabulates all these QD-types. The QDs were characterized in terms of their size, shape, surface charge and fluorescence efficiencies (see Table 6.1). Despite the different surface functional groups, all the QDs had hydrodynamic diameters of $\approx$ 20 nm, except for the reacted QDs, where $\approx$ 100nm aggregates were observed. Electron microscopy revealed that the QDs had an ellipsoid geometry, contrary to general expectation of these semiconductor nano crystals to have a spherical geometry. The charge of all the QD-types were mainly dictated by the nature of the surface of pristine QDs. The surface chemical groups (carboxyl and amine) had little influence on the zeta-potential. However, presence of large macromolecules, such as PEG or Sav, caused charge neutralization, resulting in the lowering of zeta-potential towards zero. The fluorescence quantum efficiencies of the QDs supplied by the two vendors were different by a factor of 4.

Chemical reactions further affected their quantum efficiencies, which was evident to the naked eye by the color change from orange to pale brown. This reduction was possible because of the disintegration of the stabilizing polymer coating under the highly reactive conditions. Disintegration of the polymer-coating also resulted in aggregation of QDs, when suspended in physiological buffers.

Comparison of non-specific internalization of the QDs by cells: Three types of cells were used to investigate the rates of internalization of the different QD-types. The overall trend in the variation of internalization rates between the seven QD-types were comparable across the different cell lines (see Figure 6.7). This suggested that the different QD-surface properties determined the rate of internalization, and their interaction with different cells occur in more-or-less the same way. The non-specific internalization of QDs was most affected by the presence of macromolecular groups: PEG and Sav. The reduction in the internalization was also accompanied by neutralization of the surface charge. This suggested that a neutral zeta-potential may result in reduction of non-specific internalization. Several papers reported that internalization of the Sav-coated QDs was promoted via alternate mechanisms, including one which was supported by biotin present in the culture media. However, our experiments did not provide any indication on such processes.

Several independent reports suggested that non-specific internalization of NPs were highly affected by their size and shape. As the QDs that were commercially available did not demonstrate much variability in these parameters, we were unable to arrive at such conclusions. However, a plot relating the rate of non-specific internalization versus the size of NPs was put together by gathering the data scattered across different reports in the literature (see Figure 6.11). The non-specific internalization was found to be most efficient in particles with an average diameter of ≈ 50 nm.

6.6   Conclusions

The non-specific internalization of nanoparticles can cause background-noise in many labeling applications designed to probe specific cellular processes[132]. Identifying the

properties of nanoparticles that dictate the efficiency of such non-specific processes can aid better design of nanoparticles to reduce the noise. Several types of fluorescent quantum dots served as model nanoparticles in our experiments to identify such parameters. We found that the surface coating, zeta-potential, size and other experimental conditions regulated the rate of QD internalization. A preliminary investigation on the internalization mechanisms revealed that it had some sort of specificity and may have been mediated by receptor(s). However, the type of these receptors remained unidentified. The conclusions from these observations became invaluable for designing a QD-based labeling tool to image the specific internalization pathways of a neurotransmitter in cells, which will be discussed in Chapter 8.

7

Biofunctionalizing Fluorescent Nanodiamonds

This chapter is based on the journal publication:

Varun K. A. Sreenivasan, Ekaterina A. Ivukina, Wei Deng, Timothy A. Kelf, Tatyana A. Zdobnova, Sergey V. Lukash, Boris V. Veryugin, Oleg A. Stremovskiy, Andrei V. Zvyagin* and Sergey M. Deyev, "Barstar:barnase a versatile platform for colloidal diamond bioconjugation", *J. Mater. Chem.*, 2011[239]

This chapter is focused on the development of an easy and versatile, yet robust platform for functionalizing nanoparticles with biomolecules – the core element required to develop a fluorescently labeled somatostatin. The chapter begins with a brief introduction of labeling, and why the fluorescent nanodiamonds are suitable as probes for molecular labeling. This is followed by a brief literature review on the existing methods

of functionalization and their drawbacks, ushering the need for a versatile biofunction-alization strategy, using which several nanodiamond based complexes were synthesized. The recombinant proteins, reported in this chapter, were generously provided by our collaborator, Prof. Sergey M. Deyev.
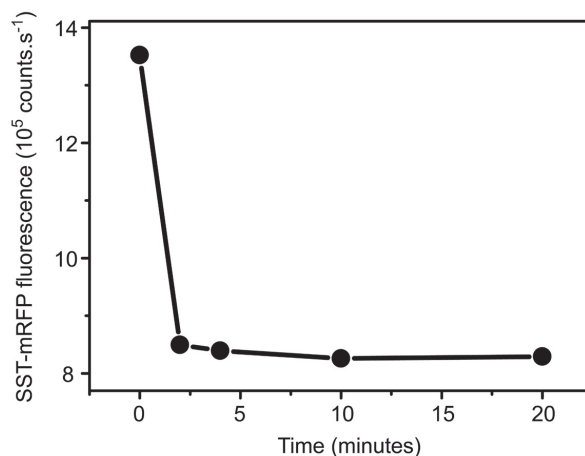
Contents

Figure 7.1: The temporal reduction in the fluorescence of the red fluorescent protein upon addition of paraformaldehyde at 0 min. See Chapter 5 for more description.

7.1 Introduction

Visualization of biomolecules using a fluorescence microscope rely on labeling them using extrinsic fluorophores (or fluorescent probes). Some of the conventional fluorescent probes used for labeling include small organic molecules, such as alexa fluor and fluorescein, and large macromolecules, such as green- and red-fluorescent proteins. However, such molecular probes are non-ideal, because of their susceptibility to chemical perturbations (see Figure 7.1) and photobleaching[277]. Nanoparticles demonstrate high chemical and optical stability and are well suited for live biological imaging, where they are subject to such harsh conditions. Several types of nanoparticles that are suitable as fluorescent probes were introduced in Chapter 2, of which the fluorescent nanodiamonds (FNDs) was the nanoparticle of choice in this chapter.

FNDs satisfy many of the stringent conditions to qualify as an ideal fluorescent probe, including the qualities of being (1) non-toxic, (2) stable, (3) small and (4) amenable to biofunctionalization. Non-toxicity and physical/chemical stability are two intrinsic properties that are inherited from bulk diamonds[277]. Nanodiamonds are available in a several sizes ranging from a few nanometers to hundreds of micron, suiting a variety of needs. Biofunctionalization or bioconjugation is the process of labeling (or attaching) a biomolecule with a fluorescent probe, which, in turn, renders the whole

complex biologically active. For example, in the previous chapter (Chapter 5), a Red Fluorescent Protein (mRFP) was biofunctionalized with somatostatin in order to label somatostatin receptors in cells. Biofunctionalization of FNDs can be performed using chemical or physiochemical approaches that are facilitated by reactive chemical groups present on the FND-surfaces. The objective of this chapter was to develop a relatively simple and stable, yet versatile method for biofunctionalizing FNDs. Various stages of biofunctionalization including, the design, chemistry, purification, characterization and application of the FND-based complexes are discussed hereafter.

7.2 Existing Methods for FND-Biofunctionalization

The existing methods of FND-biofunctionalization can be broadly classified as (1) adsorption, (2) polymer or micelle encapsulation and (3) covalent biofunctionalization, and are shown in Figure 7.2 and detailed in following subsections.

7.2.1 Adsorption

Adsorption is based on the adhesion of atoms, ions and biomolecules to a surface. It is facilitated by two classes of interactions between the surface and the molecules - physisorption and chemisorption. Here, we only consider physisorption as adsorption, which is governed primarily by van der Waal's forces, hydrophilic or electrostatic forces. Adsorption is a straight-forward method for attaching biomolecules to FNDs as these interactions are spontaneous, that is, they do not require specialized conditions and chemical-catalysts. For example, in solutions at neutral pH values, FNDs that possess a negative surface charge (due to abundance of acidic surface groups) can electrostatically attract positively charged (amine group-rich) proteins, resulting in rather strong binding. This approach of biofunctionalization was initially reported by Huang and Chang [120], where poly-Lysine molecules were adsorbed onto the nanodiamond[†] surface.

[†]Note that Huang and Chang [120] and others used non-fluorescent nanodiamonds to demonstrate adsorption-based biofunctionalization

(a) Adsorption

(b) Polymer or micelle capping
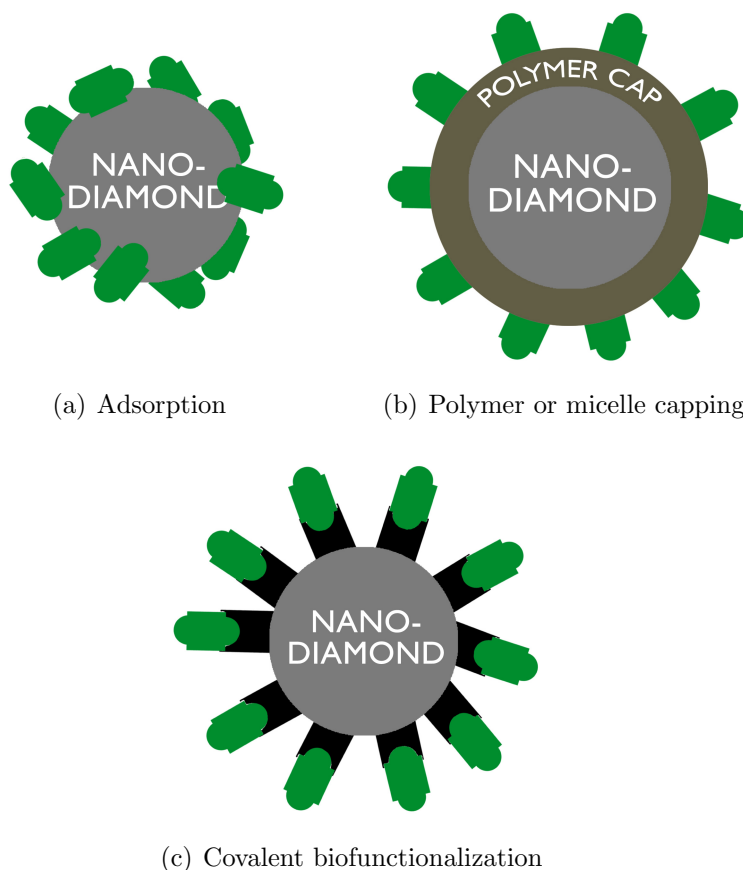

(c) Covalent biofunctionalization

Figure 7.2: Classification of (fluorescent) nanodiamond biofunctionalization strategies. Green shape represents a biomolecule, the black linkers represent covalent bonds in (c).

However, at a later stage, the adsorbed poly-Lysine molecular-coat was used as a platform for the chemisorption of dye molecules. The schematic diagram of this method is shown in Figure 7.3.

Perevedentseva et al.[194] and Chao et al.[50] studied the interactions of the enzyme lysozyme with *Escherichia coli* (*E. coli*) using nanodiamonds as fluorescent probes. This was carried out using lysozyme molecules adsorbed on the nanodiamonds. Instead of using color-center fluorescence, they used the intrinsic Raman scattering property of diamonds as the source of optical contrast to highlight these molecules.

Liu et al.[155] used FND as a fluorescent probe to evaluate the interaction of α-bungarotoxin with acetylcholine receptors. Huang et al.[119] used nanodiamonds adsorbed with doxorubicin hydrochloride, an anti-cancer drug used in chemotherapy, to study cell-apoptosis and its use as a chemotherapeutic delivery tool. They also

Figure 7.3: Physisorption of poly-Lysine on nanodiamond surface, followed by chemisorption of dye or Yeast cytochrome C molecules. Reprinted with permission from Huang and Chang. Adsorption and immobilization of cytochrome c on nanodiamonds. Langmuir, 20(14):58795884, 2004. Copyright (2004) American Chemical Society[120].
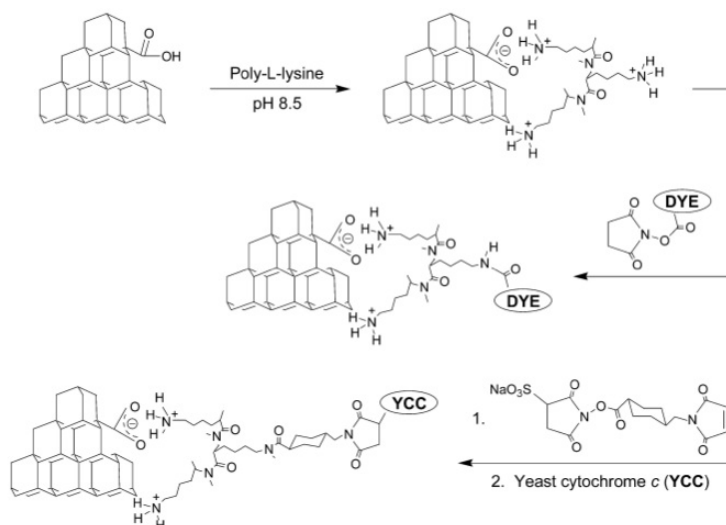
demonstrated that the efficiency of adsorption was enhanced by increasing the salinity of the nanodiamond-protein solution. The pH-dependence of adsorption of insulin molecules was carried by Shimkunas et al.[232], for the demonstration of nanodiamond-based molecular delivery vehicles. In an different application, the adsorption property of the NDs was utilized for high-efficiency purification of the proteins - luciferase and apobelin - after being extracted from bacteria[32]. Despite these efforts, nanodiamond/FND biofunctionalization via adsorption is mostly unreliable due to the possibility of dissociation of adsorbed molecules under physiological conditions, where the solvent properties like pH and temperature may vary, resulting in changes to physisorption.

7.2.2   Polymer/Micelle Encapsulation

A critical criterion for choosing a method of biofunctionalization is the colloidal stability in buffer solutions. We observed that while the pristine FNDs remained stable in water, they formed agglomerates upon addition of, as low as, 10 mM of salt - a basic constituent of physiological solutions (see table 7.1). An FND aqueous-colloid is stabilized by the electrostatic repulsion between individual FND-particles due to their surface charge[81,281]. However, in the presence of salt, the surface charges are screened by the salt-ions, resulting in reduced repulsion, causing aggregation.

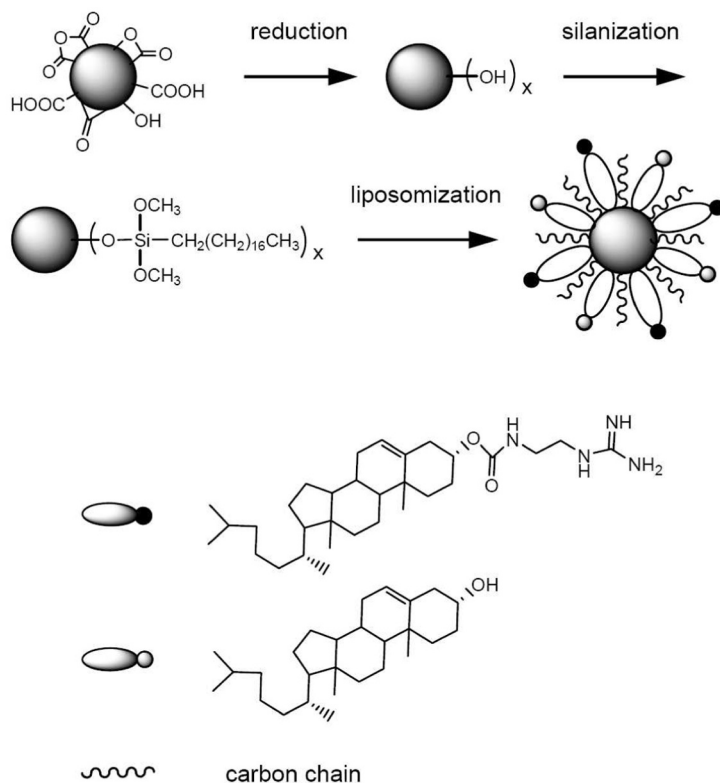A preventive measure to reduce aggregation under salt-containing physiological

Figure 7.4: Modification of N-V center-containing FNDs by reduction, silanization, and lipid encapsulation reactions. Reproduced with permission from Hui et al.[122].

conditions is to increase the surface hydrophilicity and introduce spatial hindrance[142]. These surface characteristics can be achieved by capping the FND using amphiphilic molecules or polymers. Smith et al.[235] demonstrated the transfection and optical imaging of nanodiamonds inside cells, where highly scattering particles exhibited good contrast. They used lipofectamine and lipid-rich solutions to encapsulate nanodiamonds in order to achieve colloidal stability in physiological solutions. A similar approach was utilized by Hui et al.[122], where the diffusion dynamics of the lipid-encapsulated, N-V center containing FNDs were studied using two-photon fluorescence correlation spectroscopy (see Figure 7.4). They demonstrated that the lipid encapsulation had little effect on the fluorescence properties of FNDs, and also enhanced the mobility of the particles in the cytoplasm of HeLa cells.

The amphiphillic coatings that improve colloidal stability of FNDs can be utilized as platforms for further biofunctionalization. However, these methods introduce additional steps making the biofunctionalization protocol increasingly complex, and also lead to larger particle sizes. Besides, other molecules in physiological solutions can
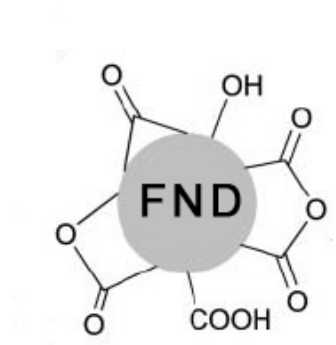
Figure 7.5: The chemical groups available on the surface of an acid-cleaned FND surface.

replace the FND-bound amphiphilic polymers, because this method relies on spontaneous hydrophobic interactions. Therefore, these complexes are generally unstable, unless additional steps are carried out to permanently affix the amphiphillic molecules on the surface using stable chemical bonds.

7.2.3 Covalent Biofunctionalization

Covalent biofunctionalization is based on the attachment of biomolecules to FND surface, by the formation of stable covalent bond(s) between a chemical group on the FND-surface and a biomolecule-terminal. Covalent bonds are formed by atomic pairing wherein one or more electrons are shared among the participating atoms. These bonds are usually very stable and facilitate the formation of a robust nanodiamond-biomolecular complex, unlike those formed by adsorption or amphiphillic molecular encapsulation. Some of the reactive chemical groups available on acid-cleaned FND surfaces that are suitable for covalent biofunctionalization include carboxyl, ketone, aldehyde and anhydride groups, and are presented in Figure 7.5[15].

One of the initial work that promoted research on the covalent functionalization of biomolecules on diamond surfaces was carried out by Ushizawa et al.[259], who immobilized DNA on the bulk diamond surface. Their approach was to introduce chloro-carbonyl groups on the diamond surface by acid cleaning followed by treatment with
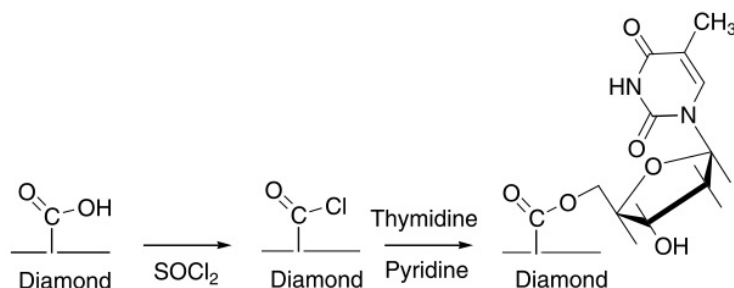
Figure 7.6: Attachment of thymidine on bulk diamond surface using chlorocarbonyl groups, generated by treatment with acid and thionyl chloride. The thymidine nucleotide acted as a surface anchor for further attachment of DNA. Reproduced from Ushizawa et al.[259] with permission from Elsevier.
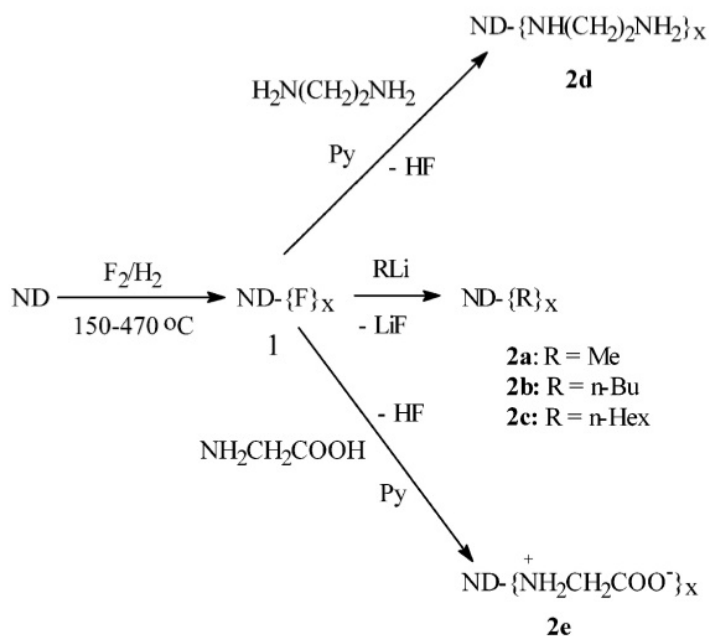
Figure 7.7: Fluorination of nanodiamonds followed by attachment of alkyl or amino acid group. Nanodiamonds are abbreviated as ND. Reprinted with permission from Liu et al., Functionalization of nanoscale diamond powder: Fluoro-, alkyl-, amino-, and amino acid-nanodiamond derivatives, Chemistry of Materials, 16(20):39243930, 2004 Liu et al.[157]. Copyright (2004) American Chemical Society.

thionyl chloride. Afterwards, an anchor point made of thymidine nucleotide was covalently attached to the chlorocarbonyl group, which facilitated further attachment of DNA. These steps are shown in Figure 7.6.

Another method of anchoring biomolecules on nanodiamond surface was demonstrated by Liu et al.[157]. Instead of generating chlorocarbonyl groups, the nanodiamond-surface was subject to fluorination using a highly acidic reagent, HF. The fluorinated surface was reacted in a second step to form nanodiamonds functionalized with alkyl groups (methyl or butyl) or amino acids. A schematic of the chemical reaction is presented in Figure 7.7.

Kruger et al.[141], in 2006, prepared amino acid functionalized nanodiamonds using a

very different approach. They questioned the homogeneity of surface chemical groups on the nanodiamonds cleaned using oxidizing acids, because oxidization procedure did not affect hydroxyl groups. Therefore, they used a reduction reaction to convert carbonyl groups to hydroxy groups, in an attempt to achieve a homogenized surface. Later, silanization was carried out to facilitate the attachment of numerous types of biomolecules, although the yield of this reaction was not very well characterized, after all.

Hens et al.[105] carried out a combination of several methods to produce amine group (-NH$_2$) terminated nanodiamonds. Nanodiamonds were first processed to re-dress the surface with hydroxyl groups[141]. Using three further steps that involved treating the nanodiamonds with tosyl chloride, potassium cyanide and lithium aluminum hydride, aminated nanodiamonds were prepared. These particles were cleaned with sodium hydroxide and linked to reactive biomolecules and dyes.

Dahoumane et al.[60] reported on the functionalization by a different approach using electroless grafting of $^+$N$_2$-C$_6$H$_4$-CH(CH$_3$)-Br (bromoethyl benzene diazonium salt) onto the FND surface, by mere sonication of the two components for a certain period of time. Later, carboxyl groups were introduced in the grafted bromoethyl benzene diazonium molecules by a few chemical reactions. Using the carboxyl group, a protein, bovine serum albumin (BSA), was anchored onto the FND via a EDC/NHS [1-ethyl-3(3-dimethylaminopropyl) carbodiimide/N-hydroxysuccinimide]-assisted chemical reaction.

Purtov et al.[202] compared the performances of adsorption and covalent methods of FND-biofunctionalization. The covalent biofunctionalization with BSA and immunoglobulin was carried out using benzoquinone molecules as the linker, as shown in Figure 7.8. The complexes prepared by the covalent biofunctionalization method demonstrated sustainability and high colloidal stability in blood-serum.

Several more demonstrations of covalent biofunctionalization of biomolecules to nanodiamonds has since been reported in the literature. Most of them use one of the above mentioned techniques or variants. For example, Takimoto et al.[250] used a combination of covalent functionalization and amphiphilic molecules to attach dye
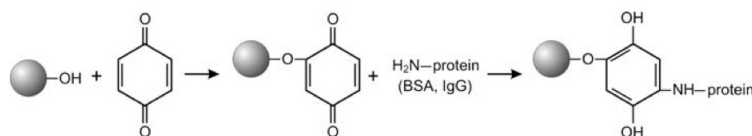
Figure 7.8: Immobilization of of protein on benzoquinone activated nanodiamond. Proteins could be immunoglobulin or BSA. Reproduced from Purtov et al.[202] with permission under Creative Commons license agreement.

molecules on the surface of nanodiamonds. The reaction schematic and the illustration of this stable, encapsulated nanodiamond is shown in Figures 7.9(a) and 7.9(b).

Despite the progress in the field of nanodiamond biofunctionalization, many of these reported techniques are specialized for a particular type of molecule to be grafted. Moreover, they are seldom easy, versatile and stable at the same time. We addressed this issue by designing a simple, yet, robust and versatile method. This method of FND-functionalization was based on a pair of affinity molecules. Although the biofunctionalization of quantum dots and magnetic nanoparticles[179,278] have been demonstrated using this method, FND-biofunctionalization presented several challenges that will be discussed below.
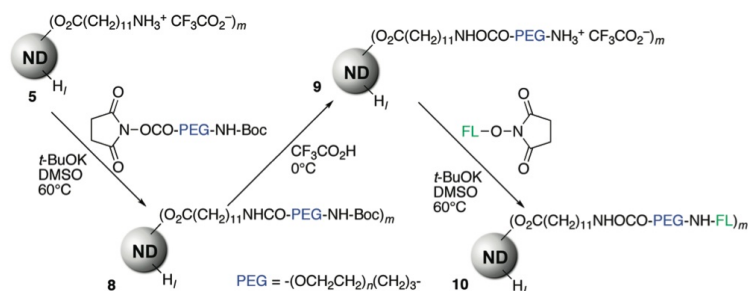
7.3 Biofunctionalization Strategy

### 7.3.1 Barstar:Barnase - the Molecular *Lego* Pair

Barstar (Bs) and barnase (Bn) are eminent examples of proteins that constitute an affinity molecular pair. In the nature, Bn is a ribonuclease[†] found in *Bacillus amyloliquefaciens*[101], whose intracellular activity is suppressed by Bs, by forming a tight complex. This complex, abbreviated as Bs:Bn[‡], has a dissociation constant (K_D) of 10 fM[65]. The highly affine and specific pairing can be visualized as a magnetic *lego* system. The 3D molecular structure and a lego representation of the Bs:Bn complex

---

[†]Nucleases are enzymes that degrade nucleic acids. Specifically, a ribonuclease degrades ribonucleic acids (RNA)

[‡]':' in Bs:Bn denotes the complex formed by the natural intermolecular binding affinity between barstar and barnase, primarily based on hydrogen bonding and electrostatic interaction

(a) Reaction scheme for producing buffer nanodiamond-dye complexes
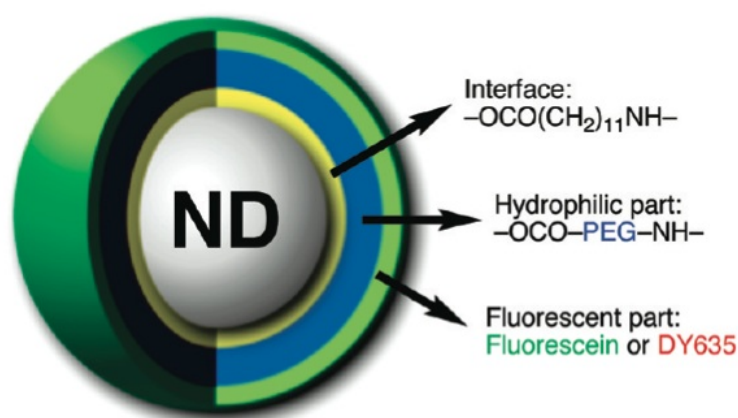
(b) Illustration of 'capped' nanodiamond (ND) functionalized with dyes

Figure 7.9: The reaction and structure of a dye-capped nanodiamond - a combined biofunctionalization strategy using micelle encapsulation and covalent biofunctionalization. Reprinted with permission from Takimoto et al., Preparation of Fluorescent Diamond Nanoparticles Stably Dispersed under a Physiological Environment through Multistep Organic Transformations. Chemistry of Materials, 22(11):34623471, 2010[250]. Copyright (2010) American Chemical Society.

are presented in Figure 7.10.

Bs and Bn are relatively small (10.2 and 12.4 kDa, respectively) proteins that are water-soluble and stable in both paired and unpaired forms[65]. One of the peculiarities of these proteins is that their tertiary structures are stabilized only by hydrogen bonds, whereas most other proteins rely on specific disulfide bonds. The implications of the absence of disulphide bonds manifests as their tolerance to harsh temperature (up to 50 ^{o}C) and pH (2 - 12) conditions[133]. Deployment of a mutant form of Bs (C40A, C82A) also facilitates the recombinant design of multivalent fusion proteins[65], where uncontrollable disulfide bonds can often be inconvenient. These qualities enable the
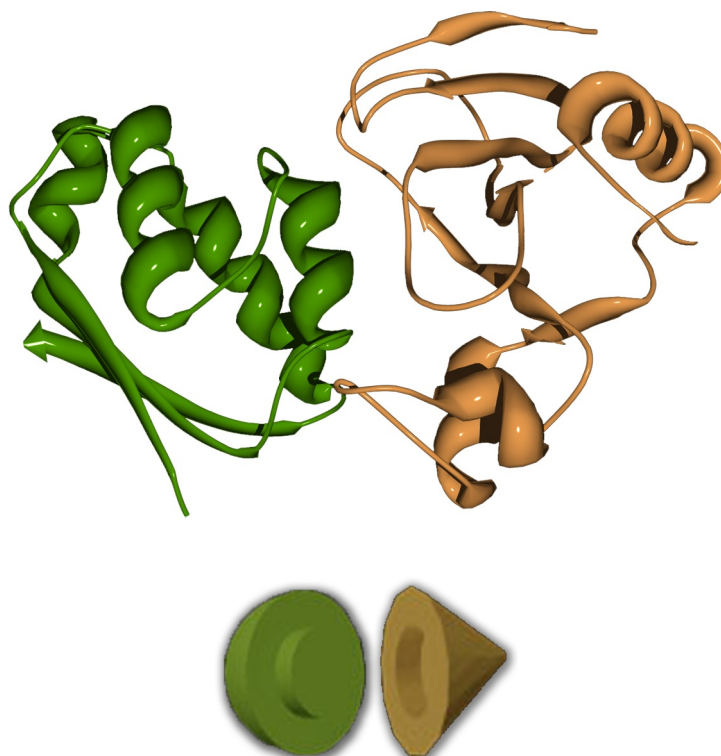
Figure 7.10: The 3D molecular structures (top) and the respective block models (bottom) of the barstar (Bs) and barnase (Bn) approaching each other to form a complex. Bs and Bn are colored green and brown, respectively. The 3D molecular structures were rendered using the Swiss PDB viewer using the X-ray diffraction-based data published by Urakubo et al.[258]. Courtesy RSC Protein data bank.

use of Bs:Bn lego pair in applications, where it constitutes as a strong, modular base for design of molecular and nanoparticular complexes of exquisite variety and complexity, as will be addressed in the following sections.

7.3.2   Design and Strategy

Using the versatile Bs:Bn lego pair, it is conceivable to functionalize FNDs with numerous types of proteins. For example, to produce FNDs functionalized with Enhanced Green Fluorescent Protein (EGFP), two lego counterparts FND-Bs[†] and Bn-EGFP can be synthesized separately. Later, mixing these two counterparts would produce the complex FND-Bs:Bn-EGFP. This idea is graphically portrayed in Figure 7.11. The

---

[†]'-'symbol denotes covalent bonds between the groups

covalent links in the FND-Bs and Bn-EGFP along with the high affinity Bs:Bn link ensures that the final complex is stable. FND-Bs, can be prepared by a covalent functionalization of -COOH groups on the FND-surface and -NH$_2$ terminals of a Bs molecule. The counter sub-unit module, Bn-EGFP, can be produced by recombinant methods, which is a robust and reproducible. Replacement of the EGFP with other proteins (e. g. mRFP or antibody) or nanoparticles (e. g. gold nanoparticles) can yield a variety of complexes that are conceptualized in Figure 7.12. These complexes demonstrate the versatility of Bs:Bn-based biofunctionalization platform.

The steps required for FND-biofunctionalization, using the Bs:Bn lego pairing, are enlisted below:

1. Characterization of the FND

2. Synthesis and characterization of FND-Bs

3. Verification of the covalent bonding in FND-Bs

4. Biofunctionalization of FND-Bs with Bn-containing counterparts, and

5. Characterization of the final complexes.

7.3.3   Characterization of FNDs

An aqueous colloid containing 0.1% w.v^{-1} of 140-nm, N-V center-containing FNDs was purchased from Academia Sinica, Taiwan. The acid-treated FND-surfaces harbored -COOH groups enabling easy biofunctionalization. The size, colloidal stability, concentration, zeta-potential and fluorescence properties of the FND were characterized as described in the following subsections.

7.3.3.1   FND Size and Colloidal Stability

The hydrodynamic diameter of the FND, suspended in water, was assumed to be a representative of the *true* size of the FND. The size distribution measured by using a
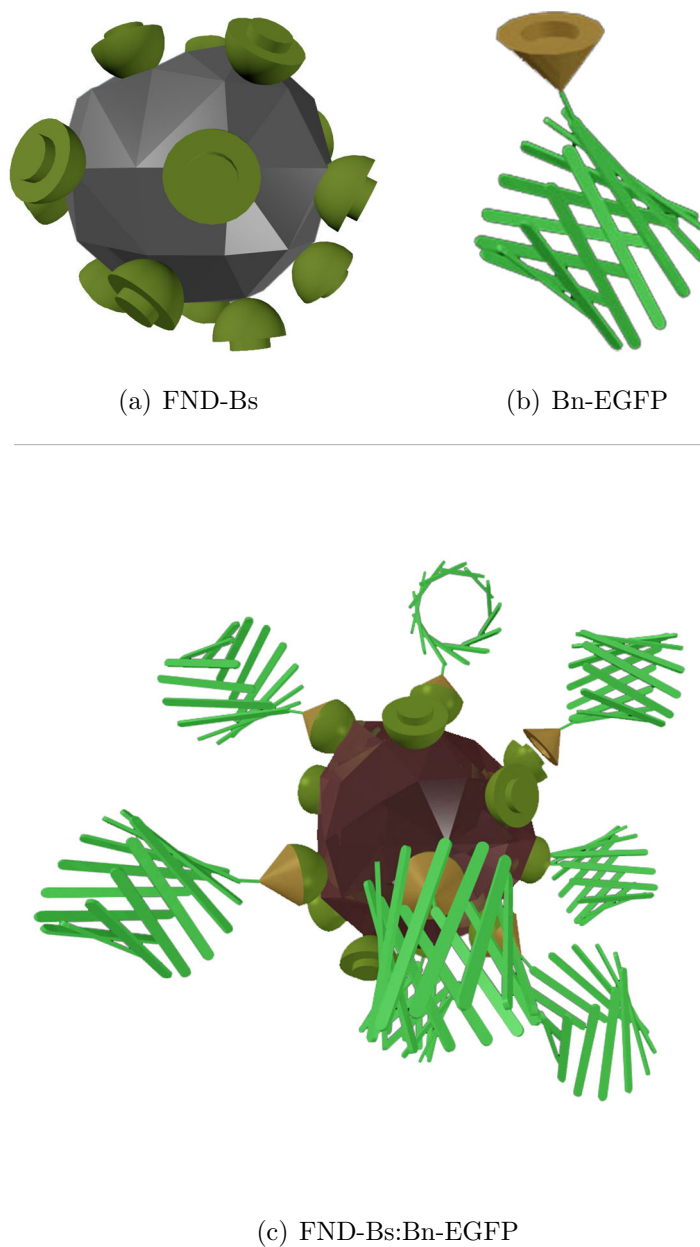
(a) FND-Bs

(b) Bn-EGFP

(c) FND-Bs:Bn-EGFP

Figure 7.11: Biofunctionalization of FND with EGFP (enhanced green fluorescent protein) using the Bs:Bn linker. The multifaceted crystal, brown cones, green hemispheres and green barrel structure represents FND, Bn, Bs and EGFP, respectively.
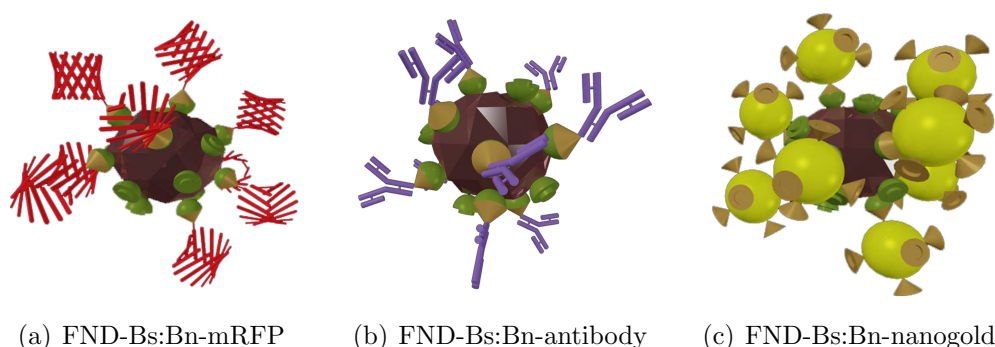
(a) FND-Bs:Bn-mRFP   (b) FND-Bs:Bn-antibody   (c) FND-Bs:Bn-nanogold

Figure 7.12: Design of the other possible complexes of FND based on the barstar and barnase modular approach.

dynamic light scattering method (see Section 4.1.3 for detailed methodology) is presented in Figure 7.13. The measured size was found to be smaller ($\approx$100 nm) than that provided in the supplier data sheet.

In order to investigate the colloidal stability in salt-containing solutions, FND was centrifuged and re-suspended in three model buffers of varying pH and salinity: PBS (pH 7.2), MES buffer[†] (pH 6.0) and PB20[‡] (pH 7.2). The FND size-distributions, presented in Figure 7.13, revealed the increase in the hydrodynamic diameter (200 nm - 1 μm), which was interpreted as agglomeration. Therefore, we concluded that the FND was not colloidally stable in salt-containing solutions. The observed agglomeration was likely due to the salt-induced charge screening, resulting in reduced coloumb repulsion between the individual particles.

7.3.3.2   FND Concentration

It was necessary to determine the molar concentration of FNDs in the colloid to design the biofunctionalization procedure. Using the known values of size and mass/volume concentration (0.1% w.v^{-1}), the molar concentration of the 140-nm FND in the as-received colloidal sample was calculated as follows:

[†]MES buffer contains 50 mM 2-(N-morpholino)ethanesulfonic acid and 2 mM EDTA (ethylene diamine tetraacetic acid)

[‡]Phosphate buffer containing 20 mM NaCl, in contrast to PBS which contains 155 mM NaCl
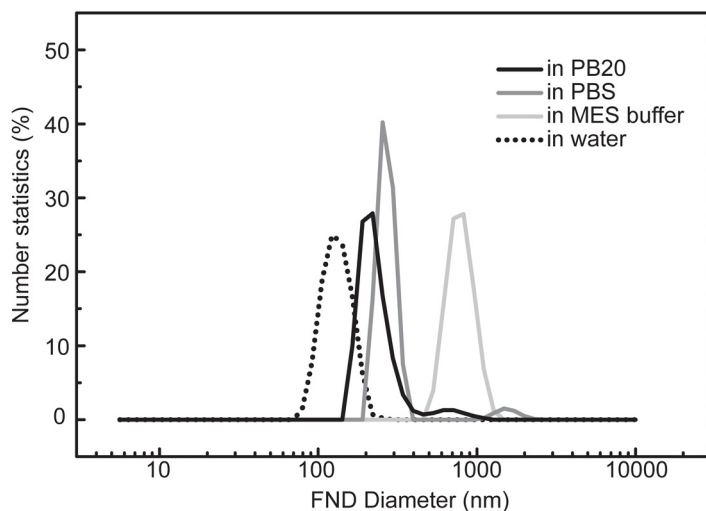
Figure 7.13: Size distribution of 140 nm fluorescent nanodiamonds in four different solvents, as measured with zetasizer. FNDs aggregate in the presence of salt.

$$\text{Volume of one 140-nm FND} = \frac{4\pi}{3}\text{r}^3$$
$$= \frac{4\pi}{3}\frac{(140 \times 10^{-9})^3}{8} \text{ m}^3$$
$$= 1.43 \times 10^{-21} \text{ m}^3$$
$$\text{Thus, mass of one 140-nm FND} = \text{Volume} \times 3.53 \times 10^6 \text{ g.m}^{-3}$$
$$= 5.07 \times 10^{-15} \text{ g}$$
$$\text{thus, } 0.1\%\text{w.v}^{-1} \text{ FND in water is equivalent to} = \frac{1}{5.07 \times 10^{-15} \times \text{N}_\text{A}} \text{ M}$$
$$= 32.7 \times 10^{-11} \text{ M} \qquad (7.1)$$

where, N_A is the Avogadro's constant.

7.3.3.3   FND Surface Charge and Fluorescence

The chemical groups present on FND surface contributed to the net surface charge. Generally, static charges associated with surfaces are characterized in terms of zeta-potentials (see section 4.1.4 for details). The zeta-potential of 140-nm FNDs, suspended in PB20 (pH 7.2), was measured to be $\approx$ -47 mV, using a Zetasizer. The negative surface charge at the neutral pH value (pH 7) was an indication of the carboxyl groups
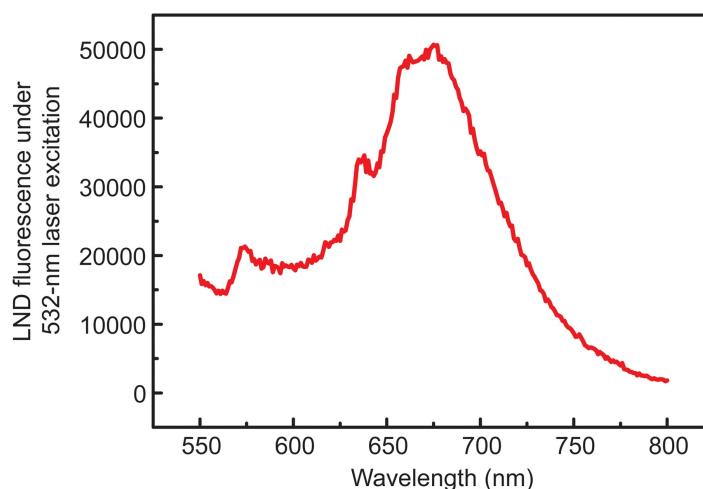
Figure 7.14: The fluorescence emission spectra of N-V center-containing, 140-nm FND colloid suspended in water, under 532-nm laser excitation.

present on the FND surface.

The optical properties of the N-V center-containing FNDs were characterized by acquiring their fluorescence spectra. Figure 7.14 shows the fluorescence emission spectra of the FND, measured by using a fluorimeter with a laser excitation at 532 nm (see Section 4.1.2 for detailed methodology).

7.4 Synthesis of FND-Bs

Using the Bs:Bn molecular lego pair, two variants of the FND-based molecular complexes were possible: FND-Bs:Bn-X and FND-Bn:Bs-X, where X is the functional biomolecule of interest. However, the latter complex, which required the synthesis of FND-Bn lego counterpart, was not preferred since the electrostatic adsorption between the positively charged Bn (pI = 8.9) and the negatively charged FND (zeta-potential $\approx$ -47 mV), competing with covalent bonds was anticipated to yield unstable complexes. The FND-Bs, on the other hand, was expected to be stabilized only by covalent bonds, because of the negative charges of both Bs (pI = 4.6) and FND inhibiting the physisorption pathway.

Considering the manufacturer-specified prevalence of -COOH surface groups on the as-received FND sample, a covalent reaction that links the -COOH group to the -NH$_2$ group in the Bs molecule was designed[229], yielding a stable FND-Bs complex. This

covalent reaction required pre-activation of the -COOH group, which was performed using the EDC[†] and sulfo-NHS[‡]-based reaction. Addition of the activated -COOH group-containing FND to the -NH$_2$ group-containing Bs resulted in the spontaneous formation of FND-Bs.

The large surface area of FND-particles ensured several Bs-molecules to be accommodated on a single FND-surface. Geometric calculations revealed that one 140-nm FND could accommodate approximately 6000 molecules of Bs in a square packing geometry. Therefore, to ensure the complete functionalization of 300 μL stock solution containing 0.1% w.v^{-1} of 140-nm FND, 200 μL of solution containing 2.5-mg.mL^{-1} Bs was determined to be sufficient. Concentration-based calculations revealed that in order to activate 300 μL of 0.1% w.v^{-1}FND stock solution, 2.3 μL of 10 mg.mL^{-1} EDC and 50 μL of 10 mg.mL^{-1} sulfo-NHS was required. Based on these parameters, the following functionalization procedure was formulated and carried out:

1. Centrifuge 300μL of the purchased FND colloid at 4300 ×g for 3 min

2. Re-suspend the FND-pellet in water, adjusted to a pH of 4.5 (by addition of HCl)
   Low pH values reportedly increased the efficiency of the activation of -COOH groups[229]

3. Under sustained bath-sonication, add 2.3 μL of 10-mg.mL^{-1} EDC and 50 μL of 10-mg.mL^{-1} sulfo-NHS
   Sonication was necessary to avoid FND aggregation during the activation procedure. Increasing the concentrations of EDC and sulfo-NHS by 10-fold resulted in the formation of visible aggregates in the solution

4. Continue the reaction under sonication for 15 min

5. Centrifuge the activated FND at 4300 ×g for 3 min, re-suspend in 300 μL water and place in a bath sonicator

---

[†]1-Ethyl-3-[3-dimethylaminopropyl]carbodiimide hydrochloride
[‡]N-hydroxysulfosuccinimide

6. Prepare 200 μL of 2.5 mg.mL^{-1} Bs solution in PB20 and place in a bath sonicator

7. Add the activated FND solution into the Bs solution in 10 μL drops
   Slow addition prevented FND agglomeration caused by increase in salt concentration. It also ensured that FNDs were immediately coated with Bs-molecules, preventing agglomeration

8. Continue the covalent binding reaction for 2 hr

9. Centrifuge the product 'FND-Bs' at 4300 $\times$g for 3 min and re-suspend the pellet in 500μL of PB20

7.4.1   Characterization of FND-Bs

The covalent biofunctionalization reaction between FND and Bs was carried out according to the procedure detailed above. The resultant FND-Bs solution was characterized and compared with the pristine FNDs in terms of size, colloidal stability and zeta-potential, aiming to confirm the binding. These results are summarized in Table 7.1.

Colloidal stability in the salt-containing PB20 was an immediate observation followed by the biofunctionalization. FND-Bs remained stable when suspended at a concentration as high as 0.1% w.v^{-1}. In contrast, the pristine FND formed aggregates in PB20 at concentrations >0.001% w.v^{-1}. The surface-bound Bs molecules most likely increased the FND-surface hydrophilicity and spatial stability. In addition to the improvement in the colloidal stability, a notable positive increase in the zeta-potential was also observed. The zeta-potential of FND-Bs was found to be -32 mV, in comparison to that of -47 mV of the pristine FND. That is, the surface-bound Bs-molecular layer resulted in screening of the FND-surface charge. These results provided confirmation on the existence of the Bs-molecular layer on the FND-surface. However, the nature of the binding between FND and Bs required further verification.

Table 7.1: Characterization of FND-based complexes at various stages of reaction, as measured using a Zetasizer.

Sample	Reaction status	Solvent; Concentration (w.v⁻¹)	Diameter (nm)	Stable?	Zetapotential (mV)
	Pristine	Water; 0.1%	120	✓	-40
	Pristine	PBS; 0.1%	1500 [a]	✗	-
FND	Pristine	MES buffer; 0.1%	800	✗	-
	Pristine	PB20; 0.1%	220	✗	-47
	Pristine	PB20; 0.001%	120	✓	-46
	EDC/sulfo-NHS activated	PB20; 0.001%	160	✓	-43
	Reaction time = 30 min	PB20; ≈0.1%	150	✓	-35
	Reaction time = 60 min	PB20; ≈0.1%	140	✓	-32
FND-Bs	Reaction time = 90 min	PB20; ≈0.1%	150	✓	-39
	Reaction time = 120 min	PB20; ≈0.1%	150	✓	-30
	Final product	PB20; ≈0.1%	160	✓	-32
FND-Bs:Bn	Final product	PB20; ≈0.1%	130	✓	-20
FND-Bs:Bn-EGFP	Final product	PB20; unknown	150	✓	-18
FND+Bs [b]	Final product	PB20; ≈0.1%	130	✓	-43

[a] Signal quality was unreliable because of aggregation
[b] '+' in FND+Bs denotes non-covalent (physisorption) of Bs molecules to FND surface

7.4.2   Proof of the Covalent Biofunctionalization

One of the straightforward methods to test the covalent nature of the bonding in FND-Bs was to carry out a similar reaction without the catalysts that activated the -COOH groups. Therefore, a dummy reaction was performed, where the FND and Bs were treated as before, but in the absence of EDC and sulfo-NHS. This reaction resulted in the production of FND+Bs complexes, where Bs molecules were expected to be merely physisorbed on the FND-surface. Comparisons of physiochemical properties of FND-Bs and FND+Bs was expected to reveal the nature of the bonding between the FND and Bs in these two complexes.

To our surprise, it was observed that FND+Bs was also stable in PB20 at colloidal concentration of 0.1% w.v^{-1} (see table 7.1). This suggested that the adsorption of Bs-molecules rendered FNDs stable in, salty solutions, which would otherwise undergo aggregation. Therefore, the property of colloidal stability was unable to reveal differences between the nature of bonding in FND-Bs and FND+Bs. It should be noted that both FND-Bs and FND+Bs suffered from aggregation at saline conditions (data not shown). At the same time, zeta-potential measurements provided a definite distinction between the FND-Bs and FND+Bs complexes. The zeta-potential of FND+Bs remained at -43 mV, close to -47 mV of the pristine FND, in comparison to that of the covalently bound FND-Bs (-32 mV).

Further confirmation of the covalent nature of the bonding of the FND-Bs complex was provided by means of the X-ray photoelectron spectroscopy (XPS). XPS is a quantitative technique used to empirically determine the elemental composition of materials, with the probing depth limited to 10 nm from the sample-surface. A sample is irradiated with X-rays of a fixed energy, which is dissipated along two main pathways: for electrons to escape the inner atomic orbitals, and as the kinetic energy of released (scattered) electrons. Therefore, the energy of the inner atomic orbitals is calculated by detecting the kinetic energy of the scattered electrons. The stochiometric chemical composition of the sample can be derived from the energy spectrum, as an elemental signature. The nitrogen signature can be used to determine the presence of Bs, bound

to FND, which otherwise contain negligible quantities of nitrogen. However, in corroboration with the observation of identical colloidal stabilities, it was observed that both the FND+Bs and FND-Bs contained nitrogen-signature, indicating the presence of a Bs-molecular coat. Therefore, additional treatments were required to unveil the differences in the nature of bonding between FND and Bs.

Adsorption of molecules onto the surface has been shown to be dependent on pH[232]. This is because the net electrostatic charge of particles/biomolecules is dependent on the pH. When the pH is fixed at the isoelectric point (pI)[†] of a biomolecule or a nanoparticle, either one of them becomes electrically neutral. Therefore, adjusting the pH to the pI value of Bs (4.6)[239] was expected to minimize the adsorption of the Bs-molecules on the FND surfaces. The FND-Bs and FND+Bs complexes were rigorously washed using acidic and basic solvents several times to remove the adsorbed Bs-molecules, prior to XPS analysis. The following steps were carried out to prepare the washed FND-Bs and FND+Bs samples before the XPS analysis:

1. FND-Bs and FND+Bs solutions in PB20 were centrifuged at 4300 $\times$ g for 3 min and re-suspended in PB20 pH 4[‡]

   This procedure made both FND and Bs electrically neutral

2. The resulting solutions were centrifuged at 4300 $\times$g for 3 min and re-suspended in PB20 pH 7.2

3. The solutions were centrifuged and re-suspended in PB20 pH 10[§]

   This step caused an increase of the negative charges of FND and Bs, resulting in a stronger electrostatic repulsion

4. The solutions were centrifuged and re-suspended in PB20 pH 7 (twice).

The XPS spectra obtained from these two samples are shown in Figure 7.15. The spectra of FND-Bs contained a nitrogen peak, indicating the presence of the barstar molecules on the surface. In case of the FND+Bs, the rigorous wash removed the

---

[†]Isoelectric point is the pH at which the molecule/particle is neutrally charged
[‡]PB20 of pH 4 was prepared by adding dilute HCl to PB20
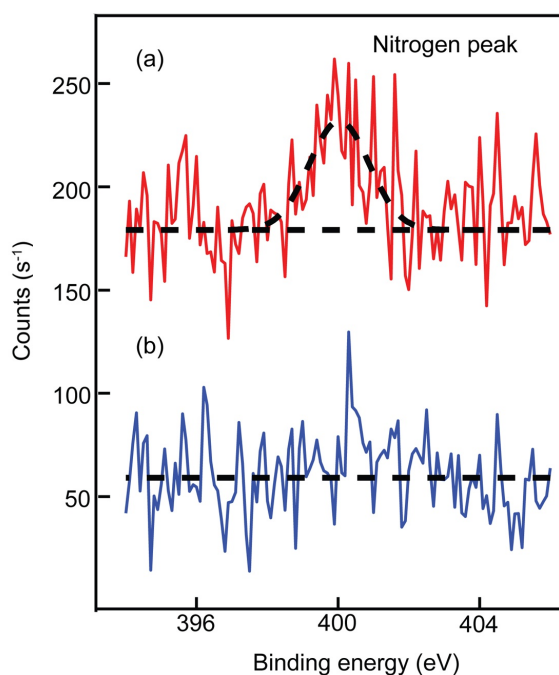[§]PB20 of pH 10 was prepared by adding dilute NaOH to PB20

Figure 7.15: Comparison of the XPS signals from nitrogen traces (present in the protein attached to the FND) in FND-Bs (a) and FND+Bs (b). Dashed lines are to aid the visual comparison.

adsorbed Bs-molecules from the surface, resulting in the lack of a nitrogen signal. These observations confirmed that the FND-Bs complex was of covalent nature and was able to withstand multiple washing steps.

Thus, the first stage of the FND-biofunctionalization was proven to be successful, yielding colloidally stable FND-Bs complexes that were resistant to multiple washing steps. Linking Bn-containing counterparts to the FND-Bs, using the Bs:Bn lego-pairing interaction is discussed in the following sections.

7.5   Bs:Bn-based FND complexes

In order to demonstrate the simplicity, robustness and versatility of the molecular lego-based FND-biofunctionalization strategy, two complexes were designed. Two Bn-based counterparts were synthesized for binding to FND-Bs:

1. Complex of Bn and EGFP, hereafter represented as Bn-EGFP, was produced by expressing the corresponding recombinant plasmid in bacteria[239]

2. Complex of Bn and nanogold, hereafter represented as Bn-nanogold, was produced by using a heterobifunctional poly-ethyleneglycol linker. One end of this linker contained a gold-binding, -SH, group and the other end was coupled to a Bn-molecule[239]
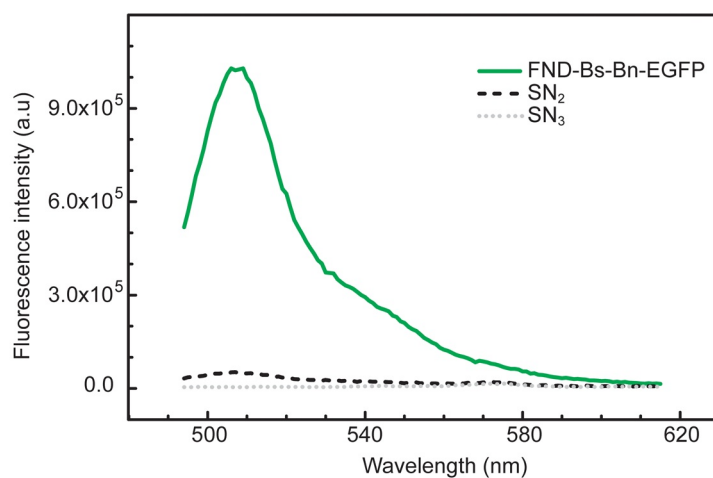
7.5.1   FND-Bs:Bn-EGFP

The complex – FND-Bs:Bn-EGFP – was synthesized using the counterparts FND-Bs and Bn-EGFP. Solutions containing the FND-Bs and Bn-EGFP were mixed and incubated for 30 min at room temperature. Excess of the unreacted Bn-EGFP was removed by centrifugation (14,000 × g) based cleaning, three times. Each time the FND-Bs:Bn-EGFP pellet was resuspended in fresh PB20. The three corresponding supernatants that presumably contained the un-reacted Bn-EGFP were collected and consecutively labeled as SN_1, SN_2 and SN_3.

The final FND-Bs:Bn-EGFP suspension was thoroughly characterized by measuring its hydrodynamic size, colloidal stability, zeta-potential, fluorescence and biocompatibility. The first three characteristics are collated in Table 7.1. Similar to FND-Bs, the FND-Bs:Bn-EGFP was also found to be stable in PB20 at relatively high concentrations ($\approx 0.1\%$ w.v^{-1}). The zeta-potential of the FND-Bs:Bn-EGFP was more positive than FND-Bs, FND+Bs or FND, confirming a stable link between the FND and EGFP moieties.

A direct confirmation of the biofunctionalization of FND and EGFP was obtained by measuring the fluorescence spectra of the FND-Bs:Bn-EGFP solution and the supernatants collected at the completion of the three cleaning steps. Two fluorescence emission spectra, acquired at wavelengths corresponding to those of the EGFP [Figure 7.16(a)] and FND [Figure 7.16(b)], provided confirmations on their presence in the solution. The observation of little EGFP signal in the supernatant solutions SN_2 and SN_3 suggested that the EGFP was bound to FND.

In order to obtain further confirmation of the bound nature of FND and EGFP, the synthesized FND-Bs:Bn-EGFP containing solution was deposited on a glass substrate followed by imaging using a fluorescence confocal microscope (see Section 4.4 for details

(a) Fluorescence emission spectrum under 480-nm excitation
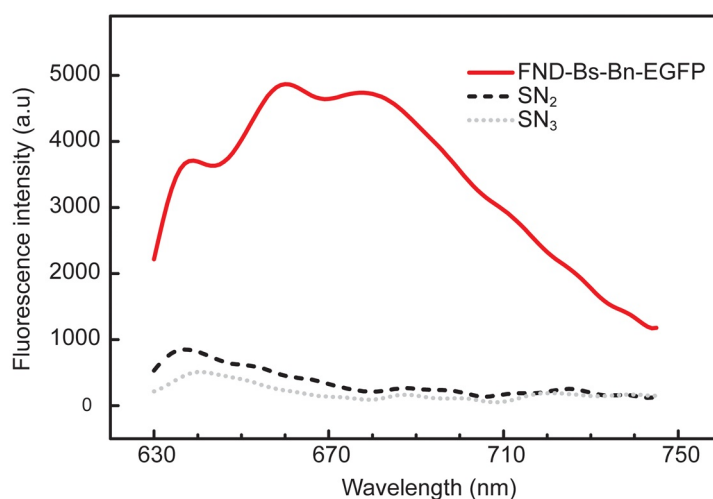
(b) Fluorescence emission spectrum under 532-nm excitation

Figure 7.16: The fluorescence emission spectra of FND-Bs:Bn-EGFP and the supernatants SN_2 and SN_3 obtained during the washing procedure, using two excitation bands at wavelengths of 480 nm and 532 nm - falling into the optical absorption bands of EGFP and FND, respectively.

on microscopy techniques). A 488-nm laser was used to excite both EGFP and FND and a set of 30 images were acquired with fluorescence emission wavelengths scanning from ≈ 500 nm to 800 nm. The fluorescence from the EGFP and FND were the brightest in the images corresponding to the wavelengths of 513 nm and 674 nm, respectively. In Figure 7.17, they appeared as bright diffraction limited spots and their spatial overlap was a direct confirmation of their bound state. The spectra were

(a)   FND-Bs:Bn-EGFP; 513 nm emission
(b)   FND-Bs:Bn-EGFP; 674 nm emission
(c)   FND-Bs:Bn-EGFP; 513 nm & 674 nm combined
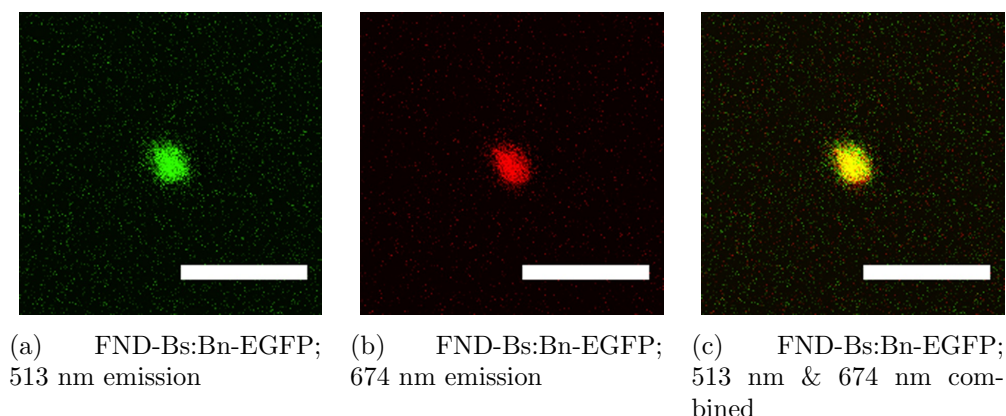
Figure 7.17: Representative fluorescence confocal images of FND-Bs:Bn-EGFP under 488-nm laser excitation in a fluorescence confocal microscope. The EGFP and FND fluorescence are visible at 513 nm and 674 nm, respectively. An overlay of these two images revealed their co-localized behavior suggesting they existed as a single unit. Scale-bar 3 μm.

obtained by plotting the average pixel intensity from the brightest region in the images at each wavelength, and is presented in Figure 7.18. Comparison of these spectra with that of the pristine FND confirmed the contribution of EGFP to the net fluorescence signal and their colocalization.

7.5.1.1   Quantification of the Functionalization Ratio

A simplistic geometry-based calculation presented in Section 7.4 suggested that a 140-nm FND particle can accommodate $\approx$ 6000 molecules of EGFP, on its surface. To verify this calculation, the concentrations of FND and EGFP moieties in the FND-Bs:Bn-EGFP solution were measured using the fluorescence intensity-based analysis. The fluorescence intensities from the FND-Bs:Bn-EGFP solution were measured and compared to a set of intensity calibration curves (shown in Figure 7.19), generated from the tabulated concentrations of FND and EGFP. Note that the EGFP calibration curve was obtained using fluorescein (exhibiting similar fluorescence spectrum to EGFP), accounting for their relative fluorescence throughputs, due to the large uncertainty in the EGFP stock concentration.

The concentrations of FND and EGFP were estimated to be 0.000189% (w.v^{-1}) and 0.826 nM, respectively. Using density-based calculations, the molar concentration of
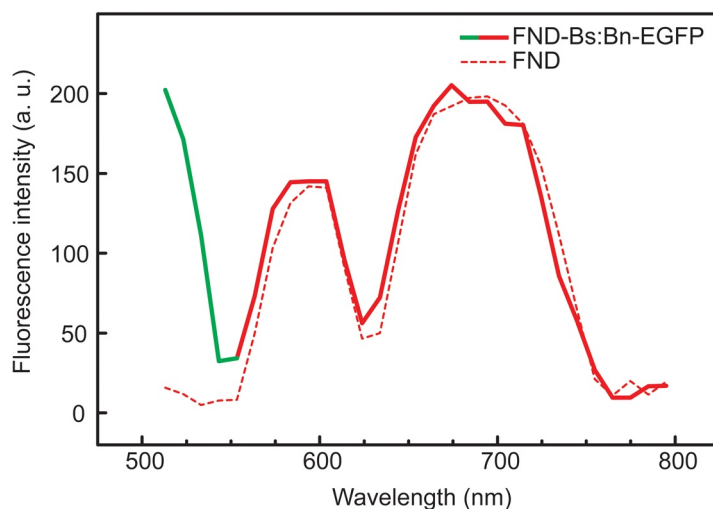
Figure 7.18: Fluorescence emission spectra of FND and FND-Bs:Bn-EGFP under 488 nm excitation. The spectra of FND-Bs:Bn-EGFP was obtained from the bright spot in Figure 7.17. The reduction in the fluorescence intensity at 625 nm is due to the wavelength dependent response of the detection system confocal microscope, which has a dip in the sensitivity at 625 nm to 650 nm. Correction of the spectra gave rise to artefacts, likely to be due to non-reproducibility of the spectral acquisition system in-built in the microscope.

FND was found to be 620 fM. These values suggested that, in average, ≈1300 EGFP molecules were bound to each 140-nm FND, which is considered to be close to the estimate of 6000:1, obtained using the geometric modeling.

7.5.1.2   Cell labeling with FND-Bs:Bn-EGFP

The usefulness of the FND as a probe for labeling applications demanded stability of the biofunctionalized FND-particles at physiological conditions. In order to verify the required stability, the FND-Bs:Bn-EGFP particles were incubated with cells and examined by using the fluorescence confocal imaging. The chinese hamster ovarian (CHO-K1) cells (see Section 4.2), grown on a 4-well imaging slide, were incubated with an FND-Bs:Bn-EGFP solution, prepared in PBS+CM[†], for 1 hr at 37 ^{o}C. Subsequently, the cells were fixed with a 3.7 % paraformaldehyde solution and the slide was sealed for imaging. Figure 7.20(a) presents a micrograph of a representative CHO-K1 cell, where the fluorescence image was overlaid over the corresponding phase contrast image. The

---

[†]PBS with additional 0.1% BSA, 20 mM D-Glucose, 0.9 mM $CaCl_2$ and 0.5 mM $MgCl_2$
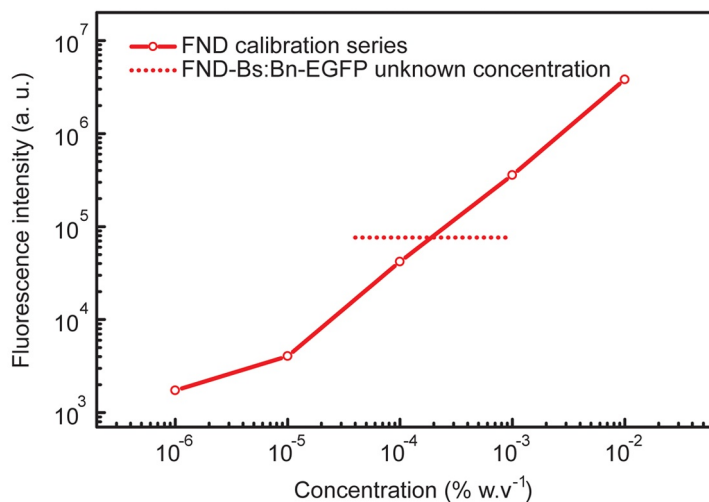
(a) FND fluorescence calibration; FND-Bs:Bn-EGFP emission intensity under 532 nm excitation
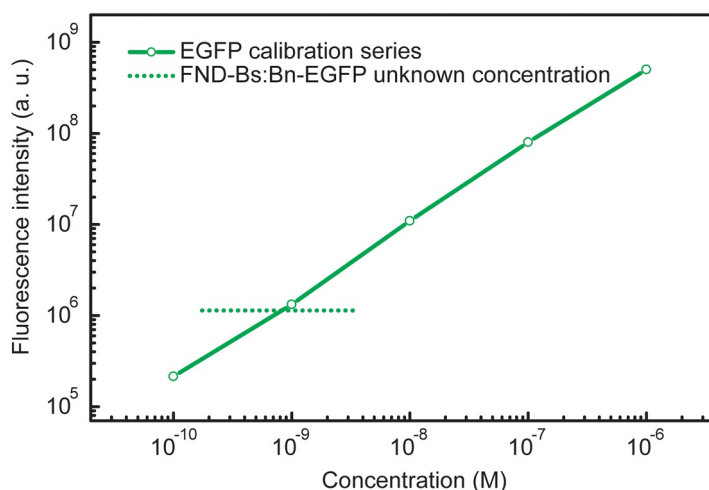

(b) EGFP fluorescence calibration; FND-Bs:Bn-EGFP emission intensity under 482 nm excitation

Figure 7.19: Fluorescence intensity based concentration calibration charts for FND and EGFP, along with the fluorescence intensity measured from the unknown concentration of FND-Bs:Bn-EGFP solution.

fluorescence emission spectra, presented in Figure 7.20(b), was acquired from the bright spot demarcated by a yellow arrow in the micrograph. This indicated that EGFP and FND were colocalized and that the endocytosed FND-Bs:Bn-EGFP particles remained as intact complexes, thus, confirming their stability.
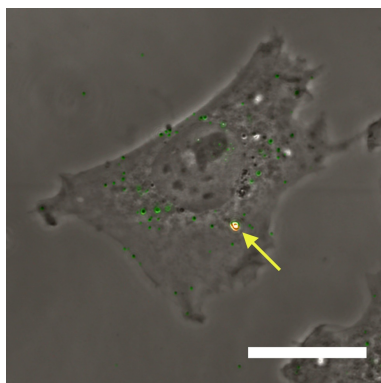
(a) Fluorescence confocal image of
CHO-K1; Scalebar 20 μm
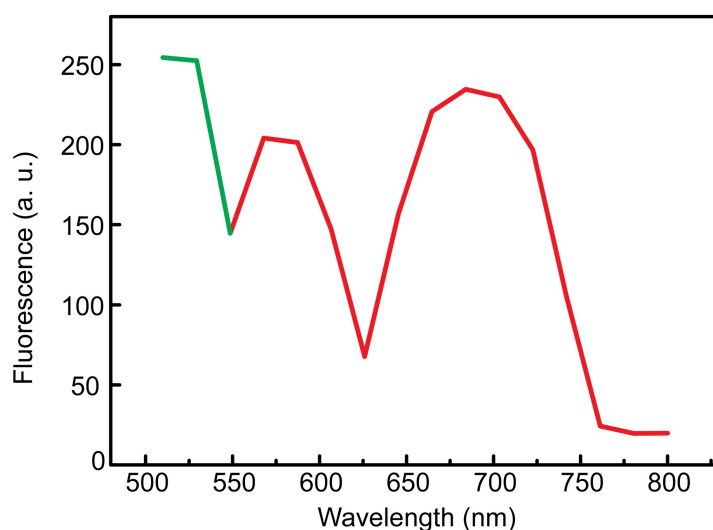
(b) Fluorescence spectrum from the spot demarcated by the arrow
in (a), under 488-nm laser excitation

Figure 7.20: (a) An overlay of phase-contrast and fluorescence images of a CHO-K1 cell, treated with FND-Bs:Bn-EGFP solution. The fluorescence image was obtained under a 488-nm laser excitation. (b) Fluorescence emission spectra of the bright spot, marked by a yellow arrow, in subfigure (a). The green and red sections of the spectra represent the contributions of the EGFP and FND to the net fluorescence, thus, confirming the integrity of the FND-Bs:Bn-EGFP complex.

7.5.2   FND-Bs:Bn-nanogold

The complex FND-Bs:Bn-nanogold was synthesized using the pre-fabricated lego counterparts FND-Bs and Bn-nanogold, by Ms. Ekaterina A. Ivukina. Solutions containing the two counterparts were mixed and reacted for 60 min at room temperature. The mixture was centrifuged at 6000×g and the pellet, presumably, containing the complex

FND-Bs:Bn-nanogold, was re-suspended in PB20 to remove unbound Bn-nanogold. The complex's diameter was measured by using dynamic light scattering and transmission electron microscopy to yield $\approx$ 200 nm, with additional peaks of larger sizes, probably represented by the aggregates. The zeta-potential was found to have two peaks at $\approx$-21 and -40 mV, as shown in Figure 7.21(a). These two peaks were likely to be associated with FND-Bs-Bn-nanogold (-21 mV) and un-reacted Bn-nanogold (-40 mV). The electron microscopy images presented in Figure 7.21(b)) confirmed the binding of several gold nanoparticles to an FND crystal, as expected.

7.6 Summary

Fluorescent nanodiamond (FND) is an emerging nanomaterial, suitable for biolabeling applications as a fluorescent probe. The challenges of making FNDs biologically compatible and functional have been addressed by using a molecular lego pair barstar:barnase (Bs:Bn). The ease, versatility and stability of FND-biofunctionalization using the Bs:Bn strategy is demonstrated by the design, preparation and applications of two supra-nanoparticular structures.

Properties of pristine FNDs: 140 nm acid-treated FNDs that contained N-V color centers were characterized for their size, colloidal stability, surface charge and fluorescence. The hydrodynamic diameter of FNDs was found to be $\approx$ 110 nm and were stable in a aqueous colloidal form. However, the FNDs agglomerated upon the addition of salt, forming clusters with diameters ranging from 200 nm to 1 μm. The surface charge of FND, in terms of the zeta-potential, was found to be $\approx$ -47 mV, due to the negatively charged surface carboxyl groups. The FND fluorescence spectrum exhibited a broad emission, peaked at 670 nm.

Biofunctionalization of FNDs: The existing literature reports on wide variety of FND biofunctionalization methods. Some methods are easy and unstable, while the others are extremely stable, but demands complex chemical reactions. A new FND-biofunctionalization strategy based on a molecular lego pair represents an appealing
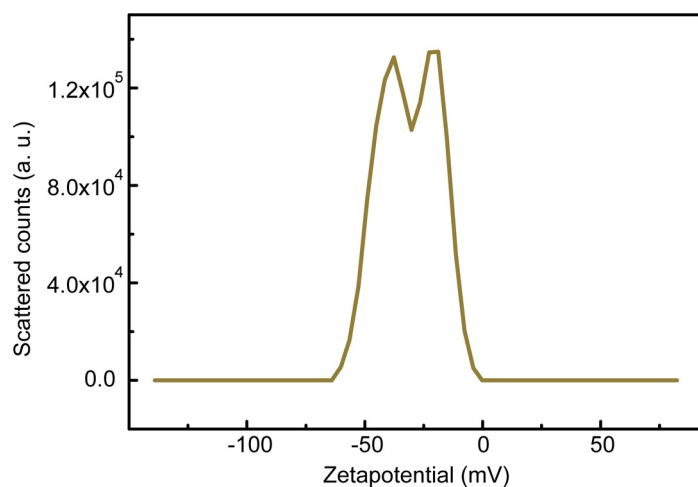
(a) Zetapotential of FND-Bs-Bn-nanogold, as measured by Malvern's Zetasizer
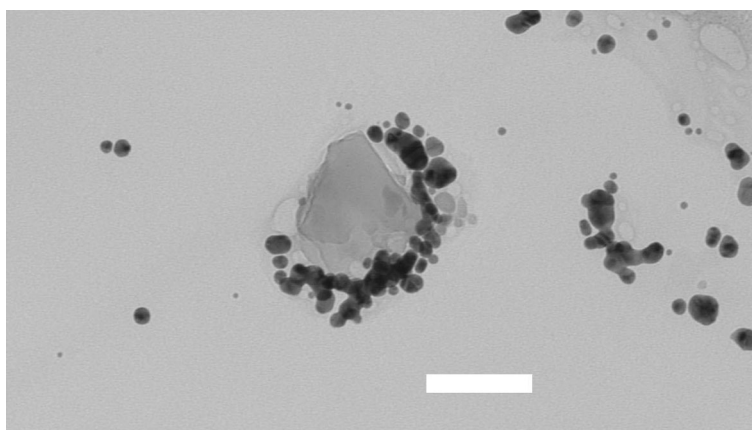
(b) TEM image of 140 nm FND functionalized with nanogold particles via the Bs:Bn linker. The diamond nanocrystal is the semi-transparent crystal, whereas the black dots are the nanogold particles. Scale-bar 100 nm.

Figure 7.21: Characterization of the FND-Bs:Bn-nanogold complex using zeta-potential and electron microscopy measurements.

trade-off between the complexity and stability, and is easy, versatile and robust.

Lego-based FND complexes: Barstar and barnase (Bs:Bn) molecular lego pair were chosen in virtue of their high pairing affinity and stability. FNDs were covalently biofunctionalized to Bs molecules, forming FND-Bs complexes. The covalent nature of the bonding between FND and Bs moieties was confirmed by the X-ray photo-electron spectroscopy and a number of control experiments. The covalent Bs-coating

also increased the colloidal stability of FND in salt-containing buffer solutions. Bn-EGFP and Bn-nanogold represented as the counterparts of the lego, which when added to FND-Bs formed the supra-nanoparticular complexes FND-Bs:Bn-EGFP and FND-Bs:Bn-nanogold. These complexes were characterized in terms of their size and zeta-potentials. The FND-Bs:Bn-EGFP was demonstrated to be stable in biological conditions, such as after being translocated into the cell cytoplasm following the endocytosis by the CHO-K1 cells.

7.7   Conclusion

Fluorescent nanodiamonds (FNDs) are suitable for biolabeling applications as a fluorescent probe. One of the important hurdles towards achieving this goal is to develop a suitable method of biofunctionalization to anchor molecules on the FND-surface. Barstar and barnase, an eminent molecular lego pair, were used to biofunctionalize FNDs with green fluorescent protein and gold nanoparticles. These two supra-nanoparticular complexes were used to demonstrate the versatility and robustness of this molecular lego strategy. This novel strategy is believed to be promising for the biofunctionalization of a variety of nanoparticles, surfaces and biomolecules. Despite the robust complex obtained after this biofunctionalization, the FND-based complexes were not colloidally stable under saline, physiological conditions. This precluded their use as probes for visualizing the endocytosis of somatostatin, as discussed in next chapter.

<div align="right">

8

</div>

Tagging Cell-Signaling Molecules with Fluorescent Nanoparticles

This chapter is based on the journal publication:

Varun K. A. Sreenivasan, Eun J. Kim, Ann K. Goodchild, Mark Connor and Andrei V. Zyvagin, "Targeting somatostatin receptors using *in situ*-bioconjugated luminescent nanoparticles", *Nanomedicine*, available online, 2012[241]

This PhD research project culminates in this chapter by demonstrating targeted delivery of nanoparticles to the cells, or more specifically, somatostatin receptor-mediated endocytosis of QDs in the cells. This experimental demonstration represents fulfillment of the main objective of the PhD project. Convergence of the previously developed techniques into this experimental demonstration requires a recap of the key concepts

that will take place in the beginning. The existing methods of biofunctionalizing quantum dots with biomolecules are reviewed, together with the design and development of somatostatin biofunctionalization approaches. Visualization of the somatostatin receptor-mediated endocytosis using quantum dots, by means of optical imaging, is described.

Contents

8.1 Recap and Introduction

In the context of biomedical applications, nanoparticles (NPs) can be thought of as agile, conspicuous and targetable transport vehicles. In this project, NPs are used as probes for biolabeling, relying on their properties of detectability by various imaging techniques and targeting capability, i. e., specific affinity to cell/tissue sites of interest. The detectability is an intrinsic property of all the NPs reported in this thesis, implemented using high-sensitivity fluorescent nanoparticles. The NP targeting capability is realized by attachment of specific targeting molecules on the NP-surface that binds to certain address in cell/tissue – a process called biofunctionalization. For example, a fluorescent NP can be biofunctionalized in such a way that it is accumulated in cancerous tissue. This results in the fluorescent labeling of the cancer, enabling the differential visualization of cancerous versus normal tissue. Organic dyes have been used for many years for biolabeling in research and, more recently, in clinical scenarios[1] . NPs have potential to outperform these dyes in virtue of their physical/chemical stability, non-cytotoxicity, photostability and, more uniquely, their ability to transport many and different molecular species.

The targeting molecule design often relies on its pre-programmed affinity towards a specific acceptor/receptor molecule. One such targeting molecule, called somatostatin (SST), was introduced in Chapters 3 and 5. SST is a small signaling molecule characterized with high binding affinity to its specific, cell membrane-bound receptor (sst). sst(s) are expressed in several cell types, where they serve specialized and significant functions. For example, their activity in neurons in the rostral ventrolateral medulla (RVLM) region of the brain controls blood pressure[41]; sst-activation in the pituitary gland by SST-binding results in the inhibition of growth[35]. In most cells, sst(s) are located at the cell-membrane, where the SST-binding region remains exposed towards the extracellular space[274]. Therefore, NPs that are biofunctionalized with SST molecules can be used to target these cells. Reubi et al.[207] proposed the use of SST-based targeting strategy for labeling neuroendocrine tumors, as the tumorous cells host a large number of sst(s) on their surface. A combination this molecular targeting strategy

and the transport capability of NPs could be used for delivering therapeutic drugs into tumors[25]. At the same time, SST-biofunctionalized NPs can be used to elucidate the SST-activated cellular machinery as well as the sst-mediated intracellular signaling.

A plethora of cell signaling events associated with sst starts with SST-binding and activation (detailed in Chapters 3 and 5). One of these events, called internalization (also known as sst-mediated internalization, or more completely, endocytosis), is manifested by cellular engulfment of the activated sst together with the bound SST, in the form of an sst:SST complex[†]. The sst-mediated internalization is one of the methods in which the number of *ready-to-bind* sst(s) at the cell-surface is externally modulated by SST[246]. An addition of excess of SST results in the removal of sst(s) by internalization, causing desensitization[24,104,136]. NP-based biolabeling of SST, can provide information on the efficiency and time scales of the internalization. Quantum dots (QDs), were our NPs of choice due to their merits, which were discussed in Chapters 2 and 6, and briefed in the following paragraph.

A QD represents a semiconductor nanocrystal core, whose photo-excitation is governed by the quantum confinement effects[11], resulting in exceptionally bright fluorescence. This effect manifests as the nanocrystal core size-dependent wavelength of fluorescence emission[49]. The QD nanocrystals are surface passivated with a semiconductor shell, in order to protect the core from environmental damage and fluorescence quenching. Moreover, the resultant core/shell structure is capped with an auxiliary polymer layer to avoid potential cytotoxicity and improve photostability. The extensive research and commercialization of QDs has resulted in improved physical, chemical and fluorescence properties of commercially available QDs. These bright, photostable and surface-functionalized QDs were eminently suitable as fluorescent probes for investigating the sst:SST internalization in cells.

In this chapter, the biofunctionalization of QDs with SST is described in detail from the stages of conceptualization, design, methodology and characterization to the *in vitro* biolabeling applications.

[†]The ":" represents the affinity binding between the two molecules

8.2 Biofunctionalization of Quantum Dots

Biofunctionalization of QDs to a vast variety of molecules, including antibodies[273,278], agonists[153], other proteins[48], drugs[220] and DNA[160,220], has been reported previously. Most methods of biofunctionalization were painstakingly chosen to suit each type of molecule. Instead of an extensive literature survey on these methods, which can be found in numerous reviews[68,166], a summary of the these methods is listed below.

1. Adsorption[160]

   This is the simplest method and includes attachment of molecules onto QD-surface using hydrophobic, electrostatic or metal-affinity interactions. Solutions containing QD and molecule(s) of interest are mixed under experimentally optimized conditions, resulting in QD-surface 'wrapped' with chosen molecules. The ease of this functionalization procedure, however, is countered by pitfalls of yielding an unstable and irreproducible QD-bioconjugate.

2. Amphiphilic encapsulation, followed by chemical functionalization[144,273]

   The semiconductor shells of QDs are generally hydrophobic in nature. This prevents their direct application in biomedicine, where aqueous compatibility is a prerequisite. Therefore, QD surfaces are treated with additional molecules. Amphiphillic molecules are suitable, because they contain both hydrophilic and hydrophobic terminals. They encapsulate the hydrophobic QDs, using hydrophobic interactions with the QD-surface to expose the hydrophilic domains towards the aqueous exterior. Later, the hydrophilic regions of this molecular layer can be used for biofunctionalization with targeting molecules, to render the QDs bioactive. However, the amphiphillic coat on the QD may be sheared off, returning the QDs to their original, hydrophobic, conditions. This shedding process may also get enhanced in the presence of other molecules in the biological media, resulting in the loss of the biofunctionalized addressing molecules.

3. Polymer coating, followed by direct covalent functionalization[186]

   The issue of shedding of the amphiphilic molecular coat could be resolved by

cross-linking amphiphillic polymers, stabilizing the coating. Besides providing aqueous stability and protection, the increasingly popular polymer coatings may also be designed to expose chemically reactive functional groups, for example, carboxyl (-COOH) or amino (-NH$_2$) groups. Biomolecules such as proteins can then be functionalized to the QDs by a covalent reaction[†] between the chemical group on the polymer coating and that in the biomolecule. Covalent functionalization yields extremely stable QD-biomolecular conjugates that are reproducible

4. Polymer coating, followed by indirect functionalization using affinity molecular pairs[227]

   The covalent functionalization of molecules to QDs demand chemical reactions to be designed exclusively for (a) each type of molecule to be anchored and (b) each type of functional group on the polymer coating. Indirect biofunctionalization methods using molecular pairs (to be discussed in the next section) can enable creating QD-biomolecular complexes that are as stable as direct covalent functionalization, in addition to being versatile. This method was used for the biofunctionalization of QDs with SST and will be discussed in detail in the following sections.

8.2.1   Molecular Lego Pairs

A class of naturally abundant molecules, referred to as affinity molecules or *molecular lego*[‡] pairs, contribute themselves as key building blocks of living systems. Some examples of molecular legos include antibody:antigen[§], complementary DNA/RNA pairs and biotin:streptavidin, each one being instrumental to furnish important biological processes[56]. They have also been utilized for various applications including NP biofunctionalization, pathogen-detection assays and other immunological procedures, in

---

[†]A covalent reaction results in the formation of a covalent bond - a form of chemical bonding that is characterized by the sharing of pairs of electrons between atoms

[‡]This term was coined by our group

[§]':' represents a stable, non-covalent bond, normally stabilized by hydrogen bonding or Van der Walls' forces; '-' represents a covalent bond

virtue of their highly specific pairing interaction[56]. Among these high-affinity molecular legos, the biotin:streptavidin (B:Sav) and barstar:barnase (Bs:Bn) pairs are of particular interest here.
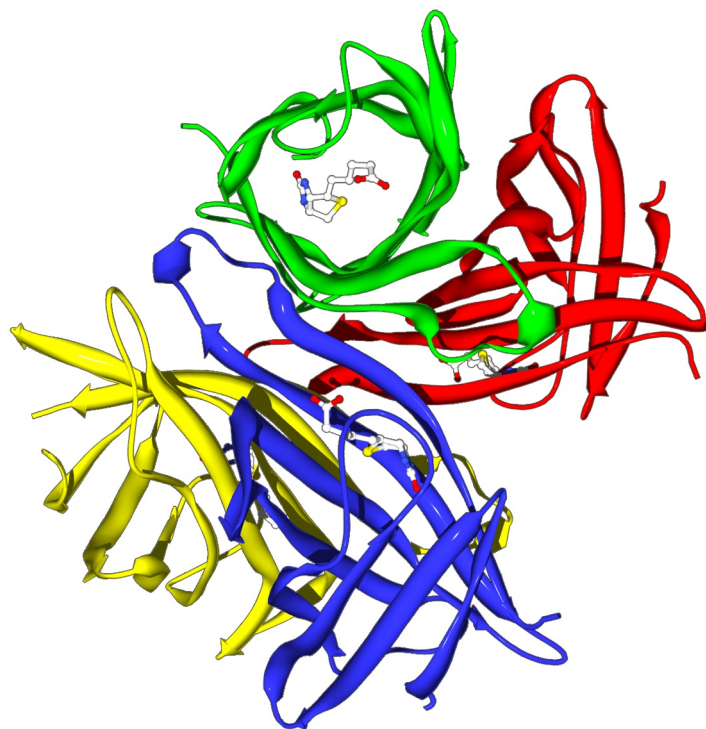
8.2.1.1 Biotin:Streptavidin

Streptavidin (Sav) is a protein isolated from *Streptomyces avidini*[23]. Soon after its discovery, it was found to posses unprecedentedly high affinity ($K_D = 1$ fM) towards the vitamin, Biotin (B)[23]. Since its discovery, this molecular lego pair has been applied in a large number of areas, including *in vivo* biomedical applications[96,131]. The 3D-rendered molecular structure of the B:Sav complex is presented in Figure 8.1(a). In this chapter, the abbreviation 'Sav' would be used to represent streptavidin as well as its natural/mutated functional analogs including the equally popular alternative - avidin (extracted from egg-white[90]). Each molecule of Sav contains 4 biotin-binding domains[271]. This multivalent binding has been flagged as advantageous in the literature for assays that require high sensitivity[56], however reports on such amplification are, to the best of our knowledge, non-existent. This is most likely because most assays use streptavidin, instead of biotin, as the carrier of the contrast agent. Unlike the Bs:Bn pair, the B:Sav-based lego structures are not amenable to genetic engineering methods as (i) biotin is a vitamin and (ii) Sav is a complex protein of quaternary structures.

8.2.1.2 Bastar:Barnase (Bs:Bn)

This molecular lego pair was described in detail in Section 7.3.1. Briefly, barstar (Bs) and barnase (Bn) are prokaryotic proteins[101] that bind to each other to form a tight complex (dissociation constant, $K_D = 10$ fM)[65]. It differs from the B:Sav by its 1:1 binding ratio and a completely protein-based integrity, which allows them to be genetically engineered to form recombinant complexes.

Bs:Bn and B:Sav molecular lego pairs were proposed to serve as the tool for the biofunctionalization of QD with SST. One sub-unit of a lego pair would be linked to SST whereas its complimentary sub-unit would be covalently immobilized on the

(a) Streptavidin:biotin (Sav:B). Streptavidin constitutes the four multi-colored barrels, whereas biotin molecules are presented in a ball-and-stick model.

(b) Barstar:barnase (Bs:Bn) complex. Bs and Bn are colored green and brown, respectively. Reproduced from Figure 7.10.

Figure 8.1: The 3D structures of two molecular lego pairs rendered using the Swiss PDB viewer using the X-ray diffraction-based data published by Le Trong et al. [147] and Urakubo et al. [258]. Courtesy RSC Protein data bank.

QD-surface. Thereafter, the affinity based interaction between the sub-units would generate a SST-QD complex. That is, biofunctionalization of SST to QDs using B:Sav or Bs:Bn pairs would yield the predictable complexes SST-B:Sav-QD or SST-Bs:Bn-QD, respectively. Furthermore, swapping the positions of the sub-units can result in the formation of SST-Sav:B-QD and SST-Bn:Bs-QD, respectively. The versatility of this approach becomes immediately apparent when SST is to be replaced by another molecule, for example, octreotide, an analog of SST[197].

8.3 Somatostatin Sub-units of the Molecular Lego Pairs

As the first step towards the biofunctionalization of QD with SST, using the molecular lego pairs, the sub-units that contained SST were designed, procured and biologically characterized. These will be detailed in the following sub-sections. Table 8.1 summarizes all the characterization and imaging experiments presented in this chapter.

8.3.1 Somatostatin-Biotin (SST-B)

Two different designs of the SST-QD complexes were conceivable using the Sav:B lego pair: (a) SST-B:Sav-QD and (b) SST-Sav:B-QD. Only the choice (a) was further investigated for the following reasons:

1. Commercial availability of Sav-coated QD (Sav-QD).

2. The 4:1 binding stoichiometry of B:Sav dictates multivalency. Therefore, the preparation of SST-Sav:B-QD would result in attachment of more than one QD particle to a molecule of SST, causing undesirable aggregation.

3. On contrary, the preparation of SST-B:Sav-QD facilitates the attachment of multiple molecules of SST per QD particle, without aggregation. This complex also renders multivalency to the QD-particles.

Table 8.1: Number of cell-based experiments carried out with biotinylated SST, Sav-dy and Sav-QD

Experiment type	Section	Ligand	Mode	Cell Type	Repeats × Replicates (min)
Membrane potential assay	8.3.1.1	SST	Time	AtT-20 (WT)	3 × 3
		SST	Dose	AtT-20 (WT)	3 × 3
		SST-2B	Dose	AtT-20 (WT)	3 × 3
		SST-5B	Dose	AtT-20 (WT)	3 × 3
	8.3.2	SST-Bs	Dose	AtT-20 (WT)	3 × 3
	8.5	SST-2B + Sav-dy	Time	AtT-20 (WT)	3 × 3
		SST-2B:Sav-dy	Dose	AtT-20 (WT)	3 × 3
		SST + Sav-dy	Dose	AtT-20 (WT)	3 × 3
		SST-2B:Sav-dy	Dose	AtT-20 (WT)	3 × 3
		SST-5B:Sav-dy	Dose	AtT-20 (WT)	3 × 3
QD-assisted imaging	8.4	Sav-QD	Time	AR42J (WT)	3 × −
		SST-2B:Sav-QD	Time	AR42J (WT)	3 × −
	8.6	SST-2B + Sav-QD	in situ two-step	AR42J (WT)	7 × −
		− + Sav-QD	in situ two-step	AR42J (WT)	7 × −
		B + Sav-QD	in situ two-step	AR42J (WT)	1 × −
		SST + Sav-QD	in situ two-step	AR42J (WT)	1 × −
		SST-2B + Sav-QD	in situ two-step (37 °C)	AR42J (WT)	1 × −

Therefore, biotinylated SST molecules (SST-B) were initially designed to synthesize the SST-B:Sav-QD complex. The structure of a native SST molecule is presented in Figure 8.2(a). The amino acid-sequence -FWKT-, located at the hairpin bend of the molecule, is critical for the sst-binding[99]. To minimize the impact on SST binding capacity, the biotinylization was designed to be performed on the alanine residue in the N-terminal of the molecule, via a flexible spacer molecule, poly-ethylene glycol ($[\text{-O-CH}_2\text{-CH}_2\text{-}]_n$; $\text{PEG}(n)$), to form SST-nB. Two analogs of this complex, SST-2B and SST-5B (where $n = 2$ and 5, respectively; collectively referred to as SST-B), are presented in Figure 8.2(b). These in-house designed biotinylated somatostatin analogs were custom-prepared and supplied by Auspep, Australia and Genscript, NJ, USA, respectively.

The SST-2B and SST-5B, and their Sav-bound forms were expected to have differential biological activities. The SST-5B may be characterized with a reduced binding affinity as compared to SST-2B, because of its larger size. On the other hand, its long PEG spacer was designed to ensure that, after the SST-5B:Sav formation, the SST moiety was well exposed for receptor-binding. This will be discussed in detail shortly. Firstly, the biological function of the two analogs in the unbound form was characterized.

8.3.1.1 Biological Characterization of Somatostatin-Biotin

A cellular membrane potential assay was used for this characterization, similar to that in Section 5.6.1. Briefly, the AtT-20 cells that endogenously expressed sst(s) responded to SST by hyperpolarization, which was read out by a membrane potential-sensitive fluorescent dye. Figure 8.3(a) presents the time course of the cell membrane potential in response to addition of SST. Addition of 100-nM SST resulted in a steep decrease of the fluorescence intensity. The maximum fall in fluorescence was used as a quantitative measure of the hyperpolarization.

Similar data were also obtained using the two biotinylated analogs SST-2B and SST-5B. The hyperpolarization responses evoked by these SST-analogues were also determined and are shown in Figure 8.3(b) as dose-response curves. The horizontal
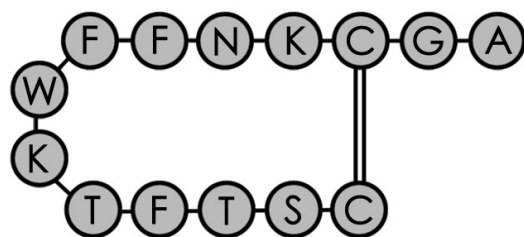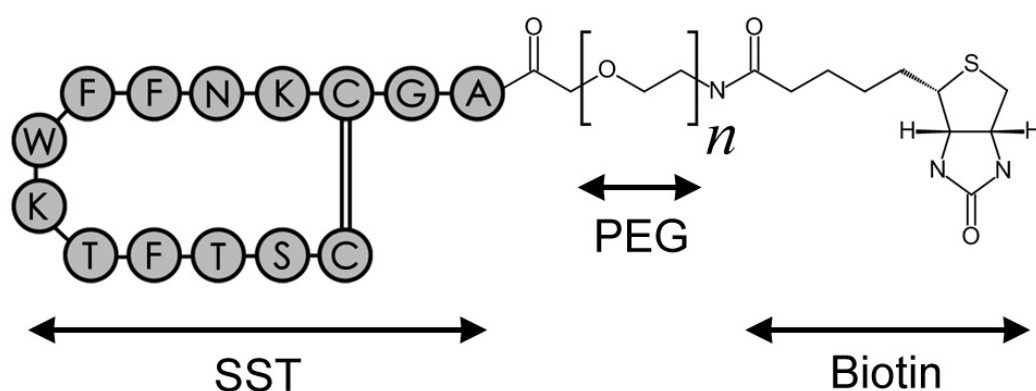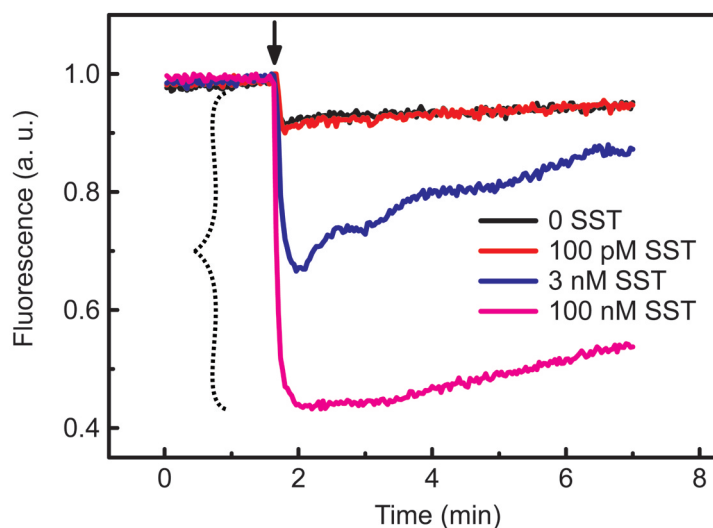
(a) Native SST. Reproduced from Figure 3.4

(b) Biotinylated SST (SST-nB)

Figure 8.2: Schematic of the (a) native and (b) biotinylated SST molecules, presented as a chain of amino acids in a single letter code. A double line represents the naturally existing disulfide bond between the two cysteine residues. The value of n determines the length of the ethylene glycol spacer.

shift of the dose-response curve of the analogs with respect to that of the native SST was indicative of their relative potencies. Quantitatively, their potencies were characterized in terms of pEC_{50}[†] values, obtained by fitting the dose response curve to a logistic equation (see equation 4.5). The SST-2B was found to be as potent as the native SST with their pEC_{50} values of 8.1 ± 0.6 and 8.1 ± 0.1, respectively. However, the SST-5B analog was found to be less potent with a pEC_{50} of 7.2 ± 0.1 (p-value = 0.05).

The lower potency of SST-5B is most likely to be due to its larger size, resulting in lower binding affinity. This hypothesis was corroborated by our results described in Chapter 5, where SST-mRFP showed even lower potency, because of larger size.

[†]pEC_{50} is defined as the negative log of the drug concentration required to stimulate half of the maximum response

(a) Time course of the fluorescence intensity from the membrane potential sensitive dye; before, during and after SST addition to the AtT-20 cells at the time-point demarcated by the black arrow. Reproduced from Figure 5.8.
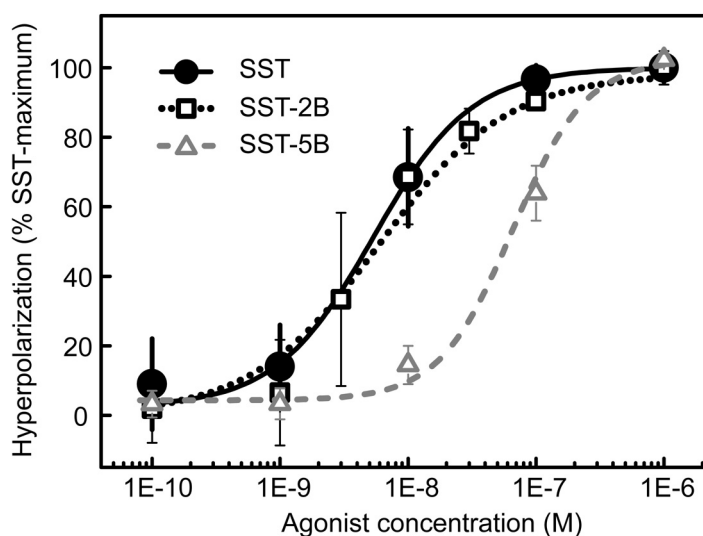
(b) Concentration versus hyperpolarization response curve of SST, SST-2B and SST-5B. The hyperpolarization values were obtained from the normalized values of maximum drop in the fluorescence, marked by the dashed '{', in (a) above.

Figure 8.3: AtT-20 cell membrane hyperpolarization responses evoked by the addition of SST, SST-2B or SST-5B, as measured using a membrane potential-sensitive dye. The data presented is a representative of at least three independent experiments, each performed in triplicates. The error bar corresponds to standard error of means determined from one of the triplicates.
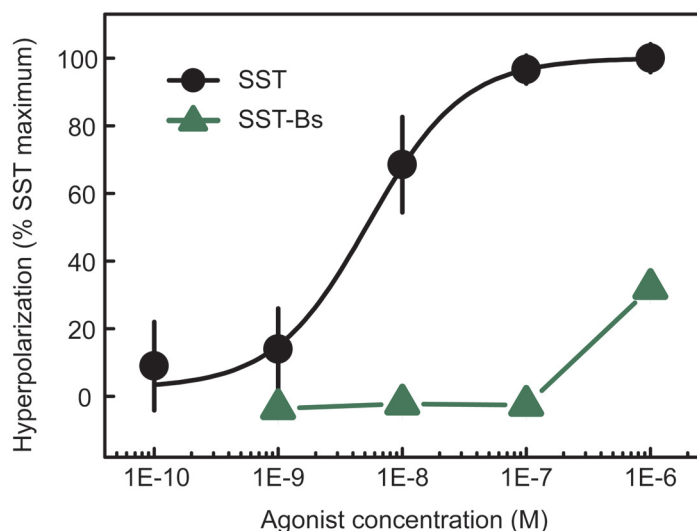
Figure 8.4: AtT-20 cell membrane hyperpolarization responses evoked by the addition of SST or SST-Bs, as measured using a membrane potential-sensitive dye. The data presented is a representative of two independent experiments, both performed in triplicates. The error bar corresponds to standard error of means determined from one of the triplicates. Error bars are not visible, when they are smaller than the symbol.

Therefore, the SST-5B complex was not used for the synthesis of the SST-QD complexes.

8.3.2 Somatostatin-Barstar (SST-Bs)

The recombinant protein SST-Bs was designed and synthesized by our collaborator Prof. Sergey M. Deyev. Functionalization of QD using the Bs:Bn lego pairing was not pursued due the low potency of SST-Bs complex, as shown in Figure 8.4. The low potency was most likely due to aggregation in the solution, visible to naked eye.

8.4 Somatostatin-Quantum Dot Internalization

QDs functionalized with SST molecules, via the B:Sav lego pairing, were used to study internalization of the sst:SST complexes in the AR42J cells. These cells efficiently internalize the sst(s), following the activation by SST[270]. The fluorescence of QDs was expected to enable optical visualization of the sst-mediated internalization. The

SST-QD complex was prepared by mixing solutions containing SST-2B and Sav-QD (Qdot 605 ITK™ streptavidin conjugate; Invitrogen, Australia) in a 24:1 molar ratio, because each QD was attached to $\approx$ 6 Sav-molecules according to the product data sheet.

Images of the AR42J cells treated with SST-QD for time periods ranging from 15 min to 90 min are shown in Figure 8.5. sst-mediated internalization reportedly occurs within few minutes after the SST-exposure[270]. Little SST-QD fluorescence was detected after short incubation times, contrary to our expectation. The internalization at longer incubation times (>60 min) occurred in the control (Sav-QD) as well, most likely via non-specific internalization processes, rather than a specific, sst-mediated process. A detailed study on the non-specific internalization of several types of QDs was presented in Chapter 6.

8.4.0.1   Method

AR42J cells (see Section 4.2 for details) were seeded on a 4-well slide (BD Falcon) on a day before the experiment. SST-2B:Sav-QD (SST-QD, in short) was prepared by mixing the solutions containing SST-2B and Sav-QD (Qdot® 605 ITK TM Streptavidin Conjugate; Life Technologies, Australia) at a molar ratio of 24:1, taking into account of the two factors (a) an Sav molecule contains 4 biotin-binding terminals and (b) each QD was functionalized to 6-8 Sav molecules, according to the product data sheet. AR42J cells, grown on the slides, were incubated with 40 nM SST-QD (or Sav-QD, as control) solution, prepared in phosphate buffered saline (PBS), for time varying from 15 min to 90 min at 37 ^{o}C. After washing with PBS, the cells were fixed with 3.7% paraformaldehyde. 10-μM Hoechst 33342 was incubated for 12 min to stain the nucleus. In experiments where the nuclear stain was not used, laser back reflection imaging was used to obtain cell-morphological contrast. The cells were mounted using PBS (phosphate buffered saline) and imaged by using fluorescence confocal microscopy (see Section 4.4 for details).

(a) 15 min; SST-QD

(b) 15 min; Sav-QD

(c) 40 min; SST-QD

(d) 40 min; Sav-QD

(e) 60 min; SST-QD

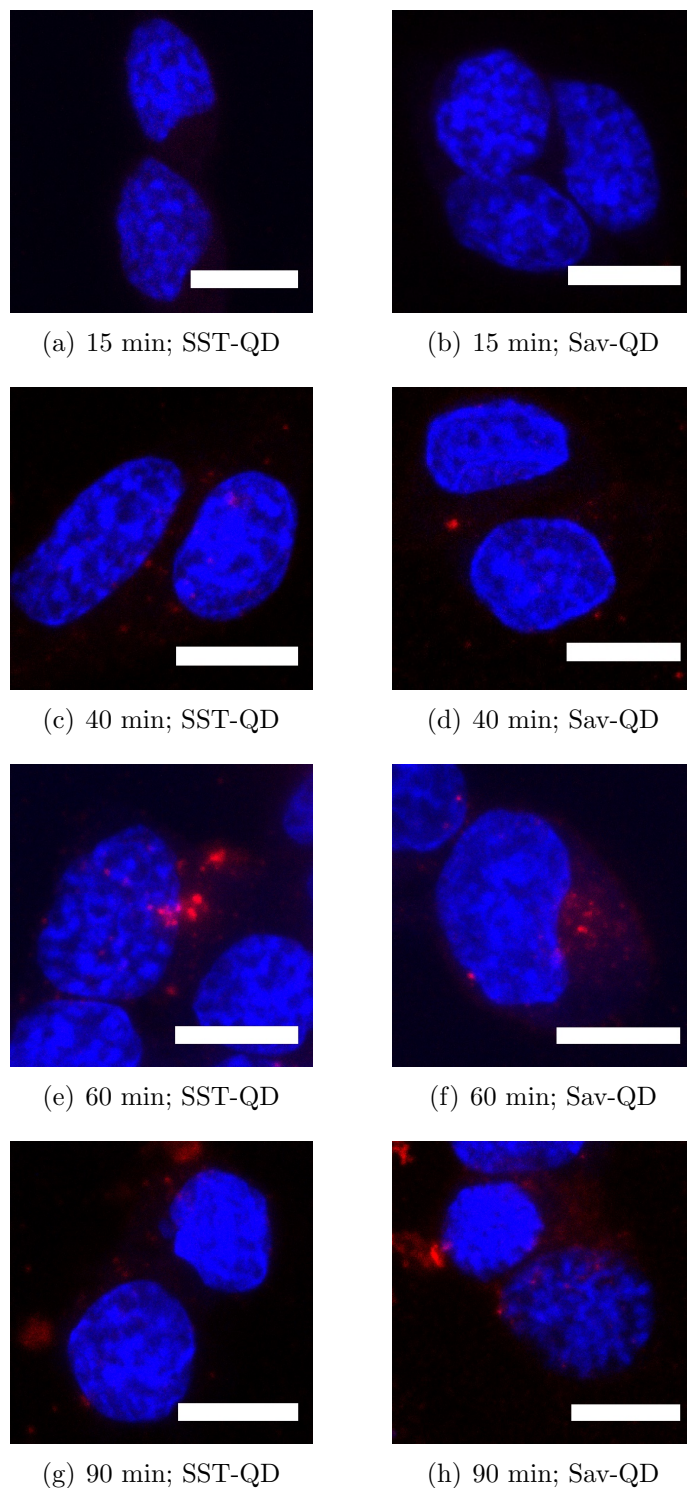(f) 60 min; Sav-QD

(g) 90 min; SST-QD

(h) 90 min; Sav-QD

Figure 8.5: Fluorescence confocal images of the AR42J cells treated with 40-nM SST-QD or the negative control Sav-QD for various time durations. The QD-originated fluorescence is coded in red color and blue is the fluorescence from the nuclear stain. The images presented here are representative of multiple images acquired from three independent experiments, however, carried out with slightly different incubation time periods and imaging conditions. Scale-bar 10 μm.

8.5   The Effect of Streptavidin-Binding

Possible reasons for the undetected specific, sst-mediated internalization of SST-QD are listed below:

1. SST-2B lost its biological function after the Sav-binding.

2. The attachment of relatively large QD-particle resulted in inhibition of the SST-2B activity.

3. Oligomerization of the sst(s) after the SST binding[85,209], resulted in the formation of nanoparticular aggregates, precluding the clathrin-dependent internalization.

The affinity-mediated binding between streptavidin and biotin is the core process behind the formation of the SST-QD complex, and its effect was investigated first. As in the Section 8.3.1.1, this analysis was performed by carrying out an assay of the membrane potential. Streptavidin-dylight594 (Sav-dy; Vector laboratories) was used instead of Sav-QD in order to eliminate any inhibitory effect of attaching the large QD particle. It was also less expensive, when compared to Sav-QD. Solutions containing SST-2B and Sav-dy were mixed at 4:1 molar ratio to prepare the SST-2B:Sav-dy complexes. The final solution was filtered using a desalting column to remove unbound SST-2B. The hyperpolarization of the AtT-20 cells, in response to the addition of SST-2B:Sav-dy, is presented as a dose-response curve in Figure 8.6. The Sav-bound form of SST-2B was unable to evoke a response in the cells, in contrast with the pristine SST-2B that clearly evoked a dose-dependent hyperpolarization, as presented earlier.

Further experiments also corroborated this finding. A fixed concentration of Sav-dy (20 nM) was added to the SST-2B solutions prepared at concentrations ranging from 0.1 nM to 1 μM. Depending on their relative concentrations in these solutions, either SST-2B or Sav-dy was in surplus. Hyperpolarization responses evoked by the addition of these solutions to the AtT-20 cells were measured, and an unconventional dose-response curve was plotted, as presented in Figure 8.7(a). In virtue of 4:1 binding ratio of the B:Sav pair, 20-nM Sav-dy was able to bind to 80-nM SST-2B molecules

Figure 8.6: Plots of the dose versus hyperpolarization response of the AtT-20 cells. SST-2B was added to the cells in Sav-bound or unbound form. The data presented is a representative of three independent experiments, each performed in triplicate. The error bars correspond to the standard error of mean calculated from one of the triplicate.
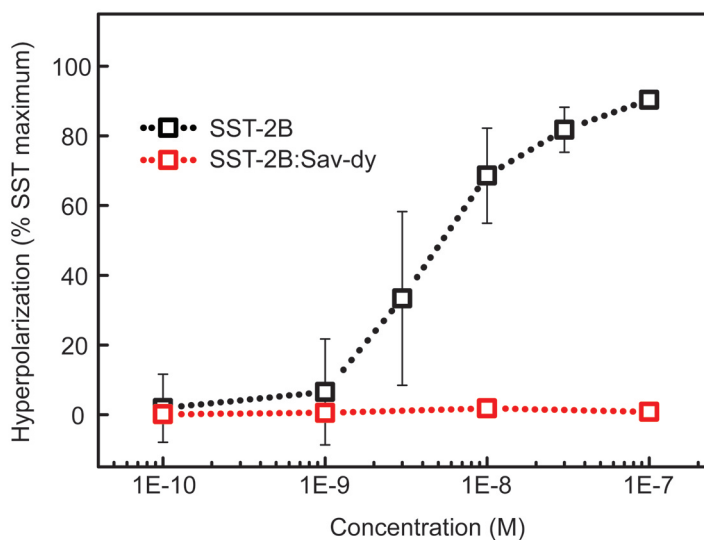
to form the, apparently impotent, SST-2B:Sav-dy complexes. As expected, the dose-response curve appeared to be shifted to the right by 80 nM, in comparison with the pristine SST-2B control. These observations indicate that the Sav-binding resulted in the complete inhibition of SST-2B to bind and activate the sst (receptors).

To clearly portray the radical effect of Sav-binding on the SST-2B potency, membrane potential assays with real-time Sav-additions were carried out. 1-μM SST-2B was known to generate a long-lasting (several minutes) hyperpolarization response in the AtT-20 cells. The time course of the hyperpolarization, measured using a membrane potential-sensitive dye, in response to stimulation by 1-μM SST-2B, is presented in Figure 8.7(b). Second addition of 0.27-μM Sav-dy to the cells under this condition resulted in depolarization and reversal of the membrane potential to basal values. 0.27-μM Sav-dy scavenged most of the free SST-2B in the extracellular medium. In comparison, the cells that were treated with native SST remained hyperpolarized, irrespective of the Sav-dy addition. This corroborated the previous finding that B:Sav binding abolished the potency of SST-2B molecules at activating the somatostatin receptors.

The lack of sst-mediated internalization of SST-B:Sav-QD observed in Section 8.4 was most likely due to the same inhibitory effect of the B:Sav binding. However, the reason for this inhibition is unclear. According to a study carried out by Green et al.[89]
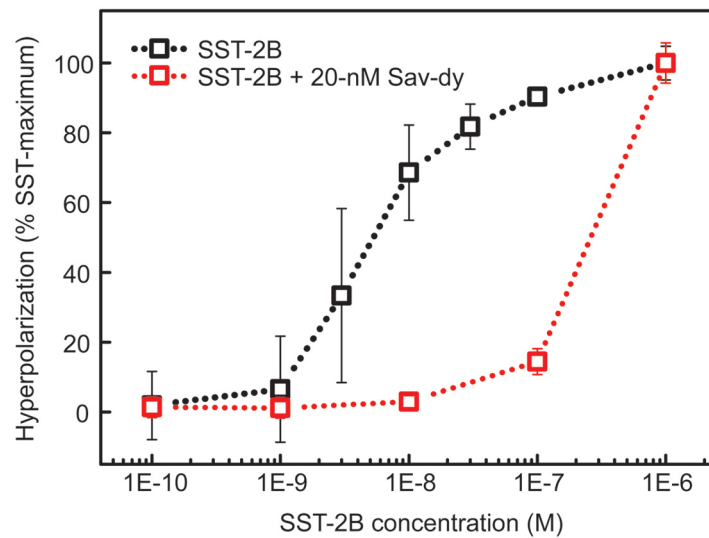
(a) Hyperpolarization responses evoked in the AtT-20 cells by solutions containing 20 nM Sav-dy and varying concentrations of SST-2B, in comparison with SST-2B alone.
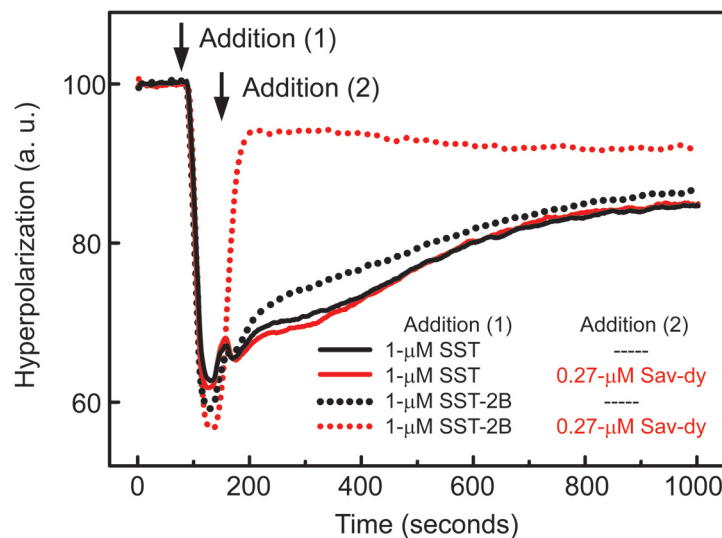

(b) Effect of addition of 0.27-μM Sav-dy on the time course of AtT-20 hyperpolarization, evoked by addition of 1-μM SST-2B, in comparison with that by native SST.

Figure 8.7: Plots of hyperpolarization of the AtT-20 cells induced by the addition of SST or SST-2B, which demonstrates the scavenging effect of Sav-dy on the SST-2B analog. The data presented here is a representative of three independent experiments, each performed in triplicate. The error bars correspond to the standard error of mean, calculated from one of the triplicate.

biotin molecules are buried deep inside the Sav-barrel structure, in the B:Sav complex [see Figure 8.1(a)]. The distance from the carboxyl terminal of biotin molecule to the mouth of the Sav-binding pocket was determined to be $\approx$ 9 Å[89,93]. Even though the PEG linker, between the biotin and SST, in the SST-2B analog was $\approx$ 11 Å long, it was possible that the excess 2 nm was insufficient to fully expose the SST moiety for receptor-binding. This hypothesis was tested using the SST-5B, which had a much longer spacer between the SST and biotin groups [see Figure 8.2(b)]. We found that the SST-5B was also susceptible to the inhibitory effects of Sav-binding, yielding inactive SST-5B:Sav-dy complexes [see Figure 8.8(a)], potentially ruling out the hypothesis. Surprisingly, we also found that addition of Sav-dy and incubation for 40 min reduced the activity of even the native SST [see Figure 8.8(b)]. This suggested that the SST molecules became associated with Sav-molecules via non-specific interactions, rendering the sst-binding region inaccessible. In short, the SST-QD cell-targeting became problematic and a new approach was designed and tested to circumvent the inhibitory effect of Sav-binding.

8.5.1   Method

Membrane potential assays were carried out similar to that described in Section 5.6.1. The SST, SST-2B and SST-5B solutions were prepared to obtain final concentrations ranging from 0.1 nM to 1 μM. For experiments evaluating the inhibitory effect, Sav-dy was added to these solutions at $^1/_4$ th of agonist concentration and incubated for 30 - 40 min. For experiments to obtain unconventional dose response curves, as presented in Figure 8.7(a), 20-nM Sav-dy was added to SST-2B solutions with concentrations ranging from 0.1 nM to 1 μM and incubated for 30 min. For time course measurements presented in Figure 8.7(b), the Flexstation was programmed to add Sav-dy after the SST- or SST-2B-induced hyperpolarization reached a plateau. The final concentrations of Sav-dy and the agonists were ensured to be in a 1:4 ratio, respectively, to ensure complete binding.
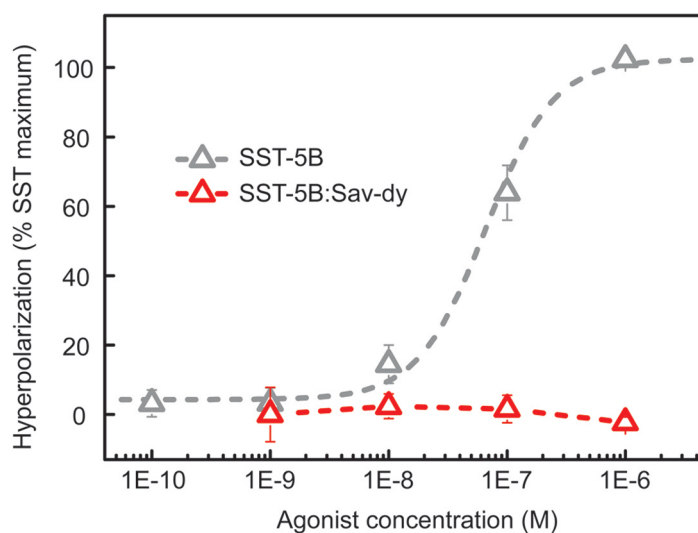
(a) Hyperpolarization evoked by different concentrations of SST-5B
and SST-5B:Sav-dy.
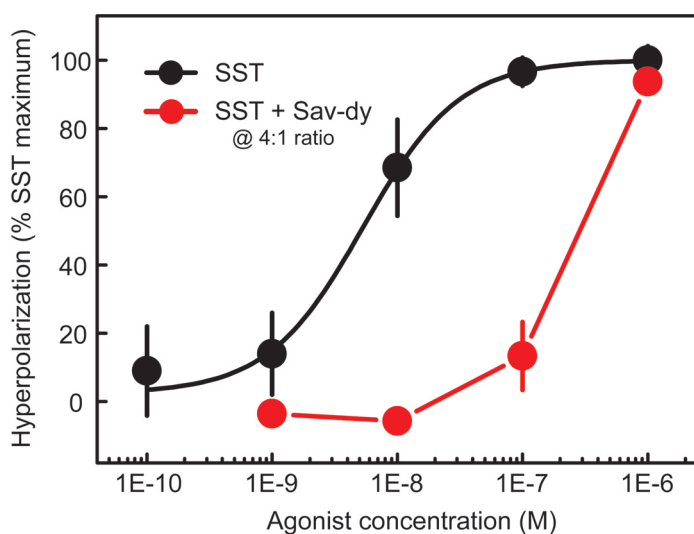
(b) Hyperpolarization evoked by a range of serially diluted solutions
containing either SST by itself or as a mixture of SST and Sav-dy,
at a 4:1 molar ratio.

Figure 8.8: The dose-hyperpolarization response curves obtained using the AtT-20 cells
stimulated by adding Sav-dy bound or unbound forms of (a) SST-5B and (b) SST. The
biological activities of SST-5B and SST are affected by Sav-dy addition. The data presented
here is a representative of three independent experiments, each performed in triplicate. The
error bars correspond to the standard error of mean, evaluated from one of the triplicates.

8.6 *In situ* Biofunctionalization of Quantum Dots

Formation of the SST-B:Sav-QD and its ability to form the receptor-ligand complex, sst:SST-B:Sav-QD, are dictated by two discrete binding steps:

Step 1. Binding of SST-2B to Sav-QD, via the biotin:streptavidin molecular lego pairing, to form the SST-2B:Sav-QD complex.

Step 2. Binding of the sst to the SST moiety in the above complex, via the receptor:ligand pairing.

Our previous results indicated that the binding step 1 prevented step 2 from occurring. One method to overcome this was to reverse the order of these steps i. e., by allowing the receptor:ligand pairing to occur before the biotin:streptavidin lego pairing. This required specialized conditions, because the sst:SST-2B binding quickly activated the cells and initiated internalization, resulting in withdrawal of the biotin moieties into the intracellular space.

Several mechanisms exist by which the internalization can be ceased or suspended temporarily. For example, active cellular processes come to a halt at low temperatures, mainly because of lower diffusion rates and reduced ATP-energy supply [see Figure 6.2 for example][38]. Cells treated with SST at low temperatures were observed to be inefficient at sst-mediated internalization, which was recovered to normal conditions upon restoring the temperature back to physiological values[137,267]. Informed by the study reported by Jaiswal et al.[125], an *in situ* two-step biofunctionalization strategy was used to link the sst:SST-2B complexes to the Sav-QDs, by exploiting the temperature-modulated suspension of the internalization.

Representative images of the AR42J cells, subject to the *in situ* two-step biofunctionalization, are presented in Figure 8.9. At the first step, the incubation of the cells with SST-2B solution at low temperatures resulted in the formation of membrane-immobilized sst:SST-2B complexes. Low temperature was expected to prevent the sst:SST-2B internalization, and allow exposure of the biotin-moieties towards the extracellular space. Subsequent addition of Sav-QD resulted in the formation of the

membrane-bound sst:SST-2B:Sav-QD complexes. Elevation of temperature to physiological levels (37 ^{o}C) resulted in internalization of the sst-bound QD complexes, observable as bright red patches inside the cells in Figure 8.9(a). The internalization was highly specific, as confirmed by several control experiments. For example, replacement of the SST-2B at the first step with a pure buffer, SST or biotin resulted in the absence of internalization [see Figures 8.9(b), 8.9(c) and 8.9(d), respectively]. Minimal QD uptake [see Figure 8.9(e)] was also observed in an additional control experiment, where all the steps of the *in situ* biofunctionalization were carried out at 37 ^{o}C. Under this condition, it was predicted that the sst:SST-2B complexes were internalized soon after their formation, resulting in withdrawal of the biotin-moieties before the Sav-QD could bind.

8.6.1 Method

The AR42J cells were seeded on a 4-well slide and allowed to grow until clusters containing 3-4 cells were abundant. Reduction of temperature for the experiment was achieved by placing the slide on an ice-cold substrate, covered with a thin latex sheet. The temperature was not lowered for one set of control experiments. 20-μM SST-2B solution (SST, biotin or PBS represented as the negative controls), prepared in cold PBS, was added to the cells and incubated for 12 min. After washing the cells once with cold PBS, 2-nM cold Sav-QD solution was added, while maintaining the temperature for 12 min. The cells were washed twice with PBS and moved to a 37 ^{o}C incubator, in order to resume the internalization of the receptor-ligand complexes, which were *in situ*-biofunctionalized to the QDs. Thirty minutes later, the cells were fixed with 3.7% paraformaldehyde and prepared for imaging using fluorescence confocal microscope (see Section 4.4). Where Hoechst-based nuclear staining was not used, laser epi-reflection provided the cell morphological contrast.
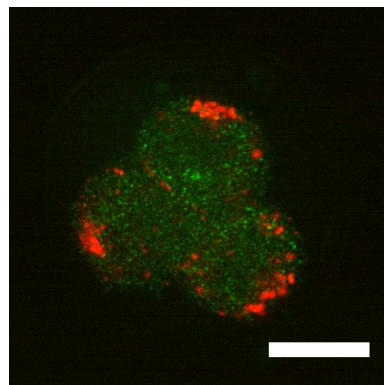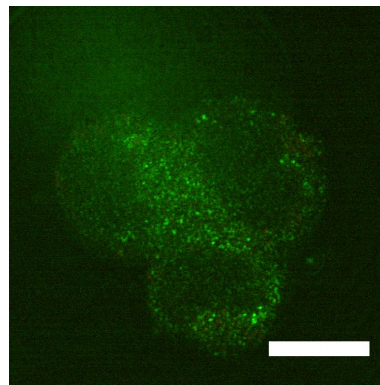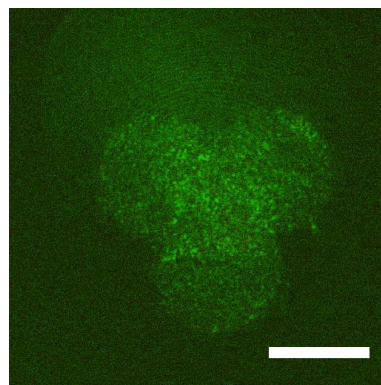
(a) 20-μM SST-2B + 2 nM Sav-QD; Ice-cold
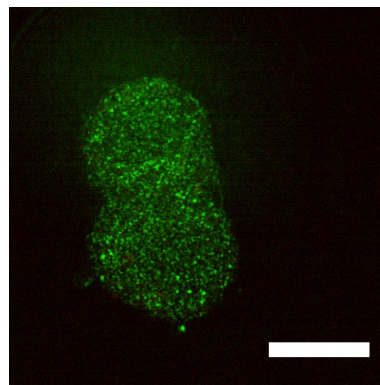
(b) — + 2 nM Sav-QD; Ice-cold
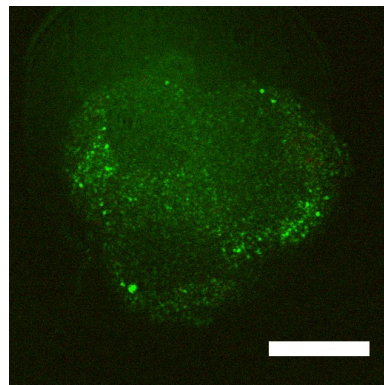
(c) 20-μM SST + 2 nM Sav-QD; Ice-cold

(d) 20-μM B + 2 nM Sav-QD; Ice-cold

(e) 20-μM SST-2B + 2 nM Sav-QD; 37 ^{o}C

Figure 8.9: Fluorescence confocal images of the AR42J cells treated with 20-μM SST-2B (or controls) followed by 20-nM Sav-QD at ice-cold conditions (or 37 ^{o}C control) followed by elevation of temperature to 37 ^{o}C. QD-originated fluorescence is coded in red, whereas the laser back reflection that highlights cell-morphology is coded green. The images presented here are a representative of multiple images acquired from at least two independent experiments. Scale-bar 10 μm.

8.7   Summary and Discussions

Biofunctionalization is one of the major milestone in nanoparticle-based biological and biomedical research, specifically in the fields of biomolecular imaging[29]. It mostly relies on one or more types of physiochemical interactions between the nanoparticle surface and the molecule. Somatostatin (SST) is an abundant and physiologically significant peptide hormone and neurotransmitter molecule[40,187] and its biological functions and biomedical relevance have been investigated for several decades[25,181]. Biofunctionalization of QDs with SST would enable attaining deeper insight into these functions and offer a sensitive tool for biomedical applications.

First of the three reports ever on biofunctionalization of SST (or its analog) to a nanoparticle was published in 1985[69], where colloidal gold particles were used to investigate SST internalization in rat anterior pituitary cells. It is interesting to note that this report was published even before the somatostatin receptors (ssts) were identified, in 1992. Despite the progress in nanoparticle technology and development of high-sensitivity fluorescent nanoparticles, for example quantum dots (QDs)[110], fluorescent nanodiamonds[277] and fluorophore impregnated matrices[218], the later two reports nanoparticle-SST complex were also based on nanogold[140,249]. Indeed, biofunctionalization strategies to attach other molecules like drugs[119], proteins[278] and nucleic acids[227] to these recent nanoparticles have been reported. This chapter reported on the biofunctionalization of QDs, with somatostatin (SST), and various stages in the preparation of the SST-QD complex and its application in cell-labeling were addressed.

First attempt on QD-biofunctionalization: Two SST-QD complexes were designed based on the popular molecular lego pairs streptavidin:biotin (Sav:B) and barstar:barnase (Bs:Bn)[56], to produce SST-B:Sav-QD and SST-Bs:Bn-QD, respectively. These two pairs enable easy, versatile and stable biofunctionalization of different types of molecules to various nanoparticles[28,177,239]. The SST-Bs was characterized by very low potency to activate sst(s), and was not used further. The likely reasons for low activity were the increase in size and aggregation found in the solution, which reduced the effective monomeric concentration.

For biofunctionalization using the Sav:B pair, two types of biotinylated SSTs – SST-2B and SST-5B – were designed and procured to synthesize SST-2B:Sav-QD and SST-5B:Sav-QD, respectively. Characterization of the biological activity showed that the SST-2B remained as potent as the native SST, whereas SST-5B was found to be significantly less potent. The reduction was presumably due to the increased size of the SST-5B, due to the longer polymer linker. Despite the high potency of the free SST-2B, the complex that it formed after QD-biofunctionalization, SST-2B:Sav-QD, was unable to trigger a cellular response and failed to undergo sst-mediated internalization. This was unexpected, because most reports in the literature on similar Sav:B-based biofunctionalization reported on synthesizing active conjugates[28,146].

Sav-binding induced loss of SST-2B potency: Reasons for the loss of potency of SST-2B bound to Sav-QD were investigated using a hyperpolarization-based cell assay. These experiments indicated that the loss occurred mainly because of Sav-binding to the biotin moiety. This inhibitory binding of Sav-dy to the SST-2B groups occurred within several seconds. Our initial arguments were based on early reports on the deep (≈ 9 Å) biotin-binding sites in an Sav-molecule, which can inhibit the SST activity, if the spacer was any shorter[20,90,93]. However, this was not the case, because (a) the PEG spacer in SST-2B was marginally longer than this threshold and (b) the activity of SST-5B, with much longer spacer, was also inhibited upon Sav-binding. Moreover, the potency of native SST was also affected by Sav-dy addition, suggesting that SST was also vulnerable to non-specific binding. In the case of SST-2B and SST-5B, the specific binding could have promoted the non-specific binding resulting in a complete suppression of activity. Another possible reason for reduction in affinity could be the large size of streptavidin (66 kDa), causing reduction in sst-binding affinity, similar to the reduction in affinity observed after the attachment of mRFP, in Chapter 5.

In situ two-step biofunctionalization: The inhibitory effect of Sav-binding on the activity of the SST-2B was overcome by using an alternative approach, where the order of the two constituent binding steps was reversed. This method was demonstrated previously, where other biomolecules, including transferrin[88], biotin ligase[114],

P-glycoprotein[125] etc., were conjugated to QDs. Using this *in situ* biofunctionalization strategy SST-2B molecules were allowed to bind to sst(s) at the first step to form sst:SST-2B receptor:ligand complexes. The consequential internalization of the activated sst(s) was prevented by carrying out this step at low temperatures[137]. Subsequent addition of the Sav-QD solution yielded membrane bound sst:SST-2B:Sav-QDs – receptor-bound nanoparticles. These complexes were found to be internalized by sst-mediated effects after restoring the cells to physiological temperatures.

8.8 Conclusion and Perspective

Various stages in the development of a QD-based SST complex were described. Molecular lego-based approach of biofunctionalization was expected to offer a versatile way of synthesizing a stable and functional SST-QD complex. However, it posed several challenges in the form of reduced potency, which were eventually overcome using a two-step biofunctionalization strategy, where the binding of SST to the QD was performed *in situ*, under controlled experimental conditions. The *in situ* biofunctionalized SST-QD complex enabled optical visualization of sst-mediated internalization, for the first time in the literature.

The developed SST-QD and its analogs are envisaged to be useful for wide variety of applications in both basic and applied research. For example, the same two-step strategy is applicable towards identification of sst-expressing neurons and ligand internalization characteristics, which at present is mostly limited to immunochemical techniques to visualize the receptors. In virtue of the over-expression of sst(s) in neuroendocrine tumors, SST-QD is a promising candidate for fluorescent tumor detection. However, for *in vivo* applications, the biofunctionalization strategy may require optimizations, because lowering the temperature might not be straightforward. One method to circumvent this is to use an antagonist of sst, instead of SST, to ensure that the biotin moiety remains exposed for the Sav-binding. Apart from the fluorescent labeling of diseased tissues, such nanoparticle-based sst-targeting agents can also serve as therapeutic carriers.

9

Summary and Prospects

9.1 Motivation

Somatostatin is a neurotransmitter/hormone that serves numerous significant functions in the body, ranging from regulation of blood pressure to influencing memory. Most of our understanding of the molecular level dynamics behind these functions have relied on investigations using radiolabeled somatostatin and immunocytochemical approaches, which have limitations of resolution and sensitivity. Fluorescently labeled somatostatin can provide a deep insight into the molecular dynamics of somatostatin, especially related to the post-endocytotic events that occur after the cellular activation. All the reports on fluorescently labeled somatostatin analogs contain organic fluorophores as probes that suffer from potential toxicity, instability and photobleaching, which can be overcome by using fluorescent nanoparticles. Development and demonstration of a

nanoparticle-based fluorescent probe for investigation of the molecular pathways in a somatostatin-receptor activated cell was the goal of this project.

9.2   Summary

The stages of research carried out to realize a nanoparticle-based fluorescent somatostatin probe is summarized in Figures 9.1 – 9.5, and systematically detailed below.

Figure 9.1: A range of nanoparticle types, including quantum dots and fluorescent nanodiamonds, were characterized in terms of their physical, chemical and photo physical properties, aimed at facilitating the selection of the nanoparticle types suitable as probes for biomolecular labeling. While the quantum dots presented advantages of fluorescence brightness, spectral multiplexing and commercial availability, the fluorescent nanodiamonds were bright, non-cytotoxic, and physically, chemically and photo physically robust.

Quantum dot   Fluorescent   Up conversion   Gold
                     nanodiamond   nanoparticle   nanoparticle
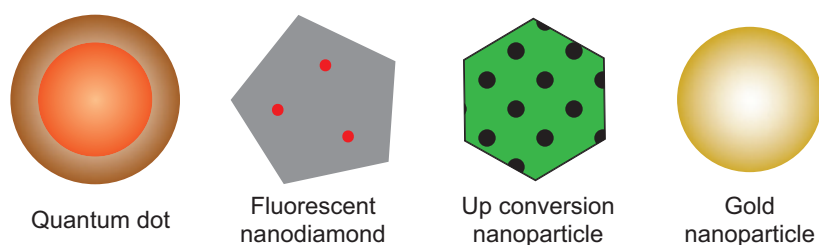
Figure 9.1: Types of nanoparticles commonly used as fluorescent probes for molecular labeling.

Figure 9.2: The surface chemistry of quantum dots and fluorescent nanodiamonds were redesigned to render them biocompatible. The introduced chemical groups served as anchor points for immobilization of targeting biomolecules. In the case of fluorescent nanodiamonds, the introduced groups were predominantly carboxyl groups (COOH) and the biomolecules were anchored by the formation of amide bonds.

Figure 9.3: New, versatile methods for anchoring a range of biomolecules to the surface of nanoparticles were developed. These methods were based on two high-affinity molecular pairs (or molecular lego pairs): streptavidin:biotin and barstar:barnase,
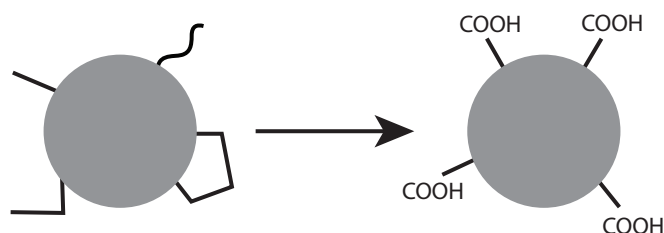
Figure 9.2: Chemical modification of nanoparticle the surface to render it biocompatible. COOH-groups facilitate the covalent attachment of biomolecules.

which served as linkers between the pre-engineered nanoparticle- and biomolecular-building blocks, facilitating a pot-mix procedure for nanoparticle biofunctionalization. The obtained biomolecule-nanoparticle-probe was robust and colloidally stable in aqueous solvents.
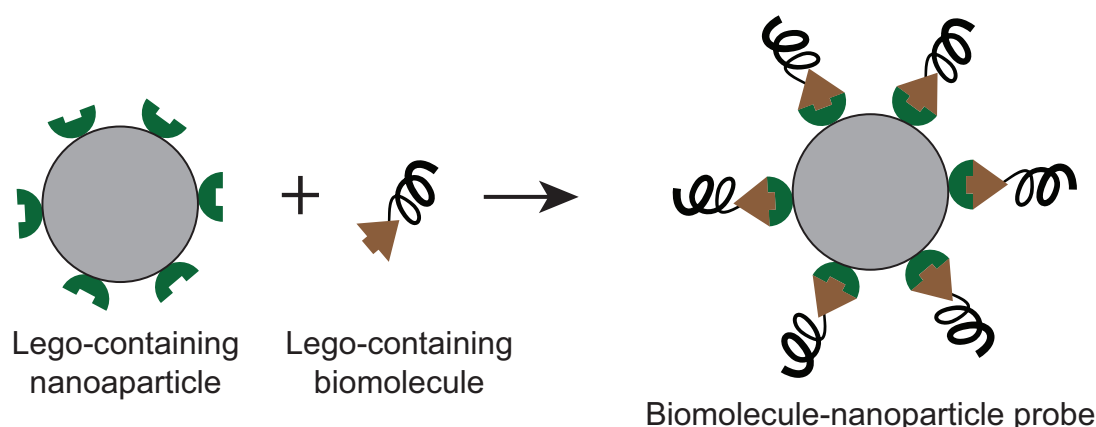

Lego-containing nanoaparticle

Lego-containing biomolecule

Biomolecule-nanoparticle probe

Figure 9.3: Versatile platform for biofunctionalization of nanoparticles with biomolecules. Pre-prepared lego counterparts – one containing a nanoparticle and the other containing a biomolecule facilitates the formation of a nanoparticle-biomolecule complex.

Figure 9.4: The effect of attachment of an external fluorescent probe to the somatostatin molecule was first investigated by using a fluorescent dye-based somatostatin probe. The developed probe was able to bind to somatostatin receptors and evoke a SST-specific cellular response, confirming that the attachment of a fluorescent moiety did not inhibit the biological activity of somatostatin. This probe allowed visualization of the cellular processes associated with somatostatin internalization.

Figure 9.5: Based on the developed techniques, a nanoparticle-based somatostatin probe was engineered using the high-affinity molecular pair – streptavidin:biotin. The
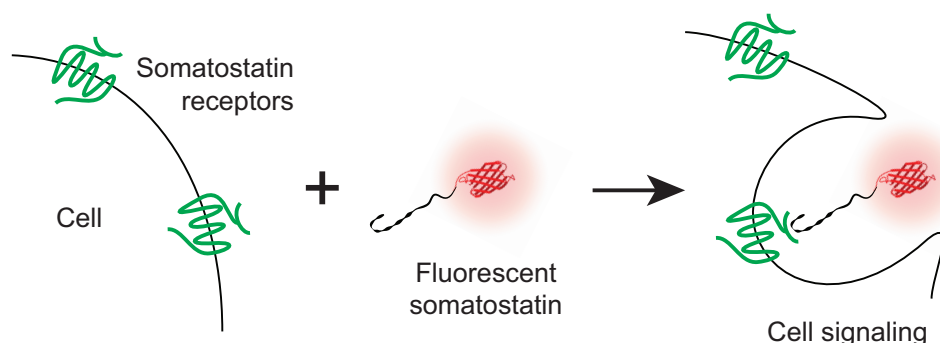
Figure 9.4: The fluorescent somatostatin probe based on a red fluorescent protein was designed, synthesized and characterized for optical and biological activity.

probe, prepared using an *in situ* two-step biofunctionalization strategy, was able to evoke a somatostatin-specific cellular activity, and enabled the visualization of somatosatin-receptor internalization. Therefore, a complete approach for fluorescent nanoparticle-based labeling of molecular trafficking has been developed!
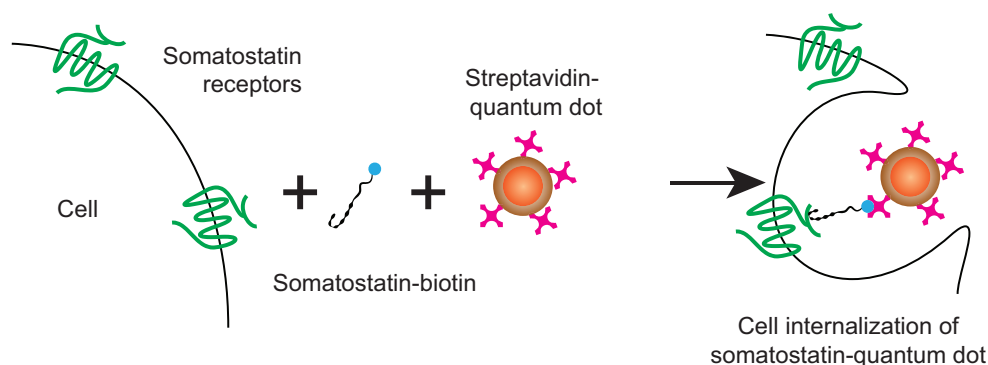

Figure 9.5: The fluorescent nanoparticle-based somatostatin probe is biologically active, and evokes a somatostatin-specific cellular response.

9.3   Prospects

The developed nanoparticle-based somatostatin probe has far-reaching prospects, based on the abundance and physiological significance of somatostatin. Firstly, the developed fluorescent nanoparticles will serve as molecular probes for visualization of the cellular processes activated by somatostatin. These studies can provide deeper understanding of the molecular pathways that underlie somatostatin-regulated physiological functions.

In vivo optical imaging of specific tissue sites labeled with somatostatin fluorescent probes opens exciting prospects in life sciences and clinical medicine. One such application is based on the increased level of somatostatin receptor expression in neuroendocrine tumors. Currently, detection and localization of these tumors is based on PET (positron emission tomography) or SPECT (single-photon emission computed tomography) imaging, whereby radiolabeled somatostatin analogs accumulated in these tumor sites are localized. Nanoparticle-based probes will not only improve the sensitivity of tumor localization in the sub-surface tissues, but also enable fluorescence-guided surgery, where the fluorescent nanoparticles accumulated in the tumor site can be optically visualized in real-time during a tumor resection procedure. One of the main disadvantages of these fluorescent probes arises from the limited depth of optical penetration (≈ 10 μm), which precludes deep-tissue tumor detection. Recent advances in nanotechnology and the development of up conversion nanoparticles are aimed at increasing the penetration depth up to a few millimeters[67].

Besides providing fluorescence contrast, many nanoparticles also embody the characteristics required for a molecular cargo transport vehicle. Their large biocompatible surface can accommodate molecules such as drugs and genes, together with the tumor targeting groups (e. g., somatostatin). Therefore, they can be designed for preferential release of the drugs after reaching tumor sites, enabling targeted drug transport and delivery. These applications of nanoparticle:somatostatin and other related complexes crucially rely on advances in the fields of biotechnology, biochemistry, nanotechnology and optical microscopy.

In summary, the work presented here extends far beyond the development of a fluorescent probe of somatostatin, and a complete methodology ranging from fluorescent nanoparticle engineering to its targeted delivery is established. Nanoparticles with improved qualities, such as the emerging nanoruby[71], can be precisely tailored to specific bio-applications, leading to new applications, such as single nanoparticle imaging in a heavily stained cell. Biofunctionalization is now easy, almost a mix-pot procedure. Nanoparticle targeting relies on the developed receptor:ligands and other agents, including antibodies and metabolites, with which one can deliver therapeutic drugs or

genetic material to a great variety of cell and tissue sites, *in vitro* and *in vivo*.

# Appendices

A

Program for Cell Counting

The following program was built to count the growth density of the CHO-K1 cells. The graphical user interface (GUI) was built using the GUI Design Environment (GUIDE) package, in-built in Matlab R2009A. The code and interface for cell counting are presented in the following sections.

Graphical Interface

Executing the program initiates two windows - a control window and the output window, which are presented in Figures A.1(a) and A.1(b), respectively. The control
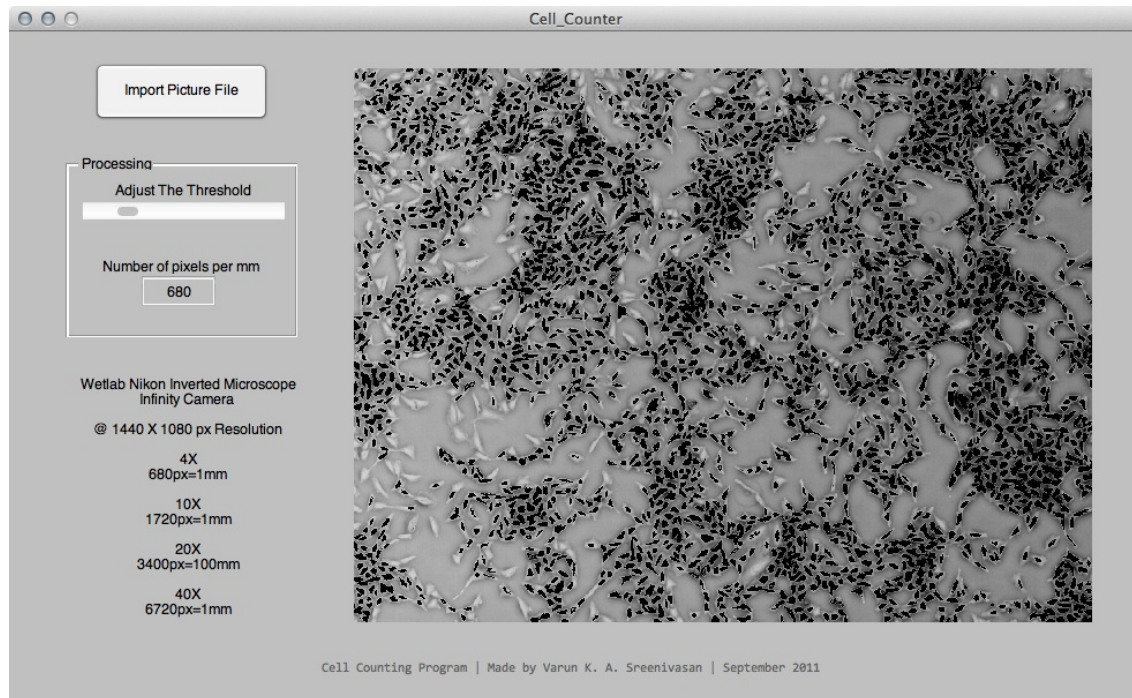
(a) Control window. Black patches indicate the cells have been counted.
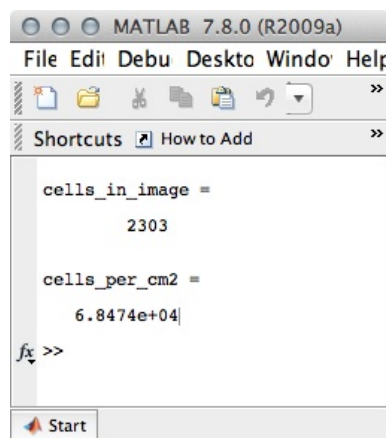
(b) Output window.

Figure A.1: The graphic user interface of the cell counting program.

window allows the user to choose a picture, set the threshold for counting and adjust the scale. Upon adjusting the threshold-slider, the program executes a counting algorithm and displays the total number of cells in the output window. Adjusting the scale, the program determines the no of cells per sq. cm, based on the total number calculated previously. This program also includes an easter egg [see http://en.wikipedia.org/wiki/Easter_egg_(media)].

Distribution

A self-executable version of this program is available for download at:

http://web.science.mq.edu.au/∼varun.

B

Program for Membrane Potential Assay
Data Analysis

The following program was built to analyze the membrane potential assay data generated by Softmax Pro - the software that controls the Flexstation. Membrane potential assays were performed numerous times in this project, and some of them were discussed in Sections 5.6.1 and 8.3.1.1. Each file obtained after these assays contained several thousand data points, in a tab-delimited ascii file format as shown in the snippet below.

```
Plate:  Plate#1 1.3 TimeFormat  FLEX    Fluorescence    ...
Temperature(deg C)  A1T A1  A2T A2  A3T A3  A4T A4  A5T ...
37.00           0.7412  164.037 0.7384  187.628 0.7454  ...
37.00           2.8132  162.029 2.82    188.633 2.8878  ...
```

```
37.00                4.8956  163.219 4.9328  187.743 4.9902  ...

37.00                7.0172  162.589 6.9744  187.105 7.1222  ...

...
```

Automation of data sorting and analysis significantly simplified the analysis. A graphical user interface (GUI) was designed using the GUI Design Environment (GUIDE) package, in-built in Matlab R2009A. The GUI and the code of the program for the analysis are presented in the following sections.

Graphical Interface

Launching the program initiates a GUI (shown in Figure B.1), where the raw data can be imported, analyzed and the generated output can be saved. Prior to importing the data, first value in each data file should to be changed to the number of data points. After importing the data corresponding to different columns, the display panel can be used to preview the time-course of fluorescence from each well. The user is required to define the control wells before clicking on the 'Calculate Hyperpolarization' button. The final output, in the form of % change in fluorescence in the wells can be exported as a text file for further analysis and plotting. In addition to data analysis, the program also provides a simples means to sort and consolidate the data corresponding to different columns, which is often scattered among several files, using the 'Export Raw Data' option.

Distribution

A self-executable version of this program is available for download at:

http://web.science.mq.edu.au/~varun
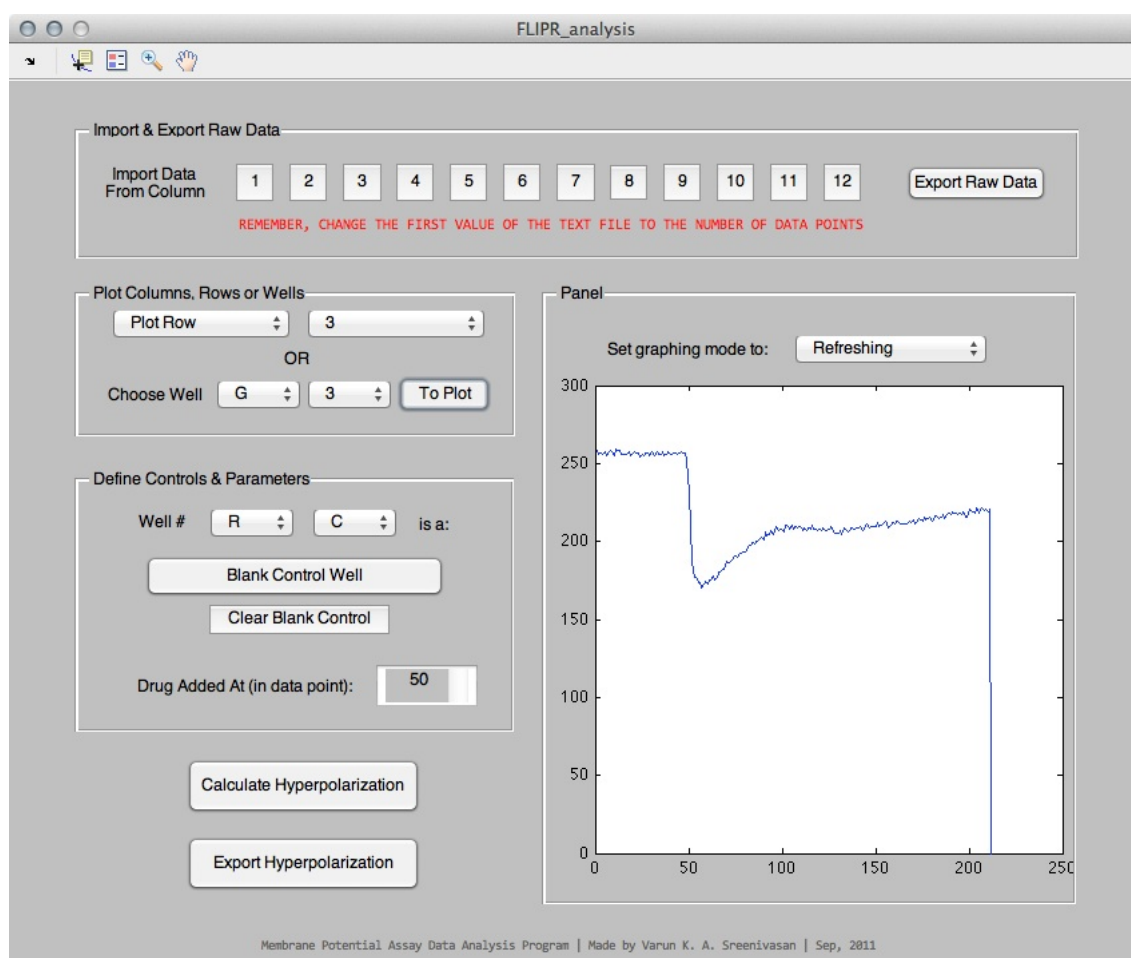
Figure B.1: The graphical user interface of the program to analyze the membrane potential assay data generated by a Flexstation.

C

Program for Calcium Mobilization Assay
Data Analysis

The following program was built to analyze the calcium mobilization assay data generated by Softmax Pro - the software that controls the Flexstation. This assay was performed numerous times in this project, for example, in Section 5.6.2. Files obtained after these assays contained several thousand data points each, in a tab-delimited ascii file format. The program compiled using Matlab served as a tool to easily analyze this enormous dataset. A graphic user interface (GUI) was generated using the GUI development environment (GUIDE) inbuilt in Matlab, for effortless analysis.

Graphical Interface

Launching the program initiates a GUI (shown in Figure C.1), where the raw data can be imported, analyzed and the generated output can be saved. Prior to importing the data, first value in each data file should to be changed to the number of data points. After importing the data corresponding to different columns, the inbuilt display panel can be used to preview the time-course of fluorescence from each well. The user is required to define the control wells before clicking on the 'Calculate [Ca] (nM)' button. The final output, in the form of increase in the concentration of Ca (in nanomolars), can be exported as a text file for further analysis and plotting. In addition to data analysis, the program also provides a simples means to sort and consolidate the data corresponding to different columns, which is often scattered among several files, using the 'Export raw data' option.

C.0.1   Using the Interface

The details on how to use the program is documented in the header of the code file, which is pasted in the following snippet:

```
1
2  %─────────────────────────────────────
3  % INSTRUCTIONS TO USE THIS PROGRAM — READ BEFORE USING
4
5  % THIS PROGRAM LETS YOU ANALYSE THE FLEXSTATION3 DATA READINGS IN ...
       A CA
6  % ASSAY USING FURA2
7
8  % ****Made by VARUN SREENIVASAN****
9
10
11 %   1. CHANGE THE FIRST VALUE IN THE DATA FILES FROM '##BLOCKS= 1' ...
       TO 'NUMBER OF
```
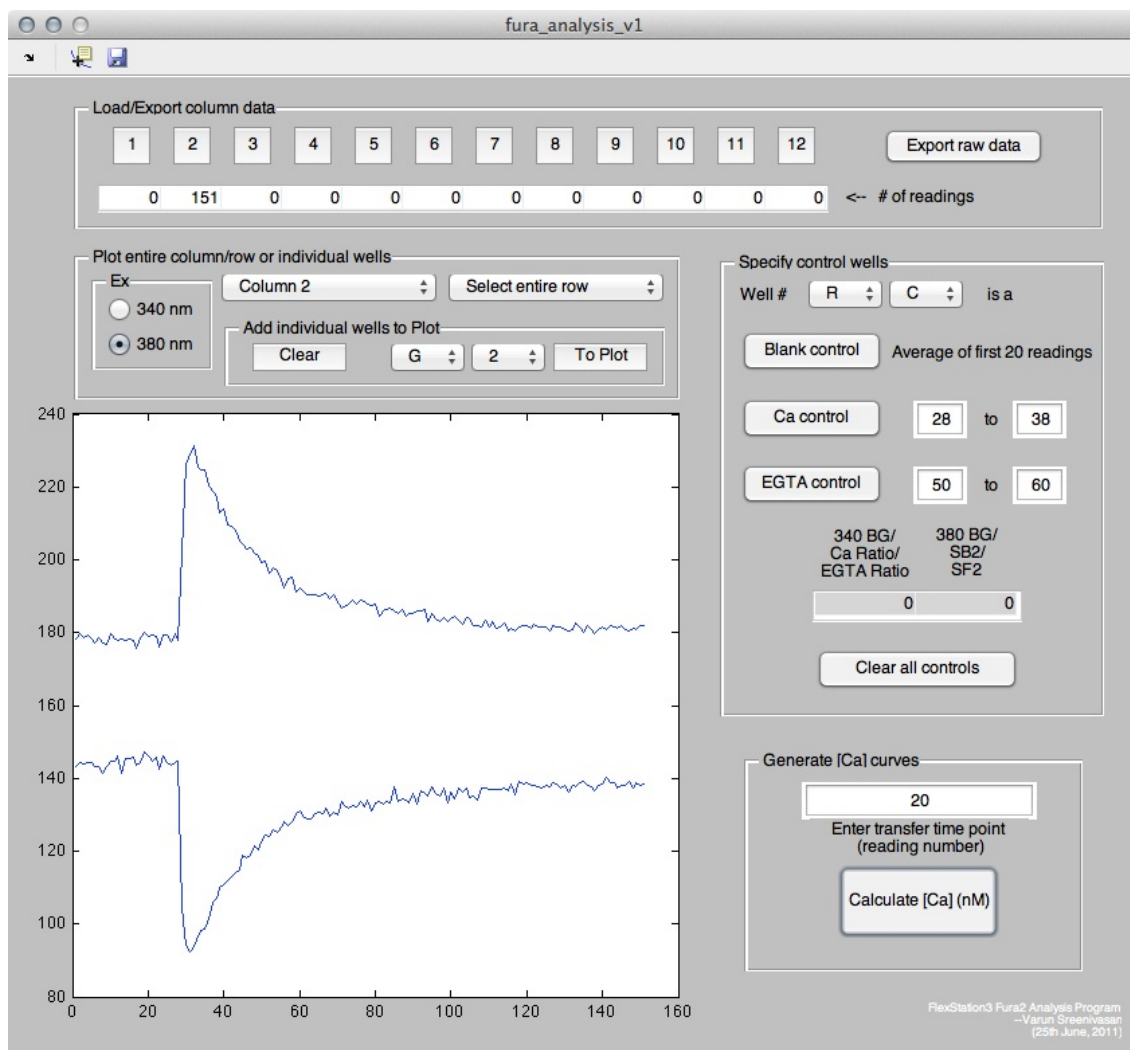
Figure C.1: The graphical user interface of the program to analyze the calcium mobilization assay data generated by a Flexstation.

```
12  %   READINGS'. THIS NUMBER CAN BE FOUND IN THE DATA FILE>SECOND ...
        ROW>THE
13  %   NUMBER JUST AFTER 'RAW FALSE'. ENSURE THAT THIS IS CORRECT...
14
15  %   2. EACH TYPE OF CONTROL (I.E. BLANK OR CA OR EGTA) SHOULD BE ...
        DONE IN A
16  %   SINGLE COLUMN. THEY CAN BE FROM DIFFERENT COLUMNS IF AND ONLY ...
        IF THEY
17  %   HAVE SAME 'NUMBER OF READINGS'.
18
```

```
19  %   3. THE MAXIMUM 'NUMBER OF READINGS' CANNOT ME MORE THAN 151. ...
        THIS CAN
20  %   VALUE CAN BE CHANGED BY ADJUSTING THE PROGRAM. DO IT YOURSELF ...
        CAREFULLY OR CONTACT ME!
21
22  %   4. IF AFTER ADDING NEW COLUMN DATA THE PLOTS DON'T CHANGE, ...
        TOGGLE THE
23  %   EXCITATION SELECTION RADIO BUTTON. IT WILL NOW UPDATE.
24
25  %   5. BACKGROUND FLUORESCENCE FROM THE BLANK CONTROL WELLS ARE ...
        AVERAGED FROM THE
26  %   FIRST 20 READINGS OF THE SELECTED SLOTS
27
28  %   6. THE VARIABLES SF2, SB2, CA RATIO AND EGTA RATIO ARE ...
        EVALUATED FROM
29  %   THE LAST 10 DATA POINTS ACQUIRED BY THE FLEXSTATION.
30
31  %   6. INCREASE IN CALCIUM CONCENTRAION IS MEASURED WITHIN 20 DATA ...
        POINTS
32  %   FROM THE SPECIFIED TRANSFER TIME. HENCE, ADJUST THE TRANSFER ...
        TIME IF
33  %   THE CA RISE TIME IS VERY SLOW
34
35  %   THE CONTROLS SHOULD BE ADDED IN THE ORDER OF 'BLANK', 'CA' AND ...
        'EGTA'
36
37  %   ****ENJOY****
38
39  %────────────────────────────────────────────────────
```

Distribution

A self-executable version of this program is available for download at:

http://web.science.mq.edu.au/~varun

D

Biosafety Approvals

Copy of the biosafety approval to work with non-gene modified eukaryotic cells.

MACQUARIE UNIVERSITY

Research Office
Research Hub, Building C5C East
MACQUARIE UNIVERSITY NSW 2109

Phone   +61 (0)2 9850 8612
Fax   +61 (0)2 9850 4465
Email   ro@vc.mq.edu.au

Biosafety Committee
Phone   +61 (0)2 9850 4194
Email   nicola.myton@vc.mq.edu.au

19 March 2010

Dr David Inglis
Department of Physics
Faculty of Science

IBC Reference: 5201000180LAB

Dear Dr Inglis

Title of project: Fluorescence imaging techniques

The above application was reviewed by the Macquarie University Biosafety Committee via the online expedited review system. The Committee raised a number of issues in relation to this application that needed to be addressed. The above application and your responses to the issues raised by the Committee were considered by the Biosafety Committee at its meeting on 17 March 2010. The Committee ratified this decision. Final Approval of the above application is granted, effective 17 March 2010.

You must inform the Committee of your willingness to accept and comply with any conditions by signing the Agreement Statement at the end of this letter, and returning one copy of this Agreement to the Committee Secretary, Ms Nicola Myton, in the Research Office at Macquarie University.

STANDARD REQUIREMENTS ATTACHED TO APPROVAL:

1. Approval will be for a period of twelve (12) months. At the end of this period, if the project is continuing then a progress report must be submitted. If, at the end of this period the project has been completed, abandoned, discontinued or not commenced for any reason, you are required to submit a Final Report. If you complete the work earlier than you had planned you must submit a Final Report as soon as the work is completed. These reports are located at the following address: http://www.research.mq.edu.au/researchers/ethics/biosafety/forms

A Progress/Final Report for this study will be due on: **17 March 2011.**

2. Please remember the Committee must be notified of any alteration to the project.

3. If you will be applying for or have applied for internal or external funding for the above project **it is your responsibility** to provide Macquarie University's Research Grants Officer with a copy of this letter as soon as possible. The Research Grants Officer will not inform external funding agencies that you have final approval for your project and funds will not be released until the Research Grants Officer has received a copy of this final approval letter.

Copy of the biosafety approval to work with gene modified eukaryotic cells.

MACQUARIE UNIVERSITY

Research Office
Research Hub, Building C5C East
MACQUARIE UNIVERSITY NSW 2109

Phone +61 (0)2 9850 8612
Fax +61 (0)2 9850 4465
Email ro@vc.mq.edu.au

Biosafety
Phone +61 (0)2 9850 4194
Email biosafety@ro.mq.edu.au

19 March 2010

Dr Timothy Kelf
Department of Physics
Faculty of Science

IBC Reference: 5201000291EX

Dear Dr Kelf

FINAL APPROVAL LETTER FOR EXEMPT DEALINGS UNDER THE GENE TECHNOLOGY REGULATIONS

Title of project: Fluorescence imaging techniques for CHO-K1 cell lines

Your application has been considered at the Macquarie University Biosafety Committee meeting held on 17 March 2010. Your application has been approved and you may now proceed with your research.

Approval has been granted subject to your compliance with the Office of the Gene Technology Regulator's standard conditions for exempt work listed below:

1. The project must be conducted in accordance with the OGTR Guidance Notes for the Containment of Exempt Dealings (http://www.ogtr.gov.au/internet/ogtr/publishing.nsf/Content/exemptdealclass-2).

2. You must inform the Biosafety Committee if you complete or abandon the exempt dealings with GMOs.

IMPORTANT INFORMATION ABOUT YOUR APPROVAL

- This approval is for a 3 year period and applies only to the organisms and procedures noted in your original Biosafety Committee application. The University requires that projects are only granted approval for up to 3 years. At the end of that period you will need to submit a Final Report and, if you wish the work to continue, you should submit a new application for the project to the Biosafety Committee.

- At the end of every 12 month period after this approval you are required to submit a progress report (if the project is continuing) to the Biosafety Committee. The progress report is located at http://www.research.mq.edu.au/researchers/ethics/biosafety. Your next progress report is due on **17 March 2011.**

IMPORTANT INFORMATION ABOUT FUNDING FOR YOUR PROJECT AND BIOSAFETY COMMITTEE APPROVAL

- If you will be applying for, or have applied for, internal or external funding for the above project **it is your responsibility** to provide Macquarie University's Grants Officer with a copy of this letter as soon as possible. The Grants Officer will not inform external funding agencies that you have final approval for your project until they have received a copy of this final approval letter. Funds will not be released by Macquarie University's Finance Office until the Grants Officer has received a copy of this final approval letter.

Macquarie University
Biosafety Committee

http://www.research.mq.edu.au/researchers/ethics/biosafety

www.mq.edu.au

List of Figures

List of Tables

References

[1] Color coded surgery - A TED video.
(Cited on page 189.)

[2] http://cellularpedia.wikispaces.com/Animal+Cell.
(Cited on page 37.)

[3] http://www.moleculardevices.com/Products/Assay-Kits/Ion-Channels/Membrane-Potential.html.
(Cited on page 101.)

[4] Paul Abbyad, William Childs, Xinghua Shi, and Steven G. Boxer. Dynamic Stokes shift in green fluorescent protein variants. *Proceedings of the National Academy of Sciences*, 104(51): 20189–20194, 2007.
(Cited on page 95.)

[5] S. Achilefu, H. N. Jimenez, R. B. Dorshow, J. E. Bugaj, E. G. Webb, R. R. Wilhelm, R. Rajagopalan, J. Johler, and J. L. Erion. Synthesis, in vitro receptor binding, and in vivo evaluation of fluorescein and carbocyanine peptide-based optical contrast agents. *Journal of Medicinal Chemistry*, 45(10):2003–2015, 2002.
(Cited on page 58.)

[6] Igor Aharonovich, Andrew D. Greentree, and Steven Prawer. Diamond photonics. *Nat Photon*, 5(7):397–405, 2011.
(Cited on page 33.)

[7] M. Akbar, F. Okajima, H. Tomura, M. A. Majid, Y. Yamada, S. Seino, and Y. Kondo. Phospholipase-C activation and Ca2+ mobilization by cloned human somatostatin receptor subtypes-1-5, in transfected COS-7 cells. *Febs Letters*, 348(2):192–196, 1994.
(Cited on pages 48, 49, 85, 104, and 126.)

[8] Ueno Akihiko. Review: fluorescent cyclodextrins for molecule sensing. *Supramolecular Science*, 3(13):31–36, 1996.

(Cited on page 12.)

[9] B. Alberts, D. Bray, J. Lewis, M. Raff, K. Roberts, and J. D. Watson. *Molecular Biology of The Cell*. Garland Publishing, 3rd edition, 1994.
(Cited on pages 35, 36, 39, 100, 104, 107, and 137.)

[10] Raphael Alford, Haley M. Simpson, Josh Duberman, G. Craig Hill, Mikako Ogawa, Celeste Regino, Hisataka Kobayashi, and Peter L. Choyke. Toxicity of Organic Fluorophores Used in Molecular Imaging: Literature Review. *Molecular Imaging*, 8(6):341–354, 2009.
(Cited on pages 13 and 17.)

[11] A. P. Alivisatos. Semiconductor Clusters, Nanocrystals, and Quantum Dots. *Science*, 271(5251): 933–937, 1996.
(Cited on pages 19, 131, and 190.)

[12] M. C. Allen and R. O. Y. Wade. Synthesis of somatostatin analogs resistant to the action of trypsin. *International Journal of Peptide and Protein Research*, 32(2):89–97, 1988.
(Cited on page 42.)

[13] Ronen Alon, Edward A. Bayer, and Meir Wilchek. Streptavidin contains an RYD sequence which mimics the RGD receptor domain of fibronectin. *Biochemical and Biophysical Research Communications*, 170(3):1236–1241, 1990.
(Cited on page 146.)

[14] Richard G. W. Anderson. The caveolae membrane system. *Annual Review of Biochemistry*, 67 (1):199, 1998.
(Cited on page 138.)

[15] Krueger Anke. New Carbon Materials: Biological Applications of Functionalized Nanodiamond Materials. *Chemistry - A European Journal*, 14(5):1382–1390, 2008.
(Cited on page 160.)

[16] N.W. Ashcroft and N.D. Mermin. *Solid state physics*. Holt, Rinehart and Winston, 1976.
(Cited on page 19.)

[17] Gopalakrishnan Balasubramanian, I. Y. Chan, Roman Kolesov, Mohannad Al-Hmoud, Julia Tisler, Chang Shin, Changdong Kim, Aleksander Wojcik, Philip R. Hemmer, Anke Krueger, Tobias Hanke, Alfred Leitenstorfer, Rudolf Bratschitsch, Fedor Jelezko, and Jorg Wrachtrup. Nanoscale imaging magnetometry with diamond spins under ambient conditions. *Nature*, 455 (7213):648–651, 2008.
(Cited on page 33.)

[18] Peter A. Banks, Darwin L. Conwell, and Phillip P. Toskes. The Management of Acute and Chronic Pancreatitis. *Gastroenterology & Hepatology*, 6(2):1, 2010.
(Cited on page 47.)

[19] C.N. Banwell. *Fundamentals of molecular spectroscopy.* McGraw-Hill, 1966.
(Cited on pages 7, 8, and 9.)

[20] M. S. Barbarakis, S. Daunert, and L. G. Bachas. Effect of different binding-proteins on the detection limits and sensitivity of assays based on biotinylated adenosine-deaminase. *Bioconjugate Chemistry*, 3(3):225–229, 1992.
(Cited on page 212.)

[21] R. Barone, P. Van Der Smissen, O. Devuyst, V. Beaujean, S. Pauwels, P. J. Courtoy, and F. Jamar. Endocytosis of the somatostatin analogue, octreotide, by the proximal tubule-derived opossum kidney (OK) cell line. *Kidney international*, 67(3):969–976, 2005.
(Cited on page 59.)

[22] Wilfried Bauer, Ulrich Briner, Wolfgang Doepfner, Roland Haller, Ren Huguenin, Peter Marbach, Trevor J. Petcher, and Janos Pless. SMS 201-995: A very potent and selective octapeptide analogue of somatostatin with prolonged action. *Life Sciences*, 31(11):1133–1140, 1982.
(Cited on pages 42 and 45.)

[23] Edward A. Bayer and Meir Wilchek. *Biotin-binding proteins: Overview and prospects*, volume Volume 184, pages 49–51. Academic Press, 1990.
(Cited on page 193.)

[24] V. Beaumont, M. B. Hepworth, J. S. Luty, E. Kelly, and G. Henderson. Somatostatin receptor desensitization in NG108-15 cells. *Journal of Biological Chemistry*, 273(50):33174–33183, 1998.
(Cited on pages 52 and 190.)

[25] A. Becker, C. Hessenius, K. Licha, B. Ebert, U. Sukowski, W. Semmler, B. Wiedenmann, and C. Grotzinger. Receptor-targeted optical imaging of tumors with near-infrared fluorescent ligands. *Nature Biotechnology*, 19(4):327–331, 2001.
(Cited on pages 12, 58, 59, 88, 124, 127, 190, and 211.)

[26] J. Bertherat, M. T. Bluetpajot, and J. Epelbaum. Neuroendocrine Regulation of Growth-Hormone. *European Journal of Endocrinology*, 132(1):12–24, 1995.
(Cited on page 42.)

[27] Alexios Beveratos, Rosa Brouri, Thierry Gacoin, Andr Villing, Jean-Philippe Poizat, and Philippe Grangier. Single Photon Quantum Cryptography. *Physical Review Letters*, 89(18): 187901, 2002.
(Cited on page 33.)

[28] V. Biju, D. Muraleedharan, K. Nakayama, Y. Shinohara, T. Itoh, Y. Baba, and M. Ishikawa. Quantum dot-insect neuropeptide conjugates for fluorescence imaging, transfection, and nucleus targeting of living cells. *Langmuir*, 23(20):10254–10261, 2007.
(Cited on pages 211 and 212.)

[29] V. Biju, T. Itoh, A. Anas, A. Sujith, and M. Ishikawa. Semiconductor quantum dots and metal nanoparticles: syntheses, optical properties, and biological applications. *Analytical and Bioanalytical Chemistry*, 391(7):2469–2495, 2008.
(Cited on page 211.)

[30] S. Boehm and H. Betz. Somatostatin inhibits excitatory transmission at rat hippocampal synapses via presynaptic receptors. *Journal of Neuroscience*, 17(11):4066–4075, 1997.
(Cited on page 46.)

[31] K. H. Bohuslavizki. Somatostatin receptor imaging: Current status and future perspectives. *Journal of Nuclear Medicine*, 42(7):1057–1058, 2001.
(Cited on pages 47 and 58.)

[32] V. S. Bondar, I. O. Pozdnyakova, and A. P. Puzyr. Applications of nanodiamonds for separation and purification of proteins. *Physics of the Solid State*, 46(4):758–760, 2004.
(Cited on page 158.)

[33] M. Born, E. Wolf, and A.B. Bhatia. *Principles of optics: electromagnetic theory of propagation, interference and diffraction of light.* Cambridge University Press, 1999.
(Cited on page 13.)

[34] C. Bradac, T. Gaebel, N. Naidoo, M. J. Sellars, J. Twamley, L. J. Brown, A. S. Barnard, T. Plakhotnik, A. V. Zvyagin, and J. R. Rabeau. Observation and control of blinking nitrogen-vacancy centres in discrete nanodiamonds. *Nature Nanotechnology*, 5(5):345–349, 2010.
(Cited on page 29.)

[35] P. Brazeau, W. Vale, R. Burgus, N. Ling, M. Butcher, J. Rivier, and R. Guillemin. Hypothalamic polypeptide that inhibits the secretion of immunoreactive pituitary growth hormone, 1973.
(Cited on pages 40 and 189.)

[36] C. D. Breder, Y. Yamada, K. Yasuda, S. Seino, C. B. Saper, and G. I. Bell. Differential Expression of Somatostatin Receptor Subtypes in Brain. *Journal of Neuroscience*, 12(10):3920–3934, 1992.
(Cited on pages 44 and 46.)

[37] W. A. P. Breeman, M. de Jong, D. J. Kwekkeboom, R. Valkema, W. H. Bakker, P. P. M. Kooij, T. J. Visser, and E. P. Krenning. Somatostatin receptor-mediated imaging and therapy: basic science, current knowledge, limitations and future perspectives. *European Journal of Nuclear Medicine*, 28(9):1421–1429, 2001.
(Cited on pages 47, 49, 58, and 87.)

[38] Michael S. Brown and Joseph L. Goldstein. Receptor-Mediated Endocytosis: Insights from the Lipoprotein Receptor System. *Proceedings of the National Academy of Sciences of the United States of America*, 76(7):3330–3337, 1979.

(Cited on pages 50 and 208.)

[39] M. Bruchez, M. Moronne, P. Gin, S. Weiss, and A. P. Alivisatos. Semiconductor nanocrystals as fluorescent biological labels. *Science*, 281(5385):2013–2016, 1998.
(Cited on pages 25 and 26.)

[40] J F Bruno, Y Xu, J Song, and M Berelowitz. Tissue distribution of somatostatin receptor subtype messenger ribonucleic acid in the rat. *Endocrinology*, 133(6):2561–7, 1993.
(Cited on pages 45, 86, 124, and 211.)

[41] P. G. R. Burke, Q. Li, M. L. Costin, S. McMullan, P. M. Pilowsky, and A. K. Goodchild. Somatostatin 2A Receptor-Expressing Presympathetic Neurons in the Rostral Ventrolateral Medulla Maintain Blood Pressure. *Hypertension*, 52(6):1127–U86, 2008.
(Cited on pages 12, 46, 53, 86, and 189.)

[42] P. G. R. Burke, S. B. G. Abbott, S. McMullan, A. K. Goodchild, and P. M. Pilowsky. Somatostatin selectively ablates post-inspiratory activity after injection into the Btzinger complex. *Neuroscience*, 167(2):528–539, 2010.
(Cited on page 86.)

[43] Daniel E. Callahan, Amna Karim, Gemin Zheng, o Paul O. P. Ts, and Stephen A. Lesko. Quantitation and mapping of integrated human papillomavirus on human metaphase chromosomes using a fluorescence microscope imaging system. *Cytometry*, 13(5):453–461, 1992.
(Cited on page 14.)

[44] R. E. Campbell, O. Tour, A. E. Palmer, P. A. Steinbach, G. S. Baird, D. A. Zacharias, and R. Y. Tsien. A monomeric red fluorescent protein. *Proceedings of the National Academy of Sciences of the United States of America*, 99(12):7877–7882, 2002.
(Cited on pages 93, 95, 97, 125, and 126.)

[45] R C Casad and R C Adelman. Aging enhances inhibitory action of somatostatin in rat pancreas. *Endocrinology*, 130(4):2420–2, 1992.
(Cited on page 46.)

[46] D. Cervia and P. Bagnoli. An update on somatostatin receptor signaling in native systems and new insights on their pathophysiology. *Pharmacology & Therapeutics*, 116(2):322–341, 2007.
(Cited on pages 42, 49, and 58.)

[47] R. Cescato, S. Schulz, B. Waser, V. Eltschinger, J. E. Rivier, H. J. Wester, M. Culler, M. Ginj, Q. S. Liu, A. Schonbrunn, and J. C. Reubi. Internalization of sst(2), sst(3), and sst(5) receptors: Effects of somatostatin agonists and antagonists. *Journal of Nuclear Medicine*, 47(3):502–511, 2006.
(Cited on pages 45, 53, 56, 57, 86, and 112.)

[48] W. C. W. Chan and S. M. Nie. Quantum dot bioconjugates for ultrasensitive nonisotopic detection. *Science*, 281(5385):2016–2018, 1998.
(Cited on pages 25, 132, and 191.)

[49] W. C. W. Chan, D. J. Maxwell, X. H. Gao, R. E. Bailey, M. Y. Han, and S. M. Nie. Luminescent quantum dots for multiplexed biological detection and imaging. *Current Opinion in Biotechnology*, 13(1):40–46, 2002.
(Cited on pages 131 and 190.)

[50] J. I. Chao, E. Perevedentseva, P. H. Chung, K. K. Liu, C. Y. Cheng, C. C. Chang, and C. L. Cheng. Nanometer-sized diamond particle as a probe for biolabeling. *Biophysical Journal*, 93 (6):2199–2208, 2007.
(Cited on page 157.)

[51] Dev K. Chatterjee, Abdul J. Rufaihah, and Yong Zhang. Upconversion fluorescence imaging of cells and small animals using lanthanide doped nanocrystals. *Biomaterials*, 29(7):937–943, 2008.
(Cited on page 13.)

[52] Yin Hoon Chew, Yoke Lin Shia, Chew Tin Lee, Fadzilah Adibah Abdul Majid, Lee Suan Chua, Mohamad Roji Sarmidi, and Ramlan Abdul Aziz. Modeling of glucose regulation and insulin-signaling pathways. *Molecular and Cellular Endocrinology*, 303(12):13–24, 2009.
(Cited on page 36.)

[53] B. Devika Chithrani and Warren C. W. Chan. Elucidating the Mechanism of Cellular Uptake and Removal of Protein-Coated Gold Nanoparticles of Different Sizes and Shapes. *Nano Letters*, 7(6):1542–1550, 2007.
(Cited on pages 132, 147, and 148.)

[54] B. Devika Chithrani, Arezou A. Ghazani, and Warren C. W. Chan. Determining the Size and Shape Dependence of Gold Nanoparticle Uptake into Mammalian Cells. *Nano Letters*, 6(4): 662–668, 2006.
(Cited on page 147.)

[55] Bonghwan Chon, Sung Jun Lim, Wonjung Kim, Jongcheol Seo, Hyeonggon Kang, Taiha Joo, Jeeseong Hwang, and Seung Koo Shin. Shell and ligand-dependent blinking of CdSe-based core/shell nanocrystals. *Physical Chemistry Chemical Physics*, 12(32), 2010.
(Cited on page 27.)

[56] J. Clark, E. M. Singer, D. R. Korns, and S. S. Smith. Design and analysis of nanoscale bioassemblies. *BioTechniques*, 36(6):992–1001, 2004.
(Cited on pages 192, 193, and 211.)

[57] A. M. Crider. Somatostatin receptor agonists and antagonists. *Expert Opinion on Therapeutic Patents*, 13(9):1427–1441, 2003.
(Cited on pages 42 and 45.)

[58] B. X. Cui, C. B. Wu, L. Chen, A. Ramirez, E. L. Bearer, W. P. Li, W. C. Mobley, and S. Chu. One at a time, live tracking of NGF axonal transport using quantum dots. *Proceedings of the National Academy of Sciences of the United States of America*, 104(34):13666–13671, 2007.
(Cited on page 27.)

[59] B. O. Dabbousi, J. Rodriguez-Viejo, F. V. Mikulec, J. R. Heine, H. Mattoussi, R. Ober, K. F. Jensen, and M. G. Bawendi. (CdSe)ZnS core - - shell Quantum dots: Synthesis and characterization of a size series of highly luminescent nanocrystallites. *The Journal of Physical Chemistry B*, 101(46):9463–9475, 1997.
(Cited on pages 24 and 25.)

[60] S. A. Dahoumane, M. N. Nguyen, A. Thorel, J. P. Boudou, M. M. Chehimi, and C. Mangeney. Protein-Functionalized Hairy Diamond Nanoparticles. *Langmuir*, 25(17):9633–9638, 2009.
(Cited on page 162.)

[61] J. H. M. de Lange, N. W. Schipper, G. J. Schuurhuis, T. K. ten Kate, Th H. M. Van Heijningen, H. M. Pinedo, J. Lankelma, and J. P. A. Baak. Quantification by laser scan microscopy of intracellular doxorubicin distribution. *Cytometry*, 13(6):571–576, 1992.
(Cited on page 14.)

[62] W Denk, JH Strickler, and WW Webb. Two-photon laser scanning fluorescence microscopy. *Science*, 248(4951):73–76, 1990.
(Cited on page 13.)

[63] Austin M. Derfus, Warren C. W. Chan, and Sangeeta N. Bhatia. Probing the Cytotoxicity of Semiconductor Quantum Dots. *Nano Letters*, 4(1):11–18, 2003.
(Cited on page 27.)

[64] Mangesh C. Deshpande, Martyn C. Davies, Martin C. Garnett, Philip M. Williams, David Armitage, Lindsey Bailey, Maria Vamvakaki, Steven P. Armes, and Snjezana Stolnik. The effect of poly(ethylene glycol) molecular architecture on cellular interaction and uptake of DNA complexes. *Journal of Controlled Release*, 97(1):143–156, 2004.
(Cited on page 142.)

[65] S. M. Deyev, R. Waibel, E. N. Lebedenko, A. P. Schubiger, and A. Pluckthun. Design of multivalent complexes using the barnase-barstar module. *Nature Biotechnology*, 21(12):1486–1492, 2003.
(Cited on pages 163, 164, and 193.)

[66] M. W. Doherty, N. B. Manson, P. Delaney, and L. C. L. Hollenberg. The negatively charged nitrogen-vacancy centre in diamond: the electronic solution. *New Journal of Physics*, 13(2): 025019, 2011.
(Cited on pages 29, 30, and 33.)

[67] Ning-Ning Dong, Marco Pedroni, Fabio Piccinelli, Giamaica Conti, Andrea Sbarbati, Juan Enrique Ramrez-Hernndez, Laura Martnez Maestro, Maria Carmen Iglesias-de la Cruz, Francisco Sanz-Rodriguez, Angeles Juarranz, Feng Chen, Fiorenzo Vetrone, John A. Capobianco, Jos Garca Sol, Marco Bettinelli, Daniel Jaque, and Adolfo Speghini. NIR-to-NIR Two-Photon Excited CaF2:Tm3+,Yb3+ Nanoparticles: Multifunctional Nanoprobes for Highly Penetrating Fluorescence Bio-Imaging. *ACS Nano*, 5(11):8665–8671, 2011.
(Cited on page 219.)

[68] D. Douroumis, O. Obonyo, E. Fisher, and M. Edwards. Quantum dots synthesis and biological applications as imaging and drug delivery systems. *Critical Reviews in Biotechnology*, 30(4): 283–301, 2010.
(Cited on pages 25, 26, and 191.)

[69] Boris Draznin, Nancy Sherman, Karl Sussman, Rolf Dahl, and Albert Vatter. Internalization and Cellular Processing of Somatostatin in Primary Culture of Rat Anterior Pituitary Cells. *Endocrinology*, 117(3):960–966, 1985.
(Cited on pages 49, 53, 87, 109, 127, and 211.)

[70] T. V. Duncan, M. A. M. Polanco, Y. Kim, and S. J. Park. Improving the Quantum Yields of Semiconductor Quantum Dots through Photoenhancement Assisted by Reducing Agents. *Journal of Physical Chemistry C*, 113(18):7561–7566, 2009.
(Cited on page 25.)

[71] A. M Edmonds, M. A. Sobhan, V. K. A. Sreenivasan, J. R. Rabeau, E. M. Goldys, and A. V. Zvyagin. Nano-ruby: A new fluorescent probe for background-free cellular imaging. under review.
(Cited on page 219.)

[72] A. I. Ekimov, F. Hache, M. C. Schanne-Klein, D. Ricard, C. Flytzanis, I. A. Kudryavtsev, T. V. Yazeva, A. V. Rodina, and Al L. Efros. Absorption and intensity-dependent photoluminescence measurements on CdSe quantum dots: assignment of the first electronic transitions. *J. Opt. Soc. Am. B*, 10(1):100–107, 1993.
(Cited on page 23.)

[73] Chang Emmanuel, Thekkek Nadhi, W. Yu William, L. Colvin Vicki, and Drezek Rebekah. Evaluation of Quantum Dot Cytotoxicity Based on Intracellular Uptake13. *Small*, 2(12):1412–1417, 2006.

(Cited on page 27.)

[74] J. Erchegyi, C. R. R. Grace, M. Samant, R. Cescato, V. Piccand, R. Riek, J. C. Reubi, and J. E. Rivier. Ring Size of Somatostatin Analogues (ODT-8) Modulates Receptor Selectivity and Binding Affinity. *Journal of Medicinal Chemistry*, 51(9):2668–2675, 2008.
(Cited on page 42.)

[75] J. Feindt, I. Becker, U. Blmer, H. H. Hugo, H. M. Mehdorn, B. Krisch, and R. Mentlein. Expression of Somatostatin Receptor Subtypes in Cultured Astrocytes and Gliomas. *Journal of Neurochemistry*, 65(5):1997–2005, 1995.
(Cited on page 47.)

[76] Kimberly A. Foster, Mehran Yazdanian, and Kenneth L. Audus. Microparticulate uptake mechanisms of in-vitro cell culture models of the respiratory epithelium. *Journal of Pharmacy and Pharmacology*, 53(1):57–66, 2001.
(Cited on page 149.)

[77] C. C. Fu, H. Y. Lee, K. Chen, T. S. Lim, H. Y. Wu, P. K. Lin, P. K. Wei, P. H. Tsao, H. C. Chang, and W. Fann. Characterization and application of single fluorescent nanodiamonds as cellular biomarkers. *Proceedings of the National Academy of Sciences of the United States of America*, 104(3):727–732, 2007.
(Cited on pages 33 and 132.)

[78] Keiichiro Fuwa and B. L. Valle. The Physical Basis of Analytical Atomic Absorption Spectrometry. The Pertinence of the Beer-Lambert Law. *Analytical Chemistry*, 35(8):942–946, 1963.
(Cited on page 63.)

[79] Susan R. George, Brian F. O'Dowd, and Samuel P. Lee. G-Protein-coupled receptor oligomerization and its potential for drug discovery. *Nature Reviews Drug Discovery*, 1(10):808, 2002.
(Cited on pages 40 and 41.)

[80] D. Gerion, F. Pinaud, S. C. Williams, W. J. Parak, D. Zanchet, S. Weiss, and A. P. Alivisatos. Synthesis and properties of biocompatible water-soluble silica-coated CdSe/ZnS semiconductor quantum dots. *Journal of Physical Chemistry B*, 105(37):8861–8871, 2001.
(Cited on pages 25 and 26.)

[81] N. Gibson, O. Shenderova, T. J. M. Luo, S. Moseenkov, V. Bondar, A. Puzyr, K. Purtov, Z. Fitzgerald, and D. W. Brenner. Colloidal stability of modified nanodiamond particles. *Diamond and Related Materials*, 18(4):620–626, 2009.
(Cited on page 158.)

[82] A G Gilman. G Proteins: Transducers of Receptor-Generated Signals. *Annual Review of Biochemistry*, 56(1):615–649, 1987.
(Cited on page 40.)

[83] I. D. Goldfine, B. M. Kriz, K. Y. Wong, G. Hradek, A. L. Jones, and J. A. Williams. Insulin action in pancreatic acini from streptozotocin-treated rats. III. Electron microscope autoradiography of 125I-insulin. *American Journal of Physiology - Gastrointestinal and Liver Physiology*, 240(1):G69–G75, 1981.
(Cited on page 49.)

[84] M. Grant and U. Kumar. The role of G-proteins in the dimerisation of human somatostatin receptor types 2 and 5. *Regulatory Peptides*, 159(1-3):3–8, 2010.
(Cited on pages 54 and 86.)

[85] M. Grant, B. Collier, and U. Kumar. Agonist-dependent dissociation of human somatostatin receptor 2 dimers - A role in receptor trafficking. *Journal of Biological Chemistry*, 279(35): 36179–36183, 2004.
(Cited on pages 53, 54, 55, and 203.)

[86] Peter Grass, Peter Marbach, Christian Bruns, and Ioana Lancranjan. Sandostatin LAR (microencapsulated octreotide acetate) in acromegaly: Pharmacokinetic and pharmacodynamic relationships. *Metabolism*, 45, Supplement 1(0):27–30, 1996.
(Cited on page 47.)

[87] Stephanie E. A. Gratton, Patricia A. Ropp, Patrick D. Pohlhaus, J. Christopher Luft, Victoria J. Madden, Mary E. Napier, and Joseph M. DeSimone. The effect of particle design on cellular internalization pathways. *Proceedings of the National Academy of Sciences*, 105(33):11613–11618, 2008.
(Cited on pages 147 and 149.)

[88] H. E. Grecco, K. A. Lidke, R. Heintzmann, D. S. Lidke, C. Spagnuolo, O. E. Martinez, E. A. Jares-Erijman, and T. M. Jovin. Ensemble and single particle photophysical proper-ties (Two-Photon excitation, anisotropy, FRET, lifetime, spectral conversion) of commercial quantum dots in solution and in live cells. *Microscopy Research and Technique*, 65(4-5):169–179, 2004.
(Cited on page 212.)

[89] N M Green, L Konieczny, E J Toms, and R C Valentine. The use of bifunctional biotinyl compounds to determine the arrangement of subunits in avidin. *Biochem. J.*, 125(3):781–791, 1971.
(Cited on pages 204 and 206.)

[90] NM Green. Avidin. *Advances in Protein Chemistry*, 29:85–133, 1975.
(Cited on pages 193 and 212.)

[91] L. Groc, M. Lafourcade, M. Heine, M. Renner, V. Racine, J. B. Sibarita, B. Lounis, D. Choquet, and L. Cognet. Surface trafficking of neurotransmitter receptor: Comparison between single-molecule/quantum dot strategies. *Journal of Neuroscience*, 27(46):12433–12437, 2007.

(Cited on page 15.)

[92] A. Gruber, A. Drabenstedt, C. Tietz, L. Fleury, J. Wrachtrup, and C. vonBorczyskowski. Scanning confocal optical microscopy and magnetic resonance on single defect centers. *Science*, 276 (5321):2012–2014, 1997.
(Cited on pages 29 and 32.)

[93] H. J. Gruber, M. Marek, H. Schindler, and K. Kaiser. Biotin-fluorophore conjugates with poly(ethylene glycol) spacers retain intense fluorescence after binding to avidin and streptavidin. *Bioconjugate Chemistry*, 8(4):552–559, 1997.
(Cited on pages 206 and 212.)

[94] G Grynkiewicz, M Poenie, and R Y Tsien. A new generation of Ca2+ indicators with greatly improved fluorescence properties. *Journal of Biological Chemistry*, 260(6):3440–3450, 1985.
(Cited on pages 14, 76, 78, and 104.)

[95] Yi-Zhong Gu and Agnes Schonbrunn. Coupling Specificity between Somatostatin Receptor sst2A and G Proteins: Isolation of the Receptor-G Protein Complex with a Receptor Antibody. *Mol Endocrinol*, 11(5):527–537, 1997.
(Cited on pages 86, 87, and 107.)

[96] Kevin J. Hamblett, Oliver W. Press, Damon L. Meyer, Don K. Hamlin, Don Axworthy, D. Scott Wilbur, and Patrick S. Stayton. Role of Biotin-Binding Affinity in Streptavidin-Based Pretargeted Radioimmunotherapy of Lymphoma. *Bioconjugate Chemistry*, 16(1):131–138, 2005.
(Cited on page 193.)

[97] R. T. Harley, M. J. Henderson, and R. M. Macfarlane. Persistent spectral hole burning of colour centres in diamond. *Journal of Physics C: Solid State Physics*, 17(8):L233, 1984.
(Cited on page 29.)

[98] Ruth L. Harold and F. M. Harold. Configuration of actin microfilaments during sporangium development in *Achlya bisexuali*: comparison of two staining protocol. *Protoplasma*, 171(3): 110–116, 1992.
(Cited on page 14.)

[99] A. G. Harris. Somatostatin and somatostatin analogues: pharmacokinetics and pharmacodynamic effects. *Gut*, 35(3 Suppl):S1, 1994.
(Cited on pages 42, 125, and 197.)

[100] J. Harrison, M. J. Sellars, and N. B. Manson. Measurement of the optically induced spin polarisation of N-V centres in diamond. *Diamond and Related Materials*, 15(48):586–588, 2006.
(Cited on page 33.)

[101] Robert W Hartley. Barnase and barstar: Expression of its cloned inhibitor permits expression of a cloned ribonuclease. *Journal of Molecular Biology*, 202(4):913–915, 1988.
(Cited on pages 163 and 193.)

[102] R.P. Haugland and M.T.Z. Spence. *Handbook of fluorescent probes and research products*. Molecular Probes, 2002.
(Cited on page 13.)

[103] S. Heer, O. Lehmann, M. Haase, and H. U. Gudel. Blue, green, and red upconversion emission from lanthanide-doped LuPO4 and YbPO4 nanocrystals in a transparent colloidal solution. *Angewandte Chemie-International Edition*, 42(27):3179–3182, 2003.
(Cited on page 19.)

[104] Seymour Heisler and Coimbatore B. Srikant. Somatostatin-14 and Somatostatin-28 Pretreatment Down-Regulate Somatostatin-14 Receptors and Have Biphasic Effects on Forskolin-Stimulated Cyclic Adenosine, 3',5'-Monophosphate Synthesis and Adrenocorticotropin Secretion in Mouse Anterior Pituitary Tumor Cells. *Endocrinology*, 117(1):217–225, 1985.
(Cited on pages 44, 47, 51, 109, and 190.)

[105] S. C. Hens, G. Cunningham, T. Tyler, S. Moseenkov, V. Kuznetsov, and O. Shenderova. Nanodiamond bioconjugate probes and their collection by electrophoresis. *Diamond and Related Materials*, 17(11):1858–1866, 2008.
(Cited on page 162.)

[106] J. R. Hepler and A. G. Gilman. G-Proteins. *Trends in Biochemical Sciences*, 17(10):383–387, 1992.
(Cited on pages 40 and 85.)

[107] John Frederick William Herschel. On a Case of Superficial Colour Presented by a Homogeneous Liquid Internally Colourless. *Philosophical Transactions of the Royal Society of London*, 135 (ArticleType: research-article / Full publication date: 1845 /):143–145, 1845.
(Cited on pages 7 and 9.)

[108] J. E. Heuser and R. G. W. Anderson. Hypertonic media inhibit receptor-mediated endocytosis by blocking clathrin-coated pit formation. *Journal of Cell Biology*, 108(2):389–400, 1989.
(Cited on pages 138, 139, and 150.)

[109] Bertil Hille. *Ion channels of excitable membranes*. Sinauer, Sunderland, Mass., 3rd edition, 2001.
(Cited on page 100.)

[110] M. A. Hines and P. Guyot-Sionnest. Synthesis and characterization of strongly luminescing ZnS-Capped CdSe nanocrystals. *Journal of Physical Chemistry*, 100(2):468–471, 1996.
(Cited on pages 19, 25, and 211.)

[111] R. W. Hipkin, J. Friedman, R. B. Clark, C. M. Eppler, and A. Schonbrunn. Agonist-induced desensitization, internalization, and phosphorylation of the sst2A somatostatin receptor. *Journal of Biological Chemistry*, 272(21):13869–13876, 1997.
(Cited on page 51.)

[112] Leo J. Hofland and Steven W. J. Lamberts. The Pathophysiological Consequences of Somatostatin Receptor Internalization and Resistance. *Endocrine Reviews*, 24(1):28–47, 2003.
(Cited on pages 47, 51, 52, and 58.)

[113] S. Hohng and T. Ha. Near-complete suppression of quantum dot blinking in ambient conditions. *Journal of the American Chemical Society*, 126(5):1324–1325, 2004.
(Cited on page 27.)

[114] Mark Howarth, Keizo Takao, Yasunori Hayashi, and Alice Y. Ting. Targeting quantum dots to surface proteins in living cells with biotin ligase. *Proceedings of the National Academy of Sciences of the United States of America*, 102(21):7583–7588, 2005.
(Cited on pages 132, 146, and 212.)

[115] Mark Howarth, Wenhao Liu, Sujiet Puthenveetil, Yi Zheng, Lisa F. Marshall, Michael M. Schmidt, K. Dane Wittrup, Moungi G. Bawendi, and Alice Y. Ting. Monovalent, reduced-size quantum dots for imaging receptors on living cells. *Nat Meth*, 5(5):397–399, 2008.
(Cited on page 25.)

[116] D. Hoyer, G. I. Bell, M. Berelowitz, J. Epelbaum, W. Feniuk, P. P. A. Humphrey, A. M. O'Carroll, Y. C. Patel, A. Schonbrunn, J. E. Taylor, and T. Reisine. Classification and nomenclature of somatostatin receptors. *Trends in Pharmacological Sciences*, 16(3):86–88, 1995.
(Cited on page 45.)

[117] Yong Hu, Jingwei Xie, Yen Wah Tong, and Chi-Hwa Wang. Effect of PEG conformation and particle size on the cellular uptake efficiency of nanoparticles with the HepG2 cells. *Journal of Controlled Release*, 118(1):7–17, 2007.
(Cited on pages 132 and 142.)

[118] Tian Hua, Zhang Xiping, Wu Chengjun, Chen Li, Ying Rongchao, Ye Jing, Yu Bingyan, Ye Qian, Pan Yan, Ma Meili, and Zhu Feibo. Effects of Baicalin and Octreotide on the Serum TNF- Level and Apoptosis in Multiple Organs of Rats with Severe Acute Pancreatitis. *Inflammation*, 32(3):191–201, 2009.
(Cited on page 47.)

[119] H. Huang, E. Pierstorff, E. Osawa, and D. Ho. Active nanodiamond hydrogels for chemotherapeutic delivery. *Nano Letters*, 7:3305–3314, 2007.
(Cited on pages 157 and 211.)

[120] L. C. L. Huang and H. C. Chang. Adsorption and immobilization of cytochrome c on nanodia-
monds. *Langmuir*, 20(14):5879–5884, 2004.
(Cited on pages 156 and 158.)

[121] Naomi Hudson, Andy Baker, and Darren Reynolds. Fluorescence analysis of dissolved organic
matter in natural, waste and polluted watersa review. *River Research and Applications*, 23(6):
631–649, 2007.
(Cited on page 12.)

[122] Y. Y. Hui, B. L. Zhang, Y. C. Chang, C. C. Chang, H. C. Chang, J. H. Hsu, K. Chang, and
F. H. Chang. Two-photon fluorescence correlation spectroscopy of lipid-encapsulated fluorescent
nanodiamonds in living cells. *Optics Express*, 18(6):5896–5905, 2010.
(Cited on page 159.)

[123] E. A. Ivukina, V. K. A. Sreenivasan, O. A. Stremovskiy, B. V. Veryugin, S. V. Lukash, A. V.
Zvyagin, S. M. Deyev, and R. V. Petrov. Fluorescent Nanodiamond Bioconjugates on the Base
of Barnase: Barstar Module. *Doklady Biochemistry and Biophysics*, 440(1):231–233, 2011.
(Cited on page ix.)

[124] S. Jacobs and S. Schulz. Intracellular trafficking of somatostatin receptors. *Molecular and
Cellular Endocrinology*, 286(1-2):58–62, 2008.
(Cited on pages 50, 51, 57, 58, and 109.)

[125] J. K. Jaiswal, H. Mattoussi, J. M. Mauro, and S. M. Simon. Long-term multiple color imaging
of live cells using quantum dot bioconjugates. *Nature Biotechnology*, 21(1):47–51, 2003.
(Cited on pages 208 and 213.)

[126] K H Jakobs and G Schultz. Occurrence of a hormone-sensitive inhibitory coupling component
of the adenylate cyclase in S49 lymphoma cyc- variants. *Proceedings of the National Academy
of Sciences*, 80(13):3899–3902, 1983.
(Cited on page 49.)

[127] F. Jelezko, C. Tietz, A. Gruber, I. Popa, A. Nizovtsev, S. Kilin, and J. Wrachtrup. Spectroscopy
of single NV centers in diamond. *Single Molecules*, 2(4), 2001.
(Cited on page 29.)

[128] I. Johnson. Fluorescent probes for living cells. *Histochemical Journal*, 30(3):123–140, 1998.
(Cited on pages 13 and 15.)

[129] Andreas Junk and Falk Riess. From an idea to a vision: There's plenty of room at the bottom.
American Journal of Physics, 74(9):825–830, 2006.
(Cited on page 2.)

[130] Brad A. Kairdolf, Michael C. Mancini, Andrew M. Smith, and Shuming Nie. Minimizing Nonspecific Cellular Binding of Quantum Dots with Hydroxyl-Derivatized Surface Coatings. *Analytical Chemistry*, 80(8):3029–3034, 2008.
(Cited on page 149.)

[131] H. P. Kalofonos, M. Rusckowski, D. A. Siebecker, G. B. Sivolapenko, D. Snook, J. P. Lavender, A. A. Epenetos, and D. J. Hnatowich. Imaging of Tumor in Patients with Indium-111-Labeled Biotin and Streptavidin-Conjugated Antibodies: Preliminary Communication. *J Nucl Med*, 31 (11):1791–1796, 1990.
(Cited on page 193.)

[132] T. A. Kelf, V. K. A. Sreenivasan, J. Sun, E. J. Kim, E. M. Goldys, and A. V. Zvyagin. Nonspecific cellular uptake of surface-functionalized quantum dots. *Nanotechnology*, 21(28), 2010.
(Cited on pages x, 13, 129, and 151.)

[133] R. Khurana, A. T. Hate, U. Nath, and J. B. Udgaonkar. pH-dependence of the stability of barstar to chemical and thermal denaturation. *Protein Science*, 4(6):1133–1144, 1995.
(Cited on page 164.)

[134] John A. Kiernan. *Microscopy Today*, 12(c):8–12, 2000.
(Cited on page 96.)

[135] C. Kittel. *Introduction to solid state physics*. Wiley, 2005.
(Cited on pages 19, 21, and 28.)

[136] J. A. Koenig, J. M. Edwardson, and P. P. A. Humphrey. Somatostatin receptors in Neuro2A neuroblastoma cells: ligand internalization. *British Journal of Pharmacology*, 120(1):52–59, 1997.
(Cited on pages 52, 53, 127, and 190.)

[137] J. A. Koenig, R. Kaur, I. Dodgeon, J. M. Edwardson, and P. P. A. Humphrey. Fates of endocytosed somatostatin sst(2) receptors and associated agonists. *Biochemical Journal*, 336: 291–298, 1998.
(Cited on pages 52, 87, 111, 208, and 213.)

[138] G. Kostenich, N. Livnah, T. A. Bonasera, T. Yechezkel, Y. Salitra, P. Litman, S. Kimel, and A. Orenstein. Targeting small-cell lung cancer with novel fluorescent analogs of somatostatin. *Lung Cancer*, 50(3):319–328, 2005.
(Cited on pages 58, 88, and 125.)

[139] K. Krempels, B. Hunyady, A. M. O'Carroll, and E. Mezey. Distribution of somatostatin receptor messenger RNAs in the rat gastrointestinal tract. *Gastroenterology*, 112(6):1948–1960, 1997.
(Cited on page 46.)

[140] Brigitte Krisch, Janka Feindt, and Rolf Mentlein. Immunoelectronmicroscopic Analysis of the Ligand-induced Internalization of the Somatostatin Receptor Subtype 2 in Cultured Human Glioma Cells. *J. Histochem. Cytochem.*, 46(11):1233–1242, 1998.
(Cited on pages 50, 54, 109, and 211.)

[141] A. Kruger, Y. J. Liang, G. Jarre, and J. Stegk. Surface functionalisation of detonation diamond suitable for biological applications. *Journal of Materials Chemistry*, 16(24):2322–2328, 2006.
(Cited on pages 161 and 162.)

[142] Svnt Kuchibhatla, A. S. Karakoti, and S. Seal. Colloidal stability by surface modification. *JOM Journal of the Minerals, Metals and Materials Society*, 57(12):52–56, 2005.
(Cited on page 159.)

[143] J.R. Lakowicz. *Principles of fluorescence spectroscopy.* Springer, 3 edition, 2006.
(Cited on pages 7, 8, 11, and 13.)

[144] D. R. Larson, W. R. Zipfel, R. M. Williams, S. W. Clark, M. P. Bruchez, F. W. Wise, and W. W. Webb. Water-soluble quantum dots for multiphoton fluorescence imaging in vivo. *Science*, 300 (5624):1434–1436, 2003.
(Cited on page 191.)

[145] Susan F. Law, Donna Woulfe, and Terry Reisine. Somatostatin receptor activation of cellular effector systems. *Cellular Signalling*, 7(1):1–8, 1995.
(Cited on page 49.)

[146] S. Le Gac, I. Vermes, and A. van den Berg. Quantum dots based probes conjugated to annexin V for photostable apoptosis detection and imaging. *Nano Letters*, 6(9):1863–1869, 2006.
(Cited on page 212.)

[147] Isolde Le Trong, Stefanie Freitag, Lisa A. Klumb, Vano Chu, Patrick S. Stayton, and Ronald E. Stenkamp. Structural studies of hydrogen bonds in the high-affinity streptavidin–biotin complex: mutations of amino acids interacting with the ureido oxygen of biotin. *Acta Crystallographica: Section D (Wiley-Blackwell)*, 59(9):1567, 2003.
(Cited on page 194.)

[148] Frederic Leblond, Scott C. Davis, Pablo A. Valds, and Brian W. Pogue. Pre-clinical whole-body fluorescence imaging: Review of instruments, methods and applications. *Journal of Photochemistry and Photobiology B: Biology*, 98(1):77–94, 2010.
(Cited on page 12.)

[149] B. Lelouvier, G. Tamagno, A. M. Kaindl, A. Roland, V. Lelievre, V. Le Verche, C. Loudes, P. Gressens, A. Faivre-Baumann, Z. Lenkei, and P. Dournaud. Dynamics of somatostatin type 2A receptor cargoes in living hippocampal neurons. *Journal of Neuroscience*, 28(17):4336–4349, 2008.

(Cited on pages 12, 53, 57, and 112.)

[150] K. Licha, C. Hessenius, A. Becker, P. Henklein, M. Bauer, S. Wisniewski, B. Wiedenmann, and W. Semmler. Synthesis, characterization, and biological properties of cyanine-labeled somatostatin analogues as receptor-targeted fluorescent probes. *Bioconjugate Chemistry*, 12(1):44–50, 2001.
(Cited on pages 58, 88, 90, and 125.)

[151] E. G. R. Lichtenauer-Kaligis, V. A. S. Dalm, Spma Oomen, D. M. Mooij, P. M. van Hagen, S. W. J. Lamberts, and L. J. Hofland. Differential expression of somatostatin receptor subtypes in human peripheral blood mononuclear cell subsets. *European Journal of Endocrinology*, 150 (4):565–577, 2004.
(Cited on page 51.)

[152] Jeff W. Lichtman and Jose-Angel Conchello. Fluorescence microscopy. *Nat Meth*, 2(12):910–919, 2005.
(Cited on page 12.)

[153] D. S. Lidke, P. Nagy, R. Heintzmann, D. J. Arndt-Jovin, J. N. Post, H. E. Grecco, E. A. Jares-Erijman, and T. M. Jovin. Quantum dot ligands provide new insights into erbB/HER receptor-mediated signal transduction. *Nature Biotechnology*, 22(2):198–203, 2004.
(Cited on page 191.)

[154] Andrew M. F. Liu and Yung H. Wong. Activation of nuclear factor κ_B by somatostatin type 2 receptor in pancreatic acinar AR42J Cells Involves $G_{\alpha 14}$ and multiple signaling components: a mechanism requiring protein kinase C, calmodulin-dependent kinase II, ERK and c-Src. *J. Biol. Chem.*, 280(41):34617–34625, 2005.
(Cited on page 48.)

[155] K. K. Liu, F. Chen, P. Y. Chen, T. J. F. Lee, C. L. Cheng, C. C. Chang, Y. P. Ho, and J. I. Chao. Alpha-bungarotoxin binding to target cell in a developing visual system by carboxylated nanodiamond. *Nanotechnology*, 19(20):10, 2008.
(Cited on page 157.)

[156] Q. S. Liu, R. Cescato, D. A. Dewi, J. Rivier, J. C. Reubi, and A. Schonbrunn. Receptor signaling and endocytosis are differentially regulated by somatostatin analogs. *Molecular Pharmacology*, 68(1):90–101, 2005.
(Cited on pages 43, 53, 56, and 111.)

[157] Y. Liu, Z. N. Gu, J. L. Margrave, and V. N. Khabashesku. Functionalization of nanoscale diamond powder: Fluoro-, alkyl-, amino-, and amino acid-nanodiamond derivatives. *Chemistry of Materials*, 16(20):3924–3930, 2004.
(Cited on page 161.)

[158] Shengcong Liufu, Hanning Xiao, and Yuping Li. Investigation of PEG adsorption on the surface of zinc oxide nanoparticles. *Powder Technology*, 145(1):20–24, 2004.
(Cited on page 144.)

[159] W. H. Ludlam and L. Anthony. Safety Review: Dose Optimization of Somatostatin Analogs in Patients with Acromegaly and Neuroendocrine Tumors. *Advances in Therapy*, 28(10):825–841, 2011.
(Cited on pages 47, 48, and 58.)

[160] R. Mahtab, H. H. Harden, and C. J. Murphy. Temperature- and salt-dependent binding of long DNA to protein-sized quantum dots: Thermodynamics of "inorganic protein"-DNA interactions. *Journal of the American Chemical Society*, 122(1):14–17, 2000.
(Cited on page 191.)

[161] N. B. Manson, J. P. Harrison, and M. J. Sellars. Nitrogen-vacancy center in diamond: Model of the electronic structure and associated dynamics. *Physical Review B*, 74(10):104303, 2006.
(Cited on page 29.)

[162] K. Manzoor, S. Johny, D. Thomas, S. Setua, D. Menon, and S. Nair. Bio-conjugated luminescent quantum dots of doped ZnS: a cyto-friendly system for targeted cancer imaging. *Nanotechnology*, 20(6):13, 2009.
(Cited on page 27.)

[163] Maria Julia Marinissen and J. Silvio Gutkind. G-protein-coupled receptors and signaling networks: emerging paradigms. *Trends in Pharmacological Sciences*, 22(7):368–376, 2001.
(Cited on page 40.)

[164] Belting Mattias. Heparan sulfate proteoglycan as a plasma membrane carrier. *Trends in Biochemical Sciences*, 28(3):145–151, 2003.
(Cited on page 149.)

[165] L. P. McGuinness, YanY, StaceyA, D. A. Simpson, L. T. Hall, MaclaurinD, PrawerS, MulvaneyP, WrachtrupJ, CarusoF, R. E. Scholten, and L. C. L. Hollenberg. Quantum measurement and orientation tracking of fluorescent nanodiamonds inside living cells. *Nat Nano*, 6(6):358–363, 2011.
(Cited on page 33.)

[166] I. L. Medintz, H. T. Uyeda, E. R. Goldman, and H. Mattoussi. Quantum dot bioconjugates for imaging, labelling and sensing. *Nature Materials*, 4(6):435–446, 2005.
(Cited on pages 26 and 191.)

[167] W. H. Melhuish. Nomenclature, Symbols, Units and their Usage in Spectrochemical Analysis VI: MOLECULAR LUMINESCENCE SPECTROSCOPY. *Pure and Applied Chemistry*, 56(2):231–245, 1984.

(Cited on pages 10 and 11.)

[168] X. Michalet, F. F. Pinaud, L. A. Bentolila, J. M. Tsay, S. Doose, J. J. Li, G. Sundaresan, A. M. Wu, S. S. Gambhir, and S. Weiss. Quantum dots for live cells, in vivo imaging, and diagnostics. *Science*, 307(5709):538–544, 2005.
(Cited on pages 15 and 26.)

[169] Graeme Milligan and Evi Kostenis. Heterotrimeric G-proteins: a short history. *British Journal of Pharmacology*, 147(S1):S46–S55, 2006.
(Cited on pages 40 and 41.)

[170] Yoshimi Mita. Change of absorption spectra in type-Ib diamond with heavy neutron irradiation. *Physical Review B*, 53(17):11360–11364, 1996.
(Cited on pages 29 and 31.)

[171] A. Miyazaki, Y. Tsuda, S. Fukushima, T. Yokoi, T. Vantus, G. Bokonyi, E. Szabo, A. Horvath, G. Keri, and Y. Okada. New cyclic somatostatin analogues containing a pyrazinone ring: Importance of Tyr for antiproliferative activity. *Bioorganic & Medicinal Chemistry Letters*, 18 (23):6199–6201, 2008.
(Cited on page 47.)

[172] Vadym N. Mochalin, Olga Shenderova, Dean Ho, and Yury Gogotsi. The properties and applications of nanodiamonds. *Nat Nano*, 7(1):11–23, 2012.
(Cited on page 33.)

[173] M R Montminy, R H Goodman, S J Horovitch, and J F Habener. Primary structure of the gene encoding rat preprosomatostatin. *Proceedings of the National Academy of Sciences*, 81 (11):3337–3340, 1984.
(Cited on page 42.)

[174] Vanessa Carla Furtado Mosqueira, Philippe Legrand, Annette Gulik, Olivier Bourdon, Ruxandra Gref, Denis Labarre, and Gillian Barratt. Relationship between complement activation, cellular uptake and surface physicochemical aspects of novel PEG-modified nanocapsules. *Biomaterials*, 22(22):2967–2979, 2001.
(Cited on pages 144, 145, and 149.)

[175] C. B. Murray, D. J. Norris, and M. G. Bawendi. Synthesis and characterization of nearly monodisperse CdE (E = sulfur, selenium, tellurium) semiconductor nanocrystallites. *Journal of the American Chemical Society*, 115(19):8706–8715, 1993.
(Cited on page 25.)

[176] Suman Nag, Arkarup Bandyopadhyay, and S. Maiti. Spatial pH Jump Measures Chemical Kinetics in a Steady-State System. *The Journal of Physical Chemistry A*, 113(18):5269–5272, 2009.

(Cited on page 15.)

[177] F. Neugart, A. Zappe, F. Jelezko, C. Tietz, J. P. Boudou, A. Krueger, and J. Wrachtrup. Dynamics of diamond nanoparticles in solution and cells. *Nano Letters*, 7(12):3588–3591, 2007.
(Cited on pages 33 and 211.)

[178] P. Neumann, R. Kolesov, V. Jacques, J. Beck, J. Tisler, A. Batalov, L. Rogers, N. B. Manson, G. Balasubramanian, F. Jelezko, and J. Wrachtrup. Excited-state spectroscopy of single NV defects in diamond using optically detected magnetic resonance. *New Journal of Physics*, 11(1): 013017, 2009.
(Cited on page 33.)

[179] M. P. Nikitin, T. A. Zdobnova, S. V. Lukash, O. A. Stremovskiy, and S. M. Deyev. Protein-assisted self-assembly of multifunctional nanoparticles. *Proceedings of the National Academy of Sciences of the United States of America*, 107(13):5827–5832, 2010.
(Cited on page 163.)

[180] M. Nirmal, D. J. Norris, M. Kuno, M. G. Bawendi, Al L. Efros, and M. Rosen. Observation of the "Dark Exciton" in CdSe Quantum Dots. *Physical Review Letters*, 75(20):3728–3731, 1995.
(Cited on pages 23 and 27.)

[181] D. Nouel, G. Gaudriault, M. Houle, T. Reisine, J. P. Vincent, J. Mazella, and A. Beaudet. Differential internalization of somatostatin in COS-7 cells transfected with SST1 and SST2 receptor subtypes: A confocal microscopic study using novel fluorescent somatostatin derivatives. *Endocrinology*, 138(1):296–306, 1997.
(Cited on pages 53, 87, 109, 124, and 211.)

[182] C. Nunn, D. Cervia, D. Langenegger, L. Tenaillon, R. Bouhelal, and D. Hoyer. Comparison of functional profiles at human recombinant somatostatin sst(2) receptor: simultaneous determination of intracellular Ca2+ and luciferase expression in CHO-K1 cells. *British Journal of Pharmacology*, 142(1):150–160, 2004.
(Cited on pages 49, 85, 98, 104, and 105.)

[183] Manfred Ogris, Peter Steinlein, Sebastian Carotta, Sylvia Brunner, and Ernst Wagner. DNA/polyethylenimine transfection particles: Influence of ligands, polymer size, and PEGylation on internalization and gene expression. *The AAPS Journal*, 3(3):43–53, 2001.
(Cited on page 149.)

[184] G. Olias, C. Viollet, H. Kusserow, J. Epelbaum, and W. Meyerhof. Regulation and function of somatostatin receptors. *Journal of Neurochemistry*, 89(5):1057–1091, 2004.
(Cited on pages 42, 45, 47, and 49.)

[185] N. Panchuk-Voloshina, R. P. Haugland, J. BishopStewart, M. K. Bhalgat, P. J. Millard, F. Mao, and W. Y. Leung. Alexa dyes, a series of new fluorescent dyes that yield exceptionally bright, photostable conjugates. *Journal of Histochemistry and Cytochemistry*, 47(9):1179, 1999.
(Cited on pages 14, 15, and 16.)

[186] W. J. Parak, D. Gerion, D. Zanchet, A. S. Woerz, T. Pellegrino, C. Micheel, S. C. Williams, M. Seitz, R. E. Bruehl, Z. Bryant, C. Bustamante, C. R. Bertozzi, and A. P. Alivisatos. Conjugation of DNA to silanized colloidal semiconductor nanocrystalline quantum dots. *Chemistry of Materials*, 14(5):2113–2119, 2002.
(Cited on page 191.)

[187] Y. C. Patel. Somatostatin and its receptor family. *Frontiers in Neuroendocrinology*, 20(3): 157–198, 1999.
(Cited on pages 42, 43, 44, 45, 49, 124, and 211.)

[188] Y. C. Patel, R. Panetta, E. Escher, M. Greenwood, and C. B. Srikant. Expression of multiple somatostatin receptor genes in AtT-20 cells - Evidence for a novel somatostatin-28 selective receptor subtype. *Journal of Biological Chemistry*, 269(2):1506–1509, 1994.
(Cited on pages 72 and 102.)

[189] S. Pathak, S. K. Choi, N. Arnheim, and M. E. Thompson. Hydroxylated quantum dots as luminescent probes for in situ hybridization. *Journal of the American Chemical Society*, 123 (17):4103–4104, 2001.
(Cited on pages 25 and 26.)

[190] George Paxinos and Charles Watson. *The Rat Brain in Stereotaxic Coordinates, Deluxe Fourth Edition (with CD-ROM)*. Academic Press, 1998.
(Cited on page 46.)

[191] Robert M. Pearlstein. A two-quantasome theory of Chlorophyll - A fluorescence in green plant photosynthesis. *Proceedings of the National Academy of Sciences*, 52(3):824–830, 1964.
(Cited on page 11.)

[192] Xiaogang Peng, Michael C. Schlamp, Andreas V. Kadavanich, and A. P. Alivisatos. Epitaxial Growth of Highly Luminescent CdSe/CdS Core/Shell Nanocrystals with Photostability and Electronic Accessibility. *Journal of the American Chemical Society*, 119(30):7019–7029, 1997.
(Cited on page 25.)

[193] P. S. Pennefather, S. Heisler, and J. F. MacDonald. A potassium conductance contributes to the action of somatostatin-14 to suppress ACTH secretion. *Brain research*, 444(2):346–350, 1988.
(Cited on pages 44, 48, 49, 85, 98, 101, and 126.)

[194] E. Perevedentseva, C. Y. Cheng, P. H. Chung, J. S. Tu, Y. H. Hsieh, and C. L. Cheng. The interaction of the protein lysozyme with bacteria E-coli observed using nanodiamond labelling. *Nanotechnology*, 18(31):7, 2007.
(Cited on page 157.)

[195] Sandeep Menon Perinchery, Unnikrishnan Kuzhiumparambil, Subramanyam Vemulpad, and Ewa M. Goldys. The influence of indoxyl sulfate and ammonium on the autofluorescence of human urine. *Talanta*, 80(3):1269–1276, 2010.
(Cited on page 12.)

[196] F. Pinaud, D. King, H. P. Moore, and S. Weiss. Bioactivation and cell targeting of semiconductor CdSe/ZnS nanocrystals with phytochelatin-related peptides. *Journal of the American Chemical Society*, 126(19):6115–6123, 2004.
(Cited on page 26.)

[197] E. Pohl, A. Heine, G. M. Sheldrick, Z. Dauter, K. S. Wilson, J. Kallen, W. Huber, and P. J. Pfaffli. Structure of Octreotide, a Somatostatin analog. *Acta Crystallographica Section D-Biological Crystallography*, 51:48–59, 1995.
(Cited on page 195.)

[198] Lucien Pradayrol, Hans Jornvall, Viktor Mutt, and Andre Ribet. N-terminally extended somatostatin: The primary structure of somatostatin-28. *Febs Letters*, 109(1):55–58, 1980.
(Cited on page 42.)

[199] T. Pradeep. *NANO The essentials.* Tata McGraw-Hill, New Delhi, 1 edition, 2008.
(Cited on page 2.)

[200] Narayan Pradhan, David Goorskey, Jason Thessing, and Xiaogang Peng. An Alternative of CdSe Nanocrystal Emitters: Pure and Tunable Impurity Emissions in ZnSe Nanocrystals. *Journal of the American Chemical Society*, 127(50):17586–17587, 2005.
(Cited on page 27.)

[201] D. H. Presky and A. Schonbrunn. Somatostatin pretreatment increases the number of somatostatin receptors in GH4C1 pituitary cells and does not reduce cellular responsiveness to somatostatin. *J. Biol. Chem.*, 263(2):714–721, 1988.
(Cited on pages 50 and 71.)

[202] K. V. Purtov, A. I. Petunin, A. E. Burov, A. P. Puzyr, and V. S. Bondar. Nanodiamonds as Carriers for Address Delivery of Biologically Active Substances. *Nanoscale Research Letters*, 5 (3):631–636, 2010.
(Cited on pages 162 and 163.)

[203] Terry D. Reisine, Yan-ling Zhang, and Ronald D. Sekura. Pertussis toxin blocks somatostatin's inhibition of stimulated cyclic AMP accumulation in anterior pituitary tumor cells. *Biochemical and Biophysical Research Communications*, 115(3):794–799, 1983.
(Cited on pages 48, 49, 107, and 126.)

[204] Joanna Rejman, Volker Oberle, Inge S Zuhorn, and Dick Hoekstra. Size-dependent internalization of particles via the pathways of clathrin- and caveolae-mediated endocytosis. *Biochemical Journal*, 377(1):159–169, 2004.
(Cited on pages 132, 147, and 148.)

[205] J. Ren, G. Bell, D. H. Coy, and F. C. Brunicardi. Activation of Human Somatostatin Receptor Type 2 Causes Inhibition of Cell Growth in Transfected HEK293 but Not in Transfected CHO Cells. *Journal of Surgical Research*, 71(1):13–18, 1997.
(Cited on pages 86 and 87.)

[206] J. C. Reubi, J. Laissue, E. Krenning, and S. W. J. Lamberts. Somatostatin receptors in human cancer: Incidence, characteristics, functional correlates and clinical implications. *The Journal of Steroid Biochemistry and Molecular Biology*, 43(13):27–35, 1992.
(Cited on pages 46, 47, and 58.)

[207] J. C. Reubi, J. C. Schaer, R. Markwalder, B. Waser, U. Horisberger, and J. Laissue. Distribution of somatostatin receptors in normal and neoplastic human tissues: Recent advances and potential relevance. *Yale Journal of Biology and Medicine*, 70(5-6):471–479, 1997.
(Cited on pages 46 and 189.)

[208] James H. Richardson. *Handbook for the light microscope: A User's Guide.* Noyes Publications, c1991, Park Ridge, N.J., U.S.A., 1991.
(Cited on page 12.)

[209] M. Rocheville, D. C. Lange, U. Kumar, R. Sasi, R. C. Patel, and Y. C. Patel. Subtypes of the somatostatin receptor assemble as functional homo- and heterodimers. *Journal of Biological Chemistry*, 275(11):7862–7869, 2000.
(Cited on pages 53, 54, 55, and 203.)

[210] A.L. Rogach. *Semiconductor nanocrystal quantum dots: synthesis, assembly, spectroscopy and applications.* Springer, 2008.
(Cited on pages 19, 22, 23, 24, and 26.)

[211] L. J. Rogers, S. Armstrong, M. J. Sellars, and N. B. Manson. Infrared emission of the NV centre in diamond: Zeeman and uniaxial stress studies. *New Journal of Physics*, 10(10):103024, 2008.
(Cited on pages 29, 30, and 31.)

[212] Susan P. Rohrer, Elizabeth T. Birzin, Ralph T. Mosley, Scott C. Berk, Steven M. Hutchins, Dong-Ming Shen, Yusheng Xiong, Edward C. Hayes, Rupa M. Parmar, Forrest Foor, Sudha W.

Mitra, Sylvia J. Degrado, Min Shu, John M. Klopp, Sheng-Jian Cai, Allan Blake, Wanda W. S. Chan, Alex Pasternak, Lihu Yang, Arthur A. Patchett, Roy G. Smith, Kevin T. Chapman, and James M. Schaeffer. Rapid Identification of Subtype-Selective Agonists of the Somatostatin Receptor Through Combinatorial Chemistry. *Science*, 282(5389):737–740, 1998.
(Cited on page 42.)

[213] D. Roosterman, N. E. I. Brune, O. J. Kreuzer, M. Feld, S. Pauser, K. Zarse, M. Steinhoff, and W. Meyerhof. Intracellular degradation of somatostatin-14 following somatostatin-receptor 3-mediated endocytosis in rat insulinoma cells. *Febs Journal*, 275(19):4728–4739, 2008.
(Cited on pages 56 and 127.)

[214] D. Roosterman, C. Kempkes, G. S. Cottrell, B. E. Padilla, N. W. Bunnett, C. W. Turck, and M. Steinhoff. Endothelin-converting enzyme-1 degrades internalized somatostatin-14. *Endocrinology*, 149(5):2200–2207, 2008.
(Cited on pages 52 and 127.)

[215] Dirk Roosterman, Oliver J. Kreuzer, Nicole Brune, Graeme S. Cottrell, Nigel W. Bunnett, Wolfgang Meyerhof, and Martin Steinhoff. Agonist-Induced Endocytosis of Rat Somatostatin Receptor 1. *Endocrinology*, 148(3):1050–1058, 2007.
(Cited on pages 57 and 127.)

[216] Daniel M. Rosenbaum, Soren G. F. Rasmussen, and Brian K. Kobilka. The structure and function of G-protein-coupled receptors. *Nature*, 459(7245):356–363, 2009.
(Cited on page 40.)

[217] G. Sallen, A. Tribu, T. Aichele, R. Andr, L. Besombes, C. Bougerol, M. Richard, S. Tatarenko, K. Kheng, and J. Ph Poizat. Subnanosecond spectral diffusion of a single quantum dot in a nanowire. *Physical Review B*, 84(4):041405, 2011.
(Cited on page 22.)

[218] S. Santra, K. M. Wang, R. Tapec, and W. H. Tan. Development of novel dye-doped silica nanoparticles for biomarker application. *Journal of Biomedical Optics*, 6(2):160–166, 2001.
(Cited on page 211.)

[219] P. Sarret, D. Nouel, C. Dal Farra, J. P. Vincent, A. Beaudet, and J. Mazella. Receptor-mediated internalization is critical for the inhibition of the expression of growth hormone by somatostatin in the pituitary cell line AtT-20. *Journal of Biological Chemistry*, 274(27):19294–19300, 1999.
(Cited on pages 54, 85, and 87.)

[220] Ronak Savla, Oleh Taratula, Olga Garbuzenko, and Tamara Minko. Tumor targeted quantum dot-mucin 1 aptamer-doxorubicin conjugate for imaging and treatment of cancer. *Journal of Controlled Release*, 153(1):16–22, 2011.
(Cited on page 191.)

[221] Jana Say, Caryn van Vreden, David Reilly, Louise Brown, James Rabeau, and Nicholas King. Luminescent nanodiamonds for biomedical applications. *Biophysical Reviews*, 3(4):171–184, 2011.
(Cited on page 33.)

[222] Andrew V. Schally. Oncological Applications of Somatostatin Analogues. *Cancer Research*, 48 (24 Part 1):6977–6985, 1988.
(Cited on pages 46 and 47.)

[223] E. W. Schlag, H. L. Selzle, S. Schneider, and J. G. Larsen. Single photon phase fluorimetry with nanosecond time resolution. *Review of Scientific Instruments*, 45(3):364–367, 1974.
(Cited on page 11.)

[224] Anja Schmidt and Michael N. Hall. Signaling to the actin cytoskeleton. *Annual Review of Cell & Developmental Biology*, 14(1):305, 1998.
(Cited on page 36.)

[225] A. Schonbrunn, Q. Liu, D. A. Dewi, W. Liu, and M. S. Bee. Distinct phosphorylation sites in the SST2A somatostatin receptor control internalization, desensitization, and arrestin binding. *Molecular Pharmacology*, 73(2):292–304, 2008.
(Cited on pages 57 and 86.)

[226] Amanda M. Schrand, Houjin Huang, Cataleya Carlson, John J. Schlager, Eiji sawa, Saber M. Hussain, and Liming Dai. Are Diamond Nanoparticles Cytotoxic? *The Journal of Physical Chemistry B*, 111(1):2–7, 2006.
(Cited on page 33.)

[227] A. Schroedter, H. Weller, R. Eritja, W. E. Ford, and J. M. Wessels. Biofunctionalization of silica-coated CdTe and gold nanocrystals. *Nano Letters*, 2(12):1363–1367, 2002.
(Cited on pages 192 and 211.)

[228] Bertrand Schwartz, Corinne Benoist, Bassima Abdallah, Daniel Scherman, Jean-Paul Behr, and Barbara A. Demeneix. Lipospermine-Based Gene Transfer into the Newborn Mouse Brain Is Optimized by a Low Lipospermine/DNA Charge Ratio. *Human Gene Therapy*, 6(12):1515–1524, 1995.
(Cited on page 149.)

[229] D. Sehgal and I. K. Vijay. A method for the high-efficiency water-soluble corbodiimide-mediated amidation. *Analytical Biochemistry*, 218(1):87–91, 1994.
(Cited on pages 26, 170, and 171.)

[230] Lahja Seveus, Mikko Visl, Stina Syrjnen, Minna Sandberg, Ari Kuusisto, Raimo Harju, Juha Salo, Ilkka Hemmil, Hannu Kojola, and Erkki Soini. Time-resolved fluorescence imaging of

europium chelate label in immunohistochemistry and in situ hybridization. *Cytometry*, 13(4): 329–338, 1992.
(Cited on page 13.)

[231] P. Sharma, S. Brown, G. Walter, S. Santra, and B. Moudgil. Nanoparticles for bioimaging. *Advances in Colloid and Interface Science*, 123:471–485, 2006.
(Cited on page 12.)

[232] Rafael A. Shimkunas, Erik Robinson, Robert Lam, Steven Lu, Xiaoyang Xu, Xue-Qing Zhang, Houjin Huang, Eiji Osawa, and Dean Ho. Nanodiamond-insulin complexes as pH-dependent protein delivery vehicles. *Biomaterials*, 30(29):5720–5728, 2009.
(Cited on pages 158 and 175.)

[233] J. Singh. *Electronic and optoelectronic properties of semiconductor structures*. Cambridge University Press, 2003.
(Cited on pages 20 and 21.)

[234] G. D. Slooter, A. Mearadji, W. A. P. Breeman, R. L. Marquet, M. De Jong, E. P. Krenning, and C. H. J. van Eijck. Somatostatin receptor imaging, therapy and new strategies in patients with neuroendocrine tumours. *British Journal of Surgery*, 88(1):31–40, 2001.
(Cited on pages 47 and 58.)

[235] B. R. Smith, M. Niebert, T. Plakhotnik, and A. V. Zvyagin. Transfection and imaging of diamond nanocrystals as scattering optical labels. *Journal of Luminescence*, 127(1):260–263, 2007.
(Cited on page 159.)

[236] W. V. Smith, P. P. Sorokin, I. L. Gelles, and G. J. Lasher. Electron-Spin Resonance of Nitrogen Donors in Diamond. *Physical Review*, 115(6):1546–1552, 1959.
(Cited on page 29.)

[237] M. A. Sobhan, V. K. Sreenivasan, M. J. Withford, and E. M. Goldys. Non-specific internalization of laser ablated pure gold nanoparticles in pancreatic tumor cell. *Colloids and surfaces. B, Biointerfaces*, 92:190–5, 2012.
(Cited on page ix.)

[238] Beatriz Sobrino, Mara Brin, and Angel Carracedo. SNPs in forensic genetics: a review on SNP typing methodologies. *Forensic Science International*, 154(23):181–194, 2005.
(Cited on page 12.)

[239] V. K. A. Sreenivasan, E. A. Ivukina, W. Deng, T. A. Kelf, T. A. Zdobnova, S. V. Lukash, B. V. Veryugin, O. A. Stremovskiy, A. V. Zvyagin, and S. M. Deyev. Barstar:barnase - a versatile platform for colloidal diamond bioconjugation. *Journal of Materials Chemistry*, 21(1):65–68, 2011.

(Cited on pages ix, 33, 153, 175, 176, 177, and 211.)

[240] V. K. A. Sreenivasan, O. A. Stremovskiy, T. A. Kelf, M. Heblinski, A. K. Goodchild, M. Connor, S. M. Deyev, and A. V. Zvyagin. Pharmacological Characterization of a Recombinant, Fluorescent Somatostatin Receptor Agonist. *Bioconjugate Chemistry*, 22(9):1768–1775, 2011.
(Cited on pages ix, 12, 13, and 83.)

[241] V. K. A. Sreenivasan, E. J. Kim, A. K. Goodchild, M. Connor, and A. V. Zvyagin. Targeting somatostatin receptors using *in situ*-bioconjugated fluorescent nanoparticles. *Nanomedicine*, 2012.
(Cited on pages ix and 187.)

[242] M. Sriram, G. A. Vandermarel, Hlpf Roelen, J. H. Vanboom, and A. H. J. Wang. Conformation of B-DNA containing O6-ethyl-G-C base-pairs stabilized by minor groove binding-drugs - Molecular structure of D(CGC E6G AATTCGCG complexed with Hoechst-33258 or Hoechst -33342. *Embo Journal*, 11(1):225–232, 1992.
(Cited on page 13.)

[243] Christopher M. Starr, R. Irene Masada, Chuck Hague, Elisa Skop, and John C. Klock. Fluorophore-assisted carbohydrate electrophoresis in the separation, analysis, and sequencing of carbohydrates. *Journal of Chromatography A*, 720(12):295–321, 1996.
(Cited on page 12.)

[244] Paul M Stewart. Current Therapy for Acromegaly. *Trends in Endocrinology & Metabolism*, 11 (4):128–132, 2000.
(Cited on pages 46 and 47.)

[245] G. G. Stokes. On the Change of Refrangibility of Light. *Philosophical Transactions of the Royal Society of London*, 142(ArticleType: research-article / Full publication date: 1852 /):463–562, 1852.
(Cited on pages 7 and 9.)

[246] T. Stroh, A. C. Jackson, C. Dal Farra, A. Schonbrunn, J. P. Vincent, and A. Beaudet. Receptor-mediated internalization of somatostatin in rat cortical and hippocampal neurons. *Synapse*, 38 (2):177–186, 2000.
(Cited on pages 54, 87, and 190.)

[247] M. Z. Strowski and A. D. Blake. Function and expression of somatostatin receptors of the endocrine pancreas. *Molecular and Cellular Endocrinology*, 286(1-2):169–179, 2008.
(Cited on pages 46, 58, and 86.)

[248] M. Z. Strowski, R. M. Parmar, A. D. Blake, and J. M. Schaeffer. Somatostatin Inhibits Insulin and Glucagon Secretion via Two Receptor Subtypes: An in Vitro Study of Pancreatic Islets from Somatostatin Receptor 2 Knockout Mice. *Endocrinology*, 141(1):111–117, 2000.

(Cited on page 46.)

[249] P. P. Surujpaul, C. Gutirrez-Wing, B. Ocampo-Garca, F. de M. Ramrez, C. Arteaga de Murphy, M. Pedraza-Lpez, M. A. Camacho-Lpez, and G. Ferro-Flores. Gold nanoparticles conjugated to [Tyr3]Octreotide peptide. *Biophysical Chemistry*, 138(3):83–90, 2008.
(Cited on page 211.)

[250] T. Takimoto, T. Chano, S. Shimizu, H. Okabe, M. Ito, M. Morita, T. Kimura, T. Inubushi, and N. Komatsu. Preparation of Fluorescent Diamond Nanoparticles Stably Dispersed under a Physiological Environment through Multistep Organic Transformations. *Chemistry of Materials*, 22(11):3462–3471, 2010.
(Cited on pages 162 and 164.)

[251] P. Tamarat, T. Gaebel, J. R. Rabeau, M. Khan, A. D. Greentree, H. Wilson, L. C. L. Hollenberg, S. Prawer, P. Hemmer, F. Jelezko, and J. Wrachtrup. Stark shift control of single optical centers in diamond. *Physical Review Letters*, 97(8), 2006.
(Cited on page 33.)

[252] J. E. Taylor. Somatostatin (SSTR2) receptors mediate phospholipase C-independent Ca^{2+} mobilization in rat AR42J pancreas cells. *Biochemical and Biophysical Research Communications*, 214(1):81–85, 1995.
(Cited on pages 49, 104, and 105.)

[253] Allan J. Tobin and Richard E. Morel. *Asking about cells.* Saunders college publising, Orlando, Florida, 1997.
(Cited on pages 35 and 36.)

[254] H. Tomura, F. Okajima, M. Akbar, M. A. Majid, K. M. Sho, and Y. Kondo. Transfected human somatostatin receptor-type-2, SSTR2, not only inhibits adenylate-cyclase but also stimulates phospholipase-C and Ca2+ mobilization. *Biochemical and Biophysical Research Communications*, 200(2):986–992, 1994.
(Cited on pages 49 and 98.)

[255] G. Tulipano, D. Soldi, M. Bagnasco, M. D. Culler, J. E. Taylor, D. Cocchi, and A. Giustina. Characterization of new selective somatostatin receptor subtype-2 (sst2) antagonists, BIM-23627 and BIM-23454. Effects of BIM-23627 on GH release in anesthetized male rats after short-term high-dose dexamethasone treatment. *Endocrinology*, 143(4):1218–1224, 2002.
(Cited on page 112.)

[256] G. Tulipano, R. Stumm, M. Pfeiffer, H. J. Kreienkamp, V. Hollt, and S. Schulz. Differential beta-arrestin trafficking and endosomal sorting of somatostatin receptor subtypes. *Journal of Biological Chemistry*, 279(20):21374–21382, 2004.
(Cited on pages 53, 55, 56, and 86.)

[257] W Uhl, M W Bchler, P Malfertheiner, H G Beger, G Adler, W Gaus, and the German Pancreatitis Study Group. A randomised, double blind, multicentre trial of octreotide in moderate to severe acute pancreatitis. *Gut*, 45(1):97–104, 1999.
(Cited on page 47.)

[258] Yoshiaki Urakubo, Teikichi Ikura, and Nobutoshi Ito. Crystal structural analysis of proteinprotein interactions drastically destabilized by a single mutation. *Protein Science*, 17(6):1055–1065, 2008.
(Cited on pages 165 and 194.)

[259] K. Ushizawa, Y. Sato, T. Mitsumori, T. Machinami, T. Ueda, and T. Ando. Covalent immobilization of DNA on diamond and its verification by diffuse reflectance infrared spectroscopy. *Chemical Physics Letters*, 351(1-2):105–108, 2002.
(Cited on pages 160 and 161.)

[260] Bernard Valeur and Mario N. Berberan-Santos. A Brief History of Fluorescence and Phosphorescence before the Emergence of Quantum Theory. *Journal of Chemical Education*, 88(6): 731–738, 2011.
(Cited on pages 7, 9, and 12.)

[261] J. van Zuylen. The microscopes of Antoni van Leeuwenhoek. *Journal of Microscopy*, 121(3): 309–328, 1981.
(Cited on page 12.)

[262] G. H. J. vanEijck, S. W. J. Lamberts, Lcjm Lemaire, H. Jeekel, F. T. Bosman, J. C. Reubi, H. A. Bruining, and E. P. Krenning. The use of somatostatin receptor scintigraphy in the differential diagnosis of pancreatic duct cancers and islet cell tumors. *Annals of Surgery*, 224(2):119–124, 1996.
(Cited on pages 47 and 58.)

[263] Mirko Vanetti, Monika Kouba, Xiaomin Wang, Gudrun Vogt, and Volker Hllt. Cloning and expression of a novel mouse somatostatin receptor (SSTR2B). *Febs Letters*, 311(3):290–294, 1992.
(Cited on page 44.)

[264] Alipasha Vaziri, Jianyong Tang, Hari Shroff, and Charles V. Shank. Multilayer three-dimensional super resolution imaging of thick biological samples. *Proceedings of the National Academy of Sciences*, 105(51):20221–20226, 2008.
(Cited on page 13.)

[265] Daniel F. Veber, Frederick W. Holly, Ruth F. Nutt, Susan J. Bergstrand, Stephen F. Brady, Ralph Hisrschmann, Monroe S. Glitzer, and Richard Saperstein. Highly active cyclic and bicyclic somatostatin analogues of reduced ring size. *Nature*, 280(5722):512–514, 1979.

(Cited on page 42.)

[266] Daniel F. Veber, Roger M. Freidinger, Debra Schwenk Perlow, William J. Paleveda, Frederick W. Holly, Robert G. Strachan, Ruth F. Nutt, Byron H. Arison, Carl Homnick, William C. Randall, Monroe S. Glitzer, Richard Saperstein, and Ralph Hirschmann. A potent cyclic hexapeptide analogue of somatostatin. *Nature*, 292(5818):55–58, 1981.
(Cited on pages 42 and 45.)

[267] N. Viguerie, J. P. Esteve, C. Susini, N. Vaysse, and A. Ribet. Processing of receptor-bound somatostatin: internalization and degradation by pancreatic acini. *Am J Physiol Gastrointest Liver Physiol*, 252(4):G535–542, 1987.
(Cited on pages 44, 50, and 208.)

[268] Arnaud Vonarbourg, Catherine Passirani, Patrick Saulnier, and Jean-Pierre Benoit. Parameters influencing the stealthiness of colloidal drug delivery systems. *Biomaterials*, 27(24):4356–4373, 2006.
(Cited on pages 142 and 149.)

[269] J. Walker. Optical absorption and luminescence in diamond. *Reports on Progress in Physics*, 42(10):1605, 1979.
(Cited on page 28.)

[270] B. Waser, M. L. Tamma, R. Cescato, H. R. Maecke, and J. C. Reubi. Highly Efficient In Vivo Agonist-Induced Internalization of sst(2) Receptors in Somatostatin Target Tissues. *Journal of Nuclear Medicine*, 50(6):936–941, 2009.
(Cited on pages 200 and 201.)

[271] P. C. Weber, D. H. Ohlendorf, J. J. Wendoloski, and F. R. Salemme. Structural origins of high-affinity biotin binding to streptavidin. *Science*, 243(4887):85, 1989.
(Cited on page 193.)

[272] G. Weckbecker, I. Lewis, R. Albert, H. A. Schmid, D. Hoyer, and C. Bruns. Opportunities in somatostatin research: Biological, chemical and therapeutic aspects. *Nature Reviews Drug Discovery*, 2(12):999–1017, 2003.
(Cited on pages 42, 44, 46, and 58.)

[273] X. Y. Wu, H. J. Liu, J. Q. Liu, K. N. Haley, J. A. Treadway, J. P. Larson, N. F. Ge, F. Peale, and M. P. Bruchez. Immunofluorescent labeling of cancer marker Her2 and other cellular targets with semiconductor quantum dots. *Nature Biotechnology*, 21(1):41–46, 2003.
(Cited on page 191.)

[274] Y Yamada, S R Post, K Wang, H S Tager, G I Bell, and S Seino. Cloning and functional characterization of a family of human and mouse somatostatin receptors expressed in brain,

gastrointestinal tract, and kidney. *Proceedings of the National Academy of Sciences*, 89(1): 251–255, 1992.
(Cited on pages 40, 44, 189, and 211.)

[275] H. S. Yang, P. H. Holloway, and S. Santra. Water-soluble silica-overcoated CdS : Mn/ZnS semiconductor quantum dots. *Journal of Chemical Physics*, 121(15):7421–7426, 2004.
(Cited on page 25.)

[276] A. D. Yoffe. Semiconductor quantum dots and related systems: Electronic, optical, luminescence and related properties of low dimensional systems. *Advances in Physics*, 50(1):1–208, 2001.
(Cited on page 25.)

[277] S. J. Yu, M. W. Kang, H. C. Chang, K. M. Chen, and Y. C. Yu. Bright fluorescent nanodiamonds: No photobleaching and low cytotoxicity. *Journal of the American Chemical Society*, 127(50):17604–17605, 2005.
(Cited on pages 31, 33, 132, 155, and 211.)

[278] T. A. Zdobnova, S. G. Dorofeev, P. N. Tananaev, R. B. Vasiliev, T. G. Balandin, E. F. Edelweiss, O. A. Stremovskiy, I. V. Balalaeva, I. V. Turchin, E. N. Lebedenko, V. P. Zlomanov, and S. M. Deyev. Fluorescent immunolabeling of cancer cells by quantum dots and antibody scFv fragment. *Journal of Biomedical Optics*, 14(2):–, 2009.
(Cited on pages 163, 191, and 211.)

[279] Leshuai W. Zhang and Nancy A. Monteiro-Riviere. Mechanism of Quantum Dot Nanoparticle Cellular Uptake. *Toxicol. Sci.*, page kfp087, 2009.
(Cited on pages 109, 132, 141, and 142.)

[280] Sulin Zhang, Ju Li, George Lykotrafitis, Gang Bao, and Subra Suresh. Size-Dependent Endocytosis of Nanoparticles. *Advanced Materials*, 21(4):419–424, 2009.
(Cited on pages 147 and 148.)

[281] A. Zhukov, F. Gareeva, A. Aleksenskii, and A. Vul. Surface charge of detonation nanodiamond particles in aqueous solutions of simple 1 : 1 Electrolytes. *Colloid Journal*, 72(5):640–646, 2010.
(Cited on page 158.)

[282] A. Zimmer, J. Kreuter, and J. R. Robinson. Studies on the transport pathway of PBCA nanoparticles in ocular tissues. *Journal of Microencapsulation*, 8(4):497–504, 1991.
(Cited on page 19.)

[283] K. R. Zinn and T. R. Chaudhuri. The type 2 human somatostatin receptor as a platform for reporter gene imaging. *European Journal of Nuclear Medicine and Molecular Imaging*, 29(3): 388–399, 2002.
(Cited on page 47.)

[284] A. V. Zvyagin and N. B. Manson. *Optical and spin properties of nitrogen-vacancy colour-centres in diamond crystals, nanodiamonds and proximity to surfaces.* Elsevier, 2 edition, in press. (Cited on page 31.)